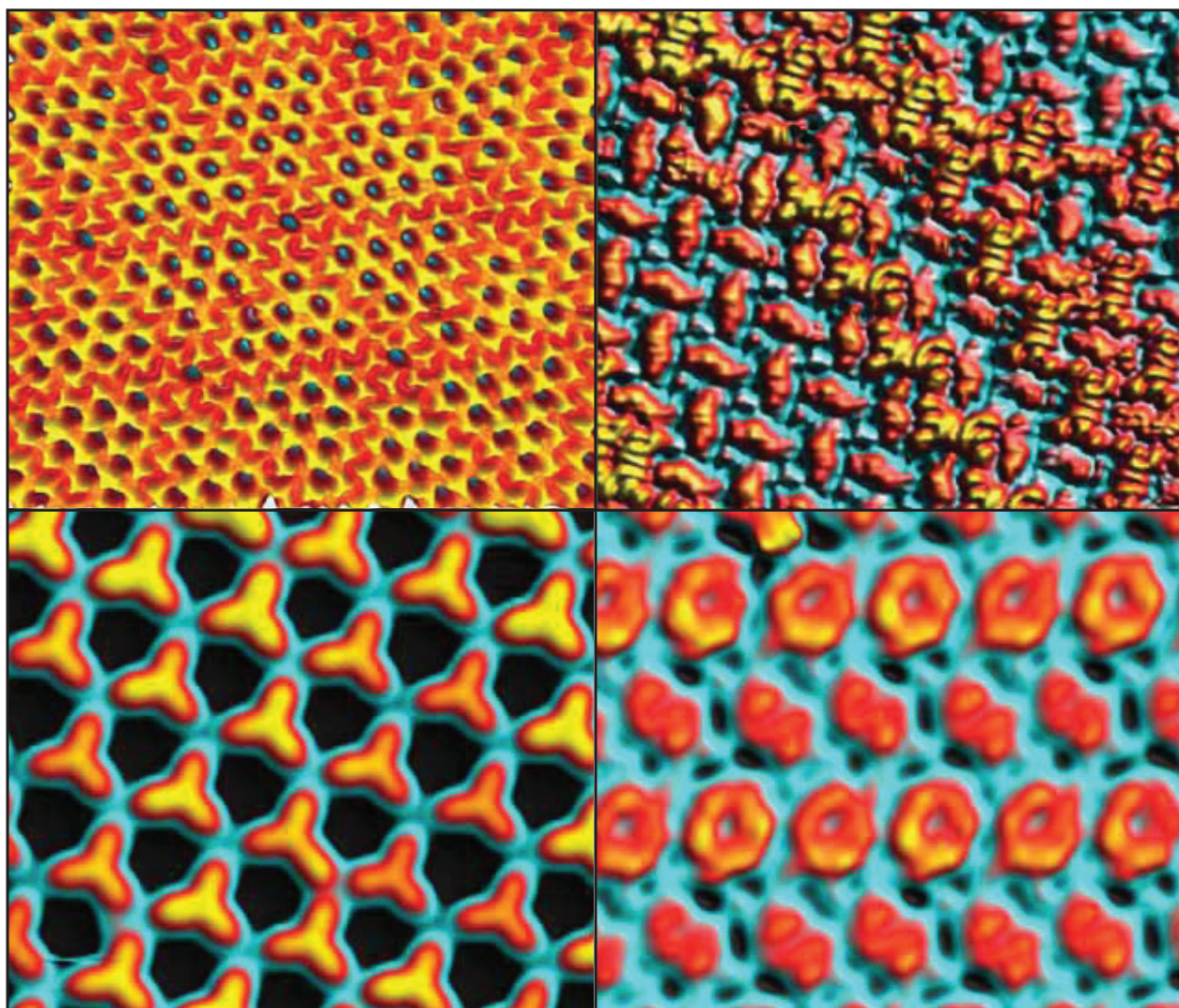# Magnetic and Electronic Properties of Supramolecular Architectures on Metal Surfaces

by Tobias R. Umbach

Magnetic and Electronic Properties of Supramolecular Architectures on Metal Surfaces

Doctoral Thesis

of

Tobias R. Umbach

submitted to the
Department of Physics
of the
Freie Universität Berlin

August 2013

Diese Arbeit entstand in der Arbeitsgruppe von Prof. Dr. Katharina Franke am Fachbereich Physik der Freien Universität Berlin.

Berlin, August 2013

Kurzfassung

Die vorliegende Dissertation beschäftigt sich mit selbstorganisierten supramolekularen Strukturen auf Metalloberflächen und deren magnetischen und elektronischen Eigenschaften. Zur Untersuchung der Systeme werden verschiedene experimentelle Methoden wie Rastertunnelmikroskopie (RTM), Röntgenabsorptionsspektroskopie (XAS), zirkularer magnetischer Röntgendichroismus (XMCD) und Dichtefunktionaltheorie (DFT) angewendet. Zum einen wird der Effekt von intermolekularen Wechselwirkungen und Molekül-Substrat-Wechselwirkungen auf die Selbstanordnung, den Ladungstransfer sowie den Ladungszustand der supramolekularen Strukturen untersucht. Zum anderen werden die magnetischen Eigenschaften und die Möglichkeit, magnetisch gekoppelte supramolekulare Strukturen herzustellen, behandelt.

Im ersten Teil der Arbeit werden drei verschiedene Systeme auf einer Au(111)-Metalloberfläche untersucht: Im ersten Fall organisieren sich Na-Atome und TCNQ-Moleküle zu geordneten Strukturen und es erfolgt ein Ladungstransfer von einem Elektron von den Na-Atomen zu den TCNQ-Molekülen. Die TCNQ-Moleküle sind negativ geladen. Das ungepaarte Elektron wechselwirkt mit den Leitungselektronen der Au(111)-Metalloberfläche und es kommt zum Auftreten einer Spin-Kondo-Resonanz. Das einfach besetzte Orbital der TCNQ-Moleküle wird durch die Anwesenheit der positiv geladenen Na-Kationen stark verformt. Tauscht man TCNQ-Moleküle durch TNAP-Moleküle aus, kann eine Wechselwirkung des Na-TNAP-Systems mit der Au(111)-Metalloberfläche beobachtet werden. Die TNAP-Moleküle im Na-TNAP-System sind ebenfalls mit einem Elektron geladen. Allerdings zeigen nur spezifische TNAP-Moleküle eine Spin-Kondo-Resonanz, abhängig vom Adsorptionsplatz bzgl. der Au(111) $23x\sqrt{3}$ Rekonstruktion. Werden Na-Atome durch das organische TTF-Molekül ersetzt, bilden sich geordnete TTF-TNAP-Strukturen. Durch das Zusammenspiel von Molekül-Molekül- und Molekül-Substrat-Wechselwirkungen sind die TNAP-Moleküle im TTF-TNAP-System mit mehr als einem Elektron geladen. Dies stellt einen erhöhten Ladungstransfer dar, verglichen mit dem entsprechenden Festkörper.

Der zweite Teil der Arbeit behandelt supramolekulare Strukturen aus Molekülen und Übergangsmetallatomen. Die Struktureigenschaften dieser metallorganischen Netzwerke können durch die geeignete Wahl der Moleküle und Metallatome gezielt verändert werden. Cu-Atome und T4PT-Moleküle auf einer Ag(111)- und Cu(111)-Metalloberfläche organisieren sich in einem supramolekularen Netzwerk mit hexagonaler Struktur. Das Cu-T4PT-System zeigt auf beiden Metalloberflächen identische elektronische und strukturelle Eigenschaften. Die Architektur des Netzwerkes wird hierbei durch die Bindung zwischen Molekülen und Metallatomen bestimmt. Tauschen wir die Cu-Atome durch Fe-Atome aus, entstehen geordnete Fe-T4PT-Strukturen auf einer Au(111)-Metalloberfläche. Das Fe-T4PT-System weist eine Doppelschichtstruktur auf. In der ersten Lage bilden jeweils drei Pyridin-Endgruppen und ein Fe-Atom ein dreifach symmetrisches Bindungsmotiv. Ein zusätzliches T4PT-Molekül ist auf jedem Fe-Atom zentriert. Die Fe-Atome befinden sich daher in einer dreidimensionalen Koordinationsumgebung und weisen einen Spinzustand $S = 2$ und eine magnetische Anisotropie auf. Zudem konnte zum ersten Mal für ein solches supramolekulares Netzwerk eine ferromagnetische Kopplung zwischen den Fe-Atomen nachgewiesen werden. Der Kopplungsmechanismus beruht dabei wahrscheinlich auf einem Superaustausch durch die T4PT-Moleküle. Im letzten Teil wird die Abhängigkeit der Netzwerkarchitektur bzgl. der funktionellen Molekülendgruppen untersucht. Dabei können die strukturellen und elektronischen Eigenschaften durch den Austausch der funktionellen Endgruppen gezielt geändert werden.

Abstract

This thesis deals with self-organized supramolecular structures on metal surfaces and their magnetic and electronic properties. To study the systems, various experimental methods such as Scanning Tunneling Microscopy (STM), X-Ray Absorption Spectroscopy (XAS), and X-Ray Magnetic Circular Dichroism (XMCD) combined with Density Functional Theory (DFT) are applied. We focus on several aspects of supramolecular structures on metal surfaces. First, the role of intermolecular and molecule-substrate interactions are discussed regarding their effect on the self-assembling, charge state, and charge transfer. Second, we are interested in the magnetic state of metal atoms embedded in metal-organic networks and the possibility of producing magnetically coupled supramolecular structures.

In the first part, three different systems of charge-transfer materials on a Au(111) surface were examined. In the first case, Na atoms and TCNQ molecules organize into ordered structures accompanied with a charge transfer from the Na atoms to the TCNQ molecules. Thus, the TCNQ molecules are negatively charged with exactly one electron. The unpaired spin can be detected by its interaction with Au(111) surface conduction electrons by a Kondo resonance. Moreover, it could be shown that the singly occupied TCNQ orbital is deformed by the presence of the positively charged Na cations affecting the spatial distribution of the Kondo resonance. When we exchange TCNQ with TNAP molecules we observe that the underlying metal surface plays a significant role on the electronic properties of the TNAP molecules. The TNAP molecules within the Na-TNAP layer are charged with one electron. But only specific TNAP molecules show a spin-Kondo resonance depending on their adsorption site on the Au(111) herringbone reconstruction. This is attributed to adsorption-site dependent molecule-substrate interactions. Replacing the Na atoms by organic TTF molecules also leads to the formation of ordered structures. By the interplay of molecule-molecule and molecule-substrate interactions the TNAP molecules in the TTF-TNAP system are charged with more than one electron enhancing the charge compared to the bulk compound.

The second part of the thesis is focused on supramolecular structures consisting of molecules and transition metal atoms. We show that the network architecture is determined by the choice of the molecules and metal atoms and can be selectively altered. The different network architectures also imply different electronic and magnetic properties. The first described network consists of Cu atoms and T4PT molecules and exhibits a hexagonal structure on both the Ag(111) and Cu(111) surfaces. The identical structural and electronic properties on both surfaces indicate that the formation of the system is mainly ruled by the metal-ligand bonds. Furthermore, the Cu atoms within the network have no magnetic moment. By replacing the Cu with Fe atoms an ordered Fe-T4PT network with a bilayer structure is formed on a Au(111) surface. The first layer exhibits a three-fold bonding node consisting of three pyridine end groups and a central Fe atom. An additional T4PT molecule is located on top of each Fe site. Thus, the Fe atoms are placed in a three-dimensional coordination cavity. The Fe atoms are in a high spin state and exhibit a magnetic anisotropy with an easy-axis out-of-plane orientation. Moreover, for the first time, a ferromagnetic coupling between the Fe atoms in such a system can be observed. The exchange coupling mechanism is presumably based on super-exchange through the T4PT molecules. In the final part the dependence of the supramolecular architecture with respect to the molecular functional end groups is investigated. In this case we could change the network structure from bilayer to single-layer by the adequate choice of ending groups. This has also an impact on the network electronic properties.

Contents

INTRODUCTION

Over the past decades the size of device components in information and storage technology was gradually decreased to match the rising demand for higher storage densities and computing power. The storage density of modern magnetic hard disks increases further and further by decreasing the individual bit size. The ultimate limit of the bit size is determined by the thermal stability of its magnetic grains. If the grain size is too small their magnetization can become thermally unstable and can not hold the stored information reliably. Another important aspect is the size of a single transistor in modern semiconductor based integrated circuits. The present value is about 22 nm [1, 2] and will be soon decreased further [3]. Today's semiconductor industry uses top-down methods allowing large-scale parallel fabrication of devices. The corresponding fabrication methods are based on optical lithography, thus, the feature size is limited by the wavelength of the light [4]. Intensive work is done by the semiconductor industry to develop new fabrication methods, short-wavelength optical elements and new radiation sources to further decrease the size of devices and therefore to increase the number of transistors per chip. On the other hand, by decreasing the size of devices new effects come into play, namely quantum effects, dominating the material properties and, thus, determining a lower limit of miniaturization [5].

Introducing new materials and new design concepts can help to overcome those limitations described above. As pointed out by R. Feynman [6], the control of matter at the atomic scale can lead to devices based on quantum effects. This opens a whole new way of device design. R. Feynman even envisioned the use of single atoms or molecules as building blocks of electronic devices. Molecules are small and the power of chemical synthesis offers an almost infinite pool of geometries and functional groups. In fact, a single atom transistor [7] or molecule transistor [8] have been demonstrated. However, the actual realization in an industrial application is still a long way off. In this prospect a key issue is the growth of molecular electronic devices or materials on surfaces. The controlled fabrication of nanostructures with atomic-precision with top-down fabrication methods is difficult to accomplish. Instead a bottom-up approach can be used.

New powerful fabrication and characterization methods have been developed, which allow to image and manipulate single atoms and molecules, namely the scanning tunneling microscope [9] and atomic force microscope [10]. The fast progress of scanning probe techniques allows today the creation of nanostructures atom by atom [11–13] or molecule by molecule [14]. However, this method is still time consuming and not suitable for large scale fabrication.

Self-assembled supramolecular structures play an important role in nature, for example the conformation of proteins or the DNA. This approach can also be used to grow ordered nanostructures on surfaces [15–27]. Self-assembling processes are based on interactions between the components, such as molecules and atoms, leading to ordered structures. The growth process itself relies on the interplay of kinetics and thermodynamics [15].

In this prospect, organic molecules exhibit the ability to form bonds mediated by their functional parts. This can lead to the formation of extended networks [15, 28, 29]. Self-assembling is based on a multitude of different interactions as illustrated in Fig. 1.1(a) in the case of molecules and single metal atoms adsorbed on a surface. These interactions can be classified in weak hydrogen [23, 26, 27, 30], Van-der-Waals [31, 32] and also strong donor-acceptor [25, 29, 33–35], metal-ligand [18, 28, 36] and covalent bonds [37, 38]. The resulting structure depends on the complicated competition between all of these interactions. However, using heterogeneous systems consisting of two species (organic/inorganic or organic/organic) presents a rather complex situation. On the other hand the use of constituents with complementary properties can turn this complexity into an advantage. For example, by combining molecular or metal species with different chemical properties, in particular the ionization energy and electron affinity, charge transfer processes can take place leading to a charge redistribution. The charge state and also the localization of charge are important quantities playing a significant role for the conductivity [25], organic magnetism [25, 29], and superconductivity [34] in such systems.

Another important aspect of molecular networks on surfaces is the understanding of molecule-surface interactions. First of all, the surface may act as a template. The symmetry of the surface can lead to a preferred adsorption at certain sites of the surface and can be used to direct molecular growth processes [38]. On the other hand, adsorbates tend to adsorb at surface sites with a high chemical reactivity or in other words with a high adsorption energy [39]. Furthermore, metal surfaces can also act as an additional charge reservoir and the adsorption of molecules can lead to charge transfer [24, 40, 41]. But also alignment of electronic levels [42, 43] or screening effects [44] can take place leading to a change of the electronic properties of the adsorbed molecules. To understand the interplay of all these interactions, it is important to tailor the properties of the molecule-substrate interfaces.

A particular interesting class of materials is based on the combination of transition metal atoms and molecules. Metal-ligand bonds are characterized by their directionality [18, 19, 28]. The self-assembling process of metal atoms combined with organic linkers is a very promising approach for the design of custom-made magnetic nanostructures and allows to grow highly ordered defect-free networks with tunable sizes and structures [18, 19, 28]. This is illustrated in Fig. 1.1(b). Within the network the metal atoms are arranged in an ordered structure (cf Fig. 1.1(c)), which can be programmed by the structure of the used functionalized molecules. Interestingly, also the type of metal atom determines the number of bonding ligands as will be shown in chapter 4 of this thesis. A continuative approach is the use of magnetic metal atoms allowing the growth of ordered spin-arrays. An intriguing question is, whether it is possible to couple the single spins and to induce a collective magnetic ground state like it is illustrated in Fig. 1.1(c) by the collinear alignment of the metal atoms spins. This would offer interesting perspectives for future spintronic and magnetic storage applications.

In this thesis an analysis of selected molecule-based systems on metal surfaces is presented. These systems are studied with different experimental techniques. The structural and electronic analysis was
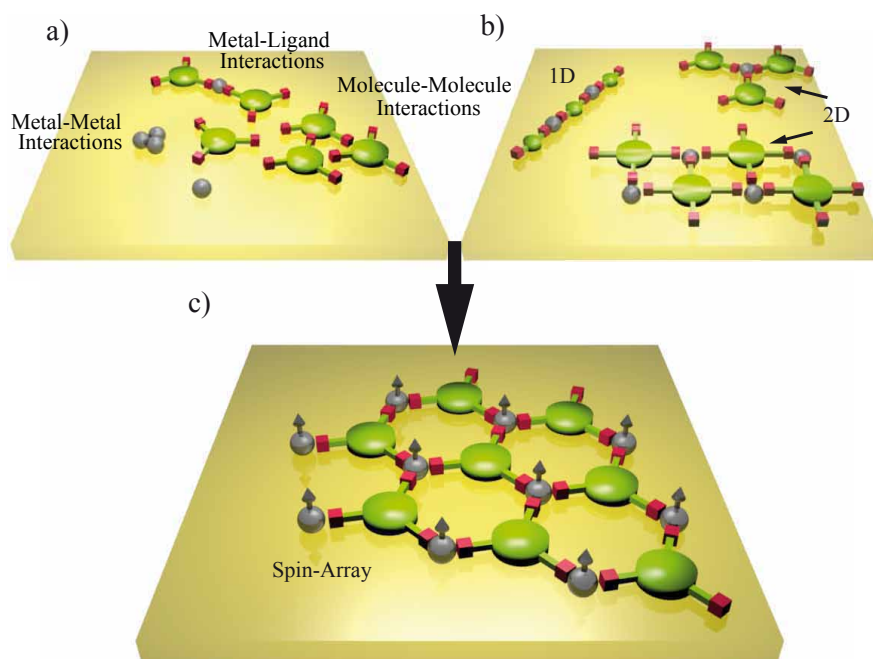
Figure 1.1: (a) Different types of interactions between molecules and metal atoms on a surface. (b) Different numbers of functional end groups lead to different self-assembled superstructures. Thus, 1-dimensional chain-like or 2-dimensional superstructures can be grown. (c) An ordered array of magnetic metal atoms within a metal-organic network.

done with a low-temperature (LT) scanning tunneling microscope (STM). The high spatial resolution of the STM combined with scanning tunneling spectroscopy (STS) measurements makes it a perfect tool to study molecular systems on surfaces. Additional x-ray absorption spectroscopy (XAS) and x-ray magnetic circular dichroism (XMCD) measurements were performed to investigate the magnetic and chemical properties of the studied metal-organic networks. The outline of the thesis is as follows:

Chapter 2 gives a short introduction of the different experimental techniques used in this thesis.

Chapter 3 starts with a brief introduction to charge transfer complexes (CTC) and the Kondo effect. We use the Kondo effect to spatially map the transfered electron within the charge transfer complex. Then we will focus on charge transfer processes and charge distributions of different CTC systems deposited on a Au(111) metal surface. The chapter is divided into three experimental parts. The first part deals with the self-assembled layer of 7, 7, 8, 8-tetracyanoquinodimethane (TCNQ) and Na atoms. This sections will focus on the corresponding charge distribution within the Na-TCNQ layer. The second part is devoted to the layer consisting of 11, 11, 12, 12-tetracyanonaptho-2, 6-quinodimethane (TNAP) molecules and Na atoms. An important aspect of this part is the influence of the surface on the charge transfer processes. Finally, we address the question if we can enhance the charge transfer to more than 1 electron in a layer composed of tetrathiafulvalene (TTF) and TNAP.

Chapter 4 is devoted to the study of different metal-organic networks on metal surfaces regarding their structural, electronic and magnetic properties. The first part of the chapter gives a short introduction to magnetism of a single atom in the framework of the spin-Hamiltonian approach used to describe the magnetic properties of the networks. The networks are studied by STM, XMCD,

and XAS. This chapter is divided into three parts. The first part describes in detail the electronic, magnetic and structural properties of the metal-organic network consisting of 2, 4, 6-tris(4-pyridyl)-1, 3, 5-triazine (T4PT) and Cu atoms. In the second part of this chapter we replaced the Cu by Fe atoms. The Fe-T4PT metal-organic network exhibits a two-layer structure and is examined regarding its magnetic properties. The Fe-T4PT network shows an easy axis magnetic anisotropy and reveals the presence of ferromagnetic exchange coupling between the coordinated Fe sites. The third part deals with different metal-organic networks consisting of Co atoms and 1, 3, 5-Tri(pyridin-4-yl)benzene (T4PB) and 2, 4, 6-Tris(4-benzonitrile)-1, 3, 5-triazine (T4CPT) molecules, respectively. Here we investigate the effect of different ligands on the structural properties of the corresponding network. The Co-T4PB network is composed of two layers similar to the Fe-T4PT system. T4CPT molecules possess different functional end groups compared to the T4PB molecules. In contrast, the Co-T4CPT network exhibits a single-layer structure. Changing the functional groups of the molecular ligand prevents the double layer formation of the resulting metal-organic network.

Chapter 5 summarizes the results of this thesis and gives an outlook.

2

EXPERIMENTAL TECHNIQUES

2.1 Introduction

This chapter deals with the experimental techniques used within this thesis. Two distinct techniques were used in order to investigate the structural, electronic and magnetic properties of the analyzed metal-organic and charge transfer networks. We used STM and STS to characterize the adsorption configuration, bonding motif and the electronic structure of the molecular-metal systems and XAS and XMCD to elucidate their chemical and magnetic properties.

2.2 Theory of Scanning Tunneling Microscopy

With the invention of the Scanning Tunneling Microscope (STM) by G. Binning and H. Rohrer in 1981 a new pathway in surface science was opened [9]. The STM provides an insight into the physics at the nanoscale in real space. Its high spatial resolution allows to investigate the locality of physical and chemical phenomena. The high spatial resolution of the STM is reached by using a local probe, a sharp metallic tip, to scan the sample. Besides the imaging capability, the STM allows also to obtain information about the electronic properties of the sample and also to manipulate atoms and molecules on the surface with the STM tip [12]. Further improvements lead to development of techniques like spin-polarized STM (SPSTM) [45], vibrational spectroscopy based on tip-enhanced Raman scattering [46], or STM induced light emission [47–51].

The working principle of a STM is based on the quantum tunneling effect. Due to the wave nature, an electron is able to penetrate into a potential barrier, which is forbidden in a classical physical picture. The STM junction, consisting of the STM tip and the metal surface (see Fig. 2.1), can be approximately described as a simple tunnel junction of two metal electrodes. When the two metal electrodes come close to each other (at a distance of a few Å) and a bias voltage is applied across the junction a net current flow I_T can be detected.

The tunneling current I_T shows an exponential dependence on the tip-surface distance z:

$$I_T \propto V e^{-2\frac{\sqrt{2m\phi}}{\hbar}z} \tag{2.1}$$

Figure 2.1: The STM tunneling geometry. The separation surface $\vec{S}$ is indicated by the red dashed line. Adapted from Ref. [52].
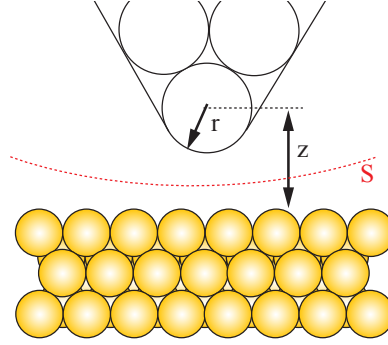
2.2.1 Tersoff-Hamann Theory of STM

Shortly after the invention of the STM, Tersoff and Hamann developed a model based on first-order perturbation theory to explain its working principle [52]. Within this model the tip and the surface are treated as two separated subsystems Σ_1 and Σ_2 with two orthogonal sets of eigenfunctions.

Using a first-order perturbation approach, the tunneling current I_T can be expressed as follows [52]:

$$I_T = \frac{2\,\pi\,e}{\hbar} \sum_{\mu\nu} f(E_\mu)(1 - f(E_\nu - eV)) |M_{\mu\nu}|^2 \delta(E_\mu - E_\nu) \tag{2.2}$$

Here $f(E_\mu)$ and $f(E_\nu)$ are the Fermi distributions of tip and sample, respectively. V is the sample bias voltage, $|M_{\mu\nu}|$ is the tunneling matrix element between the tip (ϕ_μ) and surface (ϕ_ν) electronic states and $E_{\mu,\nu}$ is the corresponding energy. The tunneling matrix element depends on the electronic states of the tip and sample and in particular on the overlap of the corresponding wave functions. Assuming small voltages V and low temperatures T the expression in equation 2.2 can be simplified to [53]:

$$I_T = \frac{2\pi}{\hbar}\,e^2 V \sum_{\mu\nu} |M_{\mu\nu}|^2 \delta(E_\mu - E_F)\delta(E_\nu - E_F) \tag{2.3}$$

Here E_F refers to the Fermi energy. The matrix element $|M_{\mu\nu}|$ can now be evaluated within the framework of Bardeen's theory of tunneling and reads [53, 54]:

$$M_{\mu\nu} = -\frac{\hbar^2}{2\,m} \int d\vec{S}(\phi_\mu \cdot \nabla \phi_\nu - \phi_\nu \cdot \nabla \phi_\mu) \tag{2.4}$$

The quantity in the parenthesis is the current operator and the surface $\vec{S}$ lies between the tip and surface electrode (see Fig. 2.1).

To evaluate the matrix element defined in equation 2.4, Tersoff and Hamann made the assumption of an asymptotic spherical potential at the tip. Hence, only the very last atom at the tip apex is considered and is described by a s-wave function. The matrix element reads then [53]:

$$M_{\mu\nu} = -\frac{\hbar^2}{2\,m}\,4\,\pi\,k^{-1}\,\Omega_t^{-\frac{1}{2}}\,k\,Re^{k\,R}\phi_\nu(\vec{r}_0) \tag{2.5}$$

Here Ω_t is the probe volume, k is the inverse decay constant of the wave function in the gap region ($k = -2\frac{\sqrt{2m\phi}}{\hbar}$), R is the radius of the curvature and $\vec{r}_0$ is the center of curvature of the tip (see
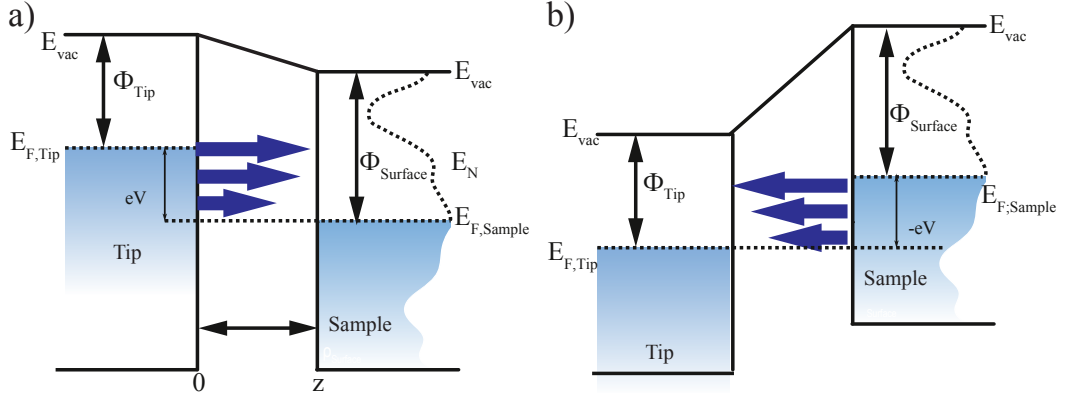
Figure 2.2: Energy level diagram of the STM junction. (a) A positive sample bias voltage is applied leading to a shift of the Fermi energies of sample and tip. Electrons can tunnel from occupied electronic states of the tip into unoccupied electronic states of the sample. (b) Reversing the sample bias voltage leads to a current flow from the sample to the tip electrode. Hence, electrons from occupied electronic states of the sample tunnel into unoccupied electronic states of the tip.

Fig. 2.1). Using the expression in equation 2.5 the tunneling current between the tip and the sample I_T reads [53]:

$$I_T = 32\pi^3 \hbar^{-1} e^2 V \phi^2 \rho_t(E_F) R^2 k^{-4} e^{2kR} \cdot \sum_v |\psi_\mu(\vec{r}_0)|^2 \delta(E_v - E_F), \qquad (2.6)$$

where $\rho_t(E_F)$ is the tip density of states per unit volume, ϕ corresponds to the work function of the tip and sample, which are assumed to be same. The expression $\sum_v |\psi_\mu(\vec{r}_0)|^2 \rho(E_v - E_F)$ refers to the local density of states (LDOS) of the sample surface ρ_S at the position defined by $\vec{r}_0$ and at E_F. Assuming that the DOS $\rho_t(E_F)$ of the tip is rather constant in the corresponding energy window one can easily see that the expression of the tunneling current I_T in equation 2.6 is proportional to the LDOS of the sample.

However, in the above described derivation of the tunneling current I_T within the framework of Tersoff and Hamann a low sample bias voltage and a s-wave tip were assumed. In particular, applying a finite sample bias voltage V to the STM junction leads to a shift of the Fermi energies of tip and sample with respect to each other (see Fig. 2.2). Hence, applying a positive sample bias voltage V lead to a net current flow from occupied tip electronic states into unoccupied sample electronic states (see Fig. 2.2(a)). On the other hand a negative sample bias voltage $-V$ shift the sample Fermi energy $E_{F,\,Sample}$ above the tip Fermi energy $E_{F,\,Tip}$. Now electrons can tunnel from occupied sample electronic states into unoccupied tip electronic states. To take the effect of a finite sample bias voltage V into account, we can generalize the expression of the tunneling current I_T in equation 2.2 and reach the WKB approximated solution:

$$I_T(V, z) = \frac{4\pi e}{\hbar} \int_{-\infty}^{+\infty} (f_T(E - eV) - f_S(E)) \rho_T(E - eV) \rho_S(E) |M_{ST}(E, eV, z)|^2 \, dE \qquad (2.7)$$

Here $\rho_T(r, E)$ and $\rho_S(r, E)$ correspond to the density of states of tip and sample, respectively, $f_S(E)$ and $f_T(E)$ are the Fermi distribution of the tip and sample electrode and M_{ST} is the tunneling matrix element. In the zero temperature regime the Fermi distribution f_T and f_S are sharp step-functions [55]

and equation 2.7 simplifies to:

$$I_T(V,z) = \frac{4\pi e}{\hbar} \int_{E_F}^{E_F+eV} \rho_T(E-eV)\rho_S(E) \left|M_{ST}(E,V,z)\right|^2 dE \tag{2.8}$$

Here $|M_{ST}(E,V,z)|^2)$ corresponds to the tunneling probability $T(E,V,z)$ and reads [55, 56]:

$$\left|M_{ST}(E,eV,z)\right|^2 = T(E,V,z) = exp\left[-\frac{2z\sqrt{2m}}{\hbar}\sqrt{\frac{\phi_S+\phi_T}{2} + \frac{eV}{2} - E}\right] \tag{2.9}$$

The tunneling probability $T(E,V,z)$ depends on the work functions of the sample and tip electrode and also on the applied sample bias voltage. Interestingly, $T(E,V,z)$ reflects the exponential behavior of the tunneling current I_T with z, as shown in the previous section 2.2. $T(E,V,z)$ also reveals that the tunneling probability is largest for states close to E_F independently of which electrode is positively biased with respect to the other. This is also illustrated in Fig. 2.2(a) and (b) by the size of the blue arrows. In the case of constant tunneling probability $T(E,V,z)$ and constant tip density of states $\rho_T(r,E)$ the tunneling current $I_T(V,z)$ is in first approximation proportional to the sample density of states $\rho_S(r,E)$ integrated over the energy window $[E_F, E_F+eV]$.

The good agreement of experimental results and theoretical simulations [57–61] based on the Tersoff-Hamann theory corroborate its approximation of flat feature-less tip density of states and the determine role of the very last atom at the tip apex.

2.2.2   STM Topography

Figure 2.3(a) shows a schematic illustration of a STM set-up. The STM tip is fixed to a piezo element. By applying appropriate voltage signals to the contacts of the piezo element, this is done by the control unit, the STM tip is approached towards the surface till a tunneling current I_T is detected. While the STM tip scans over the surface a feedback loop, regulated by the control unit, adjusts the tip-surface distance and keeps the tunneling current I_T constant. Recording the variations of the tip height, while the tip scans the surface, leads then to a topography image. The above described topography mode is known as the constant current mode and reflects a contour of constant LDOS (cf Fig. 2.3(b)). Another operation mode is the constant height mode depicted in Fig. 2.3(c), where the feedback loop is switched off. Thus, the tip-surface distance is constant and the recorded image reflects the changes in the tunneling current I_T. Since the constant current mode allows a safer operation of the STM without crashing the tip into surface it is the preferred operation mode.

2.3   Scanning Tunneling Spectroscopy

Scanning Tunneling Spectroscopy (STS) is an extension of STM allowing to obtain spectroscopic information of the sample electronic structure with sub-nanometer resolution. The expression of the tunneling current I_T in equation 2.7 is proportional to the LDOS of the sample $\rho_S(r,E)$. To learn something about the electronic structure of the sample it would be desirable to measure directly $\rho_S(r,E)$ at different energies. The problem is now that the sample LDOS ρ_S is convoluted with other signals (see equation 2.7). Let us assume a tunneling current I_T in a positive bias window $E_F + eV$,
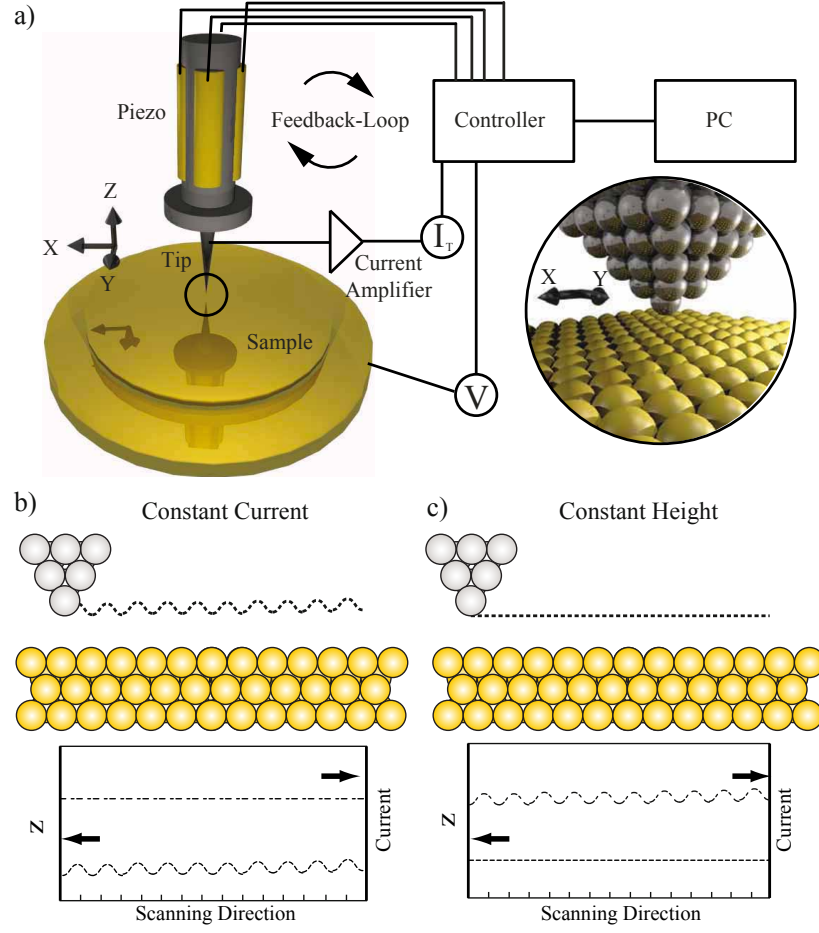
Figure 2.3: (a) Schema of a STM junction. The tunneling current I_T between tip and sample is measured. The tip is moved in the x-y plane by the movement of the piezo element regulated by the control unit, therefore, the surface is imaged. The inset shows a close-up of the STM tunneling junction. (b) Schematic illustration of the constant current topography mode (CCM). (c) Schematic illustration of the constant height topography mode (CHM).

which can be described by equation 2.8. The first derivative of the tunneling current I_T with respect to the applied bias voltage V reads [62, 63]:

$$\frac{dI_t}{dV} \propto \rho_T(E_F)\rho_S(E_F + e\,V)T(E_F + e\,V,\, eV,\, z)$$
$$+ \int_{E_F}^{E_F + e\,V} \rho_T(E - e\,V)\rho_S(E)\frac{T(E,\, V,\, z)}{dE}dE \tag{2.10}$$
$$+ \int_{E_F}^{E_F + e\,V} \frac{d\rho_T(E - e\,V)}{dE}\rho_S(E)T(E,\, V,\, z)dE$$

By using several approximation, we can simplify the above equation. Assuming that the tip LDOS ρ_T is constant leads to $\frac{d\rho_T(E - e\,V)}{dE} = 0$. Furthermore, we assume that the tunneling coefficient $T(E, V, z)$ is constant in the bias windows of interest. Therefore, the expression for the tunneling current I_T
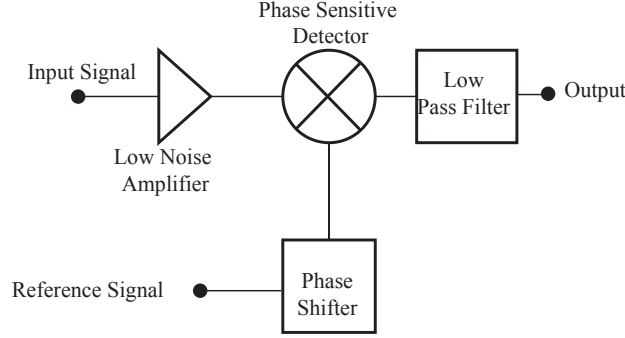
Figure 2.4: (a) Block diagram of a Lock-In amplifier used for STS.

becomes:

$$\frac{dI_T}{dV} \propto \rho_S(E_F + e\,V) \tag{2.11}$$

Hence, the dI/dV signal is proportional to the LDOS of the sample $\rho_S(E_F + e\,V)$ at the energy $E_F + e\,V$. In general this relation is sufficiently accurate and the dI/dV signal presents a good approximation of the sample LDOS $\rho_S(E_F + e\,V)$. However, for high sample bias voltages the voltage dependence of the tunneling probability $T(E, V, z)$ has to be taken into account [64, 65]. To record a dI/dV spectrum the STM tip is positioned at a spot of interest (surface or adsorbate) and the feedback loop is opened at a certain current I and voltage V. The tip-surface distance z stays constant during the dI/dV spectrum. Then the applied sample bias voltage is ramped within a defined voltage window and the dI/dV signal is recorded using a Lock-In amplifier. The main working principle of Lock-In amplifier is treated in the following section.

2.3.1 Lock-In Amplifier

A Lock-In amplifier allows to measure small AC signals and is based on a technique called phase sensitive detection (PSD). The Lock-In amplifier adds a small sinusoidal voltage $V_{mod} \cdot sin(\omega t)$ to the sample bias voltage V. This leads in the case of the STM also to modulation of the tunneling current I_T. The modulated signal is then compared to a reference signal. Only the component of the signal with the right frequency and phase is detected and contributes to the signal. Usually the modulation frequency ω is set to be much larger (≈ 1 kHz) than the typical working frequency of the STM feedback controller in order to prevent cross talk.

Now we want to derive how we can measure the first derivative of the current, the dI/dV signal, by using a Lock-In amplifier. For doing that we first add a small sinusoidal voltage to the sample bias voltage. The tunneling current I_T reads then:

$$I_T(V + V_{mod}\,sin(\omega\,t + \phi)) \propto \int_0^{e\,V + e\,V_{mod}\,sin(\omega\,t)} \rho_S(E)dE \tag{2.12}$$

Now we expand the current $I_T(V + V_{mod}\ sin(\omega\ t + \phi))$ in a Taylor series:

$$I_T(V + V_{mod}\ sin(\omega\ t)) \propto \left(\int_0^{e\ V + e\ V_{mod}\ sin(\omega\ t)} \rho_S(E) dE \right) \tag{2.13}$$

$$+ \left(\rho_S(E)\ e\ V_{mod}\ sin(\omega\ t) \right)$$

$$+ \left(\frac{\rho S(E)}{dE}\ e\ V_{mod}\ \frac{e^2\ V_{mod}^2}{2} sin(\omega\ t)^2 \right) ... \tag{2.14}$$

Hence, the modulated current $I_T(V + V_{mod}\ sin(\omega\ t + \phi))$ reads:

$$I_T(V + V_{mod}\ sin(\omega\ t)) \propto I(V) + \underbrace{\frac{dI}{dV}V_{mod}\ sin(\omega\ t)}_{1^{st}\ harmonic} + \underbrace{\frac{dI^2}{dV^2}\frac{e^2\ V_{mod}^2}{4}(cos(2\ \omega\ t)^2)}_{2^{nd}\ harmonic} \tag{2.15}$$

The first harmonic is directly proportional to the first derivative of the current dI/dV and therefore to the surface density of states ρ_S (see equation 2.15). Now the PSD comes into play. In fact, the PSD simply multiplies to incoming alternating signals with respect to their phase. A schematic block diagram of the Lock-In amplifier is shown in Fig. 2.4. A phase shifter allows to change the phase of the reference signal with respect to the measurement signal $I_{Lock-In}$. Then the two signals are multiplied and the total signal reads:

$$I_{Lock-In} \propto V_{mod}\ sin(\omega_{Ref}\ t + \phi_{Ref})(\rho_S(E)\ V_{mod}\ sin(\omega\ t + \phi) + f(\omega_{noise}\ t + \phi_{Noise})) \tag{2.16}$$

If the frequencies ω_{Ref} and ω are equal, a DC signal proportional to the first derivative of the current dI/dV is filtered out by the low-pass filter:

$$I_{Lock-In} \propto \frac{1}{2}V_{mod}\ \rho_S(E)\ cos((\omega - \omega_{Ref})\ t + \phi - \phi_{Ref}) \tag{2.17}$$

$$- \frac{1}{2}V_{mod}\ \rho_S(E)\ cos((\omega + \omega_{Ref})\ t + \phi + \phi_{Ref})$$

$$\stackrel{\omega_{Ref}=\omega}{=} \frac{1}{2}V_{mod}\ \rho_S(E)\ cos(\phi - \phi_{Ref})$$

The signal becomes maximum when the reference and measurement signal are in phase ($\phi = \phi_{Ref}$). This can be done using the phase shifter (see Fig. 2.4). All signal components with a frequency different from ω_{Ref} are removed. It is worthwhile to mention that also the second derivative of the current with respect to voltage $\frac{dI^2}{dV^2}$ can be measured in this way by choosing the second harmonic (see equation 2.15).

2.3.2 Energy Resolution of STS

The energy resolution of STS is limited by the STM temperature T and also by the used Lock-In modulation V_{mod} [62, 66]. Let us now derive an expression for the energy resolution of STS determined by the thermal and modulation broadening. Considering the Fermi-Dirac distribution of tip $f_t(E)$ and sample $f_s(E)$ gives the following expression for the tunneling current I_T [66–68]:

$$I_T(V) \propto \int f_T(E)(1 - f_S(eV + E))\ \rho_S(E) dE \tag{2.18}$$

a)

b)
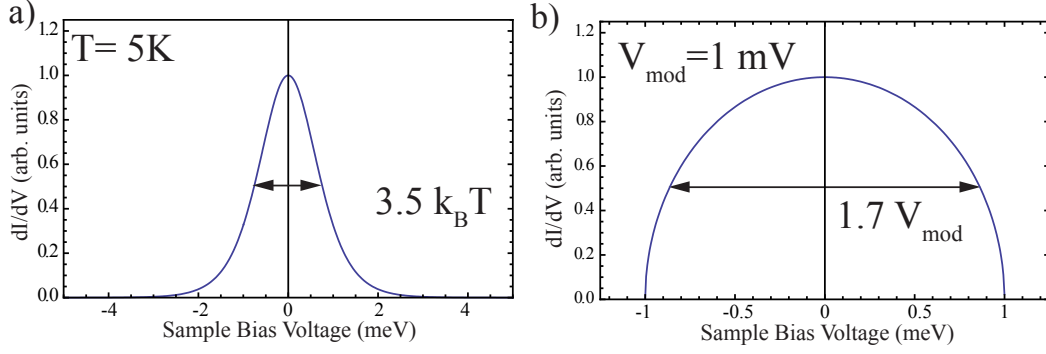
Figure 2.5:   Schematic illustration of the effect of the thermal and the Lock-In broadening on the energy resolution of STS.

The influence of both the tip DOS and the transmission coefficient $T(E, V, z)$ are neglected. The first derivative with respect to voltage can then be expressed as follows [69]:

$$\frac{dI_T(V)}{dV} \propto \rho_S(E) \frac{e^{\frac{E}{k_B T}}}{(1 + e^{\frac{E}{k_B T}})^2}$$ (2.19)

$$= \rho_S(E) \, sinh^2(\frac{E}{2k_B T})$$

$$= \rho_S(E) \, \Gamma_T$$

Here Γ_T is the thermal broadening function, which exhibits a FWHM of 3.5 $k_B T$ and a Gaussian-like line shape. Figure 2.5(a) shows the thermal broadening in the case of temperature of T= 5 K with a FWHM= 1.5 meV.

Furthermore, the applied modulation voltage V_{mod} of the Lock-In amplifier leads to an additional broadening Γ_{mod}. The first harmonic of the tunneling current (dI/dV) recorded by the Lock-in amplifier reads [53]:

$$I_\omega = \frac{dI_T}{dV} \propto \int I(e V + V_{mod} \, sin(\omega t)) \, sin(\omega t) dt$$ (2.20)

Substituting $V_{mod} \, sin(\omega t)= r$ and partial integration leads to [66, 67, 69]:

$$\frac{dI_T}{dV} \propto \int_{-V_{mod}}^{V_{mod}} \frac{dI}{dV}(V + r) \underbrace{\frac{2}{\pi V_{mod}} \sqrt{2 V_{mod} - r^2}}_{\Gamma_{mod}} dr$$ (2.21)

Figure 2.5(b) shows the modulation broadening in the case of a modulation of V_{mod}= 1 mV. The modulation broadening is described as half circle with a FWHM of 1.7 V_{mod}. The complete dI/dV signal can then be expressed as a convolution of the intrinsic signal with the thermal Γ_T and Lock-In broadening Γ_{mod}:

$$\frac{dI_T(V)}{dV} \propto \rho_S(E) \, \Gamma_{mod} \, \Gamma_T$$ (2.22)

(2.23)

The experimentally obtained width Δ_{Exp} of a spectral feature with an intrinsic width Δ_i reads:

$$\Delta_E^2 = \Delta_V^2 + \Delta_T^2 + \Delta_I^2 = (1.7V_{mod})^2 + (3.5k_BT)^2 + \Delta_I^2 \tag{2.24}$$

At a typical measurement temperature of 5 K the FWHM of the thermal broadening is about $3.5k_BT = 1.4$ meV, which also determines a lower limit for the energy resolution of STS. The same is true for broadening caused by the Lock-In amplifier. Hence, by taking STS spectra in a small sample bias windows the above discussed broadening effects should be taken into account. In particular for very sharp resonances that have an intrinsic width Δ_i of only a few meV. In this case, as we will be shown in section 3.3, the experimentally obtained Δ_{Exp} width should be corrected.

2.3.3 Spectroscopy Modes

The spectroscopy mode discussed above refers to the so called I(V) spectroscopy. Besides this one, there are two other spectroscopy modes.

In $I(z)$ spectroscopy the current signal I_T is recorded while varying the tip-sample distance z for a constant voltage V. Hence, the STM feedback loop is still closed, different to the $I(V)$ spectroscopy discussed above. By plotting the logarithm of the tunneling current $I_T(z)$ (we concentrate on the tunneling probability $T(E, V, z)$ (see equation 2.7 and 2.8) and neglect all other terms) we can extract the effective work function $\phi_{eff} = \phi_S + \phi_T$ [62]:

$$ln(I) \propto -2 \left[\sqrt{\frac{2\,m(\phi_S + \phi_T)}{\hbar}} - E + \frac{e\,V}{2} \right] \tag{2.25}$$

At large tip-surface separations the measured ϕ_{eff} should approach the surface local work function ϕ_S. However, at small tip-surface separations image potential come into play [63].

The z(V) spectroscopy mode is used to study electronic states at high energies or above the vacuum barrier of a system [70, 71]. The STM feedback loop is closed. The tip-surface distance z is measured for different sample bias voltages V at a constant current I. This has the advantage of probing the adsorbate/ surface at a fixed tunneling current I_T at high sample bias voltages V_T. Solving the equation 2.8 for z we get the following expression [72]:

$$z(V,\,\phi_T,\,\phi_S,\,E) \propto \left[1/\sqrt{\frac{\phi_S + \phi_T}{2} + \frac{e\,V}{2} - E} \right] \, ln \left[\int_0^{e\,V} \rho_T(E - e\,V)\rho_S(E)dE \right] \tag{2.26}$$

Hence for small sample bias voltages V the z(V) signal is proportional to the integrated local density of states of the sample $\rho_S(E)$. For high sample bias voltages V the change of the probability $T(E, V, z)$ has to be taken into account [72].

2.3.4 Spatially Resolved dI/dV Mapping

Another spectroscopy mode that is often used allows to spatially map contours of the sample LDOS $\rho_S(\vec{r}, E)$ at certain energies E. This mode is known as dI/dV mapping. The STM tip scans a region of interest and simultaneously a small sinusoidal voltage $V_{mod}\,sin(\omega\,t)$ is applied to the sample bias

voltage V, like it is done in the case of the dI/dV spectroscopy mode. Since the Lock-In signal at the first harmonic I_ω is proportional to the LDOS of the sample $\rho_S(\vec{r}, E)$, a spatially resolved map of $\rho_S(\vec{r}, E)$ can be recorded. The scanning speed v_s and the modulation amplitude ω play a crucial role in order to have a good signal-to-noise ratio[1]. The dI/dV mapping can be performed in two different modes. The constant current mode (CCM) works at constant tunneling current I_T and with the feedback control closed. The constant height mode (CHM) works at constant tip-surface separation z, while scanning the area of interest. In this case the feedback loop is open.

A common problem of both spatially resolved dI/dV modes is the influence of changing tip-surface distances [73–76]. Equation 2.4 reveals that the tunneling matrix element $T(E, V, z)$ depends on the tip-surface separation z. Hence, when z changes, $T(E, V, z)$ changes also. The dependence of $T(E, V, z)$ on z is usually unknown. Spatial variations of the work function ϕ can complicate the problem even more (see equation 2.4). A renormalization procedure is suggested to correct the obtained LDOS maps [76].

2.3.5   Interactions of Tunneling Electrons with Adsorbates

The STM enables not only the investigation of the elastic electronic properties of adsorbates, but also to study inelastic scattering processes (IETS).

Tunneling electrons can excite vibrational [77, 78] and spin degrees of freedom [79]. These are inelastic tunneling processes and imply a loss of electron energy. The inelastic excitation opens a new channel of conductance. That appears as symmetric steps at the energies $+\Delta$ and $-\Delta$ in the dI/dV spectrum (see Fig. 2.6). The normalized change of conductance $\Delta G/G$ is in general of the order of 10 % [78, 80] in the case of vibrational excitations. Spin-excitations imply in general much higher normalized changes of the conductance $\Delta G/G$ up to 100% or more [11, 81]. The very different excitation probabilities rely on the different vibrational and spin excitation mechanisms.

Tunneling electrons can excite single vibrations of molecules when their energy fits to the energy of the corresponding vibrational mode E_{vib}. The excitation implies an electron-phonon coupling, which is in general rather weak. Furthermore, the vibrational modes are sensitive to the local symmetry of the related initial ϕ_i and final ϕ_f wave function [81, 82] and also the molecular adsorption on metal surface can lead to a quenching of certain vibrational modes.

On the other hand, the interaction of tunneling electrons with a single and isolated spin are much more efficient, since the electron-spin coupling is rather strong. When the energy of the tunneling electrons exceeds the energy to excite the spin, that is, it overcomes the magnetic anisotropy energy (MAE), a new channel of conductance opens. Since the electron-spin coupling is strong, multiple spin excitations can be induced by the tunneling electrons in the case of high current densities and long spin lifetimes, known as spin-pumping [83].

---

[1]By lowering the scanning speed v_s the STM tip dwells longer on a particular spot. Hence, the Lock-In signal can be averaged over more oscillations and the signal-to-noise ratio becomes better.
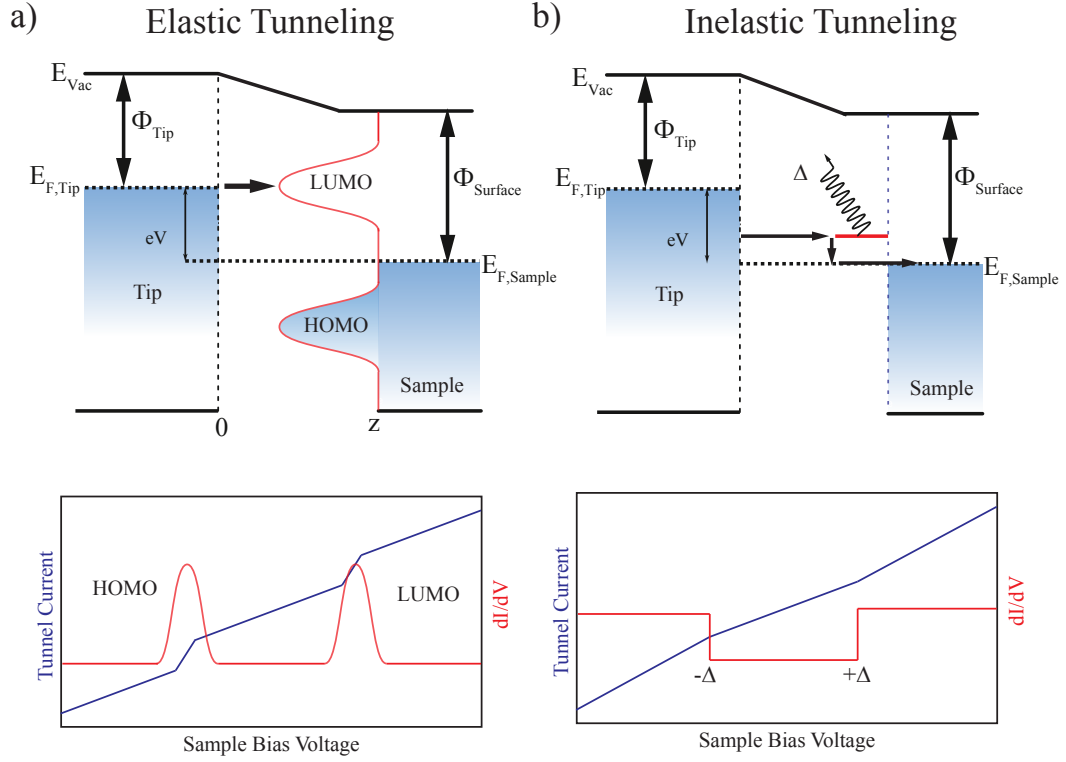
Figure 2.6: Schematic energy diagram of a tip/molecule/surface system during dI/dV spectroscopy. (a) By varying the sample bias voltage tip electrons tunnel into the unoccupied LUMO of the adsorbed molecule. The corresponding tunneling process is elastic. (b) Tunneling electrons can excite a degree of freedom (spin or vibration) of the adsorbate and lose energy. The corresponding tunneling processes is inelastic.

2.4 Core Level Spectroscopy

Two other techniques have been used to investigate in particular metal-organic networks on metal surfaces. The present section gives a brief overview about the fundamental concepts of x-ray absorption spectroscopy (XAS) and x-ray magnetic circular dichroism (XMCD). The K and $L_{2,3}$ x-ray absorption edges are studied in the present thesis, since they are important for organometallic system based on transition metal atoms. A more detailed introduction to XAS and XMCD is given in Ref. [84, 85].

2.4.1 Introduction to X-ray Absorption Spectroscopy (XAS)

When a beam of x-rays hits an absorbing sample the x-ray intensity is attenuated depending on the sample thickness z and the strength of absorption. The attenuation of the x-ray intensity I can be described as follows:

$$-dI(z) = I(z)\,\mu_x\,dz \tag{2.27}$$

Hence the total x-ray intensity after passing the sample with thickness z reads:

$$I(z) = I(0)e^{-\mu_x\,z} \tag{2.28}$$
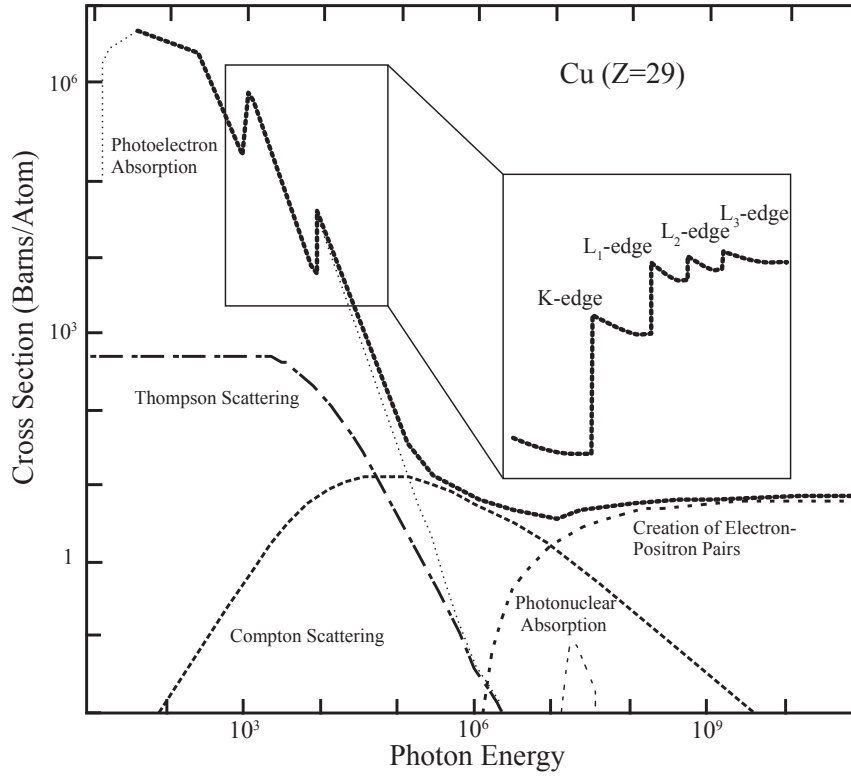
Figure 2.7: X-ray absorption cross section of a Cu sample (Z=29). Adapted from Ref. [86].

where μ_x is the linear attenuation coefficient. This coefficient is a property of the corresponding material and relies on a multitude of different scattering or absorption processes. The linear attenuation coefficient μ_x is the product of the x-ray absorption cross section σ and the atomic density ρ_D of the corresponding material:

$$\mu_x z = \sigma \cdot \rho_D \tag{2.29}$$

Figure 2.7 shows the energy dependence of the x-ray absorption coefficient σ of a copper sample. The low energy range (called soft x-ray regime) is dominated by the photoelectron absorption (see Fig. 2.7). Within this regime the x-ray absorption coefficient σ shows element specific absorption edges. Here the energy $\hbar\omega$ of the incoming photon matches to excite a core level electron.

2.4.2 X-ray Absorption Spectroscopy

X-ray absorption spectroscopy (XAS) is based on the excitation of core level electrons. The core level electron absorbs a photon emitted from an x-ray source and is then excited into an unoccupied bound state or to the continuum leaving a core hole in the corresponding electronic core level. The core hole is then filled by an electron which leads either to the emission of a photon (fluorescence) or via electron-electron correlations to the emission of an Auger electron.

Let us now derive the x-ray absorption cross section σ in the framework of a simple one-electron picture to learn about the fundamental aspects of XAS. The x-ray absorption cross section σ is defined

as the total number of excited electrons per unit time versus the total number of incident photons per unit area and unit time:

$$\sigma_x = P_{if}/F_{Ph} \tag{2.30}$$

Using *Fermi's Golden Rule* we can calculate the transition probability P_{if} of the initial state $|i\rangle$ to an excited state $|f\rangle$ per unit of time to obtain the x-ray absorption cross section σ_x. The transition probability P_{if} reads [85]:

$$P_{if} = \frac{2\pi}{\hbar}|\langle f|V|i\rangle|^2\rho_f(E) \tag{2.31}$$

here $\rho_f(E)$ is the energy density of final states and V is the perturbation Hamiltonian describing the interaction of the electromagnetic field with a spinless particle with the charge $-e$ and mass m [85]:

$$V = \frac{e}{m\,c}\vec{A}\cdot\vec{p} \tag{2.32}$$

where $\vec{A}$ is the electric field vector potential and $\vec{p} = \sum_i p_i$ is the sum over the momentum operators of the electrons. The electric field vector potential $\vec{A}$ can be described as a plane electromagnetic wave [85]:

$$\vec{A} = \vec{e}\,\frac{A_0}{2}\left(e^{i(\vec{k}\vec{r}-\omega\,t)} - e^{-i(\vec{k}\vec{r}-\omega\,t)}\right) \tag{2.33}$$

here $\vec{k}$ is the wave vector, ω the frequency and $\vec{e}$ is the polarization vector. Now we can calculate the photon flux F_{Ph} of this wave, that is the number of photons per unit of time, depending on the magnitude A [85]:

$$F_{Ph} = \frac{A_\omega^2}{8\,\pi\,\hbar\,c} \tag{2.34}$$

To evaluate σ_x we first have to evaluate P_{if}. Using equation 2.32 and 2.33 we obtain for P_{if} [85, 87]:

$$P_{if} = \frac{4\,\pi\,e^2}{2\hbar\,m^2\,c^2}A_0^2\left|\left\langle f\left|e^{i\vec{k}\cdot\vec{r}}\vec{e}\cdot\vec{p}\right|i\right\rangle\right|^2\rho_f(E) \tag{2.35}$$

By using the so called *dipole − approximation* we can simplify the above expression for P_{if}. The *dipole − approximation* assumes a large wavelength λ or a small wave vector $\vec{k}$ compared to the length operator $\vec{r}$, hence $k\cdot r << 1$ or $|r| << \frac{\lambda}{2\,\pi}$. Thus, the x-ray absorption cross section defined as $\sigma_x = P_{if}/F_{Ph}$ reads [85, 87]:

$$\sigma_x = \frac{\pi\,e^2}{\hbar\,\varepsilon_0\,c}\hbar\cdot\omega\,|\langle f|\vec{e}\cdot\vec{r}|i\rangle|^2\rho_f(E) \tag{2.36}$$

Figure 2.7 reveals that the measurement of the x-ray absorption cross section σ_x includes different inelastic and elastic processes and in a real experiment one measures the absolute x-ray absorption cross section as a sum of all these contributions. However, up to a photon energy of 100 keV the absolute x-ray absorption cross section is dominated by the process of photoelectron absorption.

A typical x-ray absorption spectrum starts 20 eV before and ends 40 eV after the absorption edge. The resonances in a x-ray absorption spectrum are linked to core level excitations to valence electronic states of the investigated system. Therefore, by varying the photon energy the unoccupied density

of states is probed as can be seen in equation 2.36. In this regard, XAS exhibits a high chemical sensitivity, since the valence electronic structure is very sensitive to the chemical environment of the investigated atomic species. For example, the formation of a chemical bond can lead to a chemical shift of the XA resonance of the corresponding atomic species compared to the non-bonded case (see section 4.3). Furthermore, the analysis of the $2p$ core level excitations to the valence $3d$ levels of transition metals allows to probe their magnetic properties (see section 2.4.3).

The evaluation of the matrix elements can be done in the one-electron picture using atomic orbitals. Hence, the initial state $|i\rangle$ is described by an atomic orbital state depending on the quantum numbers n, l, m_l, s, and m_s and reads as follows [85]:

$$|i\rangle = |R_{n,l}; n, l, m_l, s, m_s\rangle \tag{2.37}$$

Here $R_{n,l}$ is radial part of the corresponding electronic core level state. The final state $|f\rangle$ reads:

$$|f\rangle = \left|R_{n',l'}; n, l', m_l', s, m_s'\right\rangle \tag{2.38}$$

In order to evaluate the transition matrix element the electric dipole operator $\vec{e} \cdot \vec{p}$ can be expressed in terms of the Racah's spherical tensor operator accounting for the different photon polarization $q = 0$ (linearly polarized light) and $q = \pm 1$ (left (+1) and right (-1) circularly polarized light) in the coordinate system with the axis $\alpha = x$, y, and z [85]:

$$\vec{r} \cdot P_q^r = \sum_{p=0,\pm 1} e_{\alpha,p}^q C_p^{(1)} \tag{2.39}$$

$$\tag{2.40}$$

with:

$$C_m^l = \sqrt{\frac{4\pi}{2l+1}} Y_{l,m}(\theta, \phi) \tag{2.41}$$

Here $Y_{l,m}(\theta, \phi)$ are the spherical harmonics. The transition matrix element $\left\langle i \left| \vec{r} \, P_q^r \right| f \right\rangle$ then becomes:

$$\left\langle R_{n',l'}; n, l', m_l', s, m_s' \left| \vec{r} \, P_q^r \right| R_{n,l}; n, l, m_l, s, m_s \right\rangle \tag{2.42}$$

$$= \delta(m_s', m_s) \left\langle R_{n',l'}(r) \left| \vec{r} \right| R_{n,l}(r) \right\rangle \sum_{m_l, m_{l'}, p} e_{\alpha,p}^q \left\langle l', m_{l'} \left| C_p^{(1)} \right| l, m_l \right\rangle \tag{2.43}$$

Hence, the only transitions that are allowed are the ones preserving the spin. Furthermore, the transition matrix element splits into spin, radial and angular parts. The transition matrix only have non-zero values if certain conditions are fulfilled defining the dipole selection rules:

$$\Delta l = \pm 1 \tag{2.44}$$

$$\Delta m_l = q = 0, \pm 1 \ (+1 \ left \ circular, \ -1 \ right \ circular) \tag{2.45}$$

$$\Delta s = 0 \tag{2.46}$$

$$\Delta m_s = 0 \tag{2.47}$$

The here presented dipole selection rules are true in the case of a negligible $spin - orbit$ coupling (L-S coupling), since then the quantum numbers l, m_l, s, m_s are a good basis. Otherwise the basis

L, S, J, m_j can be used. In that case the dipole selection reads then $\Delta L = 0$, $\Delta S = 0$, $\Delta J = 0, \pm 1$ (except $0 \longrightarrow 0$), and $\Delta m_J = 0, \pm 1$[2].

The most important absorption edges in the case of organic molecules and transition metal based metal-organic networks are the K-edge and $L_{2,3}$-edges. The corresponding core level excitations are:

- K-edge: $1s$ state

- L-edges: L_1: $2s$, state L_2: $2p$ (j=1/2) state, L_3: $2p$ (j=3/2) state

Many organic molecules consist of elements like H, C or N. These are elements with a low atomic number Z. The absorption edge originating from $1s$ core levels is then the K-edge absorption edge. In the case of transition metals the absorption edge originating from $2p$ core levels is of great interest (L_2 and L_3 edge) as shown in the following. These core level electrons can be excited to unoccupied states. The unoccupied s, p, and d states can then be occupied in the case of the K-edge or L-edge according to the dipole selection rules (cf equations in 2.47), respectively.

Let us now discuss how a typical XA spectrum of molecular adsorbate on metal surface looks like. Figure 2.8(a) schematically depicts the experimental setting. A small molecule is adsorbed on a metal surface and x-ray photons excite core level electrons of the molecule. Let us assume that the valence molecular orbitals are occupied (bonding) σ and π orbitals and the unoccupied (antibonding) orbitals are σ^* and π^* orbitals. The corresponding energy diagram of the molecule is shown in Fig. 2.8(b). The corresponding XA spectrum (K-edge) shown in Fig. 2.8(c) shows at lower photon energies a π^* resonance stemming from transition from the $1s$ core level into the unoccupied antibonding π^* orbital. The π^* resonance is followed by a broad molecular σ^* resonance originating from $1s$ core level into the unoccupied antibonding σ^* orbital.

Furthermore, XAS allows to determine the adsorbate adsorption geometry by varying the x-ray beam incidence angle. Since the π^* or σ^* orbitals have different spatial localization and hence different directional character. Figure 2.9(b) shows the possible bonds in organic molecules. Important for the angular dependence of the XA intensity I_{XAS} is the orientation of the maximum orbital amplitude with respect to the incoming polarization vector $\vec{e}$ of the x-ray beam. In the case of single π or σ bonds the maximum orbital amplitude is oriented perpendicular or parallel to the bonding axis of the molecule, respectively. Triple bonds or aromatic systems exhibit several bonds of the same type defining a plane.

Therefore the angular dependence of XAS signals originating from π^* or σ^* orbitals should be strikingly different. In the context of organic adsorbates the K-edge (transitions from 1s states) is of particular interest, because organic molecules mainly consist of atoms with a low atomic number. In the case of the K-edge the initial state is an isotropic s-state and the final state is in general a superposition of s-states and p-states (the dipole-selection is $\Delta l = 0, \pm 1$). Therefore the angular dependence of the measured signal probes the angular dependence of the unoccupied states.

---

[2]It is worth mentioning that the above used one-electron picture does not take into account electron-electron interaction stemming from the interaction of the core hole with electrons of the final state. Hence both the initial and the final state are in fact multi-electron systems and the evaluation of the corresponding transition matrix elements needs more sophisticated theory. These electron-electron interactions have to be distinguished for example from the interactions between the $3d$ electrons itself due to magnetic exchange.

a)

b)
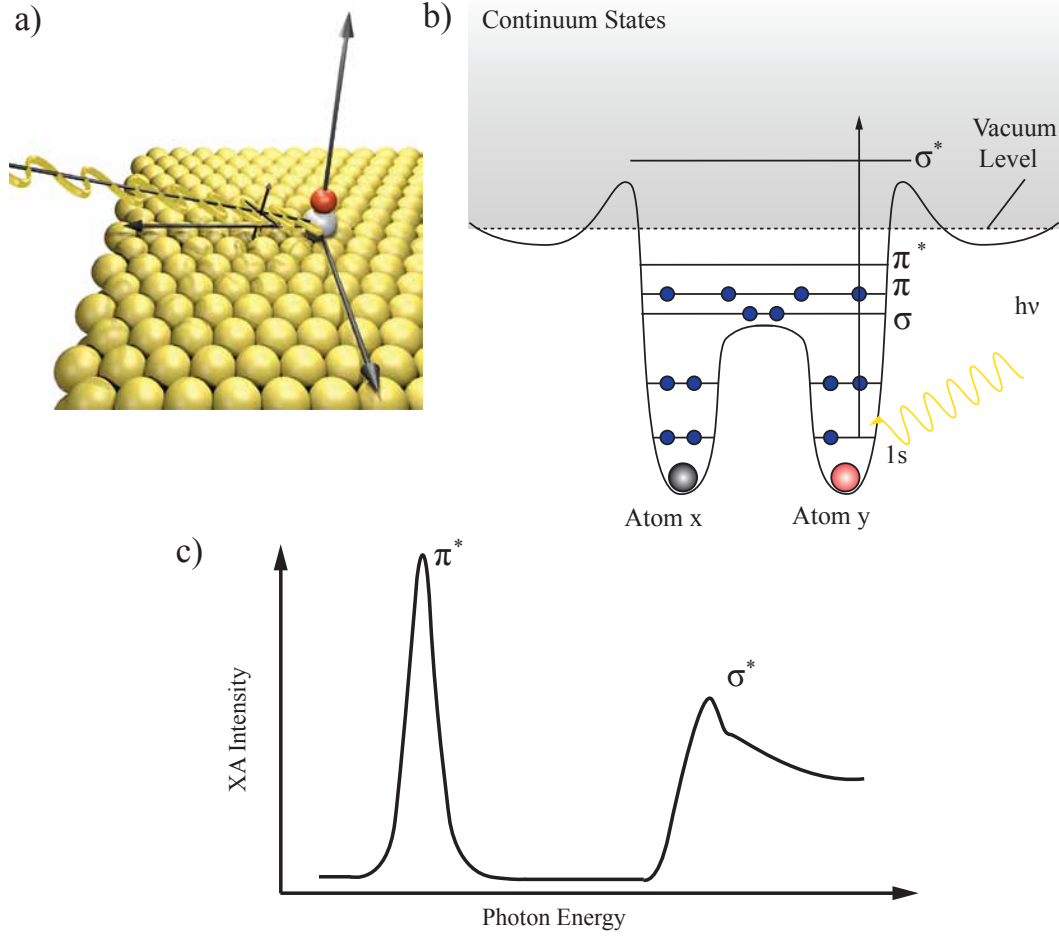
Figure 2.8:   (a) A single molecule adsorbed on a metal surface. (b) Energy potential of a simple diatomic molecule and the corresponding K-edge excitations. Adapted from Ref. [85]. (c) Schematic x-ray absorption spectrum of organic adsorbate on a metal surface.

Figure 2.9 shows a molecular adsorbate on a metal surface. The incoming x-ray beam has the polarization $\vec{e}$. The orientation of the probed molecular orbital/ plane is indicated by the vector $\vec{o}$ or $\vec{n}$, respectively (see Fig. 2.9(a)). For simplicity, let us assume linear polarized light with a polarization vector $\vec{e} = (e_x, e_y, e_z)$ and a $1s$ initial state. Hence, the initial state is isotropic. The total XA intensity I_{XAS} is proportional to the transition matrix elements defined in equation 2.29 and reads [85]:

$$I_{XAS} \propto (\cdot |\langle f | \vec{e} \cdot \vec{r} | 1s \rangle|)^2 \tag{2.48}$$

For a K-shell transition the maximum transition intensity is obtained when the orientation of the polarization vector $\vec{e}$ is collinear with respect to the p orbital component[3] of the final state [85]. Hence, the angular dependence of the XAS intensity I_{XAS} is determined by the angle α between polarization vector $\vec{e}$ and the direction $\vec{o}$ of the largest amplitude of the final state orbital [85]:

$$|\langle f | \vec{e} \cdot \vec{r} | 1s \rangle|^2 \approx |\vec{e} \cdot \vec{o}|^2 \approx cos(\alpha)^2 \tag{2.49}$$

---

[3]K-shell transition involve excitations to s and p orbitals. Since s-orbitals are isotropic the transition matrix element points in the direction of the p orbital component.
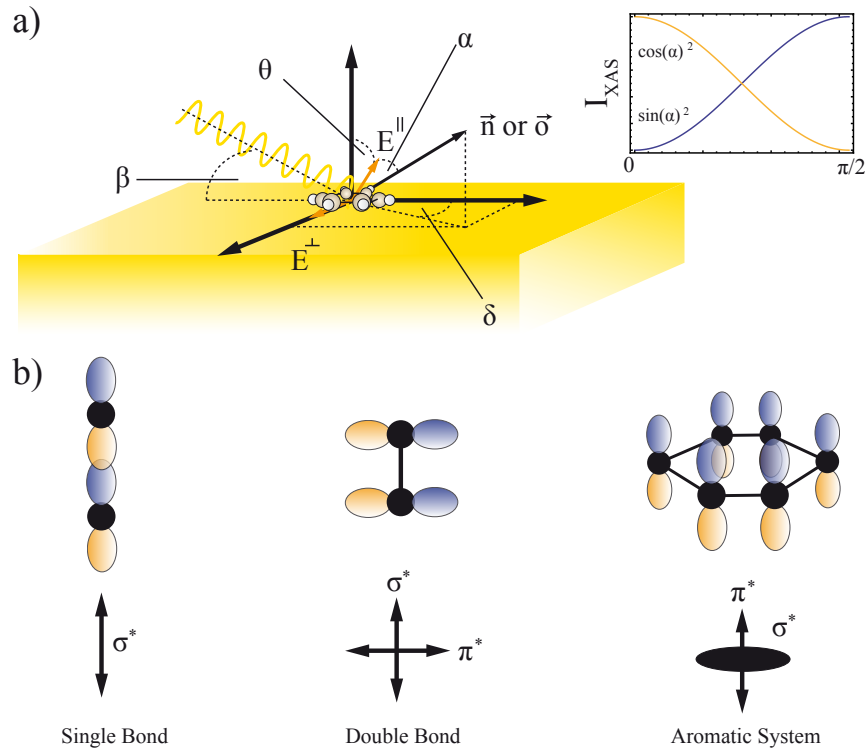
Figure 2.9: (a) Schematic diagram of an organic adsorbate on a metal surface and an incoming x-ray beam and the corresponding angles α, β, γ, and θ according to a Cartesian coordinate system. The orientation of the molecular orbital/plane is indicated by $\vec{o}$ or $\vec{n}$, respectively. The inset shows the angular dependence of the XA intensity I_{XAS} of a π^* and σ^* orbital, respectively. The angle α corresponds to the angle between the polarization vector $\vec{e}$ and the direction $\vec{o}$ of the largest amplitude of the final state orbital. (b) Different bond types of organic molecules and the corresponding spatial orientation of the maximum orbital amplitude.

In the case of molecular π^* or σ^* planes, which are defined by the plane normal $\vec{n}$, the angular dependence is obtained by integrating over all azimuthal angles in the defined plane. The angular dependence of the total XAS intensity I_{XAS} reads then [85]:

$$|\langle f \,|\vec{e} \cdot \vec{r}|\, 1s \rangle|^2 \approx |\vec{e} \cdot \vec{n}|^2 \, sin(\beta)^2 \tag{2.50}$$

where β defines the angle between the polarization vector $\vec{e}$ and the plane normal $\vec{n}$. In the case that an organic molecule is adsorbed flat with its molecular plane parallel to the metal surface the π-system is orientated perpendicular, whereas the σ-bonds are parallel with respect to the surface like depicted in Fig. 2.9(b). Hence, the angular dependence of the corresponding XAS signals is just opposite (see inset in Fig. 2.9(a)). Therefore by analyzing the angular dependence of the π^* or σ^* resonances we can obtain information of the adsorption configuration of a molecule.

2.4.3 X-ray Magnetic Circular Dichroism

The technique of X-Ray Magnetic Circular Dichroism (XMCD) opens the opportunity to directly measure the elemental resolved spin moment m_S and orbital moment m_L in magnetically ordered
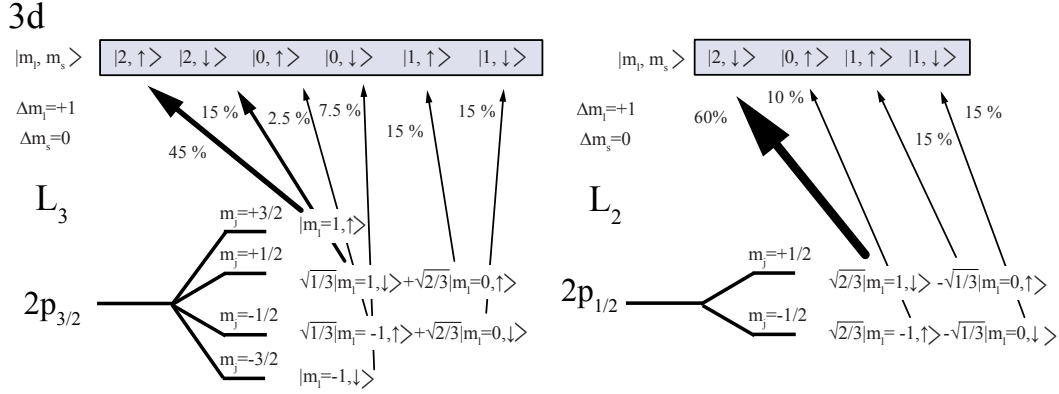
Figure 2.10: Electronic transition between the split $2p_{3/2}$ and $2p_{1/2}$ levels and the $3d$ level. The size of the arrows corresponds to the transition probability. Adapted from Ref. [89].

systems. We will focus on the XMCD of $3d$ transition metals, since the metal-organic networks discussed in the following chapters of this thesis contain Cu, Co or Fe atoms as metal centers among the organic linkers. A magnetic moment stems form an unbalance of spin-up and spin-down holes (electrons) in the corresponding orbitals, for example the $3d$ or $4f$ orbitals of transition metals or lanthanides. In these cases, the spin moment m_S reads [88]:

$$m_S = -2 \langle S_z \rangle \frac{\mu_B}{\hbar} = (N_\uparrow - N_\downarrow) \frac{\mu_B}{\hbar} \tag{2.51}$$

where $\langle S_z \rangle$ is the spin projection on the z-direction (quantization axis), and $N_\uparrow$ and $N_\downarrow$ are the number of spin-up or spin-down electrons, respectively. The orbital moment m_L reads [88]:

$$m_L = -2 \langle L_z \rangle \frac{\mu_B}{\hbar} \tag{2.52}$$

The basic idea of XMCD is sketched in Fig. 2.11(a) in the case of a $3d$ transition metal atom. Due to the spin-orbit coupling, the $2p$ orbitals are non-degenerated into the $2p_{3/2}$ and $2p_{1/2}$ levels, respectively. The energetic split is of the order of $\propto$ 10-20 eV for first row transition metals. In the following a simplified description of the XMCD effect within a two-step model is given. The absorption of photons is governed by the dipole selection rules (see equations 2.47). For circular polarized light the corresponding selection rules are $\Delta l = \pm 1$ and $\Delta m_L = \pm 1$. Hence, the absorption of circular polarized photons implies a transfer of angular momentum of $-\hbar$ or $+\hbar$ from the incoming photon to the excited electron. When the excited photo electron stems from spin-orbit split level, as it is the case for the $2p_{3/2}$ and $2p_{1/2}$ levels, the angular moment of the incident photon can be transferred to the spin moment of the electron. It is important to notice that in that particular case, right and left circular polarized light transfer opposite spin. Thus in first place the absorption of circular polarized light leads to the creation of excited and spin-polarized photoelectrons with spin-down or spin-up orientation with respect to the spin of the photon.

Figure 2.10 shows the possible electronic transitions for the L_2 ($2p_{1/2}$) and L_3 ($2p_{3/2}$) edges in the case of right circularly polarized light (with the momentum $\hbar$) [89, 90][4]. All states of the ($2p_{1/2}$)

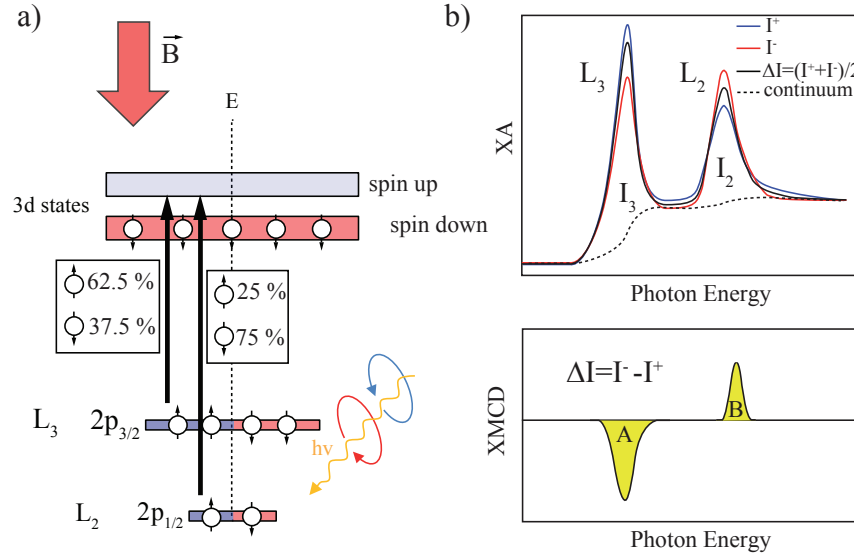[4]For left circularly polarized light the following discussion is analog, we just have to use opposite signs.

Figure 2.11: (a) Core level excitation. (b) Schematic diagram of core level excitation in the presence of an external magnetic field.

and the $(2p_{3/2})$ level are labeled regarding their m_j values. For example, there is only one possible combination of m_S and m_L to get m_J= 3/2 or -3/2. For m_J= ±1/2 several combinations of m_S and m_L are possible as shown in Fig. 2.10. In the upper half the possible m_s and m_l combinations in the case of the 3d levels are shown. Based on the electric dipole selection rules transitions induced by right circular polarized light imply $\Delta m_s = 0$ and $\Delta m_l = +1$. The probability of the allowed transition according to the selection rules can be calculated according to the transition matrix elements [89, 90]. The probability of each electronic transition is indicated by the size of the corresponding arrow and is also marked next to it. Now we can also obtain the spin polarization of the transition from the $2p_{1/2}$ and the $2p_{3/2}$ states from calculating the expectation value of the m_S final states. For example, in the case of the $2p_{1/2}$ states 25% and 75% of the transitions are excited to final states with a spin expectation value of m_S= +1/2 and m_S= -1/2, respectively [90]. Thus, using right polarized light, the excited photoelectrons stemming from the $2p_{3/2}$ (L_3) and the $2p_{1/2}$ states (L_2) show a total spin polarization of $\langle \sigma_S \rangle$ = -0.5 and +0.25, respectively [90]. The spin polarization has opposite sign in the case of the L_2 and L_3 edge. The transition of the L_2 ($2p_{1/2}$) and L_3 ($2p_{3/2}$) edges are also polarized regarding the orbital moment as can be seen from Fig. 2.10. Analog to the discussion of the spin polarization the orbital polarization is equal at both edges and is $\langle \sigma_L \rangle$=0.75 [90].

Now the exchange split d shell with its spin-up and spin-down imbalance can be used as a spin detector for the excited spin-polarized photoelectrons. Since we excite electrons into unoccupied electronic states (here the 3d levels) the XMCD effect is proportional to the number of holes. By applying an external magnetic field, in general parallel to the incoming photon beam with the wave vector $\vec{k}$, the spin polarization of the unpaired 3d electrons and also the quantization axis of this $spin-detector$ is defined. For a maximum XMCD signal the magnetic field should be collinear to the photon spin or orbital momentum, because then the XMCD effect is maximum [87]. Figure 2.11(a) shows a d^5 system probed with circular polarized light, where all d electrons are aligned parallel to the external magnetic field. Switching the magnetic field or using circular polarized light with the opposite helicity lead to a decreased absorption signal, thus, the excited spin polarized photoelectrons
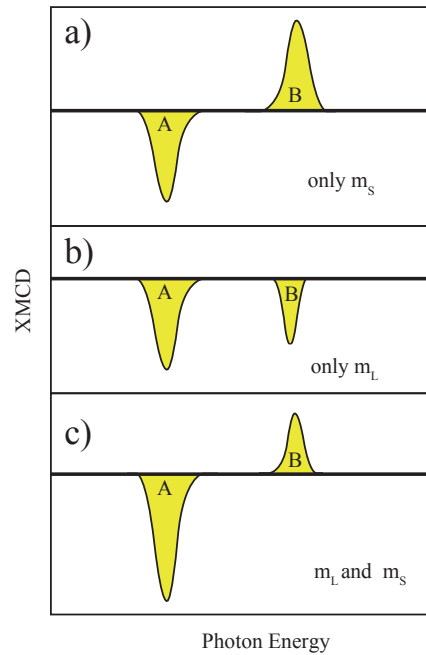
Figure 2.12: (a) XMCD difference signal of the contribution of the spin moment m_S (b) XMCD difference signal of the contribution of the orbital moment m_L. (c) Total XMCD difference signal including both the contribution from the spin m_S and orbital m_L moment. The Figure is adapted from Ref. [90].

can be excited into less d states. Since the spin-orbit splitting is opposite in the case of the $2p_{3/2}$ and $2p_{1/2}$ edge this behavior is also opposite.

Figure 2.11(b) shows a schematic XA spectrum revealing the L_2 and the L_3 edges. Depending on the helicity of the incoming circular polarized x-rays, the intensity of the L_2 and the L_3 edge increase or decrease, respectively. These so called L-edge absorption spectra contains also contributions from $p \rightarrow s$ transitions, which have in general a much smaller intensity compared to the $p \rightarrow d$ transition (a factor of 20) [87]. The difference in the x-ray absorption intensities $\Delta = I^+ - I^-$ of the $p \rightarrow d$ transition between the two x-ray polarizations (left and right circular) for a fixed magnetic field (parallel or antiparallel with respect to the spin $\hat{s}$ or orbital momentum $\hat{l}$) is called XMCD difference signal and implies information about element specific spin and orbital moment. In general the $\Delta = I^+ - I^-$ signal is chosen so that the XMCD difference signal at the L_3 is negative.

Figure 2.12 shows how the XMCD difference signal decomposes into the contributions originating from the spin m_S and orbital m_L moment [90]. As already discussed, the sign of the spin polarization is opposite for the L_2 and L_3 edge and therefore also the sign of the XMCD difference signal (cf Fig, 2.12(a)). The intensity of the XMCD difference signal stemming from the L_2 and L_3 edge is the same [5]. The contribution of the orbital moment m_L has the same sign at both absorption edges [6] but different intensities (cf Fig. 2.12(b)), due to the different occupation of the $2p_{3/2}$ and $2p_{1/2}$ states. In a real experiment a XMCD difference signal contains usually both contributions (cf Fig. 2.12(c)).

The quantities A, B, I_2 and I_3 (see Fig. 2.11(b)) can be linked to spin m_S and orbital m_L moment by so called sum rules. The sum rules require that the sample is magnetically saturated. The first one is the so called charge sum rule, which links the integrated intensities of the L_3 and L_2 (indicated

---

[5]Indeed the spin polarization is different at the L_2 and L_3 edge, but this is compensated by the different number of transitions leading to an identical intensity.

[6]The L_2 and the L_3 absorption edge have the same orbital moment polarization.

in Fig. 2.11) absorption edges to the number N of holes within the $3d$ shell and their local distribution [88]:

$$(I_3 + I_2)_\alpha = C(N + N_Q^\alpha) \tag{2.53}$$

here N corresponds to the number of holes, C is the square of the $p \rightarrow d$ radial transition matrix element, the quadrupole term N_Q^α indicates the charge anisotropy and the index α describes the orientations of the polarization $\vec{e}$ in a Cartesian coordinate system α=x, y, z.

Furthermore, the XMCD spectrum discussed above can be used to determine the spin moment [91] and orbital moment [92] of the investigated sample in the case that the sample is fully magnetized. The spin and orbital $sum - rules$ link the area of the XMCD spectrum (labeled A and B in Fig. 2.11(b)) to the spin and orbital moment [88]:

$$(A + 2B)_\alpha = -\frac{1}{C} \left(m_s + \frac{7\,\mu_B}{\hbar} \langle T_z \rangle \right)_\alpha = -\frac{1}{C} \left\langle m_{s,\,eff} \right\rangle_\alpha \tag{2.54}$$

$$(A - B)_\alpha = -\frac{2}{3\,C}\, m_l^\alpha \tag{2.55}$$

here C is the square of the $p \rightarrow d$ radial transition matrix element, A and B are the areas defined in Fig. 2.11(b), μ_B is the Bohr magneton, and the index α= x, y, z indicates the orientation of the wave vector $\vec{k}$. The term $\langle T_z \rangle$ is the so called magnetic dipole operator and accounts for the asphericity of spin density [93]. Thus, the spin moment m_s can not be estimated independently from $\langle T_z \rangle$. Therefore an effective spin moment m_{eff} can be defined [7].

The contribution of the magnetic dipole operator $\langle T_z \rangle$ is expected to be significant for low-dimensional system with an anisotropic spin density. However, in the case of systems with a spherical or cubic symmetry the contribution of the magnetic dipole operator $\langle T_z \rangle$ vanishes [93]. Lowering of the dimensionality of the system can lead to sizable contribution of the $\langle T_z \rangle$ up to 20% [95] to the effective spin moment $m_{s,\,eff}$. This can cause misleading results of the spin sum rule ignoring the contribution of the magnetic dipole operator $\langle T_z \rangle$ [95].

The second sum rule in equation 2.55 links the XMCD intensity to the orbital moment m_l^α. The size and the anisotropy of the orbital moments rely on the $spin - orbit$ coupling and on the symmetry as on the size of the crystal field [94] caused by the surrounding ligands (also see section 4.2.1). More importantly, the anisotropy of the orbital moment m_l^α is linked to the magnetic anisotropy of the corresponding system [96–98]. The orbital moment m_l^α is larger along the magnetic easy axis direction and smaller in the magnetic hard axis direction [93, 97]. Thus, the XMCD signal allows us to investigate the magnetic anisotropy of a magnetic system.

The magnetic anisotropy of a sample can be investigated by changing the angle between sample and the incoming x-ray beam or the external magnetic field. In general, the external magnetic field is aligned parallel with respect to the incoming x-ray beam. Then the sample orientation is changed and we record the field dependence of the XMCD amplitude of the L_3 edge at different incidence angles,

---

[7]In the case of the $3d$ transition metal the spin orbital coupling is in general smaller than the crystal field and exchange interactions [94]. Then spin contribution is isotropic and the anisotropy of the magnetic dipole operator T_z^α is directly related to the charge anisotropy. In this case the spin sum rule links the XMCD signal to an effective moment m_{eff} consisting of an isotropic spin moment m_s and an angle dependent component stemming from T_z^α. The magnetic dipole operator $\langle T_z \rangle$ can then be written as $T_z^\alpha = \sum_\beta Q_{\alpha\beta} S_\beta$. Q is the quadrupole moment of the charge distribution, S stand for the spin (S) components and β= x, y, z indicates the component of the charge Q [88].

that is, we record magnetization curves. The XMCD amplitude of the L_3 edge is defined as the maximum intensity of the XMCD signal at the L_3 edge of the corresponding element minus the intensity value before the L_3 edge. To obtain the magnetization curves, we multiply the obtained data points with the value of the spin moment m_S calculated from the sum rules (cf equation 2.53). Typically the magnetic field dependence is done for normal incident and grazing incident orientation. Therefore we are able to investigate, if the magnetic easy axis of, for example, a metal-organic network, is aligned parallel or perpendicular to the surface plane, or in other words, if the system shows an easy axis or easy plane magnetic anisotropy. Because of symmetry reasons, we are not sensitive to the azimuthal dependence. In fact, the magnetization curves are an average over the different domain orientations of the system.

According to equation 2.55 the measured signal, the XMCD amplitude of the L_3 edge, is proportional to the magnetization $\vec{M}$ of the probed atomic species, for example the transition metal Fe, and reads:

$$\left\langle I_{XMCD}^{L_3} \right\rangle_\alpha = \mu_l^\alpha + \mu_s + \frac{7\mu_B}{\hbar} \langle T_z \rangle \tag{2.56}$$

The magnetization curves taken at different incidence angles reflect the magnetic anisotropy and also the saturation value of the XMCD signal, i.e. the magnetization $\left| \vec{M} \right|$, since also the orbital moment m_l^α contributes to the signal. However, in the evaluation of the obtained magnetization curves we have to be careful, since the magnetic dipole operator term $\frac{7\mu_B}{\hbar} \langle T_z \rangle$ can have a different angular dependence than the magnetic anisotropy. This can lead to false estimates of the magnetic anisotropy.

An important point is the normalization of the recorded magnetic curves, if the magnetization curves are not fully saturated. This means that the individual spins are not fully aligned along the orientation of the external magnetic field. Then only the projection of the magnetization $\vec{M}$ on the wave vector $\vec{k}$ is measured.

Let us assume that our magnetic system has a preferential magnetization direction or, in other words, a magnetic easy axis. Furthermore, the external magnetic field $\vec{B}$ is not strong enough to fully align the magnetic moments. Figure 2.13 depicts the case, when the external magnetic field $\vec{B}$ is not parallel to magnetic easy axis of the sample. In this case, the magnetization $\vec{M}$ is also not aligned parallel with respect to the easy axis and only the projection of the magnetization $\vec{M}$ onto the $\vec{k}$ vector of the X-rays contributes to the XMCD difference signal (see Fig. 2.13). The definition of the angles and the relative alignment of the magnetization $\vec{M}$, $\vec{k}$-vector of the x-rays and the external magnetic field $\vec{B}$ is given in Fig. 2.13. The total intensity of the "normalized" XMCD difference signal can therefore be expressed as follows:

$$I_{XMCD} = A \cos(\theta_M - \theta_k) |\mathbf{M}| (1 - C_{T_z}(1 - 3 \cos(2\theta_M))) \tag{2.57}$$

here the parameter A is a scaling factor and C_{T_z} accounts for the relative contributions of the magnetic dipole operator T_Z, which has angular dependence $(1 - 3 \cos(2\theta_M))$.

2.5   Sample Preparation

The deposition of molecules is done *in situ* in UHV Chamber by using a Knudsen cell. The total coverage of the organic layer can be estimated from the evaporation time t_{Evap} and temperature T_{Evap} and
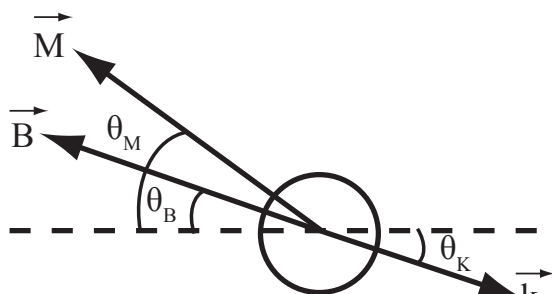
Figure 2.13: Schematic diagram of the relative alignment of the magnetic field $\vec{B}$, the magnetization $\vec{M}$, and the $\vec{k}$ vector of the x-rays in the case that the sample magnetization $\vec{M}$ is not fully aligned with the external magnetic field $\vec{B}$.

was further monitored using a micro quartz-balance. Within the framework of this thesis several organic molecules were used. Their chemical structure and the corresponding evaporation temperatures are listed in Fig. 2.14.

The evaporation of $3d$ transition metal atoms was done using a commercial Omicron UHV evaporator EFM3 equipped with high purity ($> 99.995\%$) metal rods (Cu, Fe, Co). An integrated flux monitor was used to check the metal atom flux and control the metal coverage on the corresponding sample. In general, the sample was kept at room temperature during the deposition of metal atoms. In the case of the metal-organic networks the prepared samples were subsequently annealed to 350 K to improve the network formation.

2.6 Coinage Metal Surfaces

The single crystalline metal surfaces were cleaned by repeated Ar^+ or Ne^+ sputtering and annealing cycles. The sputter time was typically about 30 min at a background gas pressure of $4 \cdot 10^{-6}$ mbar using an ion beam current of 3 μA at an acceleration voltage of 1.5 kV. Subsequently, the samples were annealed to 800 K for several minutes. The above described procedure lead to atomically clean flat surfaces, like the 3-D representation of a Au(111) surface shown in Fig. 2.15(c) reveals.

The growth of metal-organic networks or charge transfer complexes was done on low-index (111) crystalline coinage metal surfaces, namely Au(111), Cu(111) and Ag(111). All crystals have a face centered cubic (fcc) crystalline structure as shown in Fig. 2.15(a) with slightly different lattice constants. The (111) surface exhibits a trigonal surface symmetry as depicted in Fig. 2.15(b) and also different nearest neighbor distances (right hand side in Fig. 2.15(b)). Because of the similar electronic properties of these coinage metals they all exhibit a partially filled electronic surface state. The onset of the surface state band edge is located at -490 mV (Au(111)) [53], -440 mV (Cu(111)) [12], and -70 mV (Ag(111)) [99]. Figure 2.15(d) represents a STS dI/dV spectrum of a Au(111) metal surface reflecting its LDOS. The onset of the surface state band edge is clearly visible manifesting as a step-like feature located at $\propto$ -490 mV.

Additionally, to the monoatomic steps appearing in the STM topography image of the Au(111) surface in Fig. 2.15(c) parallel zigzag ridges are visible, which are due to the $23 x \sqrt{3}$ herringbone surface reconstruction of the Au(111) surface [100]. This reconstruction is not present in the case of the Cu(111) and Ag(111) metal surfaces. Such reconstruction is caused by stress due to a different equilibrium interatomic distance of the topmost Au atoms at the surface compared to the bulk. In total 46 Au atoms occupy 44 bulk lattice sites [101]. Hence, some of the Au atoms are forced to occupy
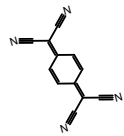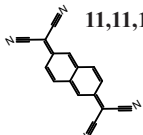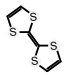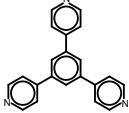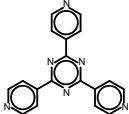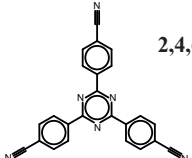
Chemical Structure	Name	Evaporation Temperature	Source
	7,7,8,8-tetracyanoquinodimethane (TCNQ)	100 °C	Sigma-Aldrich
	11,11,12,12-tetracyanonaptho-2,6-quinodimethane (TNAP)	175 °C	TCI
	tetrathiafulvalene* (TTF)	75 °C*	Sigma-Aldrich
	1,3,5-Tri(pyridin-4-yl)benzene (T4PB)	140 °C	Synthesized by C. Czekelius
	2,4,6-tris(4-pyridyl)-1,3,5-triazine (T4PT)	140 °C	TCI
	2,4,6-Tris(4-cyanophenyl)-1,3,5-triazine (T4CPT)	195 °C	Synthesized by C. Czekelius

Figure 2.14: Chemical structure, chemical name, and the evaporation temperature in UHV conditions of several molecules used in the present thesis. The molecules are either commercially available or were synthesized by C. Czekelius. (* TTF is evaporated from the TTF-TCNQ compound. Due to the different vapor pressure of TTF and TCNQ at a temperature of 75° C TTF starts to sublimate, while TCNQ remains in the powder).

high energy hcp sites or bridge sites (along the $\langle 11\bar{2} \rangle$ direction). The unit cell of the reconstructed Au(111) metal surface consists of alternating region with Au atoms on fcc and hcp sites separated by soliton lines (bridge sites) as shown in Fig. 2.16(a). Since the Au(111) surface has a trigonal surface symmetry, the reconstruction occurs with three different orientations (rotated 120°). This leads to the appearance of the zigzag lines in the STM topography. Due to the surface reconstruction the surface shows a corrugation with a height modulation of 0.2 Å [39, 101]. Molecular species tend to adsorb at the closed-pack fcc and hcp regions [102–104], avoiding adsorption sites at the bridging regions (soliton lines).

Furthermore, the different lattice sites imply also a slight difference in the electronic potential energy [39, 53, 100, 101, 105]. Figure 2.16(a) and (b) show a schematic diagram of the reconstructed Au(111) surface and the corresponding alternating potential landscape, respectively. The potential energy difference between the hcp and fcc regions amounts to ≈ 25 meV, in which the hcp regions exhibit a slightly higher LDOS compared to the fcc regions [53]. However, also the kinks of the zigzag lines are energetic favorable adsorption sites of molecules due to the diminished potential energy [106–109].
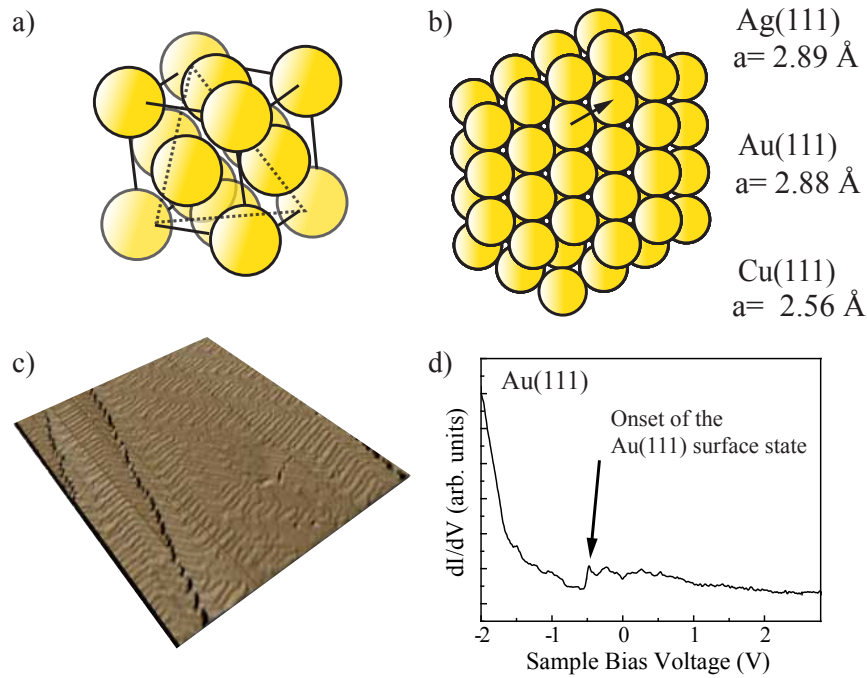
Figure 2.15: (a) Face centered cubic (fcc) crystalline structure of Cu, Au, and Ag. The (111) plane is indicated by the dashed triangular. (b) Schematic representation of the (111) surface with its trigonal surface symmetry. (c) STM topography image (3-D representation) of a Au(111) surface. (d) Representative dI/dV spectrum of the clean Au(111) surface ($I_T = 0.3$nA, $V_T = 2.7$ V the lock-in modulation is 10 mV rms at 867 Hz).

2.7   Experimental Set-up

The experimental data presented in this thesis were obtained using a custom-built ultra high vacuum (UHV) low-temperature STM located at the physics department of the FU Berlin and variable temperature STM (*OMICRON*) attached to the preparation chamber of the ID 08 beamline at the European Synchrotron Radiation Facility (ESRF) in Grenoble. The XMCD and XAS measurements were performed at the ID 08 beamline at the ESRF and at the UE-46 Beamline at BESSY.

2.7.1   Scanning Tunneling Microscope

Figure 2.17 shows an image of the UHV system of the custom-built STM. The system consists of two UHV chambers, the preparation chamber and the STM chamber. The preparation chamber is equipped with the standard UHV preparation and maintenance tools, like mass-spectrometer, sputter gun, ion-pump, turbo-pump and slots to mount molecular or metal UHV evaporators. The sample transfer is done with a manipulator, which allows to cool (by liquid helium)/heat (resistive heating) the sample (sample temperatures between 80 K and 1000 K can be reached). The manipulator can be moved independently along three axis (x, y, z). Also rotation around its role-axis is possible. In this chamber we perform the preparation of the sample: cleaning by sputtering, annealing cycles, and molecular deposition.
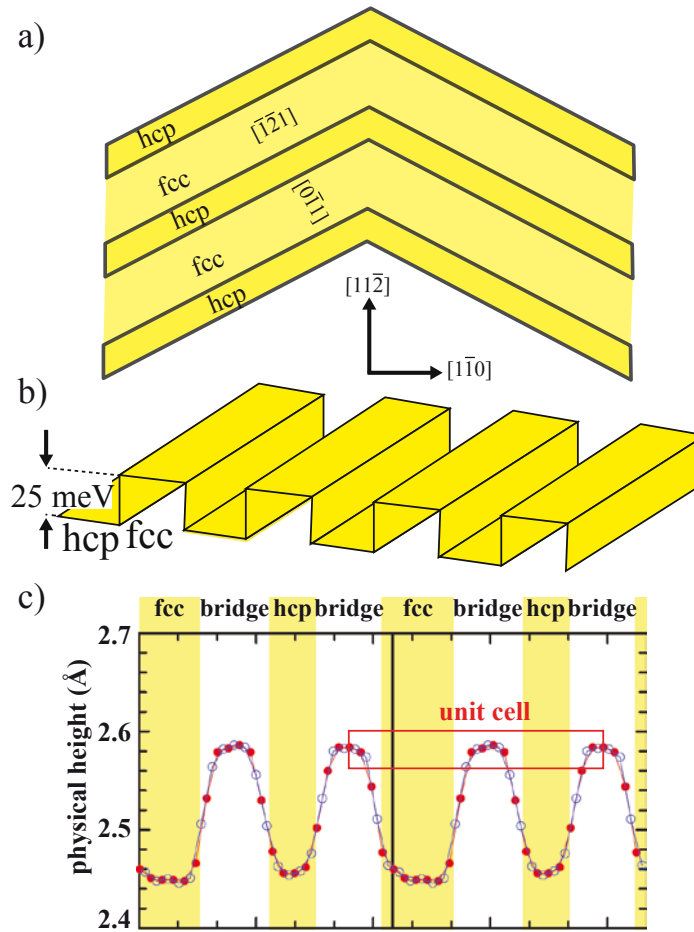
Figure 2.16: (a) Schematic diagram of the Au(111) surface reconstruction [41, 53, 101]. (b) Alternating potential landscape of the Au(111) reconstructed surface [53]. (c) Alternating physical height of the Au(111) reconstructed surface [101].

Figure 2.17(b) shows the schematic set-up of the STM UHV system. The STM scanner head is attached to a liquid-He bath (8.5 liters). The equilibrium temperature of the STM scanner head is 4.8 K with a base pressure of $3 \cdot 10^{-10}$ mbar. An outer liquid-nitrogen tank (21 liters) shields the inner liquid-He tank. Additional radiation shields improve the thermal isolation. Two shutters in the radiation shields allow sample transfer as indicated in Fig. 2.17(b). The STM scanner head can be fixed by a clamping system including a small T at the very bottom of the cryostat (see Fig. 2.17(b)). In the normal operation mode the STM head hangs on springs to damp mechanical vibrations. Additional $Eddy-Current$ damping improves the vibrational decoupling from the environment. Pneumatic vibration isolators from $NEW~PORT$ further damp low frequency vibrations.

A close-up of the STM scanner head is shown in Fig. 2.17(c) and a schematic sketch in Fig. 2.17(d). The top raceway plate is made out of Cu and consists of three ramps (see Fig. 2.17(d)). The race way stands on three piezo elements with sapphire spheres on top. This allows to move the top raceway, where also the tip is located, with respect to the sample. This is done by applying voltage signals to the contacts of the piezo elements. Horizontal and also vertical movements are possible, since the movement of the piezos lead to a rotation of the raceway. The STM tip is fixed to a central piezo at the
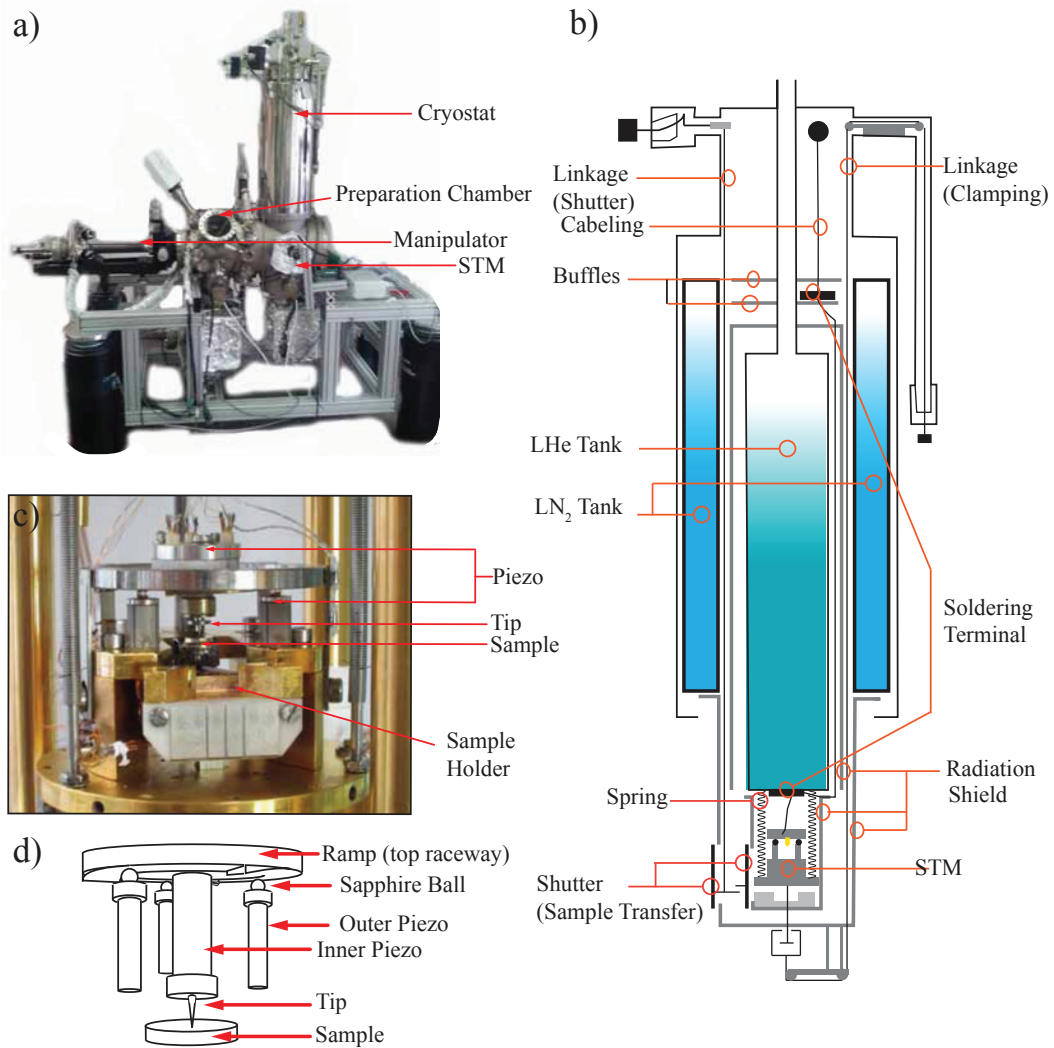
Figure 2.17: (a) Image of the UHV system including the STM head. (b) Schematic sketch of the cryostat including the STM scanning head. Adapted form Ref. [110] (c) Close-up of the STM scanning head. (d) Schematic illustration of the STM scanning head.

center of the raceway plate (see Fig. 2.17(c) and (d)), which can be independently used for scanning.

The STM tip is made out of W and was chemically etched using an electrochemical cell to get microscopic sharp tip [53]. To prepare a STM tip during operation, which is suited for the experiment, we do the following: we indent the STM tip into the bare metal surface to cover it with an unspecified amount of the clean metal. Therefore the tip apex consists presumably of metal atoms of the surface material. To check the quality of the STM tip a STS spectrum of the bare metal surface can be recorded. When the spectrum resembles the typical step-like feature of the surface state, the STM tip can be regarded to be clean.

In the case that the STM tip is functionalized or contaminated, two cleaning procedures can be performed. The first one consists of dipping the tip a few Å into a clean surface area in order to cause a rearrangement of the atoms at the tip apex. A more drastic procedure is related to controlled field

emission at the tip apex and implies the application of a high bias voltage (100 V) to the tip. This causes a current (1 mA) and leads to heating of the tip apex. The tip apex starts to melt and the contamination is therefore removed. A drawback of this procedure is that the surface area is locally destroyed.

The data acquisition was done using the *PSTMAFM* software from *CREATEC*. STS spectra were recorded using a commercial Stanford Research SR830 lock-in amplifier. All STM images were processed using the *WSxM* software [111].

2.7.2 ID08 Beamline at the ESRF and the UE-46 Beamline at BESSY

Both the ID08 beamline at the ESRF and UE-46 beamline at BESSY consist of a UHV system composed of two separated chambers. The preparation chambers are equipped with the standard UHV tools for cleaning and deposition of metal or molecular species. The preparation chamber of the ID08 beamline at the ESRF is also equipped with an *OMICRON* variable-temperature STM, which offers the possibility to analyze the coverage and cleanliness of each sample before introducing it to the XAS/XMCD measuring UHV chamber.

The XAS/XMCD UHV chambers at the ID08 and at the UE-46 beamline include a variable ± 5 and ± 6 Tesla magnetic field, respectively. The sample holder is in both cases attached to a liquid-He bath and can also be resistively heated. Therefore the experiment temperature can be varied between 8 and 300 K. In both XAS/XMCD UHV chambers the magnetic field is collinear with the incoming x-ray beam originating from the synchrotron ring. The sample orientation θ, with respect to the incoming x-ray beam, can be changed between $20°$ and $90°$. Here θ refers to the angle between the incoming x-ray beam and the surface plane of the sample. All XAS measurements were carried out in the total electron yield (TEY) detection mode, here all electrons leaving the sample are counted (Auger electrons, photoelectron, and secondary electrons). This is done by measuring the drain current.

In order to remove time and energy dependent artifacts in the measured signal, a normalization procedure has to be performed. This is done by using the signal of a gold grid recorded simultaneously for each recorded spectrum, which acts as reference for the corresponding photon flux. Furthermore the signal of the clean substrate is measured before the deposition of molecules or metal atoms. This allows to remove the spectral component of the sample and to obtain the intrinsic signal. A detailed description of the renormalization procedure is given in Ref. [112].

CHARGE TRANSFER COMPLEXES ON METAL SURFACES

The work presented in this chapter was partly published as:

- *Atypical charge redistribution over a charge-transfer monolayer on a metal surface* by T. R. Umbach, I. Fernández-Torrente, M. Ruby, F. Schulz, C. Lotze, R. Rurali, M. Persson, J. I. Pascual, K. J. Franke, accepted for publication in the *New Journal of Physics* **2013**

- *Enhanced charge transfer in a monolayer of the organic charge transfer complex TTF-TNAP on Au(111)* by T. R. Umbach, I. Fernández-Torrente, J. Ladenthin, J. I. Pascual, K. J. Franke, *J. Phys. Condens. Matter* **2012**, 5, 354003

3.1 Introduction

Over the past two decades organic thin-films have been an intensively studied research field regarding their potential application for future electronic devices. Organic thin-films are used nowadays as the active device component in organic solar cells [113, 114], lasers [115], transistors [116, 117], and light emitting diodes [118–120]. The wide range of application is based on the functional variability of the molecular constituents regarding their structural properties and types of functional groups.

However, the performance of organic thin-film based devices significantly depends on the organic/metal interface between the organic thin-film and the metallic electrodes, needed to contact the device. The presence of the metallic electrode may change the electronic properties of the molecules at the interface or affects the molecular conformation. There are several mechanisms, which can lead to a change of the molecular electronic properties based on the interaction with the metal surface. For instance, hybridization of the molecular electronic states, interfacial charge transfer or adsorption induced conformational changes. These interactions, can cause a sizable splitting, realignment or broadening of the relevant molecular electronic states [42, 43, 121]. Hence, an organic monolayer on a metal surface can show a wide variety of properties. For example, an interface band structure with free-electron metal-like dispersion [58], superconductivity [34], or a confinement of electronic surface states [122–124]. As a consequence, the electronic properties of the organic/metal interface differ significantly from that of the corresponding organic bulk material. Understanding the physical
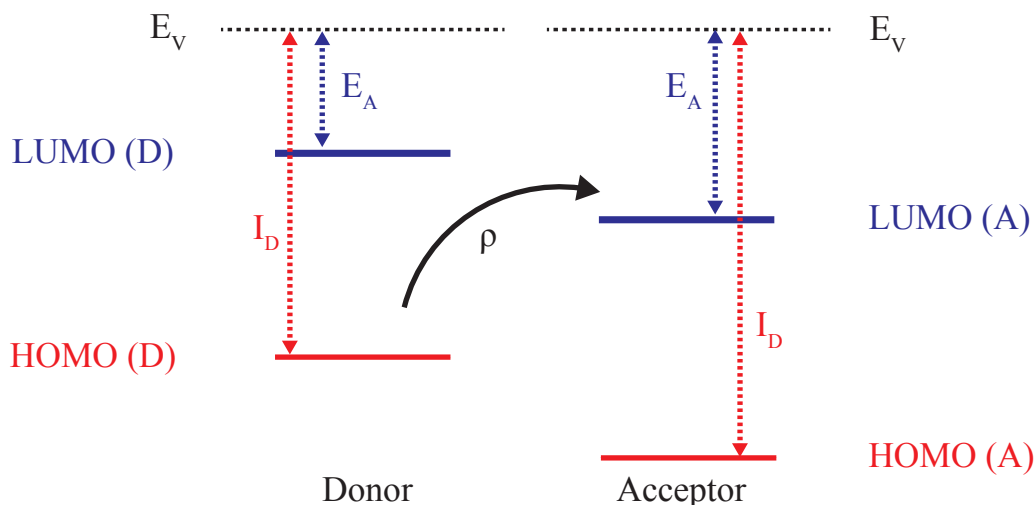
Figure 3.1: Schematic diagram of the charge transfer from a donor species to an acceptor species.

and chemical processes occurring at the interface is crucial for potential applications in molecular electronics.

An important question we want to focus on in the following chapter is the charge state and the charge distribution of organic layers and how these two physical quantities are altered at the organic/metal interface compared to the organic bulk material. In this regard the STM allows to analyze with sub-nanometer resolution such organic monolayers deposited on a crystalline metal surface.

In the following chapter we will discuss three different charge transfer complexes (CTC) deposited on a Au(111) metal surface. We will focus on the main differences with respect to the charge state of the donor and acceptor species within the charge transfer complexes and the influence of the surface.

3.2   Charge Transfer Complexes

Charge transfer complexes (CTC) define a unique class of organic materials with a wide variety of applications in molecular magnets[125–128], non-linear optics [129, 130], magneto-optics [131, 132], superconductivity [34, 133–136], organic electronics [25, 137–140] or storage devices [141–144].

In general, a CTC is composed of a donor D and acceptor A species, which interact to form a combined complex with new structural and physical properties. The donor D donates a certain amount of charge ρ to the acceptor A. Therefore the donor D is oxidized and the acceptor A is reduced. By definition the formation of a CTC is described by the following reaction path [145]:

$$D_m + A_n \longrightarrow [D_m]^{+\rho} + [A_n]^{-\rho} \tag{3.1}$$

Here n and m refer to integer numbers and ρ to the charge transfer ratio [145]. The driving force for the CTC formation is the energy gain resulting from the redistribution of charge. The following sim-

plified equation defines the energy condition for the formation of an ionic (complete charge transfer of $\rho = 1$ e$^-$) CTC complex [146, 147]:

$$\Delta E = I_D - E_A - E_I < 0 \qquad\qquad (3.2)$$

The donor species D is characterized by its ionization energy (I_D) and the acceptor species A by its electron affinity (E_A) (see Fig. 3.1). The ionization energy I_D of the donor accounts for the energy needed to remove an electron from the HOMO and the electron affinity E_A describes the energy gain upon filling the LUMO of the acceptor species. The term E_I accounts for Coulomb, polarization, and exchange energies arising from the interaction of the donor and acceptor charges [146–148]. In order to calculate the electronic structure of a CTC, a common approach is based on the frontier orbitals (in general π-orbitals for molecules or in the case of atoms the valence orbitals) of the corresponding constitutes. In the case of organic molecules this theory is known as π-orbital approximation [145]. To have a maximum charge transfer the ionization energy I_D should be small and the electron affinity E_A should be large.

The above described donor-acceptor interactions can lead to the formation of crystalline CTC solids mediated by the overlap of the frontier π-orbitals of the constituent molecules. In some cases the orbitals form metal-like electronic bands and the corresponding CTC becomes conducting. These low-dimensional bands show in general an effective mass larger than 1.0 m_0 [1], which is attributed to many-body interactions while the electron is moving throughout the crystal [145].

3.2.1 Monolayer of CTC on Metal Surfaces

The structure and electronic properties of bulk CTC are a result of the interplay of a multitude of interactions including Van-der-Waals, electrostatic, and polarizability effects between the donor and acceptor sites. The presence of an additional metal surface can not only change the structural properties of an adsorbed CTC monolayer, but also its electronic nature. The underlying metal surface may act as a template. In such a case, the adsorbed donor and acceptor species preferentially occupy certain sites on the surface. This can have an effect on the donor-acceptor self-assembling, which can be different compared to the bulk crystal structure.

The metal surface can also have an impact on the spatial charge distribution due to screening effects of the conduction electrons leading to a lowered effective Coulomb interaction, maybe helping to stabilize a radical state of the donor or acceptor. In some cases also a hybridization between the molecular and metal electronic states can occur. This can lead to conformational changes of the molecule [149], formation of interfacial hybrid-states [150], and bands with a metal-like dispersion [58]. Furthermore, the hybridization of the metal and molecule electronic states can result in an additional charge transfer. For instance, the prototype CTC of TTF-TCNQ has a fractional charge transfer of $\rho = 0.59$ e$^-$ [151, 152] from the donor TTF to the acceptor TCNQ molecule in bulk. In contrast, the monolayer system of TTF-TCNQ on a Au(111) metal surface shows a charge transfer of $\rho = 1.0$ e$^-$ [29]. A single unpaired electron is located in a π-orbital of the TCNQ acceptor species.

---

[1]Here m_0 refers the free-electron mass.
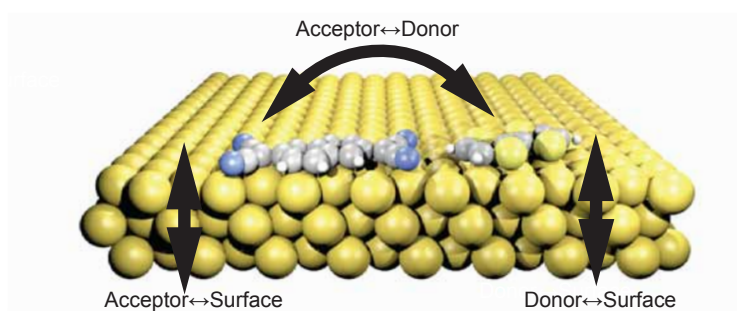
Figure 3.2:   Schematic sketch of the interactions of an CTC on a metallic surface. The underlying metal surface can act as an additional charge reservoir. Therefore not only the charge transfer between donor and acceptor species can occur, but also between the donor D or acceptor A and the metal surface.

The interplay of the above discussed interactions determines the structural and electronic properties of the CTC on the metal surface. By changing the type of acceptor or donor species we can characterize the robustness of the charge transfer and the degree of hybridization with the underlying metal surface.

We are interested in the charge state and the corresponding charge distribution of CTC monolayers on metal surfaces. To map the spatial charge distribution we use the spectroscopic fingerprint of the unpaired electron spin: the Kondo effect. The Kondo effect occurs at low temperatures and describes the interaction of a single localized electron with the conduction electron system leading to a new many-body ground state. Using STM we can measure the fingerprint of this many-body state and, hence, obtain information about the spatial distribution of the localized spin. The next section gives a brief introduction to Kondo physics and its manifestation in transport experiments like STM.

3.3   The Kondo Effect

In the early 30's De Haas and coworkers investigated the conductivity of gold wires at low temperatures and found a minimum of the electrical resistance at a critical temperature T_K [153]. In general lowering of the temperature of a material leads to a decreasing electrical resistance R. This can be explained by reducing the number of phonons responsible for the electrical resistance R due to electron-phonon scattering. At low temperatures scattering at defects and impurities becomes dominant leading to a finite electrical resistance R. However, for temperatures $T < T_K$ the electrical resistance R is increasing if magnetic impurities are present. This threshold temperature T_K is known nowadays as the Kondo temperature. It was evident that magnetic impurities are responsible for the increasing electrical resistance at $T < T_K$ [154], but the underlying physical scattering mechanism was unclear. In 1968 Kondo presented a theoretical description [155] of the behavior of the electrical resistance at low temperatures of metals doped with magnetic impurities. Within this framework the increasing electrical resistance is explained by spin scattering processes between conduction electrons and the magnetic entities, which dominate at low energies (temperatures) leading to a new many-body ground state [155, 156]. The following chapter gives a short description of the Kondo effect based on the Anderson impurity model. A more detailed description is given in Ref. [156–158].
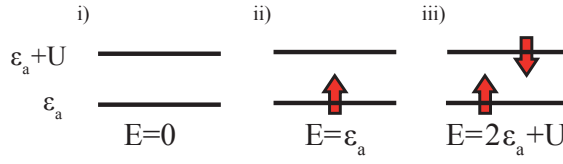
Figure 3.3: Possible electronic configurations for a single atomic/molecular level. (i) Empty atomic/molecular level with energy $E = 0$. (ii) Singly occupied atomic/molecular level with $E = \varepsilon_a$. (iii) Doubly occupied atomic/molecular level with $E = 2\varepsilon_a + U$.

3.3.1 The Anderson Impurity Model ($S = 1/2$)

The Kondo effect defines the problem of a single spin interacting with a bath of electrons [2] at low energies (low temperatures). Thus, only bath electrons close to E_F are relevant for the Kondo problem. The following discussion is based on the Anderson impurity model. Let us consider an atomic or molecular orbital, which can be occupied with up to two electrons (see Fig. 3.3). The energy of the system orbital is defined as ε_a. The orbital can be empty referring to a total energy of $E = 0$. Single occupation by an electron with spin $\sigma = \uparrow$ or $\downarrow$ corresponds to a total energy $E = \varepsilon_a$ and the related ground state exhibits a two-fold spin-degeneracy ($S = \frac{1}{2}$) depending on weather the spin is up or down. To fill the orbital with two electrons with spin $\sigma = \uparrow$ and $\downarrow$ one has to overcome the Coulomb energy U and the total energy of a doubly occupied system will be $E = 2\varepsilon_a + U$.

In the following we consider only the case of a single occupied orbital, which lies below E_F and is separated by the Coulomb energy U from the double occupied configuration. The broadening Γ of the orbitals (due to the hybridization with the conduction electronic states) has to be smaller than the Coulomb energy U to avoid overlap. An orbital overlap would imply spin fluctuations between the singly and doubly occupied state. The system is then in the so called mixed-valence regime [159]. In total three conditions have to be fulfilled:

$$\varepsilon_a < E_F \tag{3.3}$$

$$\varepsilon_a + U > E_F \tag{3.4}$$

$$\Gamma << U \tag{3.5}$$

This configuration is called the *local moment* regime referring to a singly occupied orbital.

Now we couple this single orbital to a bath of electrons (electrode) and the coupling is defined by a certain hybridization/wave function overlap of the relevant electronic states. The specified system can be described with the following Anderson Hamiltonian [156]:

$$\mathscr{H}_A = \sum_\sigma \varepsilon_a n_{a,\,\sigma} + U_{n_{a\uparrow},n_{a\downarrow}} + \sum_{k,\,\sigma} \varepsilon_a c^\dagger_{k,\,\sigma} c_{k,\,\sigma} + \sum_{k,\,\sigma} (V_k c^\dagger_{d,\,\sigma} c_{k,\,\sigma} + V_k^* c^\dagger_{k,\,\sigma} c_{d,\,\sigma}) \tag{3.6}$$

$$V_k = \sum \sigma e^{i\,k\,\cdot a_\sigma} \langle \phi_d |H| \psi_{d_\sigma} \rangle$$

The first term in equation 3.6 describes the occupancy of the non-degenerated electronic states (of the atom/molecule) by the occupation number $n_{a,\,\sigma}$ and the energy ε_a of the corresponding atomic/molecular state. The second term accounts for Coulomb interactions U between the electrons with opposite spin $n_{a\uparrow}$ and $n_{a\downarrow}$ on the atom/molecular site. The bath of conduction electrons

---

[2]For example the conduction electron system at a surface.

is characterized by $c_{k,\sigma}^{\dagger}$ and $c_{k,\sigma}$, which are creation and annihilation operators of wave vector k and spin component σ for the energy eigenvalue ε_K. The last term in equation 3.6 corresponds to the hybridization V_k of the conduction electrons and atomic/molecular states. Here $\sigma = \uparrow$ or $\downarrow$ and V_K are the hybridization matrix element between atomic/molecular level ϕ_a and the electronic states of the electron bath ψ_{k_σ} (electrode). This Hamiltonian defines the electronic structure of the local atomic/molecular system and allows us to specify the conditions to have a singly occupied orbital coupled to a bath of electrons. However, to get a more physical picture of the hybridization V_k it is better to modify the above Anderson-Hamiltonian to the so called Kondo-Hamiltonian. This is done by projecting the Anderson Hamiltonian onto the subspace of the single occupied atomic/molecular state by a canonical transformation [160]:

$$\mathcal{H}_K = \sum_{\sigma} \varepsilon_a n_{a,\sigma} \tag{3.7}$$
$$+ \sum_{k,k'} J_{k,k'} \left(S^+ c_{k,\downarrow\sigma}^{\dagger} c_{k,\uparrow\sigma} + S^- c_{k,\uparrow\sigma}^{\dagger} c_{k,\downarrow\sigma} + S_z (c_{k,\uparrow\sigma}^{\dagger} c_{k,\uparrow\sigma} + c_{k,\downarrow\sigma}^{\dagger} c_{k,\downarrow\sigma}) \right)$$

The first term in equation 3.7 accounts for the occupancy of the non-degenerated electronic states (of the atom/molecule) by the occupation number $n_{a,\sigma}$ and the energy ε_a of the corresponding atomic/molecular state. Here $c_{k,\sigma}^{\dagger}$ and $c_{k,\sigma}$ creates or annihilates an electron with momentum k and spin σ, respectively. S_z and $S^{\pm} = (S_x \pm i \cdot S_y)$ are the spin operators of the localized spin at the atomic/molecular site. J refers to Heisenberg type exchange coupling between the electrons of the bath and the local atomic/ molecular electron spin. The Hamiltonian includes terms which describe spin-flip processes upon resonant scattering events of bath electron spins with the local atomic/molecular electron spin.

In the case of the local moment regime, at low energies charge fluctuations of the local electronic state are suppressed because of the large Coulomb interaction U. The only degree of freedom at low energies in such a system is the spin degeneracy ($S = 1/2$) of the electron in the local electronic state. As was found out by Kondo [155] that spin-scattering processes involving spin-flips are the origin of the Kondo effect leading to minimization of the energy and implying a new correlated ground state. The scattering processes involve virtual intermediate states (so called second-order spin scattering processes [156]). These imply the spin flip of impurity and conduction electrons and can be expressed by the following equation:

$$|\uparrow \ k, \downarrow \ \varepsilon_a\rangle^{initial} \longrightarrow |\downarrow \ k^*, \uparrow \ \varepsilon_a\rangle^{final} \tag{3.8}$$

There are also scattering processes of second-order implying two spin-flip processes, therefore the spin orientations of the initial and final state are the same:

$$|\uparrow \ k, \downarrow \ \varepsilon_a\rangle^{initial} \longrightarrow |\uparrow k^*, \downarrow \ \varepsilon_a\rangle^{final} \tag{3.9}$$

In order to get a physical picture of these second order scattering processes let us consider a singly occupied atomic/molecular state coupled to an electron bath (electrode) like shown in Fig. 3.4(a). The colored arrows correspond to the spin orientation, which can either be up (red) or down (blue). The two different scattering processes involving spin-flips are depicted in Fig. 3.4 (a-c) and (d-f), respectively. The first one describes the scattering of conduction electrons with $|k, \downarrow\rangle$ with the localized electron spin into the intermediate hole state in Fig. 3.4(b). The atomic/molecular orbital is doubly occupied by two electrons with spins oriented in opposite directions (referring to the states $|\varepsilon_a, \downarrow\rangle$ and $|\varepsilon_a + U, \uparrow\rangle$). Then the electron in the $|\varepsilon_a + U, \uparrow\rangle$ state scatters with a spin-flip into the final state
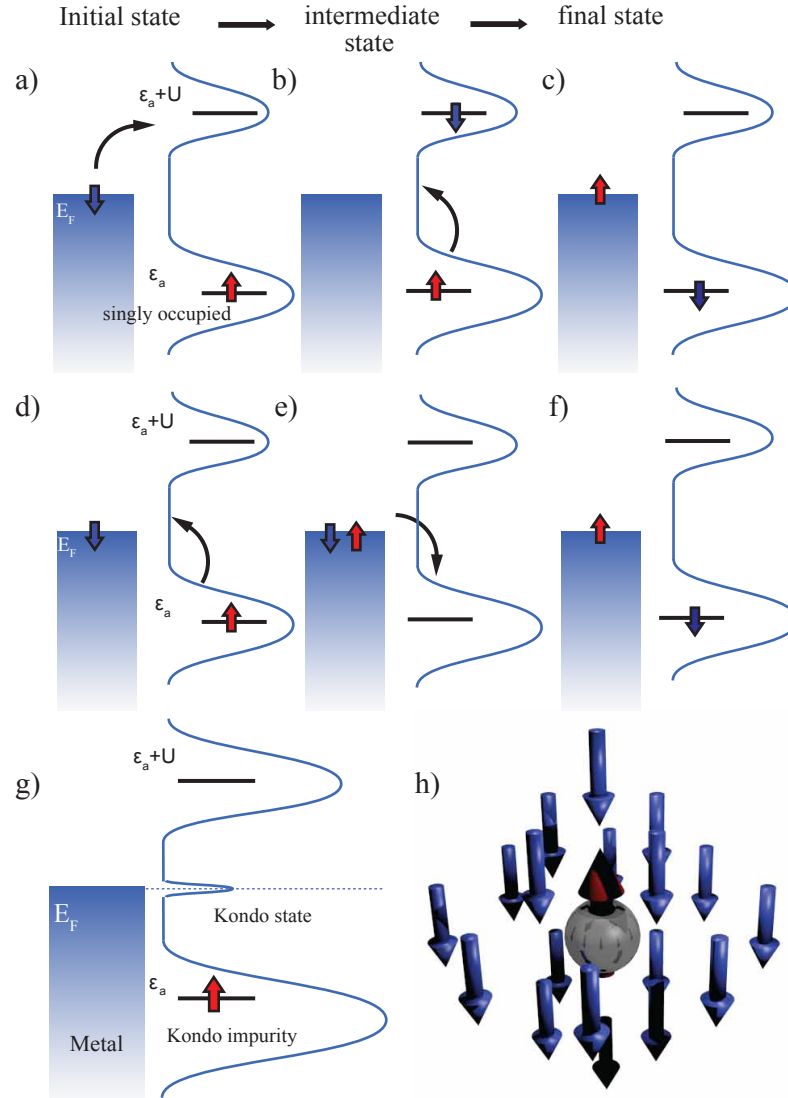
Figure 3.4: Scheme of the spin scattering processes involving spin-flips. The red and blue arrow indicate spin-up or spin-down orientation, respectively. (a) The singly occupied state is located at an energy $E = \varepsilon_a$. The double occupied level is separated by Coulomb energy U at the total energy $E = \varepsilon_a + U$. (b) A conduction electron scatters without a spin flip into to the hole state localized at $E = \varepsilon_a + U$. Since the conduction electron has to overcome the energy of $E = \varepsilon_a + U$, this is only allowed on a short time scale (femtoseconds). (c) An electron with spin down scatters into an empty state of the electron bath close to E_F. (d) First an electron of the localized state at $E = \varepsilon_a$ scatters into to an empty state of the electron bath. Then a conduction electron scatters with a spin flip into the empty localized state at $E = \varepsilon_a$. (g) The spin-flip scattering leads to the formation of a new many-body ground state implying a modification of the energy spectrum. Close to E_F the so called Kondo resonance evolves. (h) The scattering process involves an antiferromagnetic exchange coupling $J > 0$. Therefore, the local moment is screened by the conduction electrons.

$|k^*, \uparrow\rangle$. Another possible scattering process is depicted in Fig. 3.4(d-f). Here the local electron in the $|\varepsilon_a, \uparrow\rangle$ state scatters into the final state $|k^*, \uparrow\rangle$. A conduction electron then scatters without a spin-flip into remaining empty atomic/molecular orbital with $|k^*, \uparrow\rangle$.

In order to fill the atomic/molecular orbital with two electrons with opposite spin one has to overcome the Coulomb energy U (see Fig. 3.4(a-c)). On the other hand, to empty the atomic/molecular orbital and to fill one empty state in the conduction electron band one needs at least an energy of the order of $E_F - \varepsilon_a$ (see Fig. 3.4(e-f)). Therefore these processes are only allowed on a very short time scale determined by Heisenberg uncertainty principle $t < \hbar/E$. Hence the underlying time scale is of the order of femtoseconds.

We are dealing here with a many-body effect between the conduction electrons and the localized electron spin. The scattering events lead to an energy minimization and a new correlated ground state evolves at E_F. This new state close to E_F is called the Kondo resonance.

According to the Kondo Hamiltonian in equation 3.7 the interaction of the scattering conduction electrons with the spin of the localized electron can be described as an effective exchange coupling J. The conduction electrons couple to the localized single spin. The relation between the effective exchange coupling $J_{k, k'}$ (Kondo theory) and the physical variables defined within the framework of the Anderson impurity model are as follows [160]:

$$J_{k,k'} = V_k^* V_{k'} \left(\frac{1}{U + \varepsilon_a - \varepsilon_{k'}} + \frac{1}{\varepsilon_k - \varepsilon_a} \right) \tag{3.10}$$

Within the *local moment* regime ($\varepsilon_a < E_F$, $\varepsilon_a + U > E_F$, and $\Gamma << U$) the resulting exchange interaction J between the scattering bath electrons close to E_F and the local singly occupied atomic/molecular orbital is antiferromagnetic ($J_{k,k'} > 0$)[3]. Because of the antiferromagnetic exchange interaction the conduction electrons screen the single spin moment of the atom/molecule forming a singlet ground state $S = 1/2(\uparrow\downarrow - \downarrow\uparrow)$.

3.3.2 The Kondo Temperature

A requirement for the Kondo effect to occur is that the temperature of the considered system is lowered below a critical temperature T_K known as the Kondo temperature. Within this regime, spin-flip scattering processes lead to a new many-body ground state (see Fig. 3.4(g)). Hence the Kondo temperature corresponds to a binding energy $E_{Bin}^{Kondo} = k_B \cdot T_K$ of the spin singlet state and can be related to the above discussed effective exchange coupling between the conduction electrons and the localized single spin [156]:

$$T_K \propto D \sqrt{\rho J} \exp\left(-\frac{1}{\rho J}\right) \tag{3.11}$$

T_K can also be linked to the Anderson model [161]:

$$T_K \propto \frac{1}{2} \sqrt{(\Delta U)} \exp\left[-\pi \varepsilon_a \left(\frac{\varepsilon_a + U}{2 \Delta U}\right)\right] \tag{3.12}$$

---

[3]This effective exchange coupling J can be connected to the final resistivity R of the magnetic impurity (localized spin) [155, 156]. Kondo calculated the resistivity to third order in the exchange coupling J and showed the important role of the above described scattering processes involving spin-flips for the low energy scattering of the conduction electrons with the local spin [155]. The scattering processes lead to a temperature dependent correction of the resistivity [155].

System	T_K
TTF-TCNQ on Au(111) [29]	23 K
TCNE on Cu(111) [162]	29 K
Co on CuN_2 [163]	2.6 K
Co on Au(111) [164]	75 K
dehydrogenated CoPc on Au(111) [165]	208 K
FePc(Fe centered on top site) on Au(111) [166]	598 K

Table 3.1: Kondo temperature T_K of different Kondo systems.

Here U is the Coulomb energy and ε_a describes the energy of the singly occupied atomic/molecular level. The width Δ corresponds to the hybridization strength of the atomic/molecular level with the surface or bulk states. T_K defines the only relevant energy scale within this regime. The expression of T_K in equation 3.12 defines, within the framework of the Anderson model, variations of the Kondo Temperature T_K and therefore the change in binding energy E_{Kondo} in terms of hybridization, Coulomb energy and the detailed electronic structure of the system. Since the Kondo temperature T_K shows an exponential dependence on the parameters U, Δ, and ε_a it can vary on a wide range. Table 3.1 gives an overview of different molecular Kondo systems like charge transfer complexes, metal-phthalocyanines, and metal-porphyrines on different surfaces and their corresponding Kondo temperatures T_K.

3.3.3 The Kondo Resonance

In 1998 Goldhaber-Gordon et al. [167] detected a zero bias anomaly identified as a Kondo resonance in a single electron transistor (SET) based on a GaAs/AlGaAs heterostructure. Shortly after that, the research groups of Madhavan et al. [168] and Li et al. [169] independently discovered the Kondo effect for single magnetic atoms on a metal surface by using STM. In transport experiments, like in Ref. [167], the Kondo systems are coupled to two leads (electrodes) and a significant change of the conductance close the Fermi energy E_F is detected. In this case, the line shape of the resonance is a Lorentzian, as first described by Abrikosarov and Suhl [171, 172] within the framework of the Anderson theory. However, in transport experiments like STS the Kondo resonance has a Fano line-shape due to quantum interference of several competing tunneling channels [173]. The experimental setup in the case of the STM is shown in Fig. 3.5(a). The electronic states of the STM tip can couple with the surface/bulk electronic states or with the single occupied level of the adsorbate. Figure 3.5(a) illustrates the three different tunneling paths of tip electrons to the surface[158, 170] in the case of a magnetic adsorbate on a metal surface.

Path (1) corresponds to direct tunneling into empty electronic surface or bulk states close to E_F. This tunneling path does not involve the impurity bound state and therefore conserves the spin orientation of the unpaired electron in the level of the atomic/ molecular level of the adsorbate. The tip electrons can also tunnel into the Kondo resonance (path (2)). Also in the case of path (2) the spin orientation of unpaired electron in level of the atomic/ molecular level of the adsorbate is preserved. The last tunneling path (3) refers to tunneling into the singly occupied atomic/molecular level of the adsorbate via a spin-flip process. In this last case, the spin orientation is changed and the final state differs from
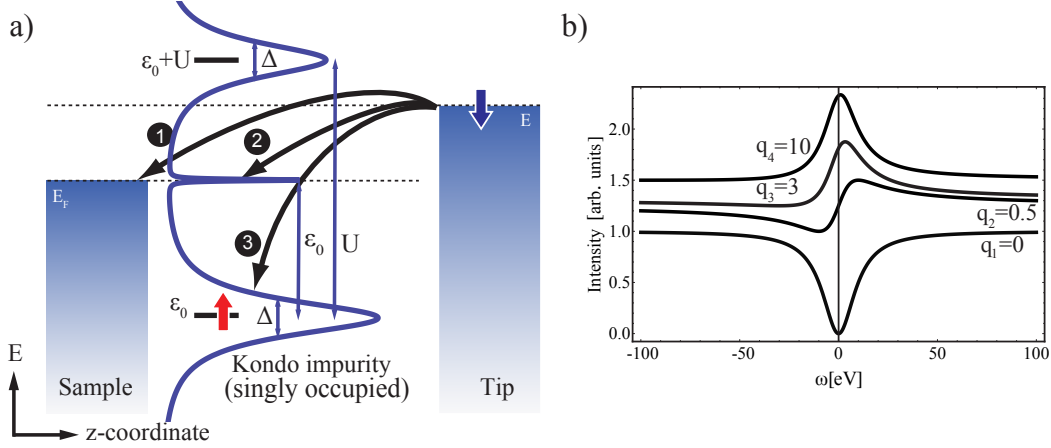
Figure 3.5: Schematic energy diagram of the STM tunnel junction consisting of the tip, sample, and the localized singly occupied atomic/molecular level of the adsorbate on the surface [170]. The singly occupied atomic/molecular orbital interacts via spin-flip processes with the conduction electrons of the underlying metal surfaces and a new correlated ground state is formed known as the Kondo resonance. The energy spectrum of the localized singly occupied atomic/molecular level and the Kondo resonance is shown as a blue line. There are in total three possible tunneling paths of electrons tunneling from the tip to the surface. Path (1) indicates the direct tunneling into empty surface or bulk states close to E_F and the Path (2) corresponds to direct tunneling into the Kondo resonance. The last tunnel path (3) refers to tunneling into the singly occupied atomic/molecular level via spin-flip process.

path (1) and (2). The Fano line shape of the Kondo resonance is a result of the quantum interference between path (1) and (2). The latter path (3) does not give rise to interference neither with path (1) nor (2) since the final spin state is different. Path (3) refers to an inelastic tunnel process known as spin-flip excitation, because the spin of the singly occupied atomic/molecular level changes its orientation.

Fano showed that a discrete electronic state coupled to continuum of states can be expressed by the following equation [170]:

$$Fano(\varepsilon) \propto \frac{(q + \frac{2(\varepsilon - \varepsilon_K)}{\Gamma_K})^2}{1 + (\frac{2(\varepsilon - \varepsilon_K)}{\Gamma_K})^2} \tag{3.13}$$

Here ε_K is the energetic position of the Kondo resonance, ε is the energy, and Γ_K is the full width of the half maximum (FWHM) of the resonance. The so called asymmetry-factor q is given by[170]:

$$q = \frac{t_2}{2\pi V t_1} \tag{3.14}$$

Here t_1 and t_2 correspond to the tunneling probabilities of the two tunnel paths (1) and (2) (see Fig. 3.5)(a). V refers to the hybridization matrix element of the local singly occupied atomic/molecular level and the continuum states of the surface/bulk. Fig. 3.5)(b) reflects the dependence of the resonance shape on the q factor. For $q \rightarrow \infty$ the line shape of the Kondo resonance is a Lorentzian, hence, only tunneling through the many body state occurs. For $q \rightarrow 0$ the Kondo

resonance has a dip-like shape. For intermediate values of q the resonance shows an asymmetric shape (Fano shape).

The atomic precision of the STM allows to spatially map the Kondo resonance. By moving the STM away from the local adsorbate the line shape of the Kondo resonance changes. This effect was already observed in the very early STM studies of Madhavan et al. [168] and Li et al. [99] on Co atoms on Au(111) and Ce on Au(111), respectively.

The FWHM Γ_K of the Kondo resonance at T = 0 K is related to the Kondo temperature T_K [174, 175]:

$$\Gamma_K(T) = 2\sqrt{2}(k_B\, T_K) \tag{3.15}$$

For temperatures T > 0 K the Kondo resonance shows a characteristic temperature dependence and its width Γ is increasing with increasing temperature T [174, 175]:

$$\Gamma_K(T) = 2\sqrt{(\pi\, k_B T)^2 + 2(k_B\, T_K)^2} \tag{3.16}$$

Here k_B is the Boltzman constant, T is the temperature and T_K is the intrinsic Kondo temperature of the corresponding Kondo system. Since the STM experiments are carried out at finite temperatures T also the temperature broadening of the Fermi edges of the leads (tip and sample) and the broadening caused by the instrumental electronics [4] have to be taken into account, when the Kondo temperature T_K is extracted from the experimentally obtained width Γ^{Exp} of the Kondo resonance. The measured Kondo Γ^{Exp} can be described with an empirical equation [159]:

$$\Gamma(T)^{Exp} = 0.758 \cdot \Gamma_K + 3.52 \cdot k_B \cdot T + V_{RMS} \tag{3.17}$$

Here Γ_K is the intrinsic width of the Kondo resonance, T is the experimental temperature and V_{RMS} is the Lock-in amplifier modulation voltage. Hence, the analysis of the Δ_K of the Kondo resonance allows to evaluate the binding energy $k_B \cdot T_K$ of the spin singlet state.

---

[4]STS in general use a Lock-in-Amplifier modulating the measured signal.

3.4   Na-TCNQ: Cloaking in a Charge Transfer Complex

In the following chapter we focus on the spatial charge distribution in monolayer of Na atoms and 7, 7, 8, 8-tetracyanoquinodimethane (TCNQ) molecules on a Au(111) metal surface. The chemical structure of the prototype organic acceptor molecule TCNQ is shown in Fig. 3.6(a). TCNQ consists of a central quinonoid ring and two dicyanomethylene termination groups, which have a strong electrophilic character [176, 177]. The central ring stabilizes the anionic system [178]: upon charge injection the central ring increases its aromaticity and gain energy [179, 180]. In the case of the bulk Na-TCNQ CTC a complete charge transfer of 1.0 e$^-$ occurs leading to the formation of an ionic-like lattice of Na cations and TCNQ anions [181–184]. The transferred electron is localized in the former LUMO orbital of the organic TCNQ acceptor species, which exhibits a high electron density at the electrophilic cyano terminations groups (see Fig. 3.6) [185, 186]. In the bulk compound the charge localization on the TCNQ acceptor is intensified by strong Coulomb interactions between the neighboring molecular sites leading to strong electron-electron correlations [187, 188].

By bringing a monolayer of Na-TCNQ on a Au(111) metal surface a new phenomenology is expected. In particular, the interaction with the underlying metal surface can influence the monolayer CTC properties. For instance, the presence of the metallic surface can lead to different molecular arrangements, because of the template-effect of the metal surface [22, 189–193]. Also additional charge transfer to the donor or acceptor species due to hybridization of the relevant electronic states might occur [25, 29, 162]. Furthermore, the metal surface can screen charges and therefore alter the charge distribution within a monolayer CTC, since the intermolecular Coulomb interactions can be reduced compared to the crystalline bulk phase of the corresponding CTC [184, 194, 195].

The interest of the Na-TCNQ system is the charge distribution, which is in general studied by Kelvin Probe Force Microscopy (KPFM). KPFM is a well established technique to measure electrostatic potentials of organic-metal interfaces with high spatial resolution [196]. Lately, KPFM was used to spatially map the electrostatic potential, related to the charge distribution, of a single molecule on an insulating NaCl layer with intramolecular resolution [197]. However, in the presence of a metal surface additional surface or interface dipoles can influence the KPFM results and make them difficult to interpret. Instead of KPFM, we use the Kondo effect, stemming from an unpaired electron (transferred charge), in order to map the spatial charge distribution within the CTC monolayers on the metal surface.

a)   b)   c)

● N ● C ○ H   HOMO   LUMO
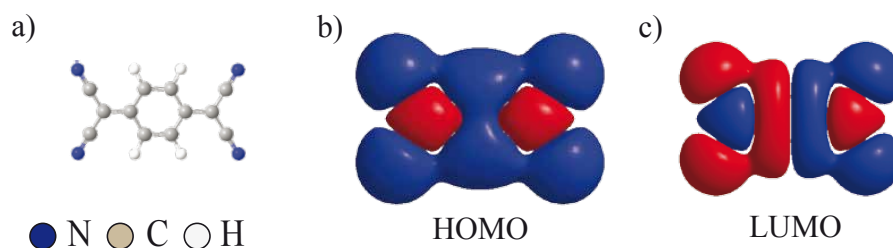
Figure 3.6:   (a) Chemical structure of TCNQ. DFT simulation of the HOMO (b) and LUMO (c) of the free gas phase TCNQ molecule.
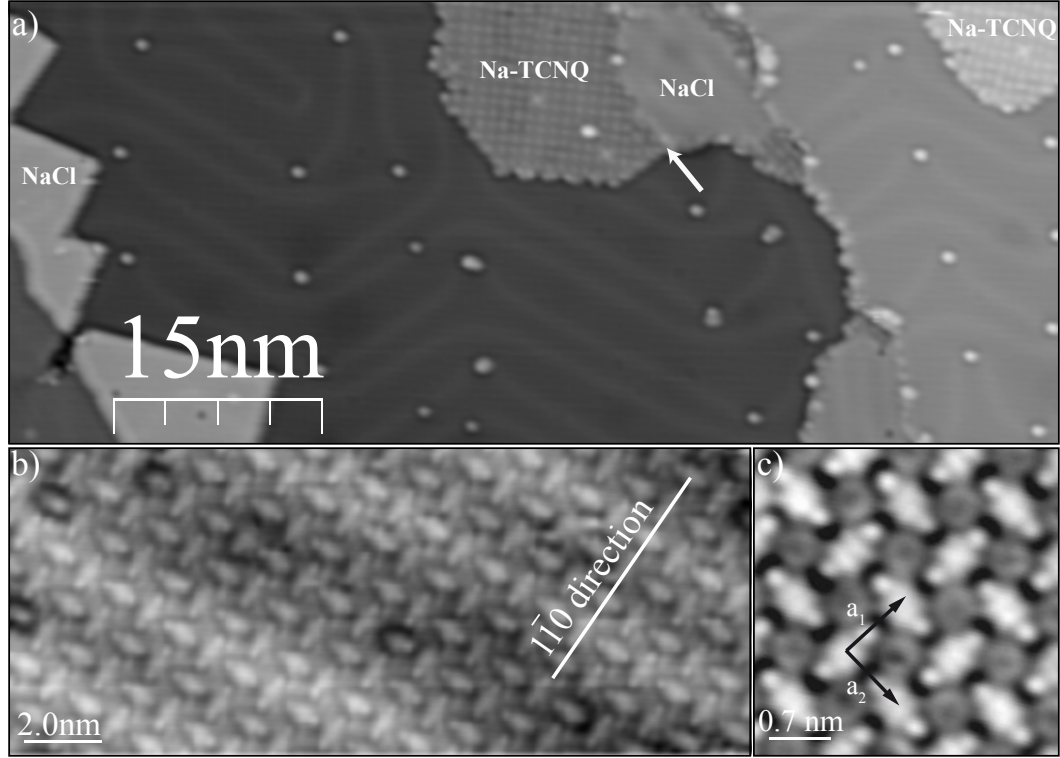
Figure 3.7: (a) Large STM topographic image of a NaCl islands and Na-TCNQ domains (scanning parameters: I = 73 pA, V = 1.5 V). The white arrow points the border between a NaCl and Na-TCNQ domain. (b) STM topographic image of the mixed Na-TCNQ layer on Au(111) (scanning parameters: I = 110 pA, V = 76 mV). (c) High resolution image of Na-TCNQ layer with the windmill-like structure (scanning parameters: I = 100 pA, V = 100 mV). The dimensions of the unit cell vectors are $|\vec{a}_1| = |\vec{a}_2|$ = (0.9 $\pm$ 0.1) nm enclosing an angle of α = 90° $\pm$ 1°.

3.4.1 Structure of Na-TCNQ on Au(111)

There are two distinct routes to grow self-assembled mixed Na-TCNQ islands on the Au(111) metal surface. The first one uses NaCl islands as Na source. The Au(111) metal surface is precovered with NaCl evaporated from a Knudsen cell heated to 550 °C. On a metal surface NaCl forms (100)-terminated islands, which consist of a bilayer [198]. The step edges are non polar and show an alternating configuration of Na cation and Cl anions [199]. Subsequent deposition of TCNQ from a Knudsen cell heated up to 380 K leads to partial dissolution of the NaCl islands. During deposition of NaCl and TCNQ on the clean Au(111) metal surface, the sample was kept at room temperature (T_{Sample} = 280 K). Fig. 3.7(a) shows a large STM topographic image of the Au(111) metal surface covered with the typical square-like NaCl patches [199] and highly ordered windmill-like structures. Fig. 3.7(b) shows a zoom-in of an island with the windmill like structure that correspond to the Na-TCNQ self-assembly. We can clearly resolve the TCNQ molecules by their characteristic orbital shape as lying flat on the surface (Fig.3.7(c)). This structure drastically deviates from the pure TCNQ phase on the Au(111) surface, where H-bonding governs the resulting self-assembly [200]. In the present case, the electrophilic cyano groups of neighboring molecules point towards each other. Such a structure can only be stabilized by the inclusion of an additional linker, which reduces the electro-
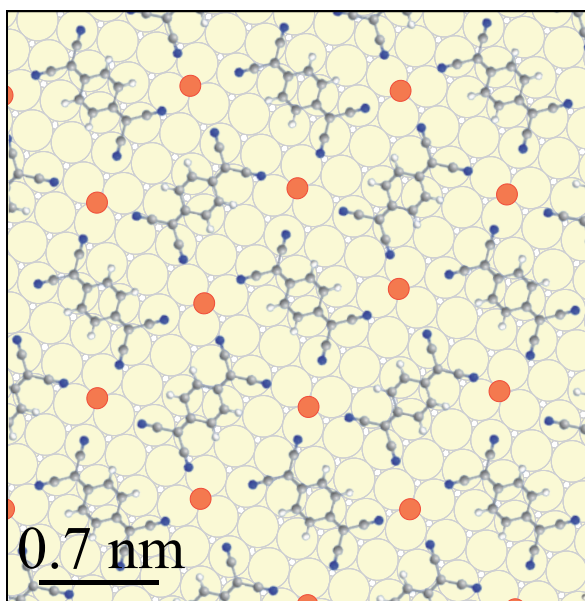
Figure 3.8: Structural model of the Na-TCNQ layer on Au(111). The Na sites occupy hollow sites.

static repulsion [18, 28, 100]. The most likely unit for this stabilization would be a Na atom, which has been dissolved from the NaCl islands.

The resulting arrangement of the self-assembled Na-TCNQ domains is depicted in the structure model in Fig. 3.8. There are two different TCNQ species almost perpendicular to each other and the Na atoms occupying hollow sites. Every Na site is surrounded by four cyano end groups of four different neighboring TCNQ molecules. The structure is very similar in terms of shape and size to the arrangement of Na-TCNQ layers of the bulk phase [201, 202]. Thus, the metal surface seems to play a minor role in the self-assembly process. This is also corroborated by the observation of the unperturbed Au(111) herringbone reconstruction underneath the mixed layer (Fig. 3.7(b)).

The structural evolution of the Na-TCNQ islands occurs at the edges of the NaCl patches as indicated by the white arrow in Fig. 3.7(a). Apparently the temperature of T_{Sample} = 280 K during preparation is sufficient to enable the above described replacement reaction. In solution, solid state replacement reactions between halogen species of alkali halides and TCNQ molecules are known [183]. The high electron affinity of TCNQ allows to oxidize the halogen species of the NaCl layer even on a metal surface and the corresponding solid state replacement reaction can be described as [33, 203–205]:

$$TCNQ + Cl^- \rightarrow TCNQ^- + \frac{1}{2}Cl^2 \tag{3.18}$$

The released Cl atoms presumably desorb into the vacuum and the anionic TCNQ reacts with the remaining Na cation:

$$Na^+ + TCNQ^- \rightarrow NaTCNQ \tag{3.19}$$

To validate the formation of Na-TCNQ ordered islands, we have co-deposited TCNQ molecules with Na atoms from a SAES getter disperser source. Both TCNQ molecules and Na atoms were deposited on a clean Au(111) metal surface kept at room temperature. Figure 3.9(a) shows large STM topography of a Na-TCNQ domain revealing the same windmill-like structure as the preparation with NaCl

Figure 3.9:   (a) STM topographic image of the mixed Na-TCNQ on Au(111). A SAES getter dispenser source is used to deposit the Na atoms (scanning parameters $I = 94$ pA, $V = 530$ mV). (b) Zoom-in of the Na-TCNQ windmill-like structure (scanning parameters: $I = 0.5$ nA, $V = 100$ mV). The dimensions of the unit cell vectors are $|\vec{a}_1| = |\vec{a}_2| = (0.9 \pm 0.1)$ nm enclosing an angle of $\alpha = 90° \pm 1°$.

(see Fig. 3.7(b)). Also the lattice constants $|\vec{a}_1|$ and $|\vec{a}_2|$ of the square lattices are identical in both cases, as shown in Fig. 3.7(c) and Fig. 3.9(a).

Both preparation routes with NaCl and from Na disperser lead to the formation of ordered Na-TCNQ islands. The dissolution of NaCl in presence of TCNQ reflects a strong acceptor-donor interaction. The electron affinity of Cl in the gas phase is about $E_A = 3.61$ eV [206] and the ionization energy of Na in the gas phase $I_D = 5.14$ eV [207]. The electrostatic energy of the Na cations and the Cl anions is about $E_B \approx 7.9$ eV [5]. The total cohesive energy of the NaCl crystal can then be calculated using equation 3.1 and amounts to $E_B = 6.4$ eV. The crystal binding energy of the Na-TCNQ bulk compound is about $E_B = 7.84$ eV [209]. The larger crystal binding energy of the Na-TCNQ bulk compound indicates that by mixing alkali halides with the strong organic acceptor TCNQ the formation of Na-TCNQ is energetically favored.

3.4.2   Electronic Properties of Na-TCNQ/Au(111)

In order to investigate the charge distribution and the electronic structure of the Na-TCNQ layer we performed dI/dV spectra on different sites of the Na-TCNQ layer (see Fig. 3.10(a)). The spectra taken at the center of TCNQ sites are featureless and show only a shift of the Au(111) surface state (see Fig. 3.10(a) indicated by the red dashed line). The shift of the Au(111) surface state amounts to ≈ 170 mV towards E_F and can be attributed to work function changes due to the presence of the Na-TCNQ layer [33]. There are additional spectroscopic features that appear only when the tip addresses the Na positions on the Na-TCNQ layer. Two resonances at 0.75 V (P1) above E_F and at -0.55 V (P2) below E_F (see Fig. 3.10(a)), respectively. The spatial location of the resonances P1 and P2 is revealed by constant current dI/dV maps depicted in Fig. 3.10(b). Both resonances P1 and P2 are clearly localized at the Na sites. The spectrum taken at the Na site also reveals the presence of a zero-bias peak (ZBP) at the Fermi energy E_F (see Fig. 3.10(a)).

To study the ZBP in more detail spectra in a smaller energy window at different positions of the Na-TCNQ layer are recorded (see Fig. 3.11(a)). This ZBP has a full width at half maximum (FWHM)

---

[5]The electrostatic energy of the NaCl bulk crystal can be calculated using $E_C = -\frac{\alpha\,e^2}{r} + \frac{C}{r^8}$. Here α is the Madelung constant ($\alpha_{NaCl} = 1.7476$ and $C = 6.97 * 10^{-96}$ [$m^6 C^2$] [208].)
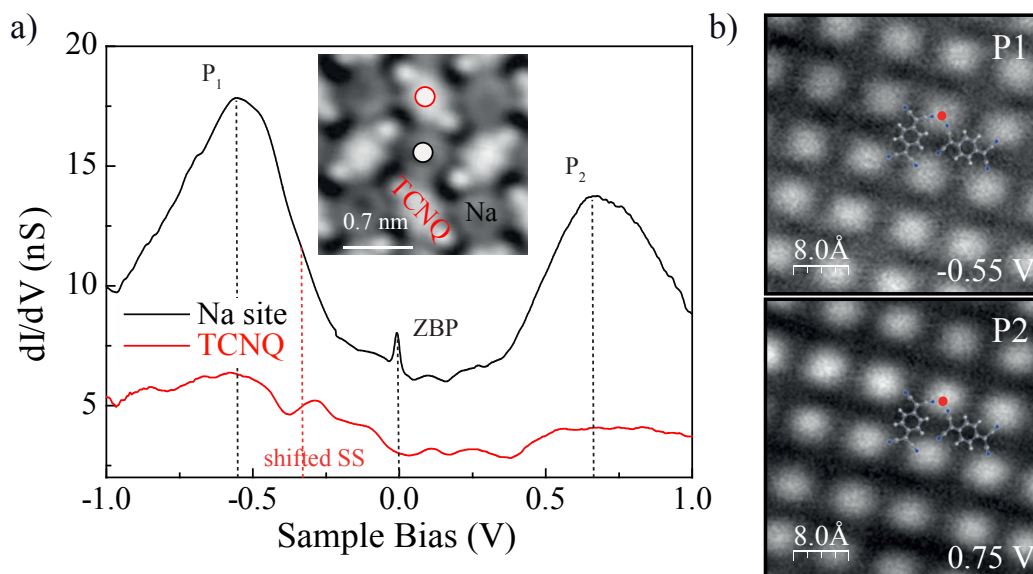
Figure 3.10:   (a) Differential conductance dI/dV spectra acquired on two different sites of the Na-TCNQ layer (V_t = 0.1 V, I_t = 0.3 nA, V_{ac} = 3 mV rms at 821 Hz). (b) Conductance maps taken at the energies of the P1 and P2 resonances. The molecular model shows the localization of the P1 and P2 resonances on top of the Na atom. The maps were taken at constant current (I_t = 0.5 nA, V_{ac} = 12 mV rms at 877 Hz).

of 7 ± 1 mV. The spatial location of the ZBP is plotted in Fig.3.11 (b). The ZBP has its maximum intensity on the Na sites, disappearing when the tip is precisely located on the TCNQ molecules.

The resonance can be related to the emergence of the Kondo effect in the Na-TCNQ monolayer, as stated in similar molecular donor-acceptor systems [25, 29, 162]. The manifestation of the spin Kondo effect in STS indicates a S = 1/2 magnetic ground state and allows us to map the transferred charge of one electron within the Na-TCNQ layer. To calculate the Kondo temperature T_K of the system the Kondo resonance is fitted by a Fano line shape (see equation 3.13) with the following fit parameters: q = 12.1 $\pm$ 0.9 and T_K = 21 $\pm$ 6 K. Presumably, the unpaired electron donated by the Na atom is located in the former LUMO of the TCNQ molecule. However, dI/dV spectra taken at the center of TCNQ molecules are rather flat (see Fig. 3.11(a)). The spatial localization of the resonances P1 and P2 and the Kondo resonance on Na sites seems to contradict the simple assumption of a charge transfer of 1 electron from the Na 3s orbital to the organic TCNQ acceptor. The Na cation would exhibit a closed-shell electronic configuration with no unpaired spin.

3.4.3   DFT Simulation of the Na-TCNQ/Au(111)

In order to shed light on the origin of the unconventional charge redistribution in the Na-TCNQ monolayer on Au(111) DFT calculations were performed by Prof. Dr. Mats Persson and Dr. Ricardo Rurali from the Surface Science Research Center at the University of Liverpool and the Institut de Ciéncia de Materials de Barcelona, respectively. The electronic structure of the Na-TCNQ layer adsorbed on Au(111) was calculated using the plane wave Vienna *Ab initio* Simulation Package (VASP) code [210]. The ion-core interactions and the exchange correlation effects were described using the
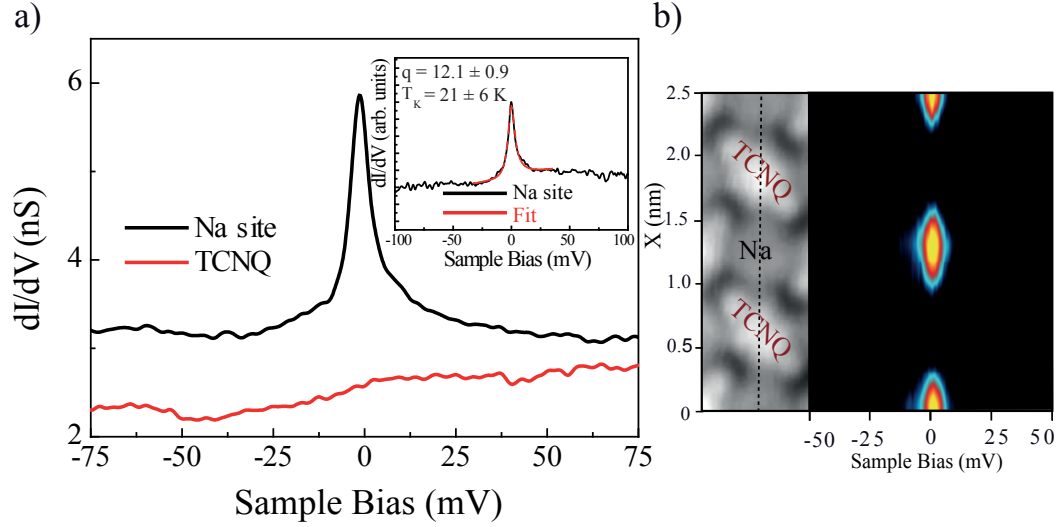
Figure 3.11: (a) High resolution dI/dV spectra around E_F on Na and TCNQ sites (V_t = 100 mV, I_t = 2.5 nA, V_{ac} =1 mV rms at 877 Hz). The spectrum on the Na site shows a narrow zero-bias peak (ZBP). The spectra are shifted vertically for clarity. The red dashed line in the inset shows a Fano fit according to equation 3.13. The best fit parameters are q = 12.1 $\pm$ 0.9 and T_K = 21 $\pm$ 6 K. The experimental settings were T = 4.8 K and V_{rms} = 1 meV. (b) Spectral map consists of 30 single dI/dV spectra along the dashed line indicated in the topographic image. The map clearly shows the localization of the ZBR on top of Na sites.

projector augmented wave method [211] and the optB86b version of the van der Waals density functional [212], respectively.

The calculated Au(111) substrate is represented in a supercell by a four layer slab of Au atoms with a c($7\times4\sqrt{3}$) surface unit cell. The adsorption configuration of the four Na and four TCNQ molecules in the surface unit cell is taken from the experimentally obtained structure model with the Na atoms adsorbed in hollow sites. The positions of all Na atoms and TCNQ molecules as well as the first two Au layers were vertically and laterally relaxed until all forces were less than 0.02 eV/Å. The last two Au atomic layers of the Au(111) slab were kept at their bulk positions during the relaxation with a calculated lattice constant of 4.137 Å. We used a plane-wave cutoff of 400 eV and the k points in the Brillouin zone were sampled by a $2\times2\times1$ grid. The vacuum region was 19.6 Å. The relaxed Na-TNQ/Au(111) revealed a small asymmetry in the bonding of the TCNQ molecules with respect to the Na sites resulting in two distinct adsorption sites of TCNQ. However, the electronic structure is similar in both molecules, as revealed by STS and DFT. In the following, we focus on the common properties of both TCNQ species.

Figure 3.12(a) shows the projected density of states (PDOS) of the Na-TCNQ/Au(111) system onto the Na and TCNQ orbitals. The Na $3s$ and $3p$ orbitals are empty and located well above the Fermi energy E_F. The Na atom clearly donates its $3s$ electron to the organic acceptor species TCNQ. The LUMO of TCNQ species is pinned at E_F and filled with one electron leading to a singly occupied molecular orbital (SOMO). The experimentally observed resonances P1 and P2 correspond to the
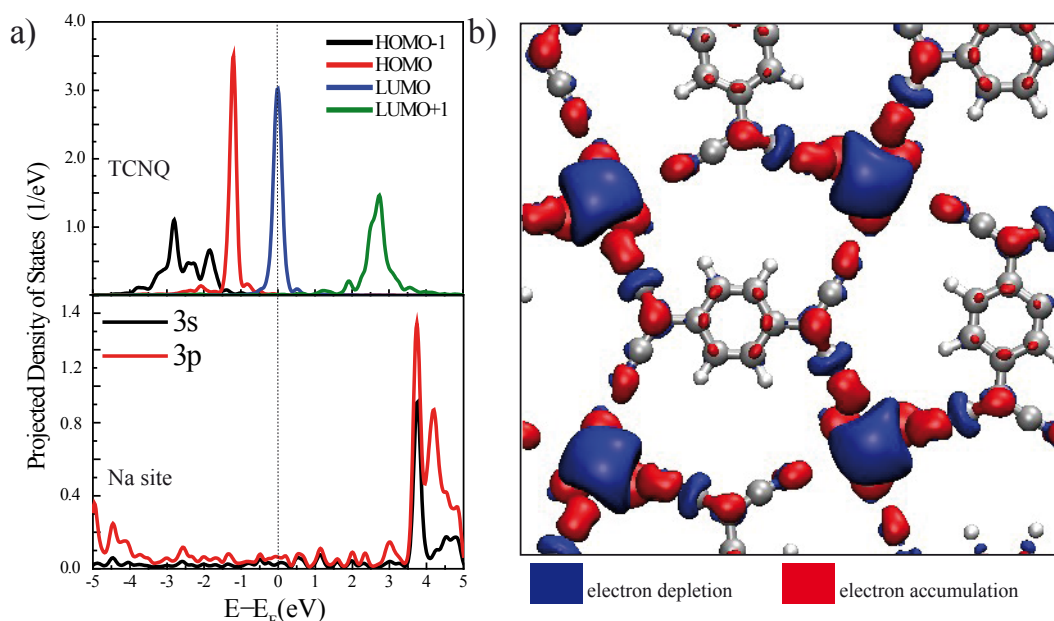
Figure 3.12:   (a) Calculated projected density of states (PDOS) of the Na-TCNQ monolayer on the frontier orbitals of an isolated TCNQ molecule and on the $3s$ and $3p$ orbitals of the isolated Na atom. The LUMO-derived state of TCNQ is aligned close to E_F and partially filled by one electron. (b) The induced electron density created by inclusion of the Na atom in the TCNQ/Au(111) layer ($n_{induced} = n_{(Na-TCNQ/Au)} - n_{(TCNQ/Au)} - n_{Na}$). The color blue corresponds to charge depletion and red to charge accumulation, respectively.

SOMO attached with an electron or a hole implying the splitting of the former TCNQ LUMO orbital [6]. This finding confirms the complete charge transfer of one electron.

The charge rearrangement within the Na-TCNQ layer can be depicted by the induced electron density upon inclusion of Na atoms in the TCNQ/Au(111) system (see Fig. 3.12(b)). It reveals a significant charge depletion at the Na site and a charge accumulation at the electrophilic cyano end groups of the TCNQ molecules confirming the charge transfer of one electron from the Na sites to the TCNQ species and also the localization of that charge at the cyano end groups of the TCNQ.

Due to the absence of relevant Na electronic states around E_F a significant hybridization between Na and TCNQ electronic states can not occur as revealed by the PDOS of the Na-TCNQ/Au(111) in Fig. 3.12(a). Thus the cohesion of the Na-TCNQ layer is mainly due to electrostatic interaction of the corresponding Na cations and TCNQ anions [35], which is different to compounds consisting of transition metal instead of alkali metal atoms, which are stabilized by metal-organic coordination bonds [35, 213, 214].

The underlying Au(111) metal surface plays only a minor role and is not involved in the charge transfer within the Na-TCNQ layer as revealed by the DFT calculations. This is also experimentally confirmed by the observation of the unperturbed Au(111) herringbone reconstruction [33].

The DFT calculations show the charge transfer of one electron to the TCNQ acceptor species and the

---

[6]Since DFT in general underestimated electron-electron correlations the energetic splitting of the P1 and P2 resonances is smaller compared to the experimental data.
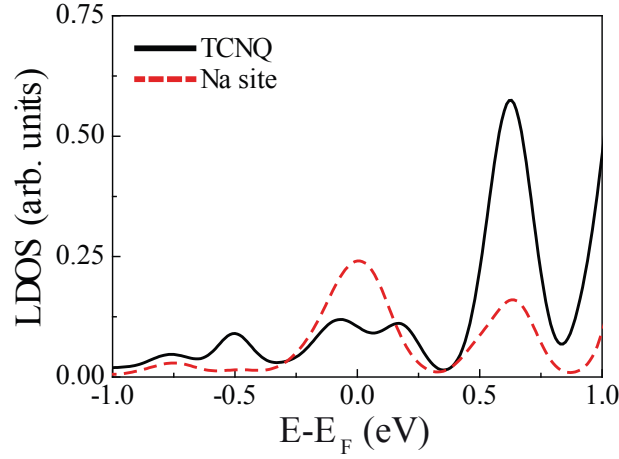
Figure 3.13: Local density of states (LDOS) at a distance of 10 Å from the surface on top of a Na site and on top of the center of a TCNQ molecule.

filling of the former TCNQ LUMO. But these findings seem to contradict the spatial localization of the Kondo resonance at the Na sites. We have taken a closer look on the spatial distribution of the TCNQ SOMO within the Na-TCNQ layer in order elucidate this contradiction by comparing the local density of states (LDOS) around E_F at the Na sites and at the TCNQ center. Figure 3.13 shows the LDOS at a distance of 10 Å [7] from the surface at the Na site (red line) and the center of the TCNQ species (black line), respectively. The LDOS exhibits a peak centered at E_F, which has a larger weight on top of the Na sites compared to the TCNQ center. This peak at E_F originates from the SOMO of the TCNQ, since there are no relevant electronic states of the Na in this energy window (see PDOS in Fig. 3.12(a)). The TCNQ SOMO resonance close to E_F gives rise to the Kondo effect. Thus, the DFT calculations unravel two experimental findings, namely the localization of the TCNQ SOMO at E_F, giving rise to the Kondo effect, and its larger weight on the Na sites compared to the TCNQ backbone.

3.4.4 The Spatial Charge Rearrangement in Na-TCNQ/Au(111)

In order to understand the weight of the Na site on the intensity of the unpaired spin we calculate the LDOS distribution. Figure 3.14 shows simulated maps of the LDOS (a,b) and experimentally recorded constant current dI/dV maps (c,d). The simulated LDOS map at a distance of 10 Å over the surface (see Fig. 3.14(a)) shows the TCNQ SOMO with a large weight on the Na cation. By decreasing the distance to the surface to 6.5 Å (see Fig. 3.14(b)) the TCNQ SOMO reflects the unperturbed free gas phase TCNQ LUMO (see Fig. 3.6(b)) with the typical nodal plane at the TCNQ center and four arm-like features at the cyano end groups (as indicated in Fig. 3.14(d)). The experimental constant current dI/dV maps measured at the energy of the resonances P2 of 550 mV at two different tip-height positions over the Au(111) surface reproduce this dependence. This supports their identification as the TCNQ's SOMO (P1) and SUMO (P2). Therefore, the Na-TCNQ/Au(111) interface is a particular example of the spatial charge rearrangement of a molecular state. The alkali atoms within the Na-TCNQ layer lead to a distortion of the TCNQ SOMO due to strong electrostatic interactions.

---

[7]This corresponds to the case of imaging the Na-TCNQ layer at low tunneling conductance.
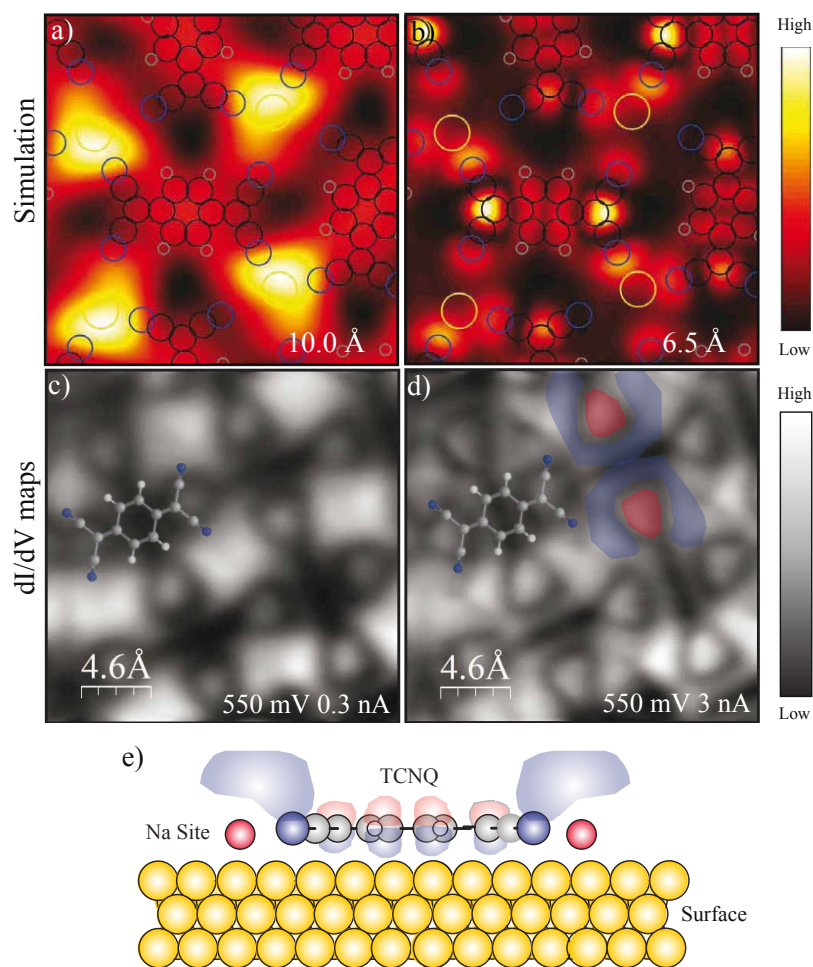
Figure 3.14: (a,b) Simulated maps of the LDOS at E_F, corresponding to the SOMO resonance at a distance of 10 Å and 6.5 Å from the surface, respectively. (c,d) Constant current dI/dV maps at the SUMO energy at 550 mV for different current set points $I_t = 0.3$ nA and $I_t = 3$ nA, respectively (V_{ac} = 5 mV rms at 821 Hz). In (d) the shape of the unperturbed TCNQ LUMO is indicated. (e) Schematic illustration of the deformed TCNQ SOMO cloaking the Na atom.

The above discussed results lead to the conclusion that the Na cation is cloaked by the three-dimensional orbital density of TCNQ SOMO. The Na cation represents a small and positively charged ion, which modifies the electrostatic landscape of the Na-TCNQ layer and the TCNQ SOMO is therefore deformed. The electrostatic potential energy map for an electron at a distance of 8 Å from the Au surface is shown in Fig. 3.15. The electrostatic potential landscape shows a ~ 90 meV local minimum on top of the Na sites implying a significant electrostatic attraction for the transferred electron above the Na cation, further confirming the three-dimensional cloaking of the Na ion by the TCNQ SOMO as indicated in Fig. 3.14(e) [8].

The Kondo temperature estimated from the Fano fit of the ZBP (see Fig. 3.11) has a value of $T_K = 21 \pm 6$ K. To extract the Anderson parameters U, Δ and ε from the dI/dV spectra in Fig. 3.10(a)

---

[8]The described effect also occurs for the free-standing layer with the identical geometry and hence is not caused by the metal substrate.
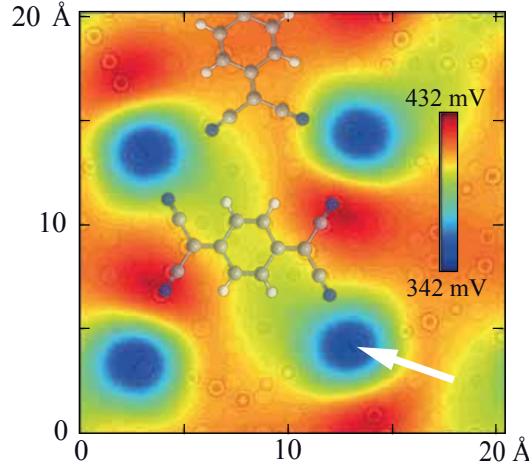
Figure 3.15: Simulated map of the electrostatic potential energy felt by an electron at a distance of 8 Å from the Au(111) top most layer. The color scale ranges from 342 meV (blue) to 432 meV (red). The white arrow indicates the region of the highest electrostatic attraction for a tunneling electron.

we can use the following equation for the spectral function A_ω to estimate the Kondo temperature of the Na-TCNQ system from the Anderson parameters [215]:

$$A_\omega = \frac{1}{\pi} ImG_d(\omega - i \cdot \delta) \tag{3.20}$$

$$G_d(\omega - i\delta) = \frac{Z_d}{\omega - \varepsilon - i \cdot \Delta} + \frac{Z_U}{\omega - \varepsilon - U - i \cdot \Delta} + \frac{Z_K}{\omega - i \cdot T_K} \tag{3.21}$$

Here U is the Coulomb repulsion, ε is the energy of the SOMO (the SUMO is located at $\varepsilon + U$), and Δ is the broadening due to the hybridization of the TCNQ SOMO/SUMO orbital with the conduction electronic states. Z_d, Z_U, and Z_k correspond to the amplitudes of the SOMO, SUMO, and the Kondo peak ,respectively. Hence we simulate the Kondo resonance located at the Fermi energy E_F as well as the Coulomb Peaks located at the energies ε_d and $\varepsilon + U$, respectively (here corresponding to the resonances P1 and P2). By using equation 3.20 we can simulate the dI/dV spectra in Fig.3.16 and obtain a Kondo temperature $T_K \approx 40$ K from the parameters U, Δ and ε. The obtained Kondo temperature T_K is in line with the Fano fit of the ZBP in Fig. 3.11(a) and further supports the identification of the ZBP as a Kondo resonance.

An interesting finding of the above results is that the TCNQ SOMO is still sufficiently hybridized with the underlying Au(111) surface to provoke a Kondo effect. Indeed, the DFT calculations show that the Na cations have no relevant electronic states close to E_F and therefore they can not interact (or hybridize) with TCNQ SOMO orbital. Thus the Kondo screening stems from a single molecular orbital with a single screening channel [216]. In the case of multiple screening channels the system can be described as a set of independent Kondo resonances, which manifests with a complicated line shape at the Fermi energy E_F [216].

3.4.5   Conclusions

In this chapter we have discussed in detail the charge distribution of a self-assembled Na-TCNQ monolayer on a Au(111) metal surface. Using STM and DFT we elucidate the electronic and struc-
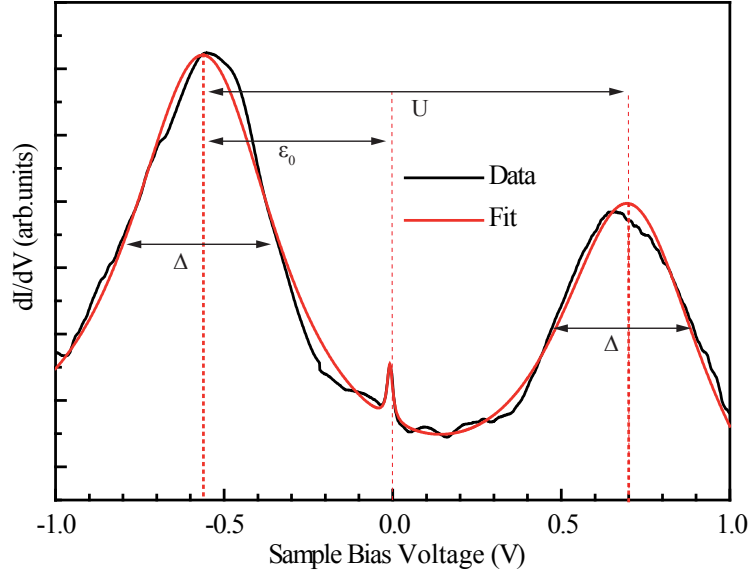
Figure 3.16: Simulation of the wide range STS spectra using equation 3.20. The best simulation (red line) is obtained for the following set of parameters: $U = 1.264$ eV, $\Delta = 0.276$ eV, and $\varepsilon = -0.561$ eV.

tural properties of the Na-TCNQ monolayer. A complete charge transfer of 1 electron from the Na $3s$ orbital to the TCNQ LUMO takes place. The singly occupied TCNQ orbital gives then rise to a Kondo resonance stemming from the spin scattering interaction with the conduction electrons of the Au(111) metal surface. Using the Kondo resonance as a detector we can map the corresponding distribution of the single electron. Surprisingly, the Kondo resonance is located on top of the Na sites as revealed by STS with the help of DFT calculations. We conclude that the TCNQ SOMO is deformed and extends above the Na atom. Therefore, the Na cation is cloaked by the TCNQ SOMO. The orbital deformation is a consequence of strong electrostatic interactions within the polar Na-TCNQ layer, as revealed by DFT.

Interestingly, the Kondo effect stemming from singly occupied TCNQ orbital persists in the presence of the Na cation underneath. The measured FWHM of the Kondo resonance and the related Kondo temperature T_K is comparable with other TCNQ based Kondo systems [25, 29]. This finding is attributed to the fact that there are no relevant electronic states of the Na atoms in this energy window. Hence, the corresponding Kondo singlet ground state originates from a single occupied molecular orbital and a single screening channel.

The presented experiments and theoretical simulations highlight the importance of electrostatic effects on the shape of the molecular orbitals that affects the charge distribution. Since the Kondo effect relies on the hybridization of a singly occupied orbital with the electronic states of the metal, the deformed molecular orbital also affects the spatial distribution of the spin singlet Kondo state.

In this prospect, it would be interesting to manipulate or change the charge state, for example, by adsorption of small gas molecules. This can be used to switch the charge state or the spin state. Another approach to tailor the charge state of the adsorbed layer is to use corrugated surfaces that imply a periodic potential modulation of surface and adsorbates. This will be shown in the following section.

3.5 Quantum Interference in Tunneling through an Extended Kondo System

In the preceding chapter we discussed in detail the charge distribution within a monolayer of Na-TCNQ. The effect of the underlying Au(111) surface is negligible for this system. However, the hybridization with electronic states of the metal surface [58] as well the adsorption site [217] can have a significant impact on the charge state of the acceptor or donor species. Since the Au(111) metal surface exhibits an exotic surface reconstruction (see section 2.6) implying also a surface corrugation, the question of how the charge state of adsorbed donor and acceptor species can be influenced by the precise adsorption site arises. The reconstructed Au(111) metal surface also exhibits small variations of the potential energy between the fcc and hcp regions. Thus, the Au(111) surface presents a perfect playground to test the adsorption site effects of CTC monolayers. Since the Na-TCNQ does not show significant adsorption site dependent properties we change to the acceptor species to 11, 11, 12, 12-tetracyanonaptho-2, 6-quinodimethane (TNAP). TNAP is larger in size due to a larger quinonoid backbone separating the cyano end groups. The molecular structure of TNAP is shown in Fig. 3.17. Due to the larger distance between the electrophilic cyano termination groups TNAP exhibits a larger electron affinity compared to TCNQ [218]. The increased size and electronic affinity can help to stabilize higher charge states. But the larger size means also that the TNAP molecules occupy a larger surface area when adsorbed flat on the surface. Since the Au(111) metal surface exhibits a corrugation of 0.2 Å and alternating fcc and hcp regions the TNAP molecules can be forced to bend or to occupy different surface sites.

The effect of the metal surface on the Na-TNAP layer electronic properties is investigated in this chapter. First we discuss the structural and electronic properties of pristine TNAP on the Au(111) metal surface. Then we will discuss the structural and electronic properties of the Na-TNAP monolayer on the Au(111) metal surface.

3.5.1 TNAP on Au(111)

We firs explore the tendency of TNAP of accepting electrons from the Au(111) metal surface. Evaporation of TNAP molecules on a clean Au(111) surface results in self-assembled ordered domains as shown in Fig. 3.18(a). A STM topography zoom-in of the TNAP island shows a molecular lattice with a rhombic unit cell with lattice parameters $|\vec{a}_1|$ = 1.0±0.1 nm, $|\vec{a}_2|$ = 1.0±0.1 nm, and an angle α = 85°± 1°. The TNAP molecules are adsorbed flat with their molecular plane parallel to the surface
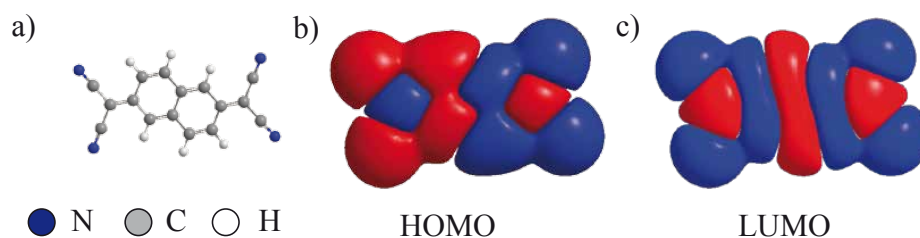
Figure 3.17:   (a) Structural model of the TNAP acceptor molecule. DFT simulations of the TNAP HOMO (b) and LUMO (c) of the free gas phase molecule.
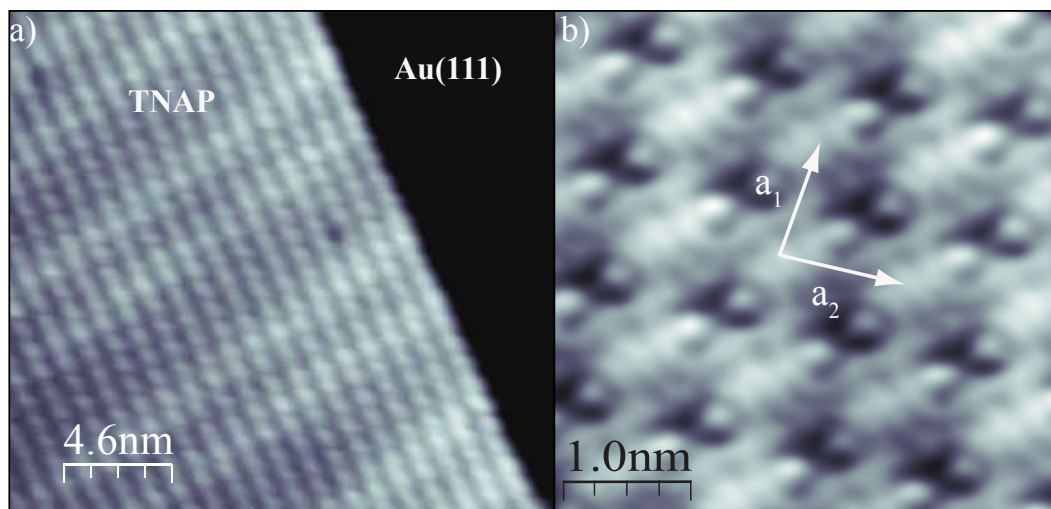
Figure 3.18:   (a) STM topographic image of a large ordered TNAP island (scanning parameters: $V_S = 1.1$ V, $I_T = 0.07$ nA). (b) Zoom-in of the ordered TNAP structure (scanning parameters $V_S = 0.4$ V, $I_T = 0.50$ nA). The TNAP molecules appear with characteristic nodal planes in STM topography images reassembling the LUMO of the free TNAP molecule (see Fig. 3.17).

plane. This is a typical adsorption configuration of two-dimensional organic molecules on metal surfaces [219]. The stabilization of the TNAP is mainly due to the formation of hydrogen bonds between neighboring nitrogens species of the cyano end groups and hydrogen atoms of the benzoic backbone of a neighboring TNAP molecules (as indicate by the red dashed lines in Fig. 3.19). All TNAP nitrogen species at the cyano end groups are involved in a hydrogen bond. The average distance between nitrogen and hydrogen species, as estimated from the structural model, is about ≈ 2 Å and is typical for such H-bond intermolecular bonding patterns. Furthermore, the presence of the Au(111) herringbone reconstruction indicates a weak interaction of the TNAP molecular layer with the underlying Au(111) surface (see Fig. 3.18(a)).

In order to corroborate the nature of the intermolecular interactions stabilizing the TNAP layer on the Au(111) surface we performed molecular dynamics simulations using the *Tinker* [220] code. We used the force field parameter set *MM*3 as implemented in the *Tinker* code to describe conjugated hydrocarbons [221]. The energetically most stable configuration was calculated using a two step process. First the preferred adsorption configuration of an ensemble of TNAP molecules placed on Au(111) crystal was investigated (for details see appendix A.1). Based on these findings a structural model was established with simultaneous consideration of the experimental findings (see Fig. 3.19). The minimized TNAP adsorption structure exhibits a rhombic surface unit cell with $|\vec{a}_1| = 0.89$ nm and $|\vec{a}_2| = 0.99$ nm and angle of $\alpha = 86° \pm 1°$. These values are in agreement with the experimentally obtained lattice parameters indicating that indeed weak non-covalent interactions, in particular, hydrogen bonding, is responsible for the cohesion of the TNAP monolayer on the Au(111) metal surface. Every nitrogen atom is involved in the layer stabilization and in total there are 4 hydrogen bonds per molecule. The average nitrogen-hydrogen distance is about 2.37 Å.

The ordered TNAP islands and the presence of the unperturbed Au(111) herringbone reconstruction indicate a neutral charge state of the TNAP molecules in spite of their large electron affinity. In order to verify this assumption, we performed STS on the TNAP/Au(111) system. Figure 3.20 shows
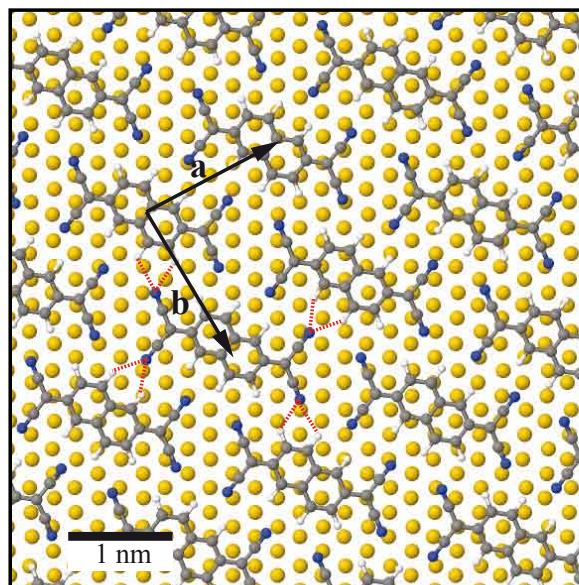
Figure 3.19:   Ball and stick model of the TNAP island on the Au(111) metal surface following force-field model simulations.

the differential conductance dI/dV spectra at different locations of the TNAP/Au(111) system. The dI/dV spectra taken at both the cyano end groups and at the center of the TNAP molecules reveal a pronounced resonance at 0.4 V. The molecular shape of the TNAP molecules at 0.4 V reproduces the shape of the TNAP LUMO (see Figure 3.18(b)) with its typical nodal plane structure (Figure 3.17(b)). The finding of the unperturbed LUMO also indicates a weak molecule-surface interactions, supported by the unperturbed herringbone reconstruction underneath the molecular layer. Furthermore, the TNAP LUMO is localized well above E_F and is therefore unoccupied.

The dI/dV spectra in Fig. 3.20 also show a shift of the Shockley type surface state of the Au(111) surface underneath the TNAP layer of about 0.13 V towards E_F. Assuming a depopulation of the surface state due to charge transfer from the Au(111) surface to the TNAP organic monolayer, the surface state shift would correspond to charge transfer ratio of $\rho = 0.13$ e$^-$ per molecule. This would imply a partial filling of the TNAP LUMO, hence the TNAP LUMO would have a considerable overlap with E_F [222], which is not found in the experimental data. Therefore, the shift of the surface state is attributed to the modification of the work function and/or image potential implying a shift of the corresponding surface state, as it is known for a similar organic acceptor species, F4-TCNQ, on noble metal surfaces[223].

It is interesting to mention that the adsorption of the achiral TNAP molecule on a metal surface induces a chirality. Therefore, two different mirror-symmetric enantiomers [9], labeled R and L, are present on the Au(111) surface. Figure 3.21 depicts both possible adsorption configurations and their different handedness (L or R). In the case of pristine TNAP we observe molecular domains consisting out of either one of the two TNAP enantiomers (see Fig. 3.21(c) and (d)). As we will shortly see, in the case of the Na-TNAP monolayer the addition of alkali Na atoms to the pristine TNAP monolayer clearly breaks the tendency of enantiomer separation.

---

[9]An enantiomer is one of the two stereoisomers. The stereoisomers are mirror images of each other.
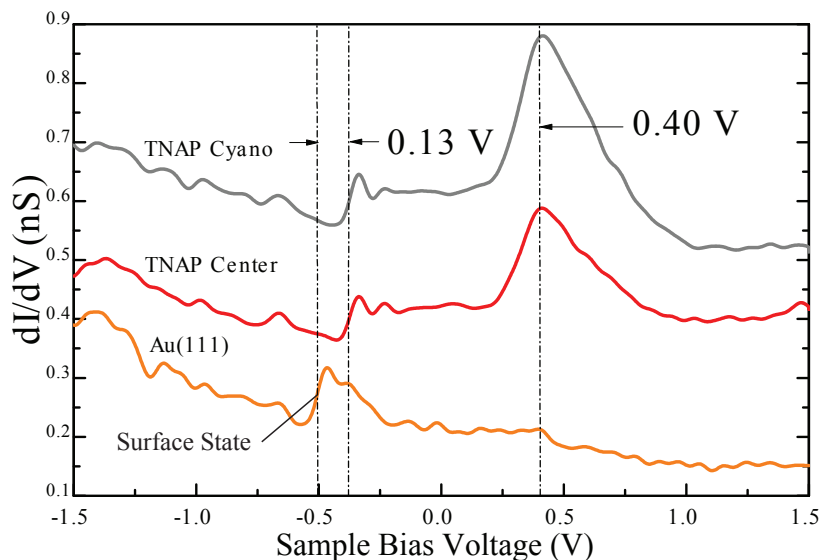
Figure 3.20: *dI/dV*-spectra obtained at different locations on the pristine TNAP layer and on the clean Au(111) surface. The spectra taken on a TNAP molecule reveal a molecular resonance at 0.4 V and a shift of 0.13 V of the onset of the Au(111) surface state (V_S = 1.5 V, I_T = 0.4 nA, the lock-in modulation is 10 mV rms at 933.1 Hz).

3.5.2   Structure of Na-TNAP Monolayer on Au(111)

Doping of the TNAP monolayer with Na atoms from SAES Na disperser leads to the formation of mixed Na-TNAP islands on the Au(111) metal surface. Similar to the case of Na-TCNQ a synthesis using NaCl as Na source is also possible. Fig. 3.22(a) shows a large scale STM topographic image revealing the high degree of order of the mixed Na-TNAP islands. The mixed Na-TNAP domains co-exist with pure islands of excessive TNAP molecules. Figure 3.22(a) shows a zoom-in STM image of the Na-TNAP structure, which is similar to the Na-TCNQ monolayer. The windmill-like Na-TNAP layer exhibits a molecular lattice with a square unit cell with the following lattice parameters: $|\vec{a_1}|$ = 1.0± 0.1 nm, $|\vec{a_2}|$ = 1.0 ± 0.1 nm, and an angle of α = 90° ± 1°. Interestingly, the Na-TNAP unit cell consists of both enantiomers as discussed in section 3.5.1.

By imaging the Na-TNAP layer at low sample bias voltages close to the Fermi energy E_F (here V_S= 30 mV)(see Fig. 3.22(b)) two different TNAP species can easily be distinguished. TNAP molecules adsorbed close to the soliton lines appear bright and show a particular nodal plane structure (see inset in Fig. 3.22(b)). In contrast, TNAP molecules located at the fcc/hcp regions exhibit a completely different shape (featureless cigar-like without a nodal-plane structure). The bright TNAP molecules appear with the characteristic nodal plane structure of the LUMO orbital of the free gas phase TNAP molecule shown in the inset of Fig. 3.22(b). The find the LUMO close the Fermi Energy E_F indicates that it is filled. Thus, the different appearance of the TNAP species indicates two different electronic properties of TNAP molecules within the Na-TNAP layer depending on the adsorption site. This can be caused by a different charge state or by a different molecule-surface interaction (hybridization).
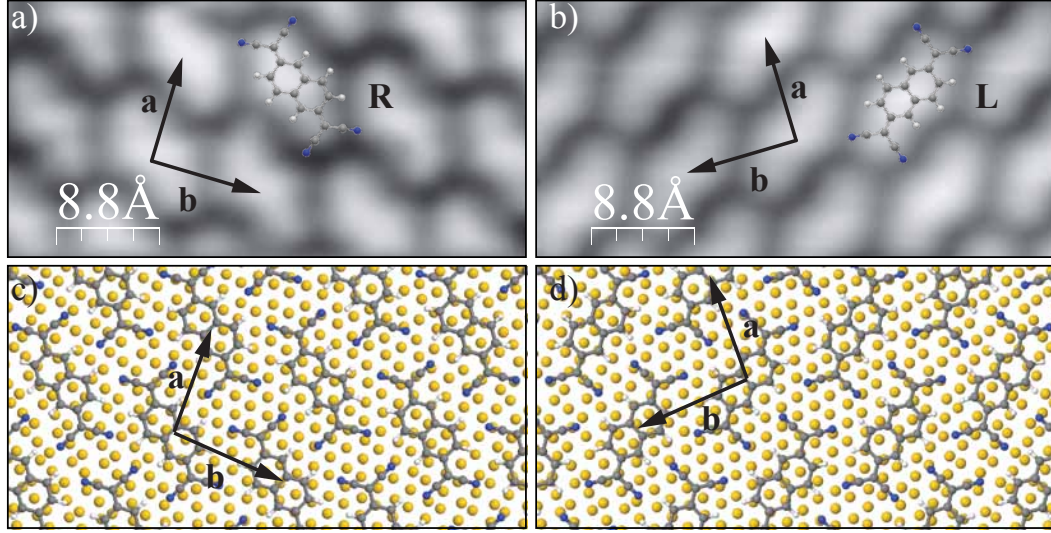
Figure 3.21:   (a) and (b) show STM zoom-in images of pristine TNAP island on the Au(111) surface consisting purely of the enantiomer *L* or *R*, respectively. (scanning parameters: V_s = -50 mV, I_t = 0.4 nA and V_s = 0.86 V, I_t = 60 pA) (c) and (d) show structural models of both entiopure TNAP domains.

3.5.3   Electronic Properties of Na-TNAP Monolayer on Au(111)

To probe the electronic structure of the system we performed dI/dV spectroscopy at different positions of the Na-TNAP layer. The dI/dV spectra taken at the Na sites and TNAP centers of TNAP molecules adsorbed close to the soliton lines (bright) and at the fcc/hcp regions (dark) are shown in Fig. 3.23(b). The dI/dV spectra taken at the center of the TNAP molecules adsorbed at the fcc/hcp region are featureless. In contrast, the Na site close to the soliton line (bright TNAP) shows a zero-bias resonance (ZBR) and two broader resonances at 0.51 V (P1) and -0.34 V (P2) (as indicated by the black arrows in Fig. 3.23(b)) above and below the Fermi energy E_F, respectively. The shape of this dI/dV spectrum is very similar to the one at the Na sites of the Na-TCNQ monolayer on Au(111) discussed in section 3.4. This indicates that also the TNAP molecules (bright) close to solition lines are presumably charged with one electron. The wide-range dI/dV spectra shown in Fig. 3.23(b) on the Na sites at the fcc/hcp region show also a resonance below and above E_F at an energy of -0.62 V (P3) and +0.91 V (P4), respectively. Both resonances P3 and P4 are shifted to higher energies compared the resonances P1 and P2. In the case of the Na-TCNQ monolayer on Au(111) DFT calculation reveal the modification of the TCNQ LUMO in the presence of the Na cations and its localization at the Na site (cf section3.4). The localization of the P1, P2, P3 and P4 resonance at the Na sites suggests, that they are related to the TNAP SOMO/SUMO orbital, in comparison to the results obtained in the case of parent Na-TCNQ system (cf 3.4).

High resolution dI/dV spectra taken in a small sample bias voltage window show the presence of a sharp ZBR localized at the Fermi energy E_F (cf Fig. 3.23(c)) at the Na site of the bright TNAP molecules. This ZBR has a full width at half maximum (FWHM) of 7 $\pm$ 1 mV. The ZBP has its maximum intensity at Na sites and can be identified with a spin Kondo resonance in the Na-TNAP monolayer implying a S = 1/2 magnetic ground state. It exhibits a very similar line shape
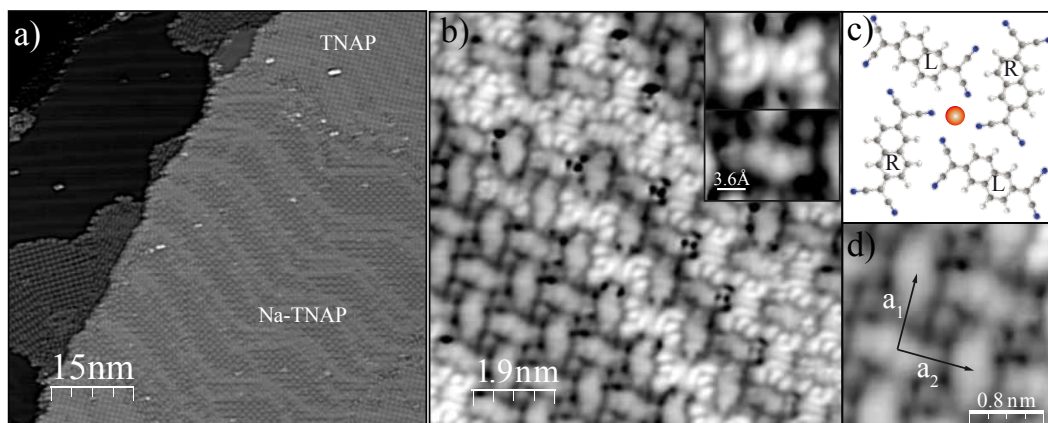
Figure 3.22:   (a) STM topographic image of a large ordered Na-TNAP island (scanning parameters:V_S = 1.3 V, I_T = 70 pA). (b) STM topographic zoom-in of the ordered Na-TNAP structure taken at low bias voltage (scanning parameters V_S = 30 mV, I_T = 0.50 nA). The two insets show the different appearance of the TNAP molecules close to a soliton line (bright) and at a fcc site (dark). (c) and (d) depict a model and a STM topography image of the Na-TNAP unit cell. The Na-TNAP layer exhibits a square unit cell with lattice parameters $|\vec{a}_1|$ = 1.0$\pm$ 0.1 nm, $|\vec{a}_2|$ = 1.0 $\pm$ 0.1 nm, and an angle α = 90°$\pm$ 1°.

compared to the Na-TCNQ layer or other molecular donor-acceptor systems [25, 29, 162]. A Fano fit of the Kondo resonance yields a Kondo temperature T_K = 21 $\pm$ 6 K with the following best fit parameter: q = 6.0 $\pm$ 0.2 (cf Fig. 3.23(d)). Compared to the Na-TCNQ system the Kondo temperature T_K of the Na-TNAP is comparable (cf section 3.3.2). However, the Na sites at fcc or hcp sites do not exhibit a ZBP. They are essentially flat like shown in Fig. 3.23(c). This indicates that the bright TNAP species at the soliton lines and the dark ones at the hcp/fcc sites have either a different charge state or exhibit a different hybridization with the underlying Au(111) surface.

Since the Au(111) herringbone reconstruction is still visible underneath the Na-TNAP layer, a sizable charge transfer from the surface can be excluded [41] and the TNAP molecules can only get the 3s electrons from the Na donors. This leads us to the conclusion that both TNAP species are charged with one electron as in the case of the Na-TCNQ monolayer (cf 3.4). The absence of the Kondo resonance at the TNAP molecules adsorbed at the fcc/hcp regions has therefore be due to a different alignment of the relevant orbitals compared to TNAP (bright) molecules adsorbed close to the soliton lines. These findings indicate that the different electronic structure and also the very different appearance in STM topography of the TNAP molecules, must be related to the reconstructed Au(111) surface [10].

The Au(111) surface reconstruction leads to a buckling of the topmost surface layer and also slightly different electronic structure (cf 2.6). Thus, the corrugation of the reconstructed Au(111) surface implies also a buckling of the Na-TNAP monolayer. The bridging regions (soliton lines) protrude from the surface and form ridges. Therefore the TNAP molecules sitting next to the soliton line have a slightly different interaction with the underlying Au(111) surface compared to TNAP molecules at the fcc or hcp regions. This effect is maybe intensified by the slightly alternating potential energy of the

---

[10]Since the bonding motif is the same throughout the layer (cf section 2.6), this also excludes that the TNAP molecules at the fcc/hcp sites are charged with more than 1 electron, because the Na and TNAP stoichiometry is 1:1 in the Na-TNAP layer.
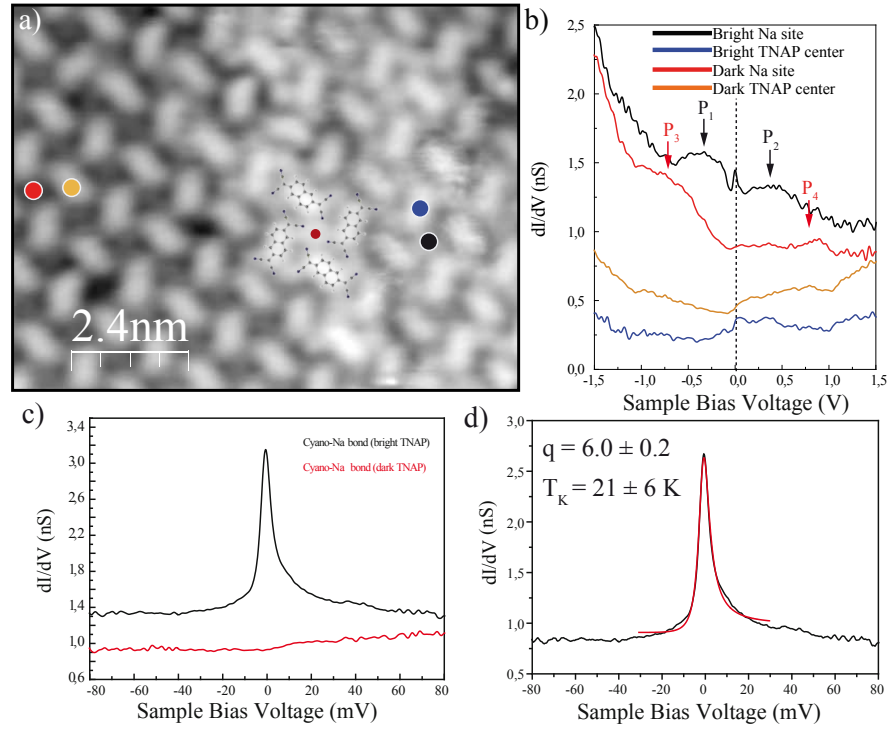
Figure 3.23: (a) STM topographic image of the mixed Na-TNAP layer (V_S = 84 mV, I_T = 0.14 nA). (b) dI/dV-spectra obtained at different locations on the Na-TNAP layer (V_S=2 V, I_T=0.8 nA, the lock-in modulation is 10 mV rms at 1.23 kHz). The spectra are shifted vertically for clarity. (c) High resolution dI/dV spectra around E_F on Na sites at the soliton line and on the fcc region of the Au(111) surface reconstruction, respectively (V_S = 100 mV, I_T = 0.5 nA, V_{rms} = 1 mV rms at 1.23 kHz). The spectra are shifted vertically for clarity. (d) The spectrum on the Na site (soliton line) shows a narrow zero-bias resonance (ZBR). The red dashed line in the inset shows a Fano fit according to equation 3.13. The best fit parameters are q = 6.0 $\pm$ 0.2 and T_K = 21 $\pm$ 6 K. The experimental settings were T = 4.8 K, V_{rms} = 1 meV rms.

Au(111) surface(cf 2.6). The small differences in terms of the adsorption geometry and hybridization can have a significant effect on the electronic properties, i.e. the alignment of the molecular orbitals with respect to E_F. For instance, Zhao et al. investigated cobalt phthalocyanine (CoPc) molecules adsorbed at step edges of the Au(111) metal surface by STM and STS [165, 217]. Only when a CoPc molecule is adsorbed at a monoatomic step implying a sizable bending of the molecules, the hybridization with the underlying Au(111) metal surface is sufficiently lowered to stabilize the S = 1/2 ground state necessary for the spin-Kondo effect to occur.

A similar effect seems to play a role for the Na-TNAP system. In the case of the Na-TCNQ monolayer (cf section 3.4) electrostatic interactions between the Na cations and TCNQ anions are responsible for its cohesion implying also the formation of surface dipoles since cationic and anionic species are present on top of the Au(111) metal surface. In order to reduce the surface dipole the former TCNQ LUMO is strongly deformed and cloaks the Na cation. In the case of Cs-TCNQ$_4$ the Cs atoms are lifted up in order to decrease the electric dipole [35]. The smaller the surface dipole, the lower the electrostatic repulsion between the neighboring Na cation or TNAP anions, respectively. Depending on the adsorption site, the described dipole formation seems to have an effect on the level alignment

of the relevant TNAP orbitals and seems to be increased at the soliton lines.

The separation of resonances P1 and P2 is about 0.85 V, in contrast P3 and P4 show a separation of 1.53 V (cf Fig. 3.23). Within the framework of the Anderson model the separation of the SOMO and SUMO is described by the Coulomb energy U (cf section 3.3.2). The energetic position and hybridization of the SOMO (here the resonances P1 and P3 in Fig. 3.23(b)) is crucial for the Kondo effect to occur. This can also easily be seen in equation 3.11 and 3.12 of the Kondo temperature. Apparently, the spin 1/2 Kondo ground state of the TNAP molecules within the Na-TNAP layer can only be stabilized close to solition lines. At the hcp/fcc sites, where the adsorption configuration and surface hybridization are different, the former TNAP LUMO simply splits in a SOMO and SUMO orbital, separated by the Coulomb energy U, upon charging with one electron [11].

3.5.4   Variation of the Kondo Line Shape in Na-TNAP

We learned in section 3.3.3 that the Kondo resonance manifests with a Fano line shape in transport experiments, due to the quantum interference of different tunneling path present between the tip and the Kondo-surface system (cf section 3.3). The analysis of the Fano line shape, more precisely the q-factor, allows to evaluate the strength of the two competing tunneling channels t_1 and t_2 (cf section 3.3.3). Figure 3.24(a) shows that in the present case of the Na-TNAP system a significant change of the q-factor can be observed, when taking dI/dV spectra from a Na site across a bright TNAP molecule to another Na site (close to the soliton line). At the Na sites the Kondo resonance appears as a Lorentzian-like resonance, also illustrated by the rather high q-factor of $\approx q = 6.0 \pm 0.2$. In contrast, for the spectra taken at the center of the TNAP molecules a q-factor of ≈ 1 is found. It is important to notice that the q-factor changes gradually by moving the STM tip from Na sites towards the center of TNAP molecular backbone, but the FWHM does not vary significantly.

The change of the q-factor can be explained in terms of changing the ratio of the two tunneling paths t_1 and t_2 (see section 3.3.3). This indicates also that in the present case both tunneling paths exhibit a comparable strength. Knorr et al. [225] investigated single Co adatoms on a Cu(111) and Cu(100) metal surface by STM and STS. The Co adatoms show a Kondo resonance on both surfaces, but with different line shapes. By moving the tip away from the Co atom on Cu(100) Knorr et al. observed also a change of the Kondo line shape, that is the q-factor. Theoretical studies using an *ab initio*, many-body wave function theory of the Co on Cu(111) and Cu(100) Kondo systems reveal that the line shape is mainly caused by both tip-Kondo state and tip-substrate tunneling pathways [226]. The different spatial extend of the relevant orbitals is responsible for the different evolution of Kondo line shape by changing the Co-tip distance. In a molecular Kondo system the localization of the unpaired spin can be related to the delocalized singly occupied molecular orbital (SOMO). Therefore, the Kondo resonance can be distributed over the entire molecule [227, 228]. Hence, the shape of the Kondo resonance (q-factor) depends on the strength of the different tunneling paths t_1 and t_2 and the extension of the relevant orbital [166, 229, 230]. As we know from Na-TCNQ system the SOMO orbital can be deformed. In the case of the Na-TNAP layer the intensity of Kondo resonance also exhibits maximum intensity at the Na sites similar to the Na-TCNQ system (cf section 3.4). But in contrast the Kondo resonance has still weight on the TNAP backbone.

---

[11]The split of the LUMO upon charging with one electron can also be observed for magnesium porphine (MgP) on a NiAl(110) surface [224].
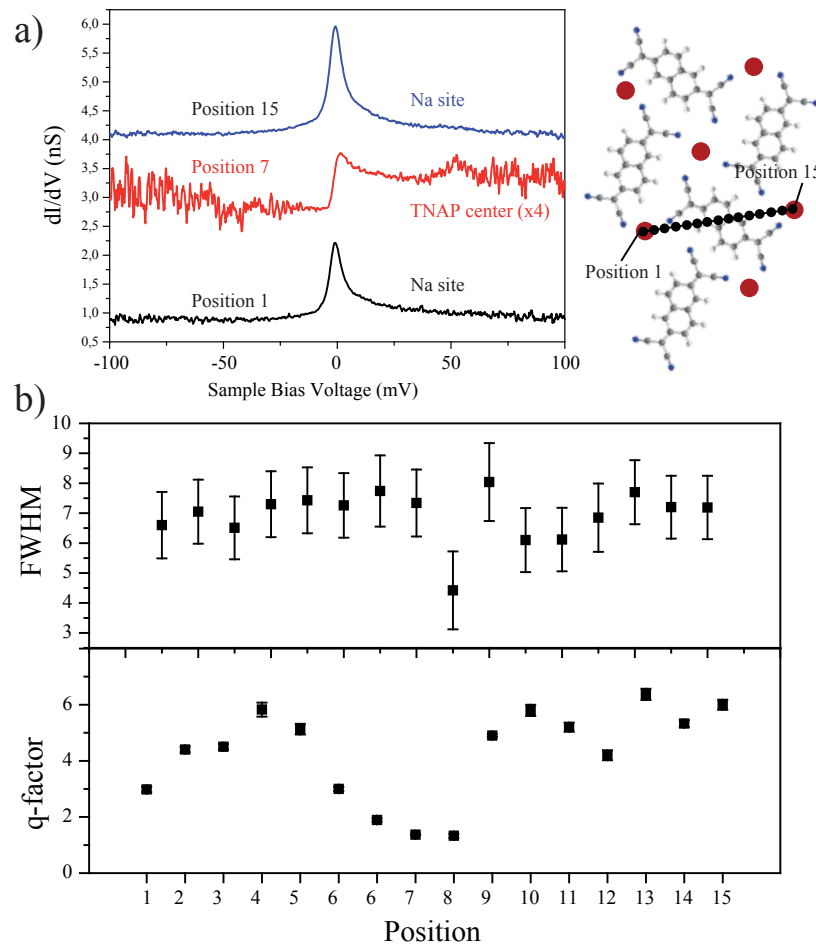
Figure 3.24: (a) A series of dI/dV spectra taken from a Na site across a bright TNAP molecule to another Na site as indicated in the sketch on the right hand side of (a)(V_S = 75 mV, I_T = 1.0 nA, the lock-in modulation is 1 mV rms at 1.23 kHz). (b) The upper panel shows the FWHM of the Kondo resonances obtained by fitting the dI/dV spectra with a Fano function (see equation 3.13) at the different positions as illustrated in (a). The lower panel depicts the q-factor for different positions obtained by fitting the dI/dV spectra with a Fano function (see equation 3.13).

The change of the q-factor in the Na-TNAP system depicts the spatial extension of the SOMO, which is connected to the distribution of the corresponding Kondo resonance. At the Na site the tip-Kondo tunneling pathway (see Fig. 3.25(a)) exhibits a larger weight compared to the tip-surface tunneling pathway. This is due to the localization of the TNAP SOMO on top of the Na site. The distance to the surface is large and therefore the corresponding tip-surface tunneling path exhibits a smaller weight. This implies also a large q-factor (see equation 3.14). In contrast, when the STM tip is localized at the TNAP center it is closer to the surface and the q-factor drops evidencing the comparable strength of the direct tip-surface pathway relative to tip-Kondo pathway. Figures 3.25(a) and (b) show a schematic sketch of the deformed TNAP SOMO (former TNAP LUMO) and how it is cloaking the Na site. The TNAP SOMO shows a very similar spatial distribution compared to the Na-TCNQ monolayer, except that the TNAP SOMO exhibits a slightly larger spatial delocalization over the molecular backbone as indicated by the presence of a small Kondo resonance with a small amplitude.
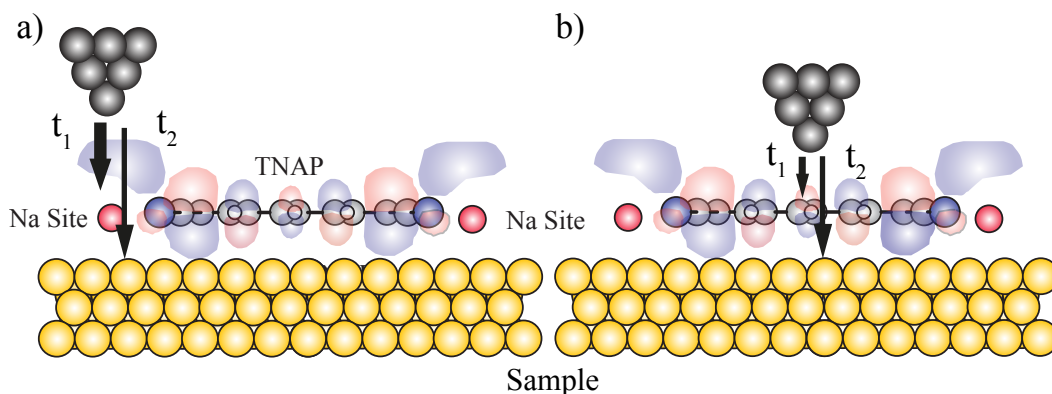
Figure 3.25:   Sketch of the deformed TNAP SOMO (former TNAP LUMO). The TNAP SOMO is cloaking the Na cation. The contribution of the tunneling paths t_1 and t_2 depend on the lateral position of the STM tip with respect to Na-TNAP layer. (a) The STM tip is localized directly above the Na site and the tip-Kondo tunneling pathway is larger compared to the tip-surface tunneling pathway. (b) The tip is vertically moved to the TNAP center and the tip-Kondo and the tip-surface tunneling pathway are comparable. The different tunneling strength (hybridization) is indicated by the different thicknesses of the arrows in (a) and (b).

This is not observed in the case of the Na-TCNQ system. We attribute this finding to the different chemical structure of TNAP compared to the smaller TCNQ species.

3.5.5   Conclusions

Summarizing, the deposition of TNAP molecules on the Au(111) metal surface leads to the formation of weakly physisorbed self-assembled molecular islands with no charge transfer interaction with the underlying surface, as revealed by STS. Since the TNAP molecule is chiral two different types of molecular islands consisting of either one enantiomer (R or L) were found. The TNAP islands are stabilized by hydrogen bonds between the cyano end groups and hydrogen atoms of neighboring TNAP molecules.

Subsequent deposition of Na atoms triggers the formation of self-assembled Na-TNAP islands with a windmill-like structure similar to the case of Na-TCNQ. The unit cell of the Na-TNAP system contains both enantiomers of TNAP. Depending on the adsorption site, two different TNAP species can be found on the reconstructed Au(111) surface. Bright TNAP molecules close to the soliton lines show a Kondo resonance with maximum intensity at the Na site, while dark TNAP molecules adsorbed at other surface areas have flat dI/dV spectra. In contrast to the Na-TCNQ case the signature of the Kondo effect at the bright TNAP molecules can still be measured at the TNAP center. An intriguing result is the change of the Kondo resonance line shape depending on the position on the TNAP molecule. A detailed position dependent analysis of the line shape reveals that the q-factor changes by almost an order of magnitude. We suggest that this change of the line shape relies on the spatial dependence of the tunneling probabilities between the tip and the surface and the tip and the Kondo state, respectively. Using the Kondo resonance as a "sensor" for the unpaired electron, the analysis of the change of the Kondo line shape and intensity allows to analyze its spatial distribution. The line shape is a result of quantum interference between different tunneling paths.

We interpret the arising of Kondo TNAP and non-Kondo TNAP molecules in terms of a different hybridization between the TNAP molecules and the underlying surface caused by the corrugation and the alternating potential landscape of the Au(111) surface. The here presented research demonstrates that changes in the molecular level alignment provoked by different adsorption sites can have a huge impact on the coupling between the magnetic moment of the unpaired electron and the conduction electron bath. Controlling the Kondo effect or, in other words, the molecule-surface interaction by the adsorption site could constitute a novel interesting route for surface patterning leading to surface regions consisting of molecules with different electronic properties. Changing the molecular species or the substrate may allow to tune the molecule-surface interaction even further. Another interesting question in this prospect is, if we can further increase the charge state of our acceptor molecules and therefore induce new interesting properties.

3.6   Enhanced Charge Transfer on a Metal Surface

The charge state of a molecule can not only have a significant impact on its conformation [231], but also affects its electronic transport properties [232–234]. A widely used approach to increase the conductivity of organic semiconductors is based on doping with alkali metal atoms [235–237] as shown in the two preceding sections. In alkali based CTC the charge transfer from the alkali donor is limited to one electron [181–184]. A higher charge transfer can only be achieved by changing the stoichiometry of the compound. Furthermore, alkali based bulk CTCs are characterized by strong Coulomb interactions, which may inhibit a further charge transfer [238, 239]. Bulk CTC based on the organic donor tetrathiafulvalene (TTF) in general show only a fractional charge transfer and significant π-π orbital overlap between the molecules [151, 152, 240, 241]. However, the presence of a surface may increase the charge transferred in CTC monolayer compared to its bulk phase. For instance, the monolayer of TTF-TCNQ on Au(111) shows a charge transfer of 1.0 electron [29, 58] compared to 0.59 electrons in the corresponding bulk phase [151, 152].

An intriguing question is, if we can further increase the charge transfer in such CTC monolayer systems on a metal surface that can act as additional charge reservoir. A possible approach is to increase the electron affinity of the acceptor species and hence its tendency to accept charge. We can do it by replacing the acceptor TCNQ with TNAP. TNAP has a slightly larger electron affinity of 4.7 eV compared to 4.23 eV of the TCNQ species [218].

3.6.1   TTF-TNAP/Au(111) System

The organic molecule TTF is a widely used donor species in bulk CTC compounds, due to its low ionization energy of $I_D = 6.83$ eV [242, 243]. The chemical structure, the LUMO, and the HOMO of the TTF molecule are depicted in Fig. 3.26. Adsorption of TTF molecules on metal surface can lead to charge transfer from the surface to the TTF molecules as it was shown in the case of TTF on Au(111) [24].

Subsequent deposition of TTF and TNAP on clean Au(111) surface kept at room temperature lead to the formation of self-assembled ordered arrays of mixed TTF-TNAP islands (see Fig. 3.27(a)). Next to the mixed TTF-TNAP also islands of excessive TNAP molecules are visible. In contrast to the pristine TNAP monolayer, the mixed TTF-TNAP layer removes the Au(111) herringbone reconstruction evidencing a sizable interaction between the organic layer and the underlying Au(111) metal surface

a)   b)   c)

● N   ● C   ○ H   ● S   HOMO   LUMO
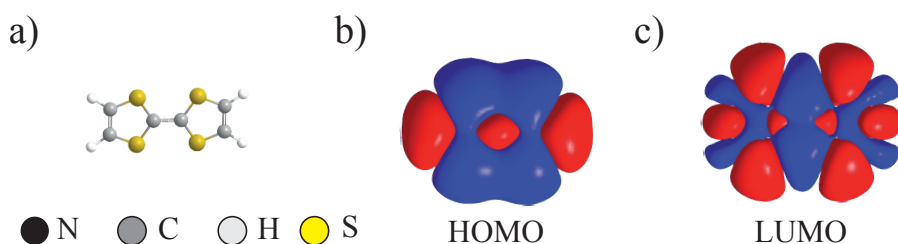
Figure 3.26:   (a) Structural model of the TTF molecule. DFT simulation of the TTF HOMO (b) and LUMO (c) of the free gas phase molecule.
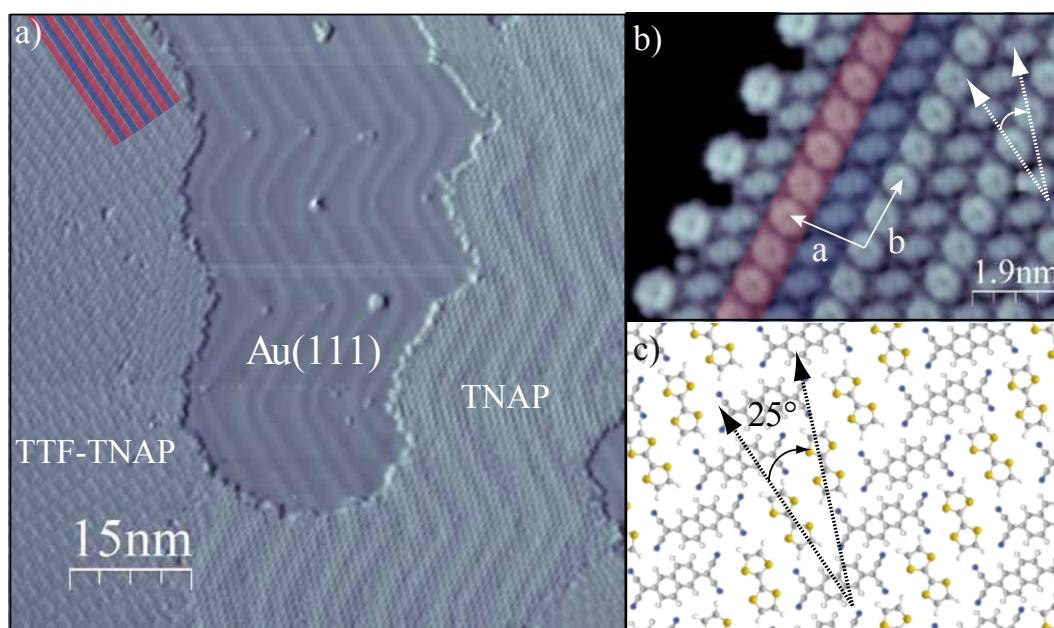
Figure 3.27: (a) STM topography image of self-assembled mixed TTF-TNAP and pristine TNAP islands on a Au(111) surface (scanning parameters: $I = 200$ pA, $V_S = 1.0$ V). The Au(111) reconstruction is vanished under the mixed TTF-TNAP layer, in contrast to the pristine TNAP layer, where the Au(111) herringbone reconstruction is still visible. (b) STM zoom-in of the mixed TTF-TNAP islands. The mixed TTF-TNAP islands consist of parallel molecular rows of TTF and TNAP molecules (scanning parameters: $I = 200$ pA, $V_S = 0.4$ V). The red and blue colored stripes indicate the TTF and TNAP rows, respectively. Neighboring TTF molecules have different orientations. (c) Structural model of the ordered mixed TTF-TNAP layer. The TTF molecules exhibit two distinct adsorption sites, which are rotated about $25°$ with respect to each other.

(see Fig. 3.27(a)). Figure 3.27(b) shows a STM zoom-in of the mixed TTF-TNAP islands. The TTF molecules appear with a donut-like shape and the TNAP molecules show a cigar-like shape. The mixed TTF-TNAP layer consists of alternating rows of TTF donor and TNAP acceptor molecules. This is very similar to the crystalline bulk compound of TTF-TNAP and the parent compound TTF-TCNQ on Au(111) [29]. Contrary to the corresponding bulk TTF-TNAP CTC compound, neighboring TTF molecules in the mixed monolayer have slightly different orientations [240]. Neighboring TTF molecules are tilted with respect to each other by an angle of $\approx 25°$. The lattice parameters of the TTF-TNAP monolayer on the Au(111) surface are $|\vec{a_1}| = 2.0 \pm 0.1$ nm, $|\vec{a_2}| = 1.6 \pm 0.1$ nm and $\alpha = 96° \pm 1°$ (as depicted in Fig. 3.27).

To investigate the electronic properties and the charge transfer process of the mixed TTF-TNAP layer, we performed differential conductance dI/dV spectra at different positions of the TTF-TNAP layer. Figure 3.28(a) shows several dI/dV spectra taken at the TNAP, TTF, and on the clean Au(111) surface. The dI/dV spectrum on the TTF-TNAP reveals a pronounced increase of the differential conductance at ≈ 0.55 V and 0.95 V. Also the Au(111) surface state at -0.49 V is not present at the TTF-TNAP layer. In order to investigate the spatial distribution of these resonances we recorded constant current dI/dV maps (see middle panel of Fig. 3.28)(b). The dI/dV map at 0.55 V reveals that the corresponding resonance is delocalized underneath the TTF-TNAP layer with a somewhat larger
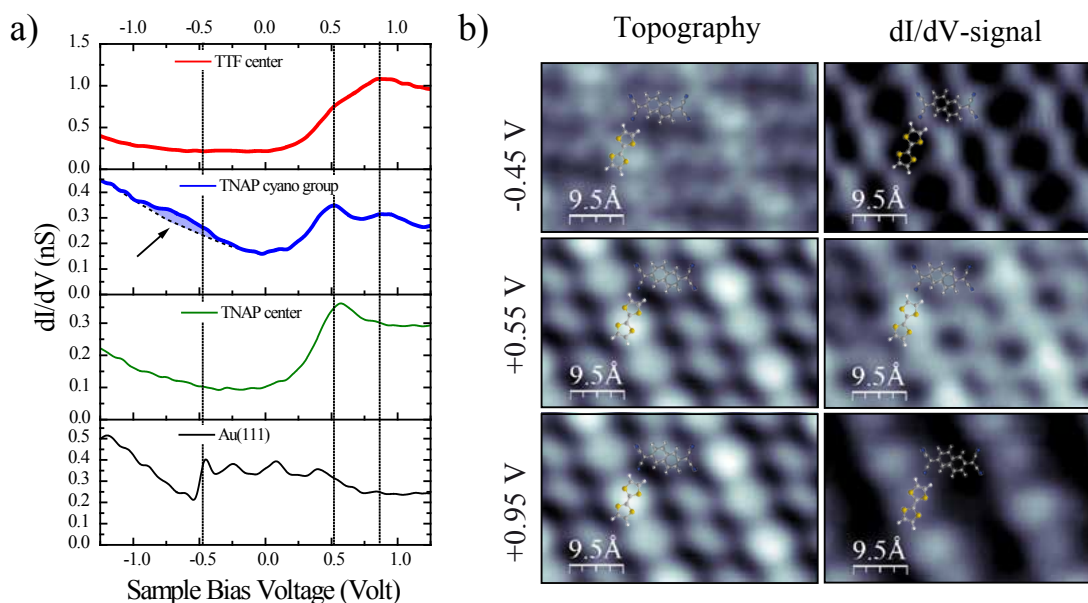
Figure 3.28: (a) Differential conductance dI/dV spectra at different positions of the TTF-TNAP layer. The dI/dV spectra reveal a pronounced increase in the differential conductance at 0.55 V (V_S = 1.5 V, I_T = 0.4 nA, the lock-in modulation is 10 mV rms at 921.1 Hz). The arrow in the dI/dV spectrum taken at the TNAP cyano group indicates a broad resonance. (b) STM topography images and constant current dI/dV-maps at different sample bias voltages of the TTF-TNAP mixed island (I_t = 0.4 nA, the lock-in modulation is 10 mV rms at 923.3 Hz). The same absolute color scale is used for all dI/dV conductance maps in order to improve comparability. At -0.45 V the corresponding dI/dV signal is located at the cyano end groups of the TNAP molecules. At the positive voltage of 0.55 V the dI/dV signal is evenly spread over the whole molecular layer including TTF and TNAP. At higher positive voltages of +0.95 V the dI/dV signal is localized mainly at the TTF sites of the mixed TTF-TNAP island.

weight on the TTF sites. The resonance at a sample bias voltage of 0.95 V is localized at the TTF sites of the TTF-TNAP island as revealed by the dI/dV map in Fig. 3.28(b).

The delocalization of the resonance at 0.55 V evidences a significant contribution of the Au(111) surface. The parent CTC monolayer TTF-TCNQ/Au(111), which has similar adsorption properties, exhibits hybrid bands having contributions from both the Au(111) surface state and the molecular orbitals. This is due to a sizable hybridization of TTF orbitals with electronic states of the underlying Au(111) surface [58]. The electronic bands underneath the TCNQ rows have a metallic character and exhibit a one-dimensional dispersion. In the case of the mixed TTF-TNAP layer an one-dimensional dispersion is not present. The alternating orientation of the TTF molecules within the TTF rows might cause a different interaction of neighboring TTF molecules with the underlying Au(111) surface. This and the larger size of the TNAP can than imply a spatial modulation of the hybridized molecular-surface states leading to a different confinement compared to the CTC monolayer TTF-TCNQ/Au(111). Hence the formation of extended electronic bands does not occur in the TTF-TNAP system.

In the case of the pristine TNAP layer on Au(111) the TNAP LUMO is localized well above E_F at an

energy of 0.4 V (see section 3.5.1). The TTF-TNAP layer exhibits two resonances at positive sample bias voltages at 0.55 V and 0.95 V, respectively. As revealed by the dI/dV maps shown in Fig. 3.28 the resonance at 0.95 V is localized at the TTF molecules and the resonance at 0.55 V is delocalized over the TTF-TNAP layer. Hence both resonances can not be related to TNAP LUMO. The absence of the TNAP LUMO at positive sample bias voltages leads to questions if the TNAP molecules within the TTF-TNAP layer are charged. The parent TTF-TCNQ CTC on Au(111) exhibits a charge transfer of 1 e$^-$ from the TTF donor to the TCNQ acceptor, this unpaired electron gives rise to a Kondo resonance (see section 3.3). High resolution STS spectra at E_F of the TTF-TNAP layer are basically flat, therefore, we can rule out that the TNAP species within the mixed TTF-TNAP is charged exactly with 1 e$^-$. This can also not be the case because it would lead to an overlap of the partially filled LUMO with E_F. Such a resonance can not be observed in dI/dV spectra of the TTF-TNAP layer. The higher electron affinity of TNAP compared to TCNQ [218] suggests a larger charge transfer in the monolayer TTF-TNAP on Au(111). Hence, the TNAP LUMO orbital would be localized at negative sample bias voltages. Indeed, constant conductance dI/dV maps at -0.45 V reveal an increased differential conductance at the cyano end groups of the TNAP molecules within the TTF-TNAP layer at that negative bias voltage of V_s = -0.45 V (see Fig. 3.28(b)). The localization at the cyano end groups agrees with the high electron density of the TNAP LUMO at that site, as revealed in section 3.5 (Na-TNAP). At that sample bias voltage the spectrum on the TNAP-cyano group is dominated by a broad resonance at $\approx$ -0.6 V. This resonance might then correspond to the LUMO of the TNAP. The large FWHM of the resonance indicates a strong interactions with the underlying Au(111) metal surface (see Fig. 3.28(a)).

In order to verify the charging of TNAP we functionalized our tip with a small impurity molecule (unknown). The functionalization of the STM tip with small molecules (for example CO) can lead to a p-wave tip [57]. The STM contrast then is altered and more sensitive to the lateral gradient of the wave function. The high spatial resolution STM image at the energy of -0.5 V shown in Figure 3.29 clearly resolves the typical donut-like shape of the TTF HOMO (highlighted in blue) and furthermore the nodal plane structure of the TNAP LUMO (highlighted in red). The interpretation of STM images taken with a functionalized tip is in general difficult, but the clear resolution of the TTF HOMO is an indication that the tip just improves the imaging of the nodal planes, without further modification of the image contrast. Hence, the appearance of the TNAP LUMO at negative sample bias voltages proves the occupation with more than 1 electron.

3.6.2 Conclusions

In conclusion, we have shown the enhanced charge transfer in the TTF-TNAP layer on Au(111). Self-assembled and ordered structures of alternating TNAP and TTF molecules are formed via donor-acceptor recognition. Neighboring TTF molecules are slightly tilted about an angle of 25°. An important observation is the vanishing of the Au(111) surface reconstruction indicating a strong hybridization between the organic TTF-TNAP layer and the underlying surface.

As revealed by STS and STM topography imaging, the lowest unoccupied molecular orbital (LUMO) of the TNAP molecule shifts well below the Fermi level of the Au(111) metal substrate indicating a charge transfer larger than 1 electron. The absence of a Kondo resonance stemming from singly occupied orbital further corroborates such large charge transfer, in contrast to bulk CTC compound, where a maximum charge transfer of 1 electron is found.
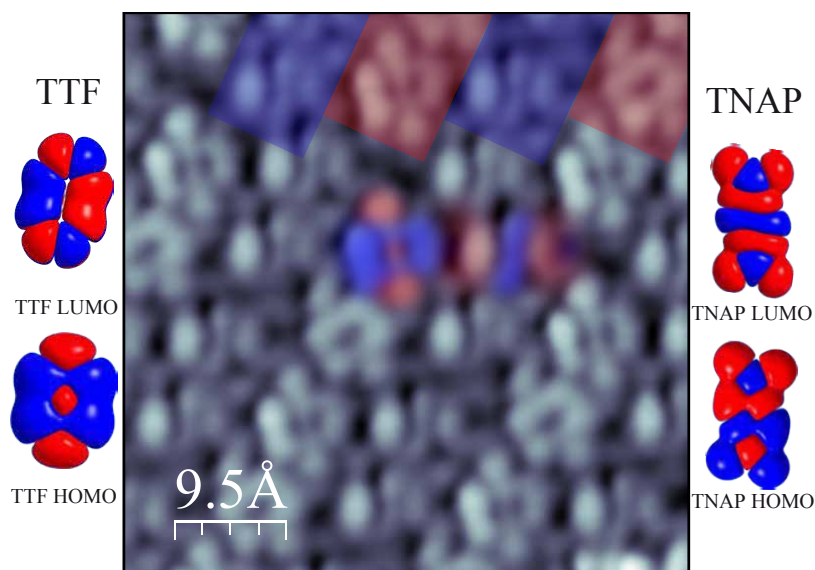
Figure 3.29: Constant current topography of the mixed TTF-TNAP island taken at sample bias voltage of -0.5 V with a functionalized STM tip. The intramolecular resolution on the TNAP molecules resolve the LUMO shape of the neutral molecule, thus indicating its charging by more than one electron.

The surprisingly high amount of charge transfer in the TTF-TNAP monolayer suggests an important role of the underlying metal surface, which can not only act as an additional charge reservoir, but also reduce the Coulomb charging energy of the molecule by screening process [44, 244], allowing thus the stabilization of the high charge state of the TNAP acceptor species.

Our results highlight the importance of the understanding of the interaction not only between the acceptor and donor species, but also the interaction with the underlying surface, which is a key issue for tailoring the surface/ interface properties.

DESIGN OF SPIN ARRAYS USING METAL-ORGANIC NETWORKS

The work presented in this chapter was published as

- *Combined STM and XAS study of a metal-organic network* by T. R. Umbach, M. Bernien, C. F. Hermanns, K. Hermann, L. Sun, H. Mohrmann, A. Krüger, N. Krane , Z. Yang, K. J. Franke, J. I. Pascual, W. Kuch in preparation

- *Ferromagnetic Coupling of Mononuclear Fe Centers in a Self-Assembled Metal-Organic Network on Au(111)* by T. R. Umbach, M. Bernien, C. F. Hermanns, A. Krüger, V. Sessi, I. Fernández-Torrente, P. Stoll, J. I. Pascual, K. J. Franke, W. Kuch *Phys. Rev. Lett.*, 2012, 109, 267207.

4.1   Introduction

There are two key issues, which have to be overcome in order to realize functional and custom designed magnetic nanostructures consisting of single magnetic atoms on surfaces. The first addresses the growth of ordered magnetic structures and the other refers to the control of the magnetic properties of such structures [245]. Furthermore a main challenge regarding future applications, for example in data storage devices, is the stabilization of the magnetization against thermal fluctuations [245, 246]. The stability of magnetic nanostructures is mainly determined by the magnetic anisotropy energy stemming from spin-orbit coupling and the symmetry of the atomic-scale surrounding implying a ligand-field [17, 245]. Additional magnetic exchange interactions can lead to a further stabilization of the magnetization [13].

There are three distinct approaches to realize ordered arrays of magnetic atoms: (1) deposition of single magnetic atoms on a surface (2) molecules with magnetic centers embedded in their structure (3) metal-organic networks.

The deposition of single magnetic atoms on a surface presents the most simple way to grow an array of spins [36] as illustrated in Fig. 4.1(1). Interestingly, single atoms can show an increased magnetic anisotropy, like in the case of single Co atoms on Pt(111) surface [36], compared to the corresponding bulk material. This reveals a complex effect of the atomic-scale environment on the magnetic prop-
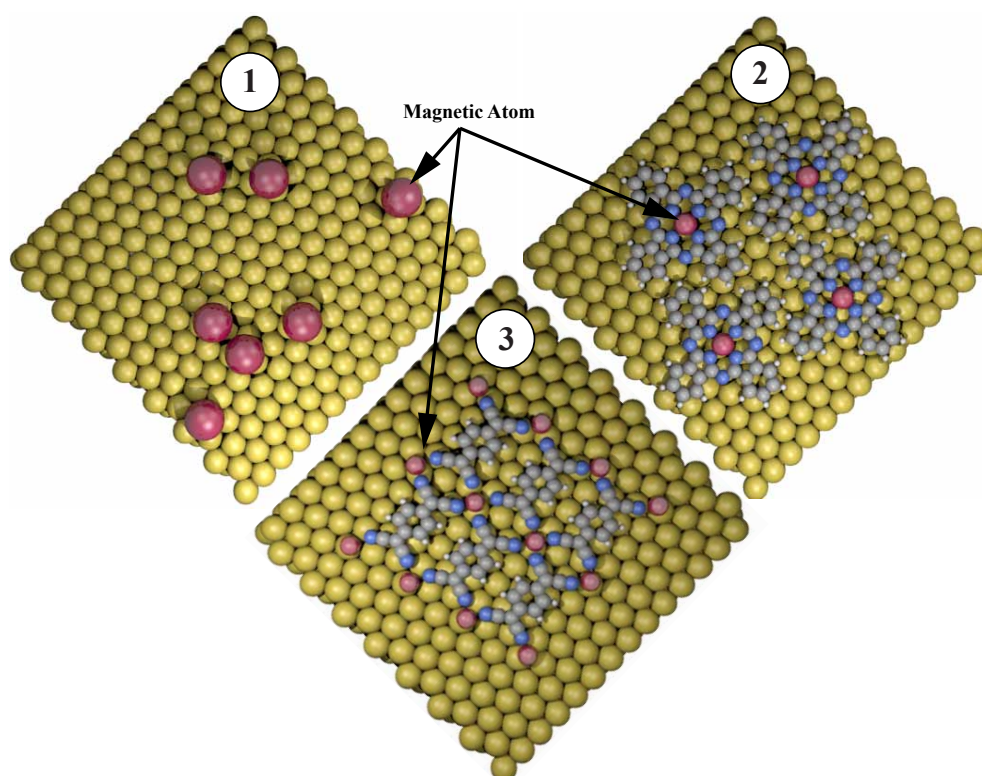
Figure 4.1: Possible approaches to realize ordered arrays of magnetic atoms. (1) deposition of single magnetic atoms on a surface (2) molecules with magnetic centers embedded in their structure (3) metal-organic networks.

erties. However, the precise control of the symmetry and atom-atom distance can be hardly achieved using individual atoms on surfaces.The realization of ordered arrangements of magnetic atoms [36] is important for the addressing and reading out of their spin state, for example, by scanning probe methods [247]. This problem can be solved nowadays in two ways: by the use of molecules with magnetic centers embedded in its structure (see Fig. 4.1(2)) or by growing metal-organic networks, where the molecules act as linkers among the metallic centers (see Fig. 4.1(3)).

One approach is the use of paramagnetic molecules to grow two-dimensional magnetic structures on surfaces [248, 249] depicted in Fig. 4.1(2). Typically, metal phthalocyanine or porphyrin molecules are used for this purpose. Weak Van-der-Waals interaction or hydrogen bonds are responsible for the self-assembling in ordered structures [40, 249]. The underlying surface can not only act as template but also mediate magnetic interactions. A magnetic substrate can help to induce a magnetic ordering of the magnetic moments [250, 251]. Or in other cases based on long-range magnetic exchange mediated by the surface electron system known as the Ruderman-Kittel-Kasuya-Yosida (RKKY)-interaction [248] might stabilize the magnetic moments of the metallic centers.

The second option, the approach using so-called metal-organic networks [17, 21, 252], presents a higher flexibility than the use of paramagnetic molecules. Metal-organic networks present a versatile approach to grow ordered nanostructures consisting of metal atoms and molecules on metal surfaces (see Fig.4.1(3)). The distance and symmetry of the network architecture can be controlled by the chemical design of the organic linkers [15, 18, 28]. The organic linkers do not only form metal-ligand

bonds, they can also cause a crystal field at the position of the associated metal atom that can produce magnetic anisotropy. Such anisotropy, can be manipulated by the right selection of number and/or type of ligands [17, 165]. In order to stabilize spin states and prevent thermal fluctuation of the spin moment, a high magnetic anisotropy is requested, being the key in view of potential applications in future storage devices. The presence of organic linking bridges among the magnetic metal centers can also mediate their spin-polarization, as it is known from bulk metal-organic frameworks [253]. Such spin-propagation is not possible in the case of paramagnetic molecules (approach (2) in Fig.4.1). This rises the question of how we can achieve a magnetically coupled metal-organic network and what are the main ingredients to accomplish this goal.

On the other hand the presence of a metal surface can have significant effects on the structural and electronic properties of the network. Single metal atoms tend to occupy specific adsorption sites [254]. This directly affects the network architectures. Also the molecular species can occupy certain adsorption sites leading to a substrate directed growth [38]. Furthermore the network constituents can interact with the electronic states of the metal surfaces implying screening effects [44], charge transfer processes between constituents of the network and the underlying surface [29] or partial/complete screening of magnetic moments [168, 169]. A detailed understanding of these effects on the network structural, electronic, and magnetic properties is required in order to tailor its properties.

In the following we discuss several metal-organic networks in terms of their structural, electronic and magnetic interactions. All metal-organic networks shown in this section were investigated in terms of low-temperature STM, STS, XAS, XMCD, and DFT.

4.2 Magnetism of Single Atoms

The present chapter starts with a short introduction of the magnetism of single atoms in a crystal field. To simulate the magnetic behavior of metal-organic networks the so called *spin*-Hamiltonian approach is used.

4.2.1 Magnetism of Magnetic Atoms in Crystal Field

For an isolated atom there is no preferred direction of the magnetic moment $\vec{m}$. Let us consider a magnetic $3d$ transition metal atom placed on a metal surface. The electrons in the $3d$-orbitals are responsible for the magnetic moment $\vec{m}$ in these atoms. Since these electrons are in the outermost atomic shell, the presence of external ligands (surface or organic linkers) lift their energetic degeneracy. These external ligands provoke a non-spherical electric field caused by their charges, the so called crystal field. The additional electrostatic potential of the crystal field reads [255]:

$$\mathcal{H}_{CF} = -\sum_i e \cdot V(x_i, y_i, z_i) \tag{4.1}$$

where $V(x_i, y_i, z_i)$ is the electrostatic potential describing the Coulomb interaction between the electrons of the magnetic atom and the neighboring charges (ligands). Crystal field theory treats the neighboring charges (ligands) as point charges, hence $V(r)$ fulfills the Laplace's equation $\nabla^2 V = 0$ [255]. Therefore, $V(r)$ can be expanded in spherical harmonics. Depending on the crystal field symmetry the electrostatic potential $V(r)$ can now be calculated [255, 256].
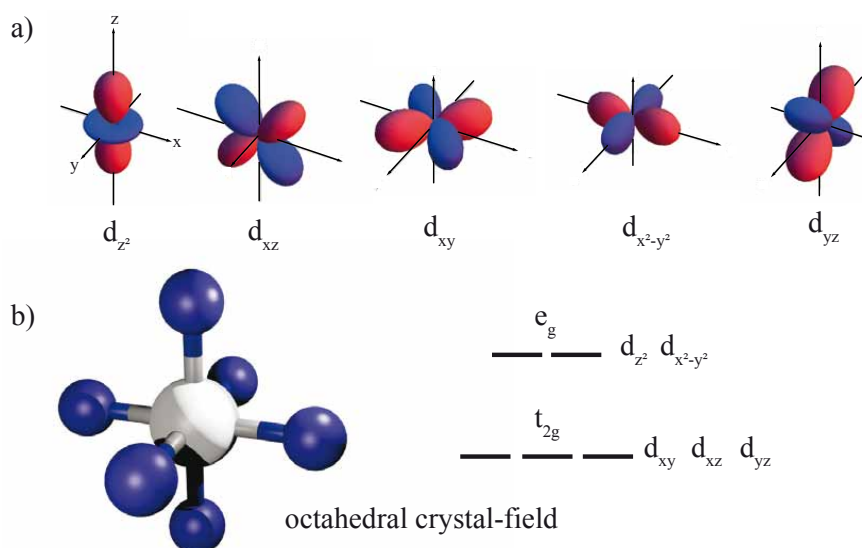
Figure 4.2:   (a) Schematic presentation of the $3d$ orbitals. (b) Crystal field splitting for a complex with octahedral symmetry. The $3d$ orbital set splits into two subsets labeled e_g and t_{2g}.

Due to the electrostatic interactions as described by the crystal field, the d orbitals split depending on its strength and symmetry. Figure 4.2 depicts an octahedral crystal field. In this case the central atom is surrounded by six ions (charges) and the d orbitals split into two sets of orbitals labeled t_{2g} and e_g with an energetic difference of Δ, called the crystal field splitting (CFS). The d_{z^2} and $d_{x^2-y^2}$ orbitals are then highest in energy (cf Fig. 4.2), since they are pointing directly towards the neighboring ions (charges), therefore, intersite interaction are larger compared to the d_{xy}, d_{xz} and d_{yz} orbitals.

A general trend for the $3d$ transition metals within a crystal field is the *quenching* of the orbital moment L. The crystal field causes a lifting of the orbital degeneracy depending on the symmetry (see Fig. 4.2). When the lowest orbital level is formed by a singlet (non-degenerated) the orbital moment L is zero to first order [255, 256][1]. Therefore, the total angular momentum J is equal to S and the magnetic behavior is primarily caused by the spin S. However, the *spin-orbit* coupling $\mathcal{H}_{SO}$ can lead to deviations of this simple picture making the orbital moment L not completely quenched. Depending on the filling of the $3d$ shell according to Hund's rules the experimental J_{exp} and the spin-only value S can differ as follows [208, 255]:

- for less than half-filled shells L and S are orientated parallel, therefore $J_{exp} < S$

- for more than half-filled shells L and S are orientated antiparallel, therefore $J_{exp} > S$

4.2.2   The *spin*-Hamiltonian Approach

A common approach to describe the magnetism of single $3d$ metal atoms [257–259] or molecules with a magnetic metal core [260] is the so called *spin*-Hamiltonian approach. In the following a

---

[1]This is an effect of the crystal field, which leads to admixture of the wave functions with $M_L= L$ and $M_L= -L$ [255], therefore the new wave functions, consisting of a super-position of both wave functions, exhibit a vanishing orbital moment L.

short description of the *spin*-Hamiltonian approach is given [255, 256, 261]. The *spin*-Hamiltonian approach is based on two essential approximations:

- The orbital moment L is quenched as a result of the crystal field

- The ground state is orbitally non-degenerated

The validity of those two approximation will be discussed at the end of this section. The *spin*-Hamiltonian approach relies on the following perturbation Hamiltonian including the *spin-orbit* coupling and the Zeeman effect:

$$\mathcal{H}_{CF} = \mathcal{H}_{SO} + \mathcal{H}_{Zeeman} = \alpha\,\hat{L}\cdot\hat{S} + \mu_B\,\vec{B}(\hat{L} + 2\,\hat{S}) \tag{4.2}$$

By using a method developed by Pryce [262], the perturbation Hamiltonian $\mathcal{H}_{CF}$ is transformed into the *spin*-Hamiltonian $\mathcal{H}_S$ by using an operator representation for the orbital moment $\hat{L}$ [255, 256]. Therefore we obtain an expression explicitly depending on the spin operator $\hat{S}$. The eigenfunctions are products of the orbital $|L, M_L\rangle$ and spin states $|S, M_S\rangle$ since neither $\mathcal{H}_{Zeeman}$ nor $\mathcal{H}_{SO}$ mix the states. In the following we consider a non-degenerated orbital ground state. Applying perturbation theory to first order yields then [255]:

$$\langle L, M_L | \mathcal{H}_{CF} | L, M_L\rangle = \langle L, M_L | \alpha\hat{L}\cdot\hat{S} + \mu_B\vec{B}(\hat{L} + 2\hat{S}) | L^*, M_{L^*}\rangle \tag{4.3}$$

Neither $\vec{B}$ nor $\hat{S}$ act on the orbital ground state $|L, M_L\rangle$ or the exited states $|L^*, M_{L^*}\rangle$. Since the ground state is orbitally non-degenerated with a zero orbital moment L all matrix terms $\langle L, M_L | L_i | L^*, M_{L^*}\rangle$ with $i = x, y, z$ vanish. The second order perturbations reads [255]:

$$\sum \frac{\langle L, M_L | \alpha\,\hat{L}\cdot\hat{S} + \mu_B\vec{B}(\hat{L} + 2\,\hat{S}) | L^*, M_{L^*}\rangle^2}{E_{L^*, M_{L^*}} - E_{L, M_L}} \tag{4.4}$$

Because of the orthogonality of the orbital states $|L, M_L\rangle$ the matrix term becomes $\langle L, M_L | \mu_B\vec{B}\cdot 2\,S | L^*, M_{L^*}\rangle = 0$ for $|L, M_L\rangle \neq |L^*, M_{L^*}\rangle$. The matrix elements $\langle L, M_L | L_i | L^*, M_{L^*}\rangle$ with $i = x, y, z$ are non-zero, therefore we define the tensor $\Lambda_{i,j}$, which reads:

$$\Lambda_{i,j} = \sum \frac{\langle L, M_L | L_i | L, M_L\rangle\,\langle L, M_L | L_j | L^*, M_{L^*}\rangle}{E_{L^*, M_{L^*}} - E_{L, M_L}} \tag{4.5}$$

with $i, j = x, y, z$. In general, the matrix elements $\Lambda_{i,j}$ with $i \neq j$ are zero [261]. Hence, the matrix elements $\Lambda_{i,i}$ with $i = x, y, z$ are directly proportional to the unquenched angular momentum along the corresponding direction $i = x, y, z$. Therefore, we obtain the following notation of the *spin*-Hamiltonian [255, 256]:

$$\mathcal{H}_S = 2\mu_B\sum_{i,\,j}(\delta_{i,\,j} - \alpha\Lambda_{i,\,j})S_i\,B_j - \alpha^2\sum_{i,j}\Lambda_{i,\,j}S_i\,S_j - \mu_B^2\sum_{i,\,j}\Lambda_{i,j}B_i\,B_j \tag{4.6}$$

Here $\delta_{i,j}$ is the Kronecker Delta and is equal to 1 for $i = j$ and 0 for $i \neq j$. The term $2(\Lambda_{i,j} - \alpha\Lambda_{i,j})$ corresponds to the g-tensor $g_{i,j}$ with $i, j = x, y, z$. The second term in equation 4.6 is responsible for the zero-field-splitting of the spin-multiplet since it is not vanishing for zero magnetic field $B = 0$ [261]:

$$\mathcal{H}_S = \alpha^2(\Lambda_{xx}\,S_x^2 + \Lambda_{yy}\,S_y^2 + \Lambda_{zz}\,S_z^2) \tag{4.7}$$
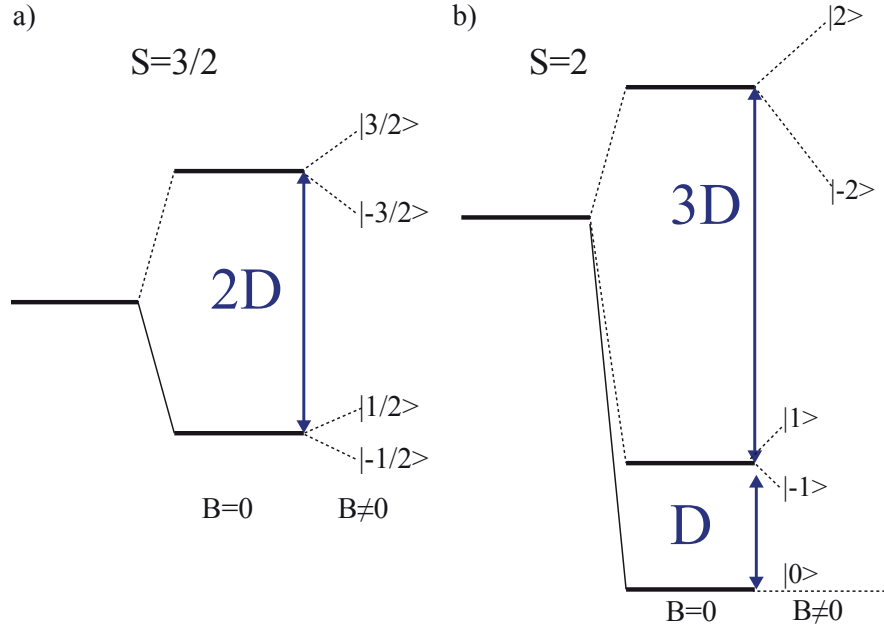
Figure 4.3: Schematic diagram of the zero-field-splitting for a crystal field with axial symmetry and $S = 3/2$ (a) and $S = 2$ (b).

A common notation of the *spin*-Hamiltonian reads [261]:

$$\mathcal{H}_S^{axial} = g_{||}\mu_B B_z S_Z + g_\perp \mu_B (B_x S_x + B_y S_y) + D[S_z^2 - \frac{1}{3}S(S+1)]$$
$$+ E(S_x^2 - S_y^2) \tag{4.8}$$

with [261]:

$$D = -\alpha^2(-\frac{1}{2}\Lambda_{xx} - \frac{1}{2}\Lambda_{yy} + \Lambda_{zz}) \tag{4.9}$$
$$E = 1/2\alpha^2(\Lambda_{xx} - \Lambda_{yy}) \tag{4.10}$$

Since the matrix elements Λ_{ii} with $i = x, y, z$ are proportional to the corresponding component of the unquenched angular momentum L the parameter D represents the magnetic anisotropy between the z-direction and the $x-y$-plane. On the other hand, E accounts for the anisotropy within the $x-y$-plane. Furthermore, in the case of $E \neq 0$ the corresponding $|m\rangle$ states mix [258].

In the case of an axial symmetric crystal field ($E = 0$) it follows $\Delta_{x,\,x} = \Delta_{||}$ and $\Delta_{y,\,y} = \Delta_{z,\,z} = \Delta_\perp$. The *spin*-Hamiltonian then reads [256]:

$$\mathcal{H}_S^{axial} = g_{||}\mu_B B_z S_Z + g_\perp \mu_B (B_x S_x + B_y S_y) + D[S_z^2 - \frac{1}{3}S(S+1)]+$$
$$\frac{1}{3}S(S+1)(2\Lambda_\perp + \Lambda_{||})\alpha^2 \tag{4.11}$$

with $D = \alpha^2(\Lambda_{||} - \Lambda_\perp)$. The last term in equation 4.11 causes only a shift of all electronic levels, therefore we can simplify the *spin*-Hamiltonian $\mathcal{H}_S$ for axial crystal field:

$$\mathcal{H}_S^{axial} = g_{||}\mu_B B_z S_Z + g_\perp \mu_B (B_x S_x + B_y S_y) + D[S_z^2 - \frac{1}{3}S(S+1)] \tag{4.12}$$

Eigenstate	$|2\rangle$	$|1\rangle$	$|0\rangle$	$|-1\rangle$	$|-2\rangle$
$|2, 2\rangle$	1	0	0	0	0
$|2, 1\rangle$	0	1	0	0	0
$|2, 0\rangle$	0	0	1	0	0
$|2, -1\rangle$	0	0.	0	1	0
$|2, -2\rangle$	0	0	0	0	1
E_i **(meV)**	0	1.05	1.4	1.05	0

Table 4.1: Eigenstates for a $S= 2$ spin system in crystal field with $D= -0.35$ meV and $E= 0$ meV.

Positive values of D correspond to an easy-plane magnetic anisotropy and the corresponding lowest $|m\rangle$ states are lowest in energy. In contrast, negative values of D account for an easy-axis magnetic anisotropy and the highest $|m\rangle$ states are the energetically most stable (see Fig. 4.4 for $S= 2$ and $D < 0$). The states $|m\rangle$ are pure eigenstates of S_z operator. The energy diagrams in the case of $D > 0$ and spin $S = 3/2$ and $S = 2$ with the external magnetic field $B_{ex} = (0, 0, B_z)$ parallel to S_z are shown in Fig. 4.3(a) and (b), respectively.

In the following chapters we want to simulate the experimental magnetization curves of metal-organic networks in order to investigate their magnetic anisotropy and the spin state of their metal centers. The question of how we can calculate the magnetization $\vec{M}(\vec{B}, S, T, D, E)$ for a given system based on the *spin*-Hamiltonian arises. In the following we will neglect the term $1/3 \cdot S(S+1)$, since it just shifts the energy origin for a given spin S. To simplify, we assume that the g-factor is isotropic $g_{||}= g_{\perp}= g$. Because of symmetry reasons, we are not sensitive to the azimuthal dependence of the magnetic anisotropy with our experimental technique (XMCD) as discussed in chapter 2. Thus, the E term in equation 4.12 is assumed to be negligible and we set $E= 0$. Thus, the *spin*-Hamiltonian simplifies to:

$$\mathcal{H}_S = g\mu_B\vec{B}_{ex}\vec{S}+D \cdot S_z^2 \tag{4.13}$$

Let us assume a system of magnetic moments with $S= 2$, a magnetic anisotropy with an easy-axis out-of-plane direction with $D= -0.35$ meV, and $g= 2$. By solving the eigenvalue problem of the *spin*-Hamiltonian in equation 4.13 for these values we obtain the eigenstates and their energies E_i listed in table 4.1. Of course, the orientation of the external magnetic field $\vec{B}_{ex}$ with respect to S_z has to be taken into account (see section 2.4.3). Here we assume the external magnetic field $\vec{B}_{ex} = (0, 0, B_z)$ parallel to S_z. To get now the magnetization $\vec{M}(\vec{B}, 2, T, D, 0)$ we have to calculate the thermal population of the resulting levels. Let us assume temperature $T= 8$ K. Now we have to calculate the expectation value $\langle S \rangle$ for each level and the corresponding population according to Boltzmann statistics. The results are summarized in Fig. 4.4 and also the corresponding magnetization curve $M(B, 2, 8\,K, -0.35\,meV, 0)$.
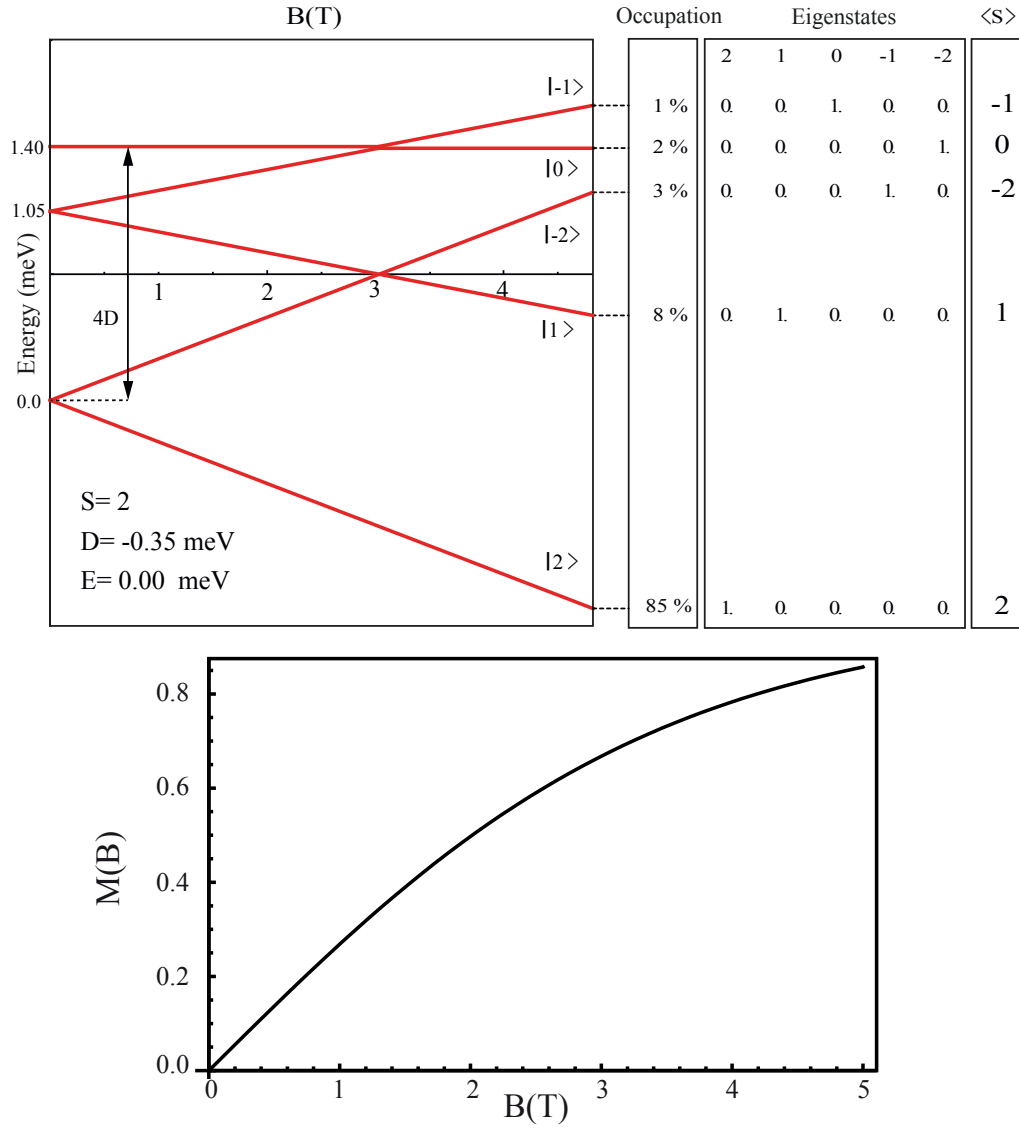
Figure 4.4: Magnetic field dependence of the energy eigenstates for a magnetic system with $S= 2$, $D= -0.35$ meV and $T= 8$ K. The occupation of the corresponding states, the spin eigenstates and the spin expectation value $\langle S \rangle$ is given on the right side. The lower panel depicts the corresponding magnetization curve $M(B)$.
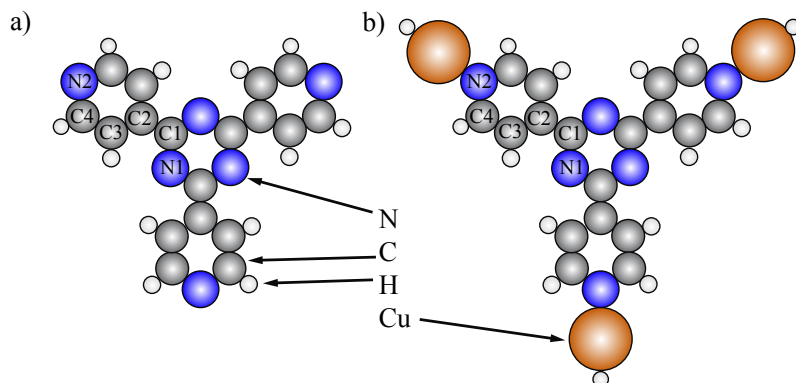
Figure 4.5: Molecular structures of (a) the free T4PT molecule, (b) the T4PT-(CuH)$_3$ model cluster. Both structures were obtained by DFT based optimization. Atoms are represented by colored balls of different radii. The atomic species (symmetry non-equivalent) considered in the DFT calculations for core excitations are labeled as nitrogen N1, N2, carbon C1-C4.

4.3 A Robust Metal-Organic Network Based on Cu Atoms

The architecture of metal-organic networks is not only based on the symmetry of the organic linkers and the interaction between the functional end groups of the molecule and the metal species [18, 263], but may also be affected by the interaction with the underlying surface. The metal atoms and molecules may prefer specific adsorption sites leading to different bonding motifs and architectures compared to the corresponding bulk compounds. In this context an intriguing question is, how robust is the network architecture regarding the underlying metal surface. Or, does the surface mainly determine the network structural properties?

The non-covalent metal-ligand bond is characterized by its directionality and allows the growth of complex nanostructures with distinct motifs depending on the metal species and the properties of the molecular linker [18, 19, 263–266]. However, a detailed understanding of structural and electronic properties is required to further tailor the properties in view of potential applications. In this regard the amount of charge transfer and the effect of bond formation on the rest of the molecular linkers is of interest.

The present section deals with the structural, electronic, and magnetic properties of the metal-organic network based on Cu atoms as metal centers. Our molecular linker of choice is 2,4,6-tris(4-pyridyl)-1,3,5-triazine (T4PT). The triangular T4PT molecule consists of three pyridine end groups and a central triazine ring. The molecular structure of T4PT is depicted in Fig. 4.5(a). A metal-ligand bond formation is favored by the lone-pair electrons of the active nitrogen sites of the pyridine end groups [19, 263–267].

4.3.1 STM Investigation of Cu-T4PT Network on Cu(111)

Deposition of a sub-monolayer amount of T4PT molecules on a clean Cu(111) metal surface leads to the formation of a metal-organic network with a honeycomb structure (Fig. 4.6(a)). Figure 4.6(b) shows a STM topography zoom-in of the honeycomb-like nanomesh. The T4PT molecules exhibit a three-fold symmetry indicating a planar adsorption on the surface as a result of π-interactions of the
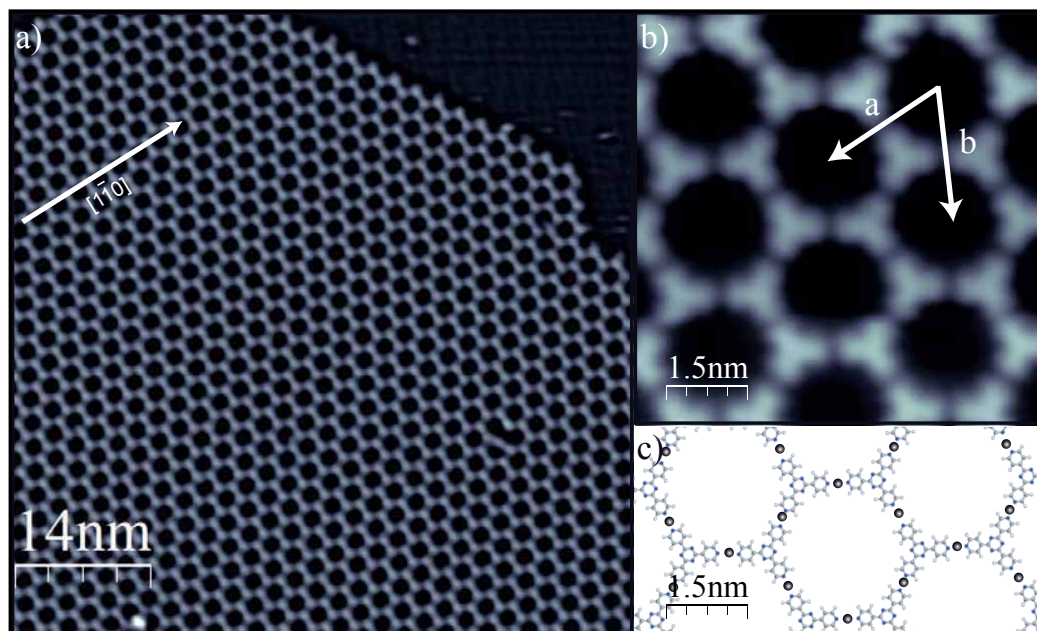
Figure 4.6:   (a) STM topography image of a Cu-T4PT islands on the Cu(111) surface (I = 10 pA, V_S = -1.0 V). (b) STM zoom-in of a Cu-T4PT island. A two-fold coordination motif of Cu and T4PT is visible leading to honeycomb-like structure(I = 10 pA, V_S= -0.5 V). The unit cell is indicated by white arrows labeled "a" and "b" with $a = b = 24\pm 1$ Å. (c) Structure model of the Cu-T4PT network.

molecules with the surface. Each nanomesh pore exhibits an inner diameter of 16.6 ± 0.1Å. The unit cell of the T4PT based nanomesh is indicated in Fig. 4.6(b) by white arrows and has the following unit cell vectors labeled "a" and "b" with $a = b = 24\pm 1$ Å enclosing an angle of $\alpha = 60.0\pm 1.0°$. Figure 4.6(b) also reveals a two-fold bonding motif between neighboring T4PT molecules. The pyridine end groups of neighboring T4PT have a face-to-face configuration. Since the face-to-face configuration of the neighboring pyridine end groups is energetically not favorable due to the repulsive character of the pyridine nitrogen lone pair electrons, this self-assembling suggests the presence of bridging Cu adatoms. This is in line with several other studies of self-assembled metal-organic networks on metals surfaces, where two-fold coordination motifs of nitrogen based functional end groups and Cu atoms have been observed [19, 22, 28, 265, 268].

To elucidate the electronic structure of the Cu-T4PT network we present in Fig.4.7(a) dI/dV spectra on different sites of the network. A step-like feature at an energy of 0.8 V and a resonance-like feature at an energy of 1.9 V are visible in the spectra acquired at the triazine rings of two opposing T4PT molecules (indicated by the colored dots). Despite their similar shape, the features in the dI/dV spectra are shifted with respect to each other and have different intensities, suggesting a slightly different electronic structure.

In order to investigate the difference in the dI/dV spectra we performed dI/dV maps at the energies of the resonances. Figure 4.7(c-d) shows two constant current dI/dV-maps taken at the energies of 0.8 V (c) and 1.9 V (d) (close to the resonance energies), respectively. The red and black colored triangles illustrate the orientation of the T4PT molecules within the coordinated Cu-T4PT network. Both dI/dV maps clearly show an alternating change of the LDOS signal from high to low between
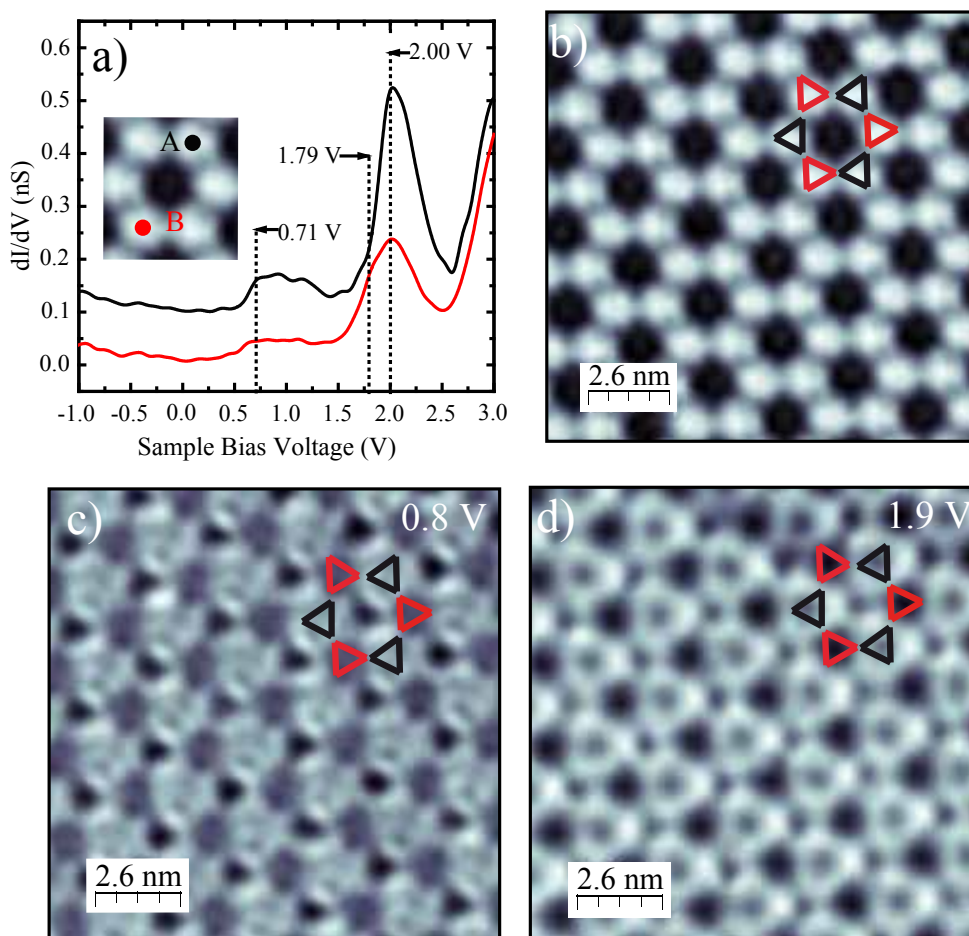
Figure 4.7: *dI/dV* spectra and maps of the Cu-T4PT nanomesh. (a) Two *dI/dV* spectra taken at the central triazine ring of two opposing T4PT molecules (indicated by the red and black dot). (b) STM topography image of the Cu-T4PT nanomesh and corresponding constant current *dI/dV* maps at sample bias voltages of 0.8 V (c) and 1.9 V (d), respectively ($I_T = 0.22$ nA).

neighboring T4PT molecules within the Cu-T4PT network. The alternating LDOS signal present in both *dI/dV* maps indicates that there are two different adsorption sites of the T4PT molecules present in each nanomesh pore (labeled *A* and *B* in Fig. 4.7(a)). Interestingly, the largest LDOS signal is localized at the outer periphery of the T4PT molecules in both *dI/dV* maps (see Figure 4.7(c-d)). Furthermore, the *dI/dV* map recorded at an energy of 0.8 V reveals that the corresponding molecular state also has some weight at the central triazine ring. This is in contrast to the molecular state imaged at an energy of 1.9 V (see Fig. 4.7(d)).

Wang et al. [265] reported on a similar metal-organic network consisting of Cu adatom and 1,3,5-tris(pyridyl)benzene (T4PB) investigated by means of STM and DFT. Similar to the Cu-T4PT network, the observed molecular resonances have their largest LDOS signal at the outer molecular periphery. T4PB is also a triangular-shaped molecule and consists of three outer pyridine end groups (cf 4.26(c)), but different to T4PT, it has a central benzene ring instead of a triazine ring. The Cu-T4PB network exhibits two phases on the Cu(111) metal surface [265]. Let us call them phase 1 (upper
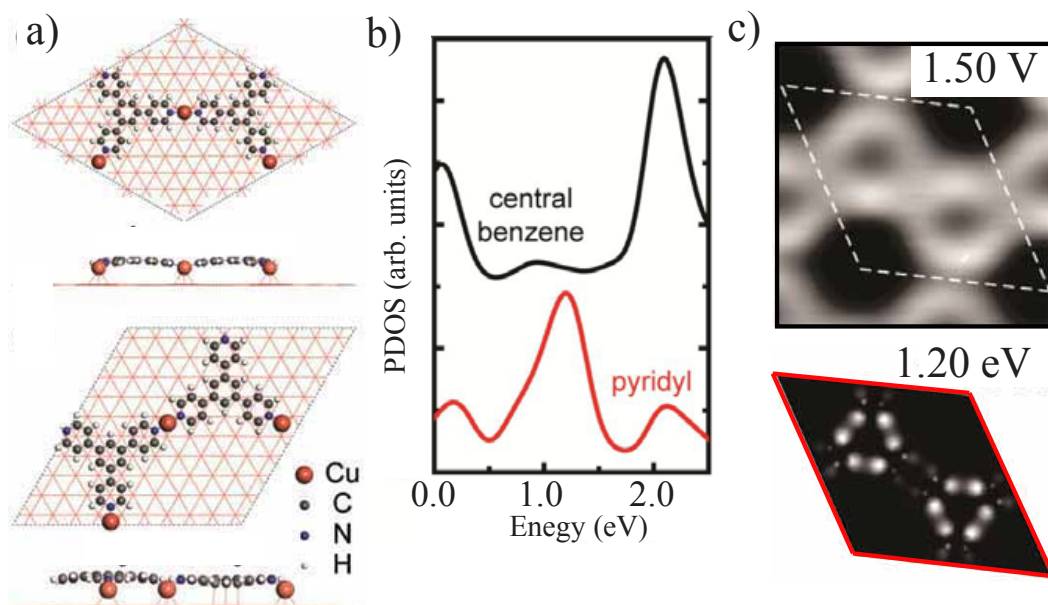
Figure 4.8: [265] (a) DFT optimized structure of the Cu-T4PB unit cell for phase 1 (upper panel) and phase 2 (lower panel). (b) PDOS at the center of the T4PB molecule (black) and at the pyridine end group (red). (c) dI/dV map and the corresponding DFT simulated PDOS maps of the Cu-T4PB network at a sample bias voltage of 1.5 V and an energy of 1.2 eV (parameters: size 4x4 nm, I_T = 0.4 nA).

panel of Fig. 4.8(a)) and phase 2 (lower panel of Fig. 4.8(a)). In phase 1 all T4PB molecules have equivalent adsorption sites and in phase 2 they occupy two different adsorption sites.

The DFT derived PDOS at the central benzene ring and at the pyridine end groups of the T4PB molecule within the Cu-T4PB network is shown in Fig. 4.8(b). The pyridine end groups (red spectrum) and the central benzene ring (black spectrum) contribute each to one pronounced peak at energies of 1.2 and 2.05 eV, respectively. Let us now focus on the spatial distribution of the electronic state at 1.2 eV corresponding to a molecular resonance. Figure 4.8(c) shows the simulated PDOS map at an energy of 1.2 eV and a dI/dV map at a sample bias voltage of 1.5 V, respectively. The molecular resonance located at 1.2 eV is mainly localized at the periphery of the pyridine end groups. This finding is in line with the experimentally obtained dI/dV maps of the Cu-T4PB and Cu-T4PT network (see Fig. 4.7(d) and Fig. 4.8(c)).

The alternating change of the LDOS signal in the case of the Cu-T4PT network suggests different molecule-surface interaction and therefore also different electronic structures of the T4PT molecules labeled A and B (see Fig.4.7). To explain the different electronic structure, Fig. 4.9(a) and (b) depict two different adsorption models of the Cu-T4PT metal-organic network on the Cu(111) metal surface. The network architecture can either be determined by the Cu adatom or T4PT adsorption sites, respectively. The coordinated Cu atoms within the Cu-T4PT network can be adsorbed at a top or hollow site of the Cu(111) surface, respectively. The dimensions of both adsorption models shown in Fig. 4.9(a) and (b) are equal, but they are slightly shifted with respect to each other. Assuming that the Cu-T4PT network is commensurate with the Cu(111) surface, both models yield a Cu-N bond length of ≈ 2 Å.
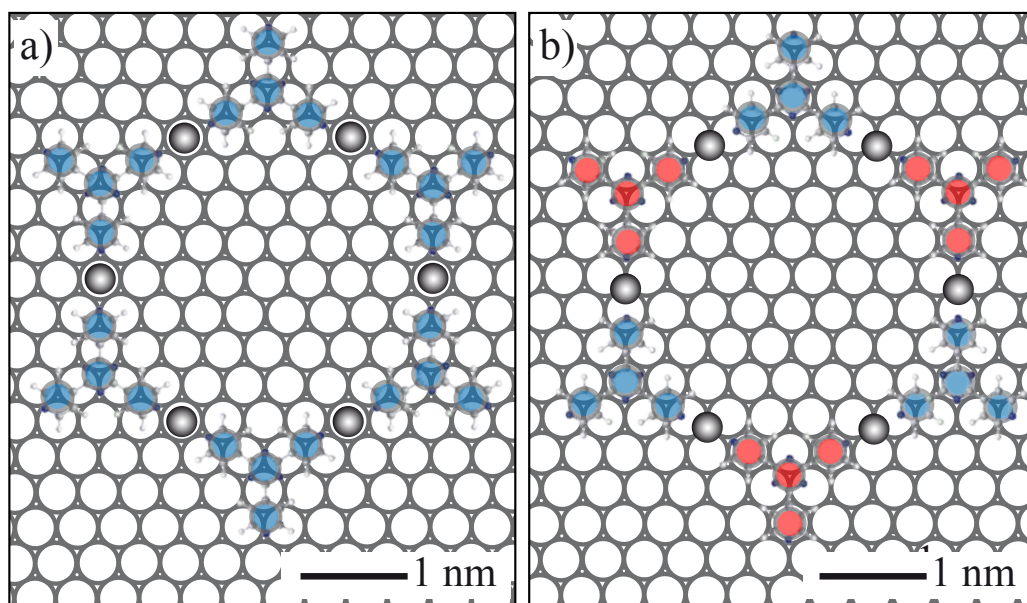
Figure 4.9: Adsorption model of the Cu-T4PT metal-organic network on the Cu(111) surface. (a) The Cu atoms are located at top sites and T4PT molecules occupy identical adsorption sites with respect to the underlying Cu(111) surface. (b) Cu adatoms are adsorbed on hollow-sites, neighboring T4PT molecules occupy different adsorption sites. The adsorption position of the pyridine groups of the T4PT molecules are highlighted in red (pyridine end groups are centered at top sites of the Cu(111) surface) or in blue (pyridine end groups are centered at hollow sites of the Cu(111) surface).

In the adsorption model in Fig. 4.9(a) all pyridine and triazine groups of the T4PT molecules occupy hollow sites (colored blue), whereas the Cu adatoms are localized at top sites. In contrast, the adsorption model for the Cu adatoms occupying hollow sites is depicted in Fig. 4.9(b) and reveals that neighboring T4PT molecules occupy different adsorption sites. The central triazine rings of the blue colored T4PT molecules in Fig. 4.9(b) are localized at top sites of the Cu(111) surface, whereas the triazine ring of the red colored T4PT molecules are adsorbed on hollow sites. However, the most probable phase observed here is the last one. The reasons for that are the following: (i) single Cu adatoms on Cu(111) surface show the tendency to adsorb on hollow sites [254] and (ii) the slightly different electronic structure of neighboring T4PT molecules (type A and B), as revealed by the STS dI/dV spectra and constant current dI/dV maps (cf Fig. 4.7). This suggests different adsorption sites and therefore a different hybridization of the molecules with the underlying Cu(111) metal surface[2].

4.3.1.1 STM Investigation of Cu-T4PT Network on Ag(111)

In order to investigate the role of the surface in the formation of the metal-organic network we subsequently deposited T4PT molecules and Cu atoms on a clean Ag(111) metal surface. Again the formation of the Cu-T4PT metal-organic network is triggered. Figure 4.10(a) shows a large scale

---

[2] Bond formation of triazine nitrogens with Cu adatoms was not observed within this work, which is in line with previous work of triazine on Cu(111) [269]. This can explained by the fact that a coordination bond of the Cu adatom to a single active nitrogen lone-pair at the triazine is sterical hindered by the neighboring hydrogen adatoms of the pyridine end groups (cf Fig. 4.5).
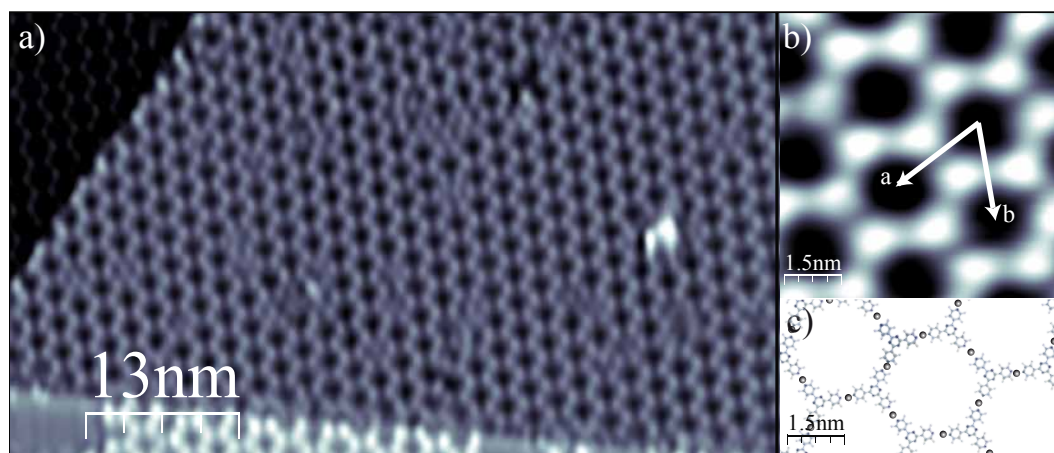
Figure 4.10: STM topography images of the Cu-T4PT nanomesh on Ag(111). (a) Large-scale STM topography image of the coordinated Cu-T4PT islands (I = 10 pA, V_S = -1.0 V). (b) Zoom-in of the Cu-T4PT island revealing a honeycomb-like structure with a two-fold coordination motif of Cu and T4PT (I = 0.45 nA, V_S = -1.5 eV). The arrows labeled "a" and "b" indicate the unit cell vectors with $a = b = 24 \pm 1$ Åenclosing an angle of $60° \pm 1°$. (c) Structure model of the Cu-T4PT nanomesh.

STM topography image of the self-assembled Cu-T4PT metal-organic network. The network also exhibits a two-fold bonding motif leading to a honeycomb-like structure, where each network pore is formed by six T4PT molecules (cf Fig. 4.10(b)). The black arrows in Fig. 4.10(b) indicate the unit cell of the Cu-T4PT network with $a = b = 24 \pm 1$ Å enclosing an angle of $60° \pm 1°$. The structure and also the dimensions of the Cu-T4PT network on both the Ag(111) and the Cu(111) metal surface are very similar. The lattice constant of the Cu(111) (a= 2.56 Å) and Ag(111) surface (a= 2.89 Å) differ about 0.48 Å(a change of 11%-13% of the lattice constant). This indicates the dominant role of the metal ligand interaction on the structural properties and the adaptability of the network regarding different surfaces.

4.3.2   X-ray Absorption and Dichroism Experiments

Further x-ray absorption (XA) and x-ray magnetic circular dichroism (XMCD) measurements are performed to analyze the electronic and magnetic properties of the Cu-T4PT metal-organic network on both the Cu(111) and Ag(111) metal surfaces. The experiments were carried in collaboration with M. Bernien, C. F. Hermanns, A. Krüger, N. Krane, and Z. Yang. XA and XMCD measurements are element specific and allow to probe the atomic species involved in the metal-ligand coordination, i.e. the Cu, N and C atoms. Additional transition potential DFT calculation of the free T4PT and also of the T4PT-(CuH)$_3$-cluster simulate the experimental XA spectra of the free uncoordinated and coordinated T4PT molecules. This allows an assignment of the peaks obtained from XA measurements and to investigate the change of the electronic properties due to the metal-ligand bond formation.

Figure 4.11: Polarization-resolved experimental N (a) and C (b) K-edge XA signal for polarization angles $\phi = 30°$ (near grazing incidence), $\phi = 55°$ (magic angle), and $\phi = 90°$ (normal incidence) of a 0.8 ML T4PT/Cu(111) sample. Polarization-resolved experimental N (c) C (d) K-edge XA spectra of the 15 ML sample. Comparison of the N (e) and C (f) K-edge XA signals of the 15 ML and 0.8 ML T4PT/Cu(111) sample ($\phi = 55°$). The spectra are scaled to match and shifted for clarity.

4.3.2.1 XAS of the Cu-T4PT Network on Cu(111)

Since the metal-coordination involves the Cu atoms and the nitrogen species of the pyridine end groups of the T4PT molecule, we first discuss the N K-edge XA signals. Therefore let us compare the N K-edge XA signal of the 15 ML and 0.8 ML T4PT/Cu(111) samples in Fig. 4.11(a) and (c). Mainly uncoordinated T4PT molecules contribute to the XA signal of the 15 ML of T4PT/Cu(111) sample. Thus we can use this sample as a reference. In the case of the 0.8 ML T4PT/Cu(111) sample all molecules are coordinated. As depicted in the structural model in Fig. 4.5(a) the T4PT molecule contains two nitrogen species labeled N1 and N2, differing by their chemical environment. There are three nitrogen atoms of type N1 and N2, respectively.

Figure 4.11(a) shows the polarization-resolved experimental N K-edge XA signals of the 0.8 ML T4PT/Cu(111) sample. A peak is visible at an energy of 398.8 eV in the π^*-region, followed by

a broad structure in the σ^*-region. The peak in the π^*-region (labeled A) shows a small shoulder at lower binding energies, indicating two different contributions. The intensity of peak A decreases as the incident angle ϕ increases, whereas the broad structure in the σ^*-region shows the opposite behavior (see Fig. 4.11(a)). Since the XA signal becomes largest when maximum amplitude of the probed orbital is parallel to the polarization vector $\vec{e}$ of the incoming x-ray beam, this behavior is typical for molecules adsorbed flat, i.e. with their molecular plane parallel to the surface. This finding agrees with the STM results.

The N K-edge XA signals of the 15 ML T4PT/Cu(111) sample shown in Fig. 4.11(c) reveals also a peak at an energy of 398.8 eV in the π^*-region, followed by a broad structure in the σ^*-region. Different to the 0.8 ML T4PT/Cu(111) sample, the peak in the π^*-region is a single peak. The angle dependence of the N K-edge XA signal of the 15 ML T4PT/Cu(111) sample is very similar to the case of the 0.8 ML T4PT/Cu(111) sample (see Fig. 4.11(c)).

A zoom-in of the π^*-region of the N K-edge XA signal of both the 0.8 ML T4PT/Cu(111) sample and 15 ML T4PT/Cu(111) sample is shown in Figure 4.11(e). It reveals that the 0.8 ML T4PT/Cu(111) sample exhibits a two-peak structure in the π^*-region with a second peak at higher binding energy in contrast to the XA signal of the 15 ML T4PT/Cu(111) sample. These findings suggest that the metal-ligand bond formation between the Cu atoms and the nitrogen of the pyridine end groups is responsible for the second peak in the π^*-region in the case of the 0.8 ML T4PT/Cu(111) sample. With the help of theoretical calculations presented in the following we can decompose the experimental XA signals into its individual contribution corresponding to the different excitation centers.

Figure 4.11(b) depicts the C K-edge XA signal of the 0.8 ML T4PT/Cu(111) sample. Three different peaks (labeled B-D) are visible in the π^*-region and a broad structure in the σ^*-region. Peak B is located at an energy of 286.0 eV followed by Peak C and D at the energies 286.7 eV and 287.6 eV, respectively. The peaks corresponds to the four different carbon species present in the T4PT molecule labeled C1-C4 (cf Fig. 4.5(b)). There are three carbon atoms of type C1 and C2, and six of type C3 and C4, respectively.

The C K-edge XA signals of the 15 ML T4PT/Cu(111) sample shown Figure 4.11(d) are very similar to the case of the of 0.8 ML T4PT/Cu(111) sample. Three peaks are visible π^*-region, followed by a broad structure in the σ^*-region. The angular dependence of the C K-edge XA signal of the 0.8 ML T4PT/Cu(111) sample and the 15 ML T4PT/Cu(111) sample reveal that the peaks B-D decreases with increasing incident angle ϕ, whereas the σ^*-region intensity increases (see Fig 4.11(b) and (d)).

A zoom-in of the π^*-region of the C K-edge XA signal of the 0.8 ML T4PT/Cu(111) and the 15 ML T4PT/Cu(111) sample is depicted in Fig. 4.11(f). The line shape and the position of the spectral features is almost identical. The peaks (B-D) are visible in both spectra. Hence, the formation of the metal-ligand bonds seems to have minor effect on the electronic properties of the carbon atoms of the T4PT molecules within the Cu-T4PT network.

4.3.2.2   XAS of the Cu-T4PT Network on Ag(111)

To investigate the magnetic and electronic properties of the Cu-T4PT network additional XAS measurements of a 0.8 ML and a 20 ML T4PT sample on a Ag(111) metal surface were carried out. The magnetic properties of the Cu-T4PT network can not be investigated on the Cu(111) sample
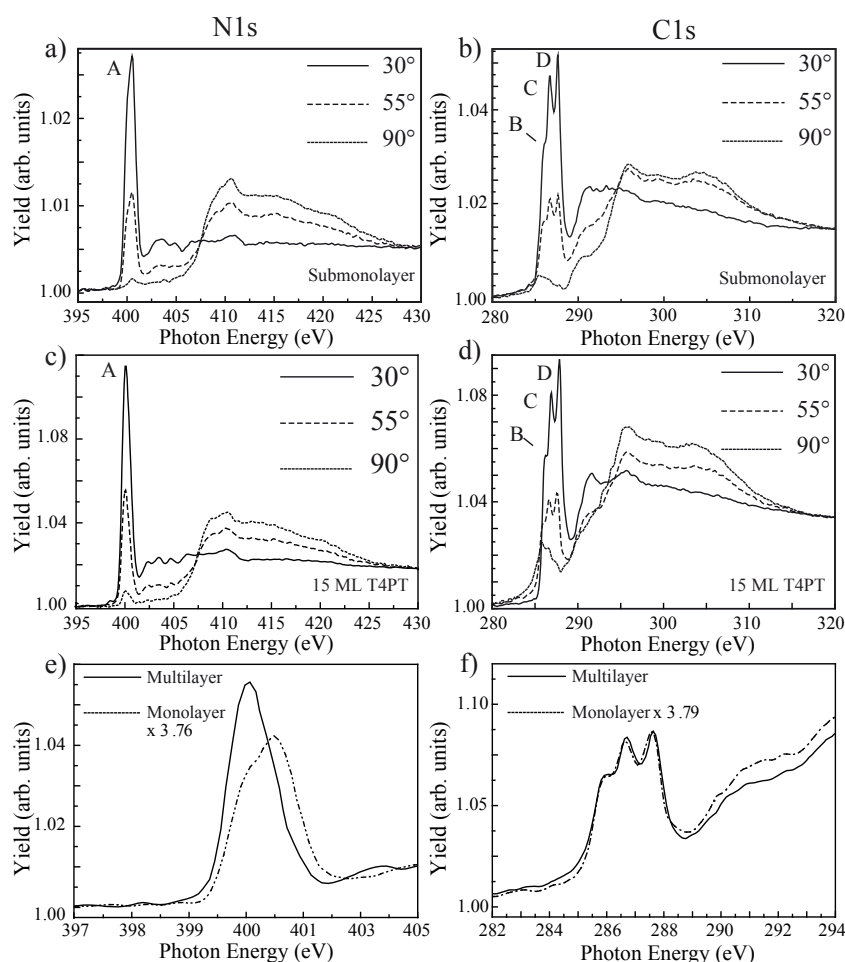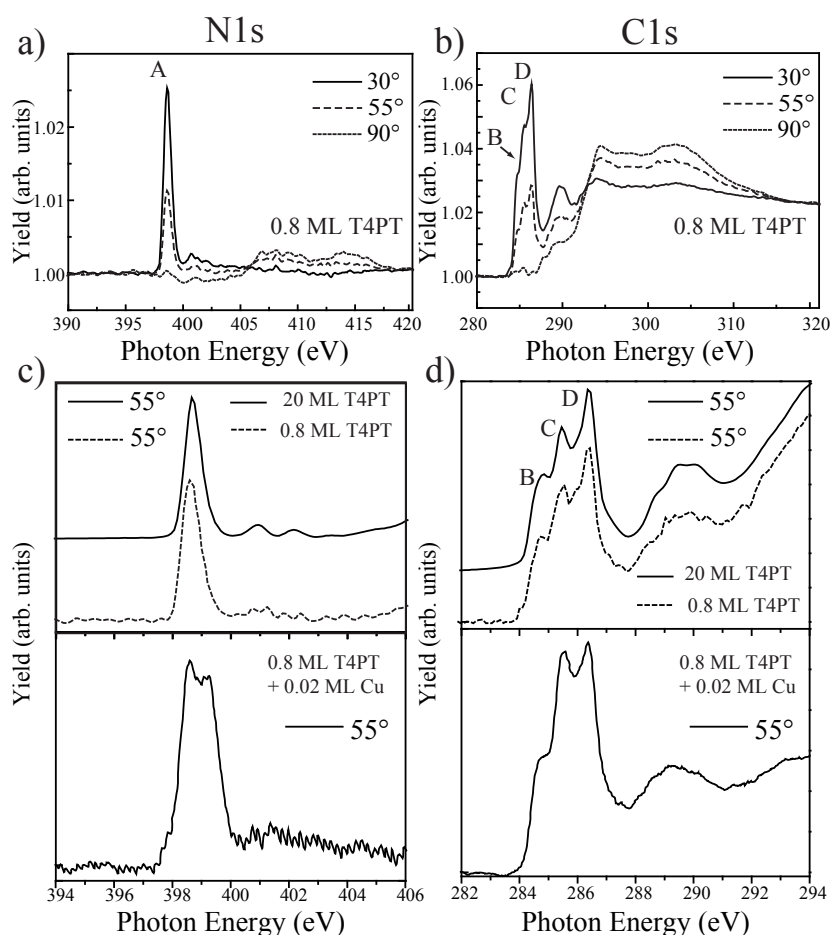
Figure 4.12: Polarization-resolved experimental N (a) and C (b) *K*-edge XA signal for polarization angles $\phi = 30°$ (near grazing incidence), $\phi = 55°$ (magic angle), and $\phi = 90°$ (normal incidence) of a 0.8 ML T4PT/Ag(111) sample. (c) The upper panel shows the experimental N *K*-edge XA signals for a polarization angle $\phi = 55°$ of a 20 ML and the 0.8 ML T4PT/Ag(111) sample, respectively. The spectra are scaled for comparison. The bottom panel of (c) depicts the experimental N *K*-edge XA signal for a polarization angle $\phi = 55°$ of a 0.8 ML T4PT/Ag(111) sample after deposition of 0.02 ML of Cu atoms. (d) The upper panel shows the experimental C *K*-edge XA signals for a polarization angle $\phi = 55°$ of the 20 ML and the 0.8 ML T4PT/Ag(111) sample, respectively. The spectra are scaled for comparison. The bottom panel of (d) depicts the experimental C *K*-edge XA signal for a polarization angle $\phi = 55°$ of a 0.8 ML T4PT/Ag(111) sample after deposition of 0.02 ML of Cu atoms.

by XCMD. But, this is possible on the Ag(111) metal surface. Furthermore, the comparison of the electronic properties of the Cu-T4PT network on the Ag(111) and the Cu(111) surface allows us to explore the role of the metal surface regarding the network properties.

The polarization-resolved N and C K-edge XA signals of 0.8 ML of T4PT on a Ag(111) metal surface for different incident angles at room temperature are shown in Fig. 4.12(a) and (b). The line shape and also the angle dependence is identical compared to the 15 ML T4PT/Cu(111) sample (see Fig. 4.11(b) and (d)).

A comparison of the π^*-region of the N and C K-edge XA signal of a 0.8 ML T4PT/Ag(111) and 20 ML T4PT/Ag(111) sample in the upper panel at an incident angle of $\phi = 55°$ is shown in Fig. 4.12(c). The N K-edge XA signals for both samples is similar, indicating the minor role of the surface regarding the electronic properties of the T4PT molecules. The lower panel in Fig. 4.12(c) shows the π^*-region of the N K-edge XA signal of a 0.8 ML T4PT/Ag(111) sample after subsequent deposition of 0.02 ML of Cu atoms. The formation of coordination bonds between the pyridine nitrogens with the Cu atoms causes a double-peak feature in the π^*-region similar to the N K-edge XA signal of the 0.8 ML T4PT/Cu(111) sample.

The upper panel in Fig. 4.12(d) shows the comparison of the π^*-region of the C K-edge XA signals of the 0.8 ML and 20 ML T4PT/Ag(111) sample at an incident angle of $\phi = 55°$. In total three different peaks (B-D) are present in both cases. The lower panel of Fig. 4.12(d) shows the π^*-region of the C K-edge XA signal of a of the 0.8 ML T4PT/Ag(111) sample upon the deposition of 0.02 ML of Cu atoms. The overall spectral change is rather small as on Cu(111).

The XA results of the Cu-T4PT metal-organic network on both the Cu(111) and the Ag(111) metal surface show very similar spectral features evidencing their resemblance in terms of their structural and electronic structure and confirming the minor role of the underlying surface.

4.3.3 Theoretical Calculations of the Cu-T4PT XA Spectra

To understand the origin of the different peaks in the C and N K-edge XA spectra theoretical DFT calculations have been carried out by Dr. L. Sun and Prof. K. Hermann from the Fritz-Haber-Institut der Max-Planck-Gesellschaft, Berlin, Germany to simulate the experimental spectra of the Cu-T4PT network and the uncoordinated T4PT layer. This allows us to assign the resonances to certain parts of the T4PT molecule and therefore to understand the electronic properties of coordinated and non-coordinated T4PT molecules and the effect of the metal-ligand bond formation. The theoretical calculations of the free T4PT molecule (cf Fig. 4.5(a)) serve as a reference for the sample with uncoordinated T4PT molecules. The building block of the coordinated Cu-T4PT is simulated by the T4PT-(CuH)$_3$ model cluster shown in Fig. 4.5(b). The three H atoms attached to Cu atoms in the T4PT-(CuH)$_3$ cluster are only added to saturate dangling bonds of the Cu atoms in the simulation, which can falsify the calculations. In both cases the T4PT molecules contain two non-equivalent nitrogen atoms labeled N1 and N2 (cf Fig. 4.5(a) and (b)) and four non-equivalent carbon atoms labeled C1-C4.

The geometrical ground state structure of the free T4PT molecule as well of the T4PT-(CuH)$_3$ cluster were obtained by a DFT approach using the cluster code StoBe [270]. We used extended basis sets of contracted Gaussians for the representation of the Kohn-Sham orbitals. The relevant atomic
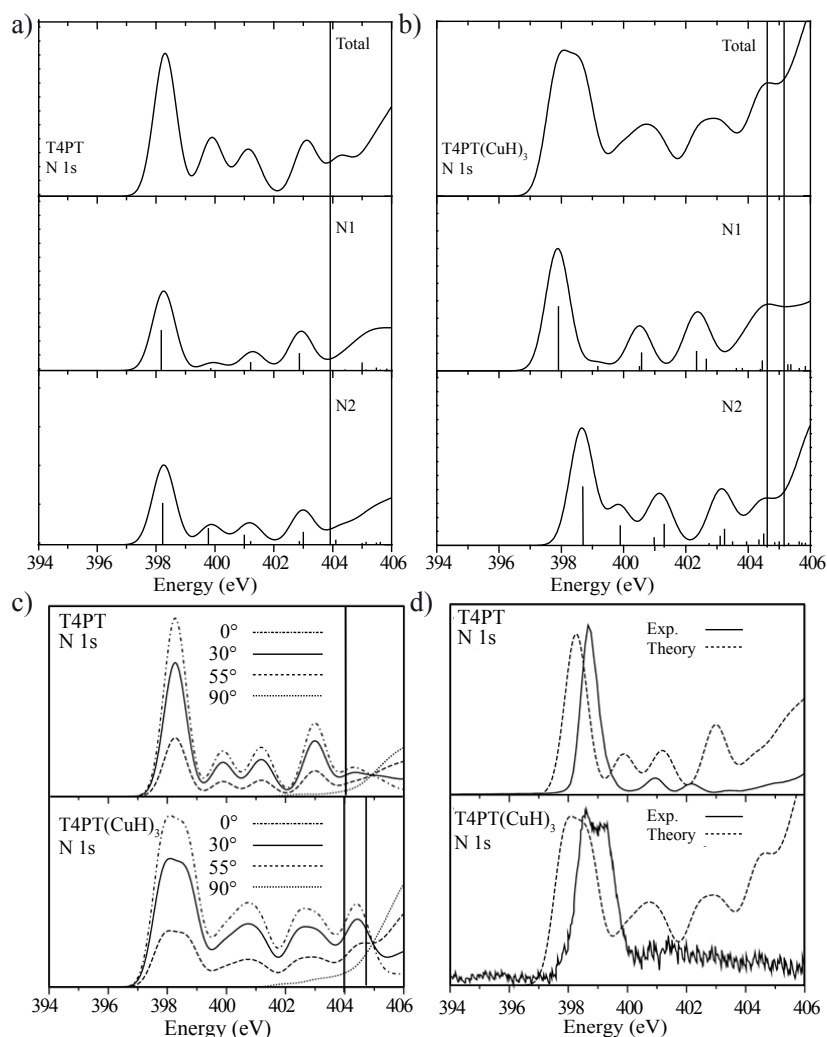
Figure 4.13: (a) Calculated N K-edge XA signals of the free T4PT molecule. The upper panel shows the total spectrum. The middle and bottom panel depict the decomposition of the total spectrum into contributions due to excitations at the nitrogen centers N1 and N2. The vertical lines close to 404 eV in (a), (b) and (c) indicate the ionization thresholds. The small vertical strokes in (a) and (b) show the discrete excitations obtained in the calculations with their lengths denoting the excitation probabilities. (b) Theoretical N K-edge XA signals of the T4PT-$(CuH)_3$ cluster. The total spectrum is shown in the top panel of (b). The decomposition of the total spectrum into contributions due to excitations at the nitrogen centers are shown for N1 nitrogen (middle panel) and the N2 species (bottom panel). (c) Theoretical polarization-resolved N K-edge XA signals for polarization angles ϕ = 0°, ϕ = 30°, ϕ = 55°, and ϕ = 90° of the T4PT molecule (top panel) and the T4PT-$(CuH)_3$ cluster (bottom panel). (d) Polarization angle integrated N K-edge XA signals (ϕ = 55°), comparison of theory with experiment. The upper panel shows a comparison of the spectrum of the T4PT molecule (theory) with data from a 20 ML T4PT/Ag(111) sample (experiment). The lower panel depicts a comparison of the spectrum for the T4PT-$(CuH)_3$ model cluster with data from a Ag(111) sample with 0.02 ML of Cu atoms and 0.8 ML of T4PT molecules.

bond distances (Å)		
	T4PT	T4PT-(CuH)$_3$
Cu-N2		1.945
N1-C1	1.353	1.355
N2-C4	1.353	1.366
C1-C2	1.500	1.495
C2-C3	1.408	1.412
C3-C4	1.404	1.395
Cu-H		1.505

Table 4.2:   The bond lengths of the free gas-phase T4PT molecule and the T4PT-(CuH)$_3$ cluster as obtained from the theoretical DFT calculations.

species (Cu, N, C, H) were represented by all-electron double-zeta-valence-plus-polarization (DZVP) basis sets. Also the gradient corrected revised Perdew-Burke-Ernzerhof (RPBE) exchange-correlation functional [271, 272] is used in our calculations. A detailed description of the theoretical framework can be found in the appendix A.2.

Table 4.2 lists the bond distances of both the relaxed free T4PT molecule and the T4PT-(CuH)$_3$ cluster as obtained from the theoretical DFT calculations. The formation of metal-ligand bonds between the nitrogen atoms of the pyridine end groups and Cu atoms has a rather small effect on the rest of the T4PT intermolecular bonds. The DFT calculation yields Cu-N bond length of 1.945 Å, which is in line with experimentally obtained value of 2 Å.

Let us first compare the theoretical and experimental XA signals in the case of the N K-edge of the free T4PT molecule (cf Fig. 4.13(a) and (c)). The upper panel in Fig. 4.13(a) depicts the total (polarization angle integrated) theoretical N K-edge XA signal of the free T4PT molecule. The calculation reveal that the total N K-edge XA signal of the T4PT molecule can be explained as the sum of two spectra with varying excitation centers, the triazine nitrogen species N1 and the pyridine nitrogen species N2. The middle and lower panel show the decomposition of the total spectrum into contributions of the nitrogen excitations centers N1 and N2. Both nitrogen species N1 and N2 have a spectral contribution to the peak at an energy 398.3 eV in the π^*-region of the N K-edge XA spectrum. This does not allow for an experimental distinction. This finding suggests that the chemical state of N in pyridine and triazine is very similar (cf Fig. 4.5(a)).

The formation of the metal-ligand bond between the Cu atoms with the T4PT molecules should have an effect on the line shape and peak positions of the N K-edge XA signal of the T4PT nitrogen species (N1 and N2). We simulated the building block of the coordinated Cu-T4PT network by a T4PT-(CuH)$_3$ model cluster. The theoretical N K-edge XA signal of the T4PT-(CuH)$_3$ cluster is shown in Fig. 4.13(b). Contrary to the case of the uncoordinated T4PT the total (polarization angle integrated) theoretical N K-edge XA signal of the T4PT-(CuH)$_3$ cluster shows double peak feature in the π^*-region. The decomposition of the total spectrum into the contributions stemming from the N1 and N2 excitation centers shown in the middle and the lower panel of Fig. 4.13(b) reveals a significant shift of the contribution of the pyridine nitrogens (N2) to higher binding energies (398.6 eV). Whereas the contribution of the triazine nitrogen shifts slightly to lower binding energies (397.9 eV).

The angle dependence of the theoretical polarization-resolved N K-edge XA signals of the free T4PT

molecule and the T4PT-$(CuH)_3$ cluster are shown in Fig. 4.13(c). In both cases the theoretical calculations reproduce the experimentally observed angle dependence of N K-edge XA signals. A direct comparison of the experimental and theoretical π^*-region of the N K-edge XA signals is shown Fig. 4.13(d) for the polarization angle $\phi = 55°$. The line shape of the XA signal is well reproduced and confirm the shift of the XAS contribution of the pyridine and triazine nitrogens upon coordination of the pyridine nitrogen atoms with the Cu atoms. The total amplitude of peak A in the π^*-region decreases, since a part of its intensity is shifted to higher photon energy.

Table 4.3 shows a Bader charge analysis of the free T4PT and the T4PT-$(CuH)_3$ cluster in order to check for possible charge transfer between the Cu atoms and the T4PT molecules. The T4PT molecule within the T4PT-$(CuH)_3$ cluster gains a total charge of $\rho = 0.03$ e$^-$ due to the metal-ligand interaction with the Cu atoms. The negligible charge transfer is in agreement with the DFT simulation of a similar metal organic network on Cu(111) [265]. The bonding of metal-ligand complexes can be described in the framework of molecular orbital theory (MOT). The driving force is the overlap of valence metal and ligand orbitals, respectively, leading to the formation of bonding and anti-bonding orbitals. In the case of Cu transition metal species these are the $3d$, $4s$, and $4p$ valence orbitals and for the T4PT molecule σ-like and π-like orbitals. The orbital overlap can imply a charge transfer from T4PT to the Cu metal atom or vice versa. For example, the overlap of an empty metal Cu s-states with an occupied T4PT σ orbital can lead to a charge transfer to the Cu metal atom. On the other hand, the overlap a Cu occupied d state with an unoccupied T4PT orbital, for example a π^* orbital, can also cause a charge transfer back to the T4PT molecule. The charge transfer from the T4PT back to the Cu metal atom is known as π back donation [273–275]. Both can happen simultaneously and in synergy. The transition of a pure ionic to a pure covalent character of the metal-ligand bond is therefore continuous and depends on all charge transfer processes. In general the $3d$, $4s$, and $4p$ orbitals of the transition metal atom form hybrid orbitals leading to polyhedral coordination geometries [273].

In the case of the Cu-T4PT layer, the T4PT N atoms exhibit lone-pair electrons. The overlap of empty valence Cu states and occupied N σ orbitals presumably triggers the formation of a metal-ligand bond, which can involve a charge transfer from the N to the Cu atoms. However, the small total charge transfer between the T4PT and the Cu, as revealed by the DFT simulations, indicates that back donation processes into unoccupied T4PT orbitals also take place. As shown later, the Cu atoms within the Cu-T4PT network exhibit a completely filled d shell (d^{10}). The bonding to the T4PT N atoms is mainly driven by the s and p orbitals, causing a linear bonding motifs [273] (the angle between the two pyridine-Cu bonds is about 180° (as can be seen in Fig. 4.9)). In the case that also d electrons are involved in the metal-ligand bond formation, bonding motifs with higher symmetry can be observed [273] (shown in section 4.4).

The experimentally and theoretically observed shift of the peaks in the π^*-region of N K-edge XA signals can be attributed to metal-ligand interactions leading to a shift of the triazine and pyridine contributions to lower and higher binding energies, respectively. The energetic shift to higher binding energies can originate from a decrease of the electron density at the core of the pyridine nitrogens or a shift of the LUMO+x to higher binding energies. The former agrees with the simple picture of bond formation. This corresponds to a charge redistribution and the electrons, which are not involved in the bond formation, are pulled away from the nitrogen core due to the Cu-N metal-ligand bond.

Figure 4.14 shows the experimental and calculated C K-edge XA signals of the free T4PT molecule
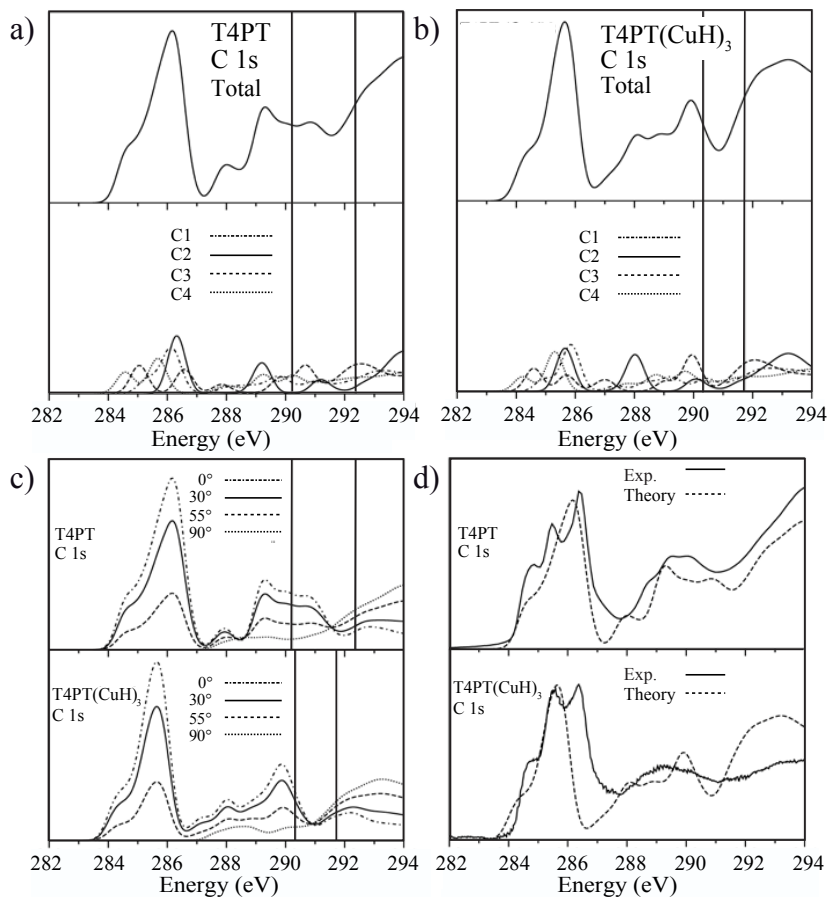
Figure 4.14: (a) Theoretical C K-edge XA signals of the free T4PT molecule. The top panel shows the total spectrum. The bottom panel depicts the decomposition of the total spectrum into contributions due to excitations at the carbon centers C1 to C4. The vertical lines in (a),(b) and (c) between 290 eV and 292 eV indicate the range of ionization thresholds for the different carbon species. (b) Theoretical C K-edge XA signals of the T4PT-(CuH)$_3$ cluster. Total spectrum (top panel) and the decomposition of the total spectrum into contributions due to excitations at the carbon centers C1 to C4 (bottom panel). (c) Theoretical polarization resolved C K-edge XA signals for polarization angles $\phi = 0°$, $\phi = 30°$, $\phi = 55°$, and $\phi = 90°$ of the free T4PT molecule (top panel) and the T4PT-(CuH)$_3$ cluster (bottom panel). The vertical lines near 290 and 292 eV indicates the range of ionization thresholds for the different carbon species. (d) Polarization angle integrated C K-edge XA signal ($\phi = 55°$), comparison of theory with experiment. The top panel shows a comparison of the spectrum for free T4PT (theory) with data from 20 ML T4PT/Ag(111) sample (experiment) and the bottom panel a comparison of the spectrum for the T4PT-(CuH)$_3$ model cluster with data from a Ag(111) sample with 0.02 ML of Cu atoms and 0.8 ML of T4PT molecules.

| | **Bader charges** | |
	T4PT	T4PT-(CuH)$_3$
Cu		28.6786
N1	8.0429	8.0458
N2	8.0430	8.1002
C1	5.0232	5.0190
C2	5.9873	5.9929
C3	5.9895	5.9913
C4	5.4626	5.4836
Outer H		1.3304
Inner T4PT		0.03

Table 4.3: The Bader charges of the free gas-phase T4PT molecule and the T4PT-(CuH)$_3$ cluster as obtained from the theoretical DFT calculations.

and the T4PT-(CuH)$_3$ cluster. The total (polarization angle integrated) theoretical C K-edge XA signals of the free gas-phase T4PT molecule is depicted in the upper panel of Fig. 4.14(a). The decomposition of the total C K-edge XA signal reveals that it consist of several contributions of the different C1, C2, C3, and C4 excitation centers. Each carbon species C1-C3 exhibits two contribution in π^*-region of the C K-edge XA signal, which are shifted to higher binding energies by going from C1 to C3. The single peak at an energy of 286.3 eV π^*-region originates from the carbon species C4. The energetic shift of the peak positions of the different carbon species is well understood in terms of the chemical environment. Only the carbon species C4 has two nitrogen neighbors. Due to the electronegativity of the nitrogen species the local charge density of the carbon is displaced towards the neighboring nitrogen atom resulting in net positive charge at the carbon. Hence the carbon core-level energy is shifted to higher binding energies.

The total (polarization angle integrated) theoretical C K-edge XA signal of the T4PT-(CuH)$_3$ cluster is shown in Figure 4.14(b), which is similar in terms of line shape and peak positions to the theoretical C K-edge XA signal of the free T4PT molecule (depicted in Fig. 4.14(a)) it shows that the formation of the Cu-N metal-ligand bond has only a small effect on the electronic structure of the carbon atoms of the T4PT molecule. The decomposition of the total theoretical C K-edge XA signal into the contributions of the individual carbon species (C1-C4) shows that the intensities and energetic positions of the individual peaks are shifted. The theoretical polarization-resolved C K-edge XA signals of the free T4PT and T4PT-(CuH)$_3$ cluster are depicted in the upper and lower panel in Fig 4.14(c). The theoretically obtained angle dependence of the C K-edge XA signals agrees well with experimental date(cf Fig. 4.12(b) and Fig. 4.11(b)). The comparison of the experimental and theoretical C K-edge XA signals for the polarization angle $\phi = 55°$ of the free T4PT molecule and the T4PT-(CuH)$_3$ cluster is shown in the upper and lower panel in Fig 4.14(d), respectively. In both cases the overall line shape of the π^*-region and σ^*-region is well reproduced by the theoretical calculations. In the case of the experimental C K-edge XA signals of the T4PT-(CuH)$_3$ cluster there is an additional peak in the π^*-region, which is not reproduced by the theoretical calculations. Hence, some of the individual contributions of the carbon excitation centers are over- or underestimated.
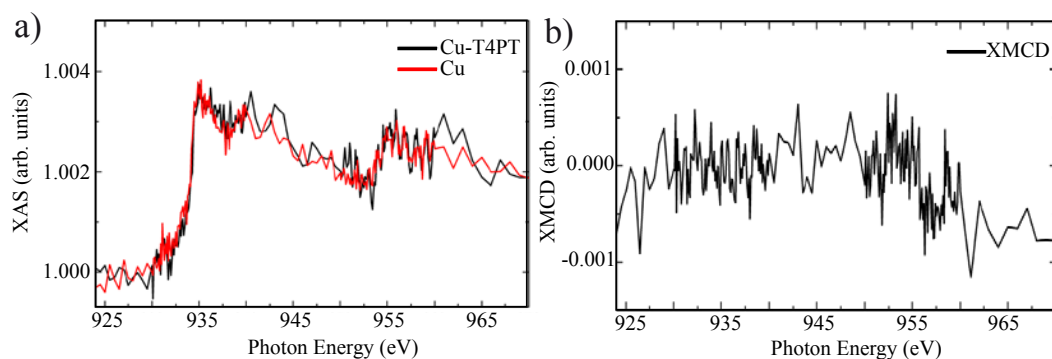
Figure 4.15: (a) Cu $L_{2,3}$ XAS spectra of 0.8 ML of T4PT on Ag(111) after deposition of 0.02 ML of Cu atoms (black line) and of 0.1 ML of Cu atoms on Ag(111) (red line) measured at ϕ=30° grazing incidence at $T = 10$ K in an applied magnetic field of 5 T. The latter is scaled by a factor of 0.23. (b) Cu $L_{2,3}$ XMCD spectra of 0.8 ML of T4PT on Ag(111) after deposition of 0.02 ML of Cu measured at 30° grazing incidence at $T = 10$ K and $B = 5$ T.

4.3.4 Magnetic Properties of the Cu-T4PT Network

Finally we rise the question of the magnetic moments of the Cu atoms within the Cu-T4PT network. We used L-edge XAS at the Cu $L_{2,3}$ edges to investigate the magnetic properties of the coordinated Cu atoms within the Cu-T4PT network on a Ag(111) metal surface. The Cu $L_{2,3}$ XA signals of a 0.8 ML T4PT/Ag(111) sample after deposition of 0.02 ML of Cu atoms (black line) and of 0.1 ML of Cu atoms on a clean Ag(111) metal surface (red line) measured at $\phi = 30°$ grazing incidence at a temperature of $T = 10$ K and in an external magnetic field of $B = 5$ T are shown in Fig. 4.15(a) (the later is scaled by a factor of 0.23 for better comparison). The XA signal of the 0.8 ML T4PT/Ag(111) sample after deposition of 0.02 ML of Cu atoms (black line) reveals a step-like feature, which corresponds to the onset of transition into unoccupied s, p-states. No peak stemming from d-states can be observed. Hence, the Cu atoms reside in a d^{10} state within the Cu-T4PT network. The XA signal of 0.1 ML of Cu atoms on the clean Ag(111) sample (red line) without T4PT molecules also shows the same step-like feature and no d-derived peak. The observed Cu $L_{2,3}$ XAS spectra are almost identical to the ones of pristine Cu metal spectra [276, 277]. The XMCD difference signal of 0.8 ML of T4PT on Ag(111) after deposition of 0.02 ML of Cu atoms measured at 30° grazing incidence at $T = 10$ K and $B = 5$ T shown in Fig. 4.15(b). There is no XMCD signal within the noise level, further confirming that the Cu atoms within the Cu-T4PT network are in a d^{10} state with no magnetic moment. These findings support that the Cu atoms within the Cu-T4PT network stay in d^{10} state and the bonding of the network is mainly driven by the s and p states of the Cu atoms as discussed above.

4.3.5 Conclusions

In conclusion, the growth of the Cu-T4PT network on different metal surfaces has been investigated. T4PT molecules and Cu atoms form a honeycomb-like metal-organic network on both the Cu(111) and the Ag(111) surface. The Cu-T4PT network shows a two-fold bonding motif, where two neighboring pyridine end groups are linked by central Cu atoms. The identical architecture of the Cu-T4PT network on both surfaces indicates that the network architecture is ruled by the Cu-pyridine metal-

ligand bonds. The interaction with the underlying metal surfaces seems to play only a minor role.

A combined approach of XAS and DFT calculations reveal that the π^* resonance of the pyridine and triazine nitrogen species in the case of uncoordinated T4PT are located at the same energy. The coordination to Cu atoms leads to an energetic shift of both π^* resonances. The analysis of this effect allows to monitor the metal-ligand bond formation.

Interestingly, the Cu-pyridine bond formation is accompanied by a rather small charge transfer of only 0.03 e^-. This finding can be understood in terms of σ-donor and π-backbonding interactions between the Cu atoms and T4PT pyridine end groups. Moreover, the remaining atomic species of the T4PT molecule are only slightly affected by the metal-ligand bond formation in terms of their electronic and structural properties as revealed by the DFT simulations and XA measurements.

The magnetic state of the coordinated Cu atoms were investigated by XMCD and XAS of the Cu $L_{2,3}$ edges. Both measurements reveal that the Cu atoms within the Cu-T4PT network have no magnetic moment since they are in a d^{10} state. In this prospect, the Cu-T4PT network represents a robust supramolecular architecture allowing the controlled patterning of different metal surfaces.

An intriguing question is, if we may induce magnetic properties to the network, for example, by changing the transition metal atom, to Fe, Ni, or Co atoms for instance. This is the topic of the following section.

4.4   Ferromagnetic Order in the Fe-T4PT Metal-Organic Network

In this section we use Fe atoms as magnetic centers and combine them with 2,4,6-Tris(4-pyridyl)-1,3,5-triazine (T4PT) molecules. Since Fe atoms, contrary to the case of Cu, have a net magnetic moment, we expect to obtain a spin array in this metal organic complex.

Recently, *Khajetoorians* et al. [13] and *Loth* et al. [11] showed how magnetic exchange interactions can stabilize small arrays of $3d$ transition metal atoms in a ferromagnetic or an antiferromagnetic ground state, respectively. In general, a number of magnetic interactions can lead to a magnetically ordered ground state such as dipole-dipole interactions, superexchange, direct wave function overlap or surface mediated RKKY interactions [278, 279]. It has also been shown that the interaction of the adsorbed metal atoms with the underlying metal surface can lead to a screening of the unpaired spin due to hybridization with the electronic states of the surface, known as the Kondo effect [99, 168]. The corresponding ground state is a spin-singlet, thus the spin is efficiently screened [156]. We may also have magnetic anisotropies induced by the adsorption site [258] or site-dependent magnetic properties [249]. Furthermore, the precise arrangement of the metal atoms and the number of nearest neighbors can have a significant impact on the magnetic ground state [280].

An intrigued question arises, if we may be able to stabilize an ordered magnetic ground state in a metal-organic monolayer.

4.4.1   Structure of the Fe-T4PT Metal-Organic Network

Subsequent deposition of T4PT molecules and Fe atoms on atomically clean Au(111) single crystal lead to the formation of self-assembled and ordered Fe-T4PT islands. The chemical structure and the DFT derived molecular orbitals of the T4PT molecule are shown in Fig. 4.16(a-c), respectively. The high degree of order of the Fe-T4PT islands implies a high tendency of the T4PT functional groups to form metal-ligand bonds with the Fe atoms as revealed by large-scale STM images. The presence of the unperturbed Au(111) herringbone reconstruction indicates a weak interaction of the molecular layer with the substrate (cf 4.17(a)). A zoom-in of the Fe-T4PT island taken at sample bias voltage of 0.4 V is shown in Fig. 4.17(b). The shape of T4PT molecular skeleton is resolved implying that each pyridine end group participates in three-fold bonding node. The present bonding motif is only stable if the repulsive interaction of the electrophilic pyridine end groups is overcome by a Fe atom bonding

Figure 4.16:   (a) Molecular structure of 2,4,6-Tris(4-pyridyl)-1,3,5-triazine (T4PT). DFT simulation of the degenerated LUMO (b) and HOMO (c) of the T4PT molecules using the B3LYP functional and the 3-21G basis set. The isocontour was set to 0.005.
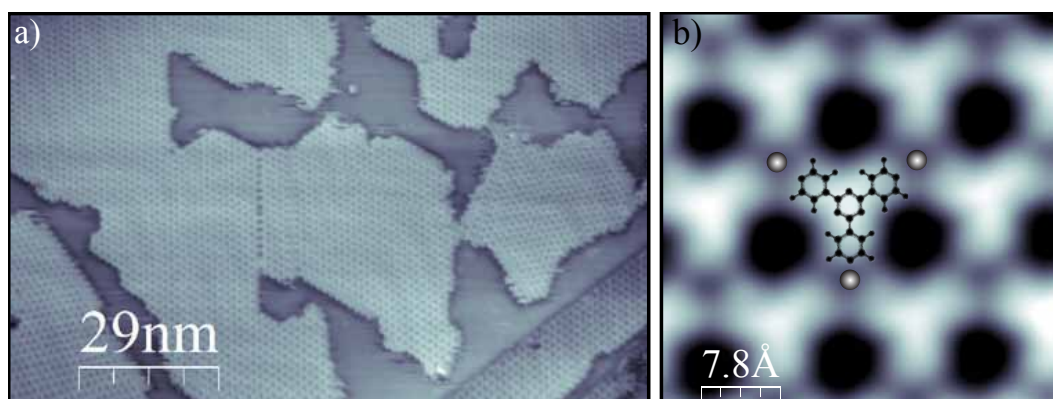
Figure 4.17: (a) Large scale STM topography image of the self-assembled Fe-T4PT islands on the Au(111) surface (I_T = 253 pA V_S = -1.5 V). The Fe-T4PT islands are homogeneous over the entire surface without indication of Fe clusters. The STM topographic image was obtained with a room temperature STM at the ID08 beamline at the European Synchrotron Radiation Facility (ESRF) directly before x-ray investigations. (b) Zoom-in STM image of the Fe-T4PT metal-organic network (I_T = 230 pA, V_S = 0.4 V). STM image processing with WSxM [111].

to each nitrogen lone pair of the pyridine end groups [28, 267]. Hence, we anticipate the formation of a three-fold bonding motif formed by three pyridine end groups and a central Fe atom. This is different to the two-fold bonding node in the case of Cu-T4PT network discussed in the previous chapter 4.3.

An intriguing finding is that the STM topography of the Fe-T4PT network depends strongly on the applied sample bias voltage. Figures 4.18(a-c) show peculiar changes of the STM contrast of a Fe-T4PT island at the sample bias voltages of 0.1, 1.0, and 3.5 V. At a sample bias voltage of 0.1 V the Fe-T4PT network reveals a three-fold coordination symmetry (cf Fig. 4.18(a)). Imaging the same Fe-T4PT island at a higher sample bias voltage of 1.0 V leads to a complete change of the molecular orientation and the network symmetry as shown Fig. 4.18(b) (indicated by the black and orange colored triangles, respectively). Now triangular shaped features consisting of three distinct protrusions can be observed, which can be related to the different pyridine end groups. In particular, the pyridine end groups are now pointing towards the centers of neighboring T4PT molecules (indicated by the orange triangles), which is in contrast to the structure of the Fe-T4PT layer at low sample bias voltage (cf Fig. 4.18(a)). By superimposing the structural model of the Fe-T4PT layer obtained at low bias voltages (cf Fig. 4.18(a)) onto the image in Fig. 4.18(b) we see that the central T4PT triazine ring is now centered at the Fe sites. The red dots in Fig 4.18 (a-c) depict the location of the Fe atoms within the Fe-T4PT island.

In order to clarify the occurrence of the different symmetries we have a closer look at Figures 4.18 (a) and (b). These STM images show a domain boundary indicated by the white dashed lines, where a change of symmetry of the T4PT molecules can be observed. Figure 4.18(a) depicts an STM image at low sample bias voltage, where all molecules show a triangular shape and the same orientation. On the right hand side of Fig. 4.18(b) taken at a sample bias voltage of 1.0 V all T4PT molecules are pointing upwards, whereas on the left hand side all T4PT molecules are pointing downwards (indicated by the orange triangles). The STM contrast shown in Fig 4.18(b) is visible in bias window between 0.75-2.8 V.
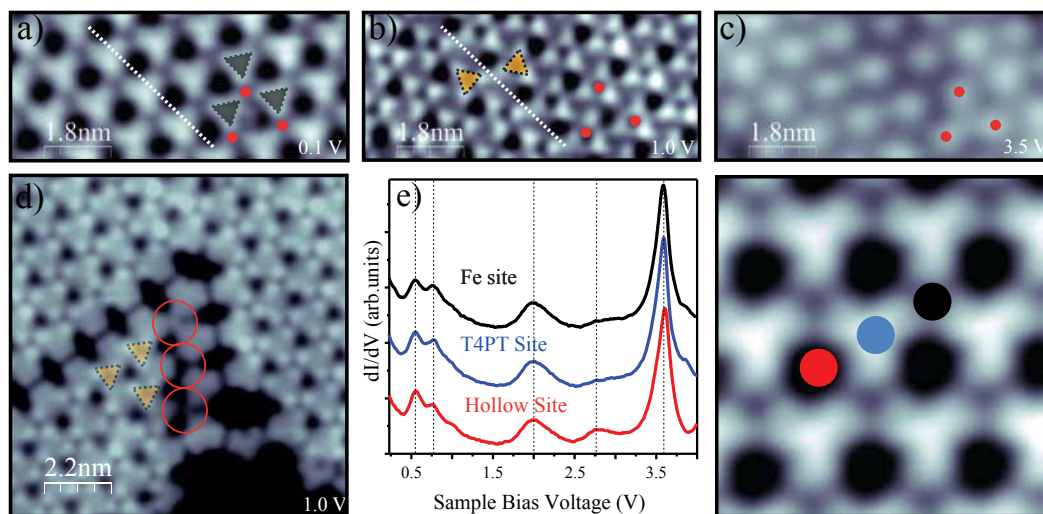
Figure 4.18:   Bias dependence of the Fe-T4PT network. (a-c) STM topography images of the Fe-T4PT network at different sample bias voltages V_S = 0.1, 1.0, and 3.5 V and I_T = 0.5 nA. Panel (a) shows the threefold-coordinated Fe-T4PT network. Three pyridine groups and one Fe form a threefold bonding node. The increase of the sample bias voltage leads to a change of the STM contrast and also of the orientation and symmetry of the features. The white dashed lines in panels (a) and (b) indicate a change of orientation of the second layer T4PT molecules. This change is not observable in the first layer (cf panel (a)). The black and orange triangles indicate the orientation of the first layer and second layer T4PT molecules, respectively. The red dots illustrate the adsorption sites of the Fe atoms within the Fe-T4PT island. (d) STM topography image of a Fe-T4PT island showing missing second layer T4PT molecules at the edges of the T4PT island (indicated by the red circles) (I_T = 0.36 nA, V_T = 1 V). (e) STS dI/dV spectra at different sites of the Fe-T4PT network. All dI/dV spectra show several resonances at 0.5 V, 2.0 V, 2.8 V, and 3.5 V (I_T = 0.5 nA, V_{ac} =13 mV rms at 853 Hz).

The presence of different molecular orientations and symmetries lead to the conclusion that the Fe-T4PT metal-organic network consists of two layers. In the first (bottom) layer we have the Fe atoms bond to pyridine end groups of three T4PT molecules as shown in Figure 4.19(a). A triazine ring of an additional T4PT molecule is located directly on top of each Fe atom originating the second layer (top), as shown in Fig. 4.19(b). A possible scenario is that the bonding of the second layer T4PT molecules is based on the three triazine nitrogen atoms forming bonds to the Fe metal atom. On the other hand the bonding can also be mediated by cation-π-interactions [281–284]. Changing the central part of the T4PT molecule from triazine to benzene can help to answer this question. This is done in following section 4.5. Furthermore the second layer T4PT molecules are slightly tilted about 29° with respect to the first layer T4PT molecules (see Fig.4.19(b)) leading to an overlap of the nitrogen atoms of the pyridine end groups of second layer T4PT and the hydrogen atom of first layer T4PT molecules. Therefore the bonding configuration of the second layer T4PT molecules is maybe further stabilized by additional π-π or H-π interactions [285, 286].

The Fe atoms are embedded in a three-dimensional coordination cavity encaged by three nitrogen atoms of the neighboring first layer T4PT molecules and an additional triazine ring of the second layer T4PT molecule. The three-dimensional coordination cavity probably leads to upward displacement

of the Fe atom [267, 287, 288]. The complex bonding motif is presumably based on Fe d states participating in the metal-ligand bond formation [273] leading to a completely different network architecture compared to the Cu-T4PT network discussed in the previous section 4.3. The Cu-T4PT and the Fe-T4PT system reveal a complex interplay of the valence orbitals of both the metal atoms and the organic linkers regarding the resulting coordination motif of the network.

The above observed bias dependence of the two layers and the disappearance of the layer at certain bias voltages can be explained in terms of localized electronic states (cf Fig. 4.19(c)). The first T4PT molecular layer is in direct contact with the underlying Au(111) metal surface implying a certain hybridization of the related molecular electronic states. In contrast, the second T4PT molecular layer is centered at the Fe sites and is more decoupled from the surface localizing more the corresponding molecular electronic states, which are then poorly screened (cf Fig. 4.19(c)). The second layer becomes transparent for the tunneling electrons at low sample bias voltages [289, 290], where only the first layer T4PT molecules are visible.

Figure 4.18(d) shows a STM topography image of a Fe-T4PT island recorded at a sample bias voltage of 1.0 V. The orange triangles indicate the orientation of the second layer T4PT molecules, which show the typical three protrusions of each T4PT molecule. Interestingly, the STM contrast at the edges of the Fe-T4PT island is strikingly different as indicated by the red circles. Here the three-fold bonding motif of the first layer molecules is clearly visible as it is the case for STM topography images recorded at low sample bias voltages (cf Fig. 4.18(a)) and indicates the absence of the second layer T4PT molecules at these sites.

Figure 4.18(c) shows the STM contrast at a higher sample bias voltage of 3.5 V and again a change of the appearance of the Fe-T4PT network can be observed. Bright protrusions at the positions of Fe sites appear (cf Fig. 4.18(c)). Figure 4.18(e) depicts dI/dV spectra at several different positions of the network indicated by the colored dots in the STM topography on the right side of Fig. 4.18(e). All spectra show several resonances at 0.5, 2.0, 2.8, and 3.5 V (cf Fig. 4.18(e)), which seem to be delocalized throughout the Fe-T4PT. One possible explanation for the bright protrusions at the position of the Fe atoms (cf Fig. 4.18) is that they originate from coordinated Fe d-states [59, 267]. This is sustained by the pronounced resonance in the dI/dV spectra at 3.5 V at these sites. However, as revealed by the dI/dV spectra the resonance is delocalized in the Fe-T4PT layer, which contradicts this assumption. Another explanation is the charging of the second layer T4PT molecules, which in general also manifests as sharp resonance in the dI/dV spectra [25, 291, 292]. Only a detailed analysis of the resonance including dI/dV mapping [25, 291, 292] can verify this assumption.

The complex coordination configuration of the Fe-T4PT network could help to minimize the hybridization of the electronic states of the Fe atoms with the underlying Au(111) surface preventing the quenching or screening of the magnetic moments [99, 168]. To elucidate the magnetic properties of the Fe-T4PT we performed XCMD measurements discussed in the following section. The XAS and XMCD experiments were carried in collaboration with M. Bernien, C. F. Hermanns, and A. Krüger.

4.4.2 Magnetic Properties of the Fe-T4PT Network

We performed XAS and XMCD measurements at T= 8 K in an external magnetic field up to 5 T in order to investigate the magnetic properties of the Fe atoms within the Fe-T4PT metal-organic net-
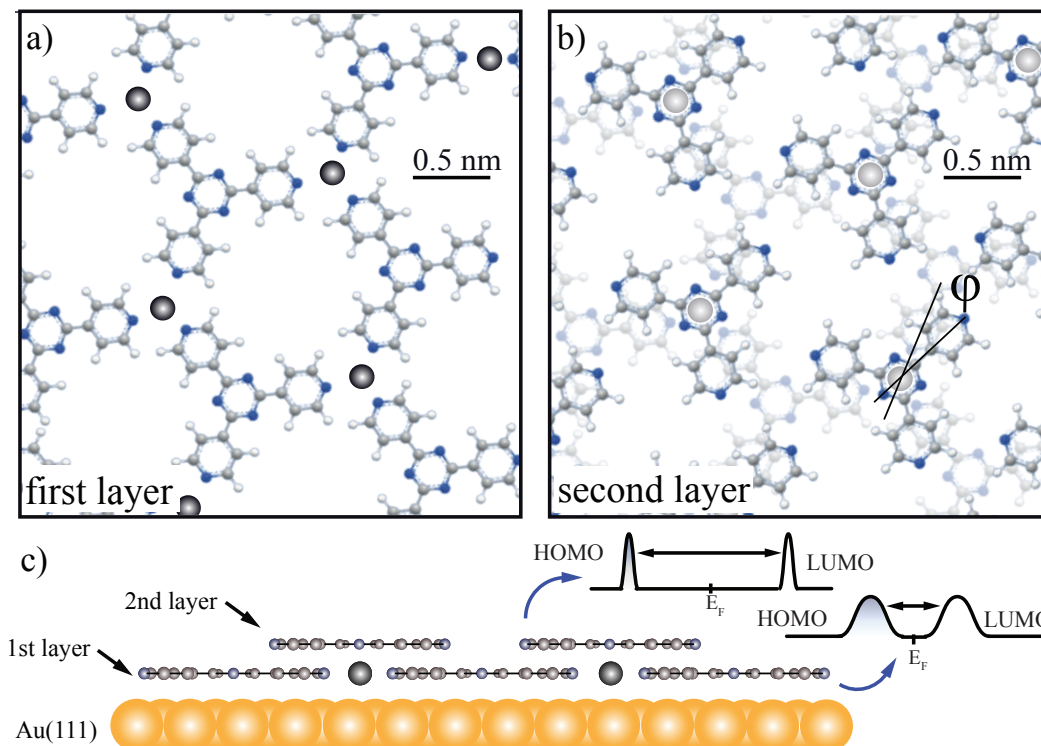
Figure 4.19: (a) Structure of the first layer of the Fe-T4PT network. Fe atoms are three-fold coordinated by three T4PT molecules in the first layer. (b) In the second layer T4PT molecules are centered at the Fe sites and are rotated about $\gamma = 29°$ with respect to the first layer molecules (indicated by the black lines). (c) Schematic diagram of the Fe-T4PT network and the electronic structure of the first and second layer T4PT molecules (right hand side).

work. Figure 4.20(a) shows the XAS spectrum of a monolayer sample of the Fe-T4PT network on a Au(111) metal surface. The position and the line shape of the L_3 peak with a maximum at 707.2 eV indicate that the Fe atoms are in +2 oxidation state [293–295]. The gray line in Fig. 4.20(a) shows an XAS reference spectrum of the $L_{2,3}$-edge in the case of Fe in a +3 oxidation state. Furthermore, the line shape of the XAS spectra of the Fe-T4PT/Au(111) sample is similar for the different incident angles. The +2 oxidation state of the Fe centers within the Fe-T4PT network is in line with mononucelar Fe(II) bulk complexes with six nitrogen based ligands [296]. This finding supports the three-dimensional coordination cavity of the Fe-T4PT network. Another feature of the XAS spectra in Fig. 4.20 is the slightly higher XAS intensity near grazing incidence evidencing a doubly-filled in-plane orbital. Hence a $S = 2$ high spin state is very likely for the Fe d^6 system present in the Fe-T4PT network.

The XCMD difference spectra of the Fe L-edge absorption is shown in Fig. 4.20(b), further corroborating the presence of a net magnetic moment. A characteristic dip-peak structure at the low-energy side of the difference signal of the L_3 peak is visible. The angle dependence of the XMCD difference signal reveals a similar line shape for the different incident angles, but a large change in size of XMCD difference signal. The maximum XMCD difference signal is observed at 90° (normal incidence) and the lowest at 20° (grazing incidence). This indicates the presence of an easy-axis magnetic anisotropy
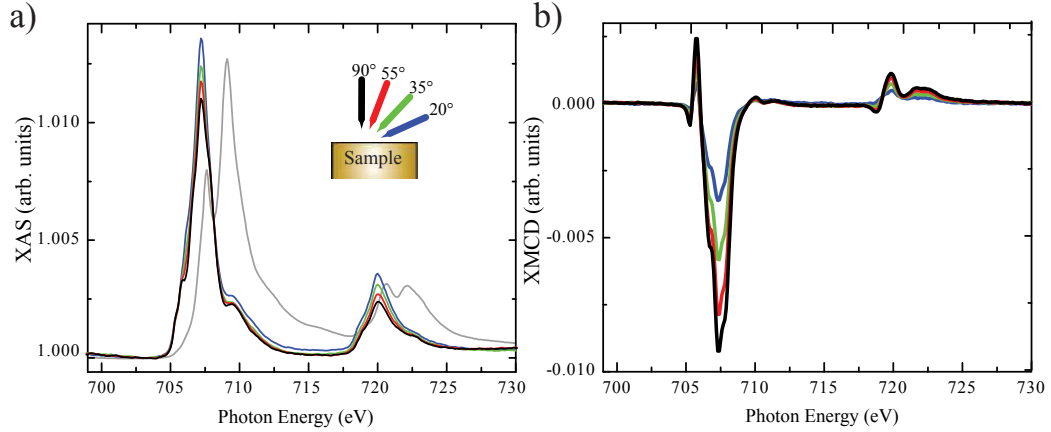
Figure 4.20: X-ray absorption spectra (a) and XMCD difference spectra (b) at the Fe $L_{2,3}$ edges of Fe-T4PT metal-organic network on Au(111) at a temperature of 8 K in an applied magnetic field of 5 T for four different angles of incidence, as defined in the sketch in the left panel. The magnetic field was always parallel to the x-ray beam. The gray line in (a) shows an XAS reference spectrum of the $L_{2,3}$-edge in the case of Fe in a +3 oxidation state.

in the Fe-T4PT network.

To further corroborate our assumption of a high spin state $S = 2$ of the Fe sites with the Fe-T4PT layer we performed multiplet calculations. Both x-ray absorption and XMCD difference spectra were simulated by additional multiplet calculation using the Cowan's code [297] and the CTM4XAS program [298]. Figure 4.21 shows the simulation and experimental spectra of the helicity-averaged x-ray absorption spectrum (a) and the corresponding XMCD difference curve (b). For the following crystal field parameters a good agreement of both, the simulation and the spectral shape of the helicity-averaged absorption spectrum and the XMCD difference curve, is found: $10D_q = 940$ meV, $D_\tau = 40$ meV, and $D_\sigma = -200$ meV. These crystal field parameters describe a trigonal (D_{3d}) crystal field and $S = 2$ spin state of the Fe ion.

Now let us discuss the experimental magnetization curves of the Fe-T4PT layer to investigate its magnetic anisotropy and the present of an exchange coupling between the Fe centers. Figure 4.22 depicts the evolution of the Fe L_3 XMCD difference signal with applied external magnetic field for both perpendicular and grazing incidence orientation of the applied magnetic field with respect to the surface plane. The higher XMCD difference signal and the higher curvature in the normal incidence orientation reveal the presence of sizable magnetic anisotropy with an easy-axis parallel to the surface normal. In order to simulate the magnetization curves in Fig. 4.21 we use a *spin*-Hamiltonian approach presented in section 4.2.1. First let us assume the simple case of paramagnetic moments and an easy-axis magnetic anisotropy in the presence of a magnetic field which reads:

$$\mathscr{H} = -\mu_B g \vec{B} \cdot \vec{S} + D S_z^2 \tag{4.14}$$

where $\vec{S}$ is the spin vector, S_z the spin component normal to the molecular plane, $\vec{B}$ the vector of the external field, g the g-factor, and μ_B the Bohr's magneton. The first term in equation 4.14 describes the Zeeman energy and the second term accounts for the magnetic anisotropy energy. The zero-field splitting parameter D describes magnetic anisotropy of the Fe ions, where a negative D stands for an
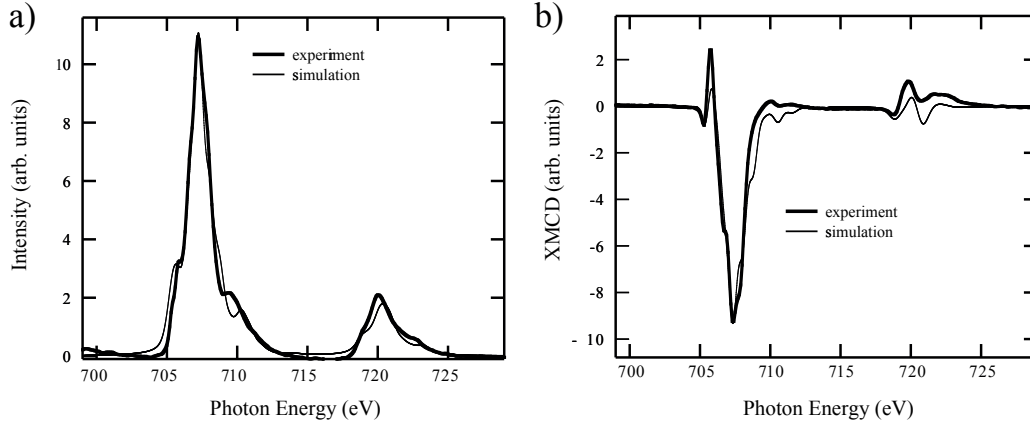
Figure 4.21:   (a) Helicity-averaged x-ray absorption spectra and (b) XMCD difference curves at the Fe $L_{2,3}$ edges of Fe-T4PT on Au(111). Thick lines: Experimental spectra, measured at a temperature of 8 K in an applied magnetic field of 5 T in normal incidence of circularly polarized radiation. Thin lines represent the result of the best fitting multiplet simulation, cf text.

easy-axis magnetic anisotropy. The D parameter also describes the curvature of the corresponding magnetization curve.

By solving equation 4.14 for the two different incidence orientation and calculating the total magnetization $\vec{M}$ from the thermal occupation of the corresponding levels we obtain the magnetization curves shown as dashed lines in Fig. 4.22 with a negative D parameter (for details see section 4.2.2). The first thing to notice is that the simulated magnetization curves (dashed line in Fig. 4.22) do not reproduce the curvature of the experimental data. In particular the curvature of the simulated magnetization curves deviate from the experimental data. Since the experimental data can not be reproduced by a model based on non-interacting paramagnetic moments with a magnetic anisotropy a magnetic coupling of the neighboring Fe sites within the Fe-T4PT networks have to be assumed [3]. This would lead to a stronger curvature of the magnetization curves.

In order to implement the magnetic exchange interactions in the Fe-T4PT network between neighboring Fe sites we use a mean-field approach to simulate the experimental magnetization curves. Let us now assume a magnetic exchange interaction between neighboring spin sites, which can be described by the Heisenberg model:

$$\mathcal{H} = -\sum_{i}^{N}\sum_{j}^{N} J_{i\,j} S_i S_j - g\,\mu_B \sum_{i}^{N} S_i \cdot \vec{B} \qquad (4.15)$$

$J_{i,j}$ is the magnetic exchange constant, where μ_B is the Bohr's magneton and $\vec{B}$ the external magnetic field. A positive value of $J_{i,j}$ corresponds to ferromagnetic coupling (spins align parallel) and negative value to an antiferromagnetic coupling (spins align antiparallel), respectively. Now let us consider a single spin interacting with the neighboring spins within the spin ensemble. For the neighboring spins

---

[3]We rule out that the magnetization is due to Fe clusters as we do not observe their presence in any STM images taken at various sample locations of the very same preparation of the Fe-T4PT network. Moreover, XAS and XMCD measurements have also been performed at even lower Fe coverage to assure the complete dissolution of eventual Fe clusters into the network. In this case sizable amounts of pure, H-bonded T4PT islands have been observed.
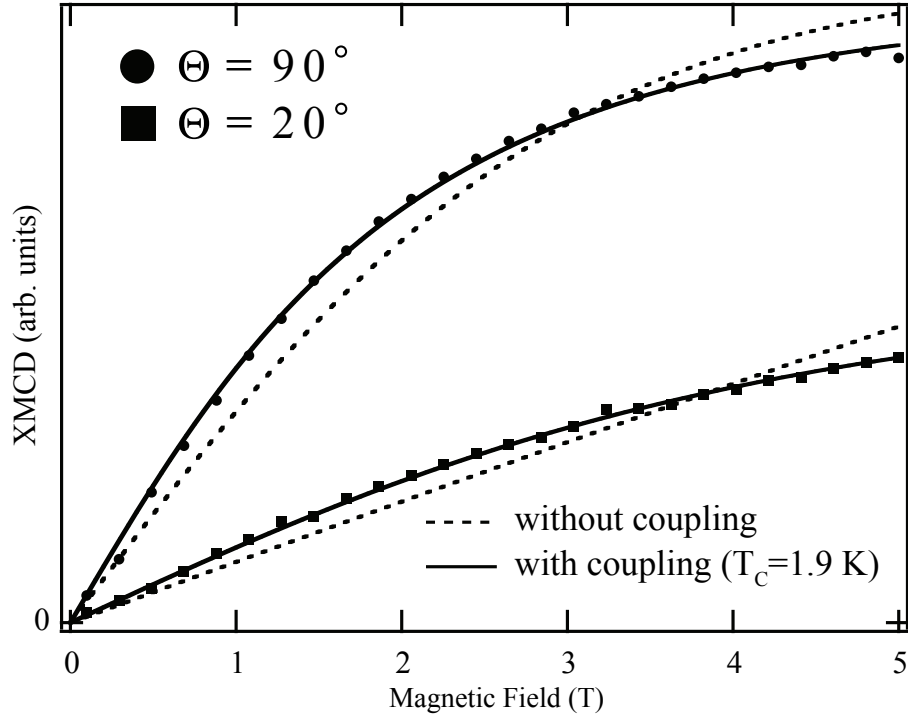
Figure 4.22: Magnetic field dependence of the XMCD at the Fe L_3 edge of Fe-T4PT on Au(111) for x-ray incidence normal to the surface (circles) and at $20°$ grazing incidence (squares), measured at a temperature of 8 K. The magnetic field was always parallel to the x-ray beam. Dashed lines are the best fits of a paramagnetic spin Hamiltonian for $S = 2$, $T = 8$ K, and $D = -0.35$ meV solid lines are the result of a simulation using mean-field-coupled magnetic moments with $T_C = 1.9$ K (cf text).

we assume $S_{iz} = \langle S_z \rangle$ and $S_{ix} = S_{iy} = 0$. The Hamiltonian describing the interaction of the single spin at site i then reads:

$$\mathscr{H}_i = \left(-2 \sum_i J_{i\,j} \langle S_z \rangle - g\,\mu_B\,B\right)S_{iz} \tag{4.16}$$

We can understand equation 4.16 in terms of a single spin at site i, which is placed in an effective magnetic field $\vec{B}_{eff}$ composed of the external field $\vec{B}$ and molecular field $\vec{B}_{Mol}$ caused by the neighboring spins:

$$\vec{B}_{eff} = \vec{B} + 2\left(\frac{\hat{J}_0}{\mu_B\,J}\right)\langle S_z \rangle = \vec{B} + \vec{B}_{Mol} \tag{4.17}$$

here $\hat{J}_0 = \sum_j J_{i,j}$ and $J_{i,j} = 0$ for $i = j$. We can express the magnetization $\vec{M}$ as follows:

$$\vec{M} = \vec{M}(\vec{B}_{eff},\,S,\,T,\,D) \tag{4.18}$$

Now the effective field $\vec{B}_{eff}$ is proportional to the magnetization of the spin ensemble with the proportionality factor:

$$T_C = \sum_i J_i/(3k_B) \tag{4.19}$$

where k_B is the Boltzmann constant, J_i is a Heisenberg-type exchange interaction of the spin at site i with spin at site j, and the sum goes over all sites with non-vanishing J_i. Without the presence of magnetic anisotropy, T_C represents the Curie temperature, which defines the critical temperature at which ferromagnetic order occur.

The result of the mean-field simulation is shown in Fig. 4.22 as a solid line assuming a spin state $S = 2$ and $T = 8$ K. Because our magnetization curves are not fully saturated we use equation 2.57. For the fit of the experimental data T_C, D, A and C_{T_z} were treated as fit parameters. The parameters of the best fit shown in Fig. 4.22 are $D = -0.35$ meV and $T_C = 1.9$ K.

Figure 4.23(b) shows the mean squared deviation between the experimentally obtained magnetic field dependence of the XMCD difference spectra at the Fe L_3 edge and the fit based on the mean-field approach of exchange-coupled spin moments with a magnetic easy-axis anisotropy as function of the coupling strength J (expressed in T_C) and the zero-field splitting D. At the parameters $D = -0.35$ meV and $T_C = 1.9$ K a global minimum of the mean squared deviation is clearly visible. Fig. 4.23(a) shows a comparison of the mean squared deviation of the mean-field model (solid line) and a paramagnetic *spin*-Hamiltonian (dashed line). The paramagnetic *spin*-Hamiltonian yields an unrealistic high and negative zero-field splitting D value. Even for such high D values the fit based on the paramagnetic *spin*-Hamiltonian can not reproduce the experimental data. The large D value leads to higher curvature of the magnetization $\vec{M}(H)$ along the magnetic easy-axis direction. But on the other hand a large D lead to a decrease of the curvature along the magnetic hard axis direction. Hence the mean squared deviation is minimized because in the experimental data the easy-axis shows a larger XMCD intensity. But even for large D the mean squared deviation is about a factor 25 larger in the case of the fit with the paramagnetic *spin*-Hamiltonian compared to the fit based on the mean-field model. This shows the significance of the exchange-coupling in order to explain the experimental data.

The good agreement of the experimental data with the mean-field simulations clearly indicates the presence of ferromagnetic exchange coupling present between the Fe sites of the Fe-T4PT network. However, the mean field approach does not provide details about the exchange coupling mechanism. Assuming the simple case that the nearest neighbor exchange interactions are the most dominant, the coupling constant $J_i = k_b T_C/2$ has to be of the order ≈ 80 μeV in order to explain the experimental data [4].

The presence of an easy-axis magnetic anisotropy is important to stabilize the ferromagnetic ordered ground state. The *Mermin−Wagner* theorem states, that there is no stable ferromagnetic ground state in a two-dimensional isotropic system with short-range exchange-interactions [299]. In particular, the isotropic two-dimensional Heisenberg model shows no magnetic order at finite temperatures [299]. This problem is caused by the fact that the mean field approximation neglects fluctuations at finite temperatures. By decreasing the dimensionality of the spin-system, collective spin excitations present at finite temperature become more important. Such spin-excitations are known as spin-waves, which are collective excitation modes of the spin system propagating through the system. The excitation of such spin waves or magnons depends on temperature. The occupation of a finite number of magnons can lead to a vanishing of the ferromagnetic order. For a two-dimensional spin-systems with an easy-plane magnetic anisotropy the magnetic moment is free to rotate within the plane. Hence, such a system has no ferromagnetic stable ground state and magnons can easily be excited [300]. In contrast

---

[4]This conclusion is robust and does not depend on the assumption of an $S = 2$ high-spin state. Even stronger magnetic coupling between Fe atoms is necessary to reproduce the experimental data if $S = 1$.
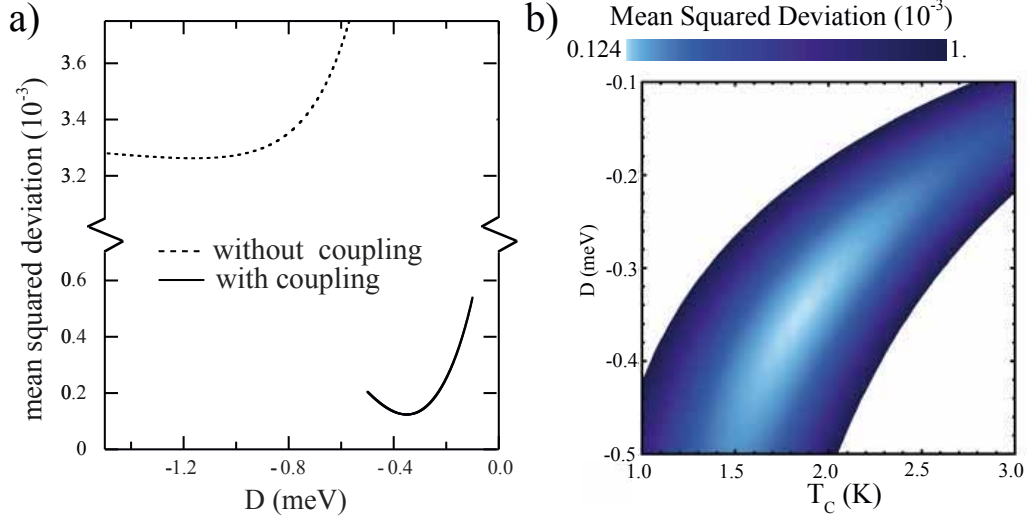
Figure 4.23: (a) The mean squared deviation between the experimental field-dependence of XMCD data and the simulation by the paramagnetic spin Hamiltonian (dashed line) and the mean-field model, as described in the main text, as a function of the anisotropy, represented by the zero-field splitting parameter D. For each value of D, all other fit parameters have been optimized. (b) Two-dimensional color plot of the mean squared deviation of the simulation calculated from the mean-field model described in the main text from the experimental field-dependence of XMCD data as a function of the magnetic anisotropy, represented by the zero-field splitting parameter D, and the magnetic coupling between the Fe ions, expressed by T_C. The deviation is calculated from the simultaneous comparison to the experimental XMCD values for $90°$ normal and $20°$ grazing incidence. The white regions outside the curved valley of minimal deviation exhibit deviation values larger than 10^{-3}.

an easy-axis magnetic anisotropy leads to the opening of gap at the bottom of the magnon spectrum, stabilizing the ferromagnetic ordered state [300]. Thus, in the case of Fe-T4PT network the presence of a easy-axis magnetic anisotropy is an important ingredient for the stabilization of the ferromagnetic ground state.

4.4.3 Ferromagnetic Coupling Mechanism

The magnetic exchange interactions between the neighboring Fe sites within the Fe-T4PT network can be caused by several different interaction mechanism, which are discussed in the following. A direct exchange coupling, caused by wave function overlap of the corresponding 3d orbitals, or dipolar coupling[5] are rather unlikely, since the nearest neighbor distance of the Fe sites is about $r_{NN} = 1.3 \pm 0.1$ nm. Another possible coupling mechanism is mediated by the polarization of the surface and bulk conduction electrons [278, 280, 301–305] known as the Ruderman-Kittel-Kasuya-Yosida (RKKY) interaction. The RKKY exchange coupling constant can be described as [304, 306, 307]:

$$J_{RKKY} \propto \frac{cos(2k_F r_{i,j})}{(2k_F r_{i,j})^d} \tag{4.20}$$

---

[5]dipolar coupling decreases as $\frac{1}{r^3}$, where r is the distance between the magnetic dipoles

Figure 4.24: (a) Coupling strength for the RKKY interaction using equation 4.20 in the case of two-dimensional conduction electron system. (b) Schematic representation of two magnetic moments coupled via the RKKY interaction mediated by the polarized conduction electrons (blue arrows).

here k_F is Fermi wave vector, $r_{i,j}$ is the distance between the neighboring magnetic moments i and j and d accounts for the dimensionalit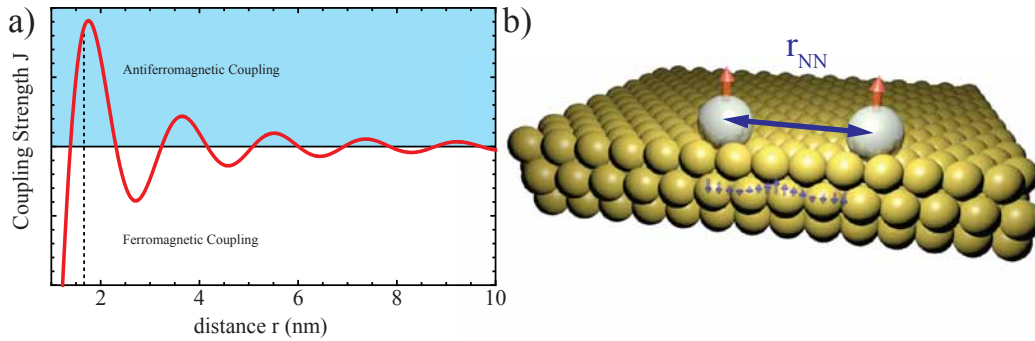y of the conduction electron system. Hence the RKKY interactions shows an oscillating ferro- and antiferromagnetic exchange coupling depending on the distance $r_{i,j}$. The Au(111) surface exhibits a Rashba-split surface state with a Fermi wave vector $k_{F,1} \approx 1.7$ nm [308]. Figure 4.24 shows that in the case of the Fe-T4PT network with a nearest neighbor distance of $r_{NN} = 1.3$ nm equation 4.20 yields a weakly coupled antiferromagnetic ground state. However, since the magnetic Fe sites are placed in a three-dimensional coordination cavity a sizable lifting from the Au(111) metal surface can be expected [287, 288]. Therefore the interaction of the Fe sites with the underlying conduction electrons would be weak. Despite small effects that may change the scattering phase shift of the conduction electrons, we may tentatively exclude a significant contribution of an RKKY-mediated coupling.

From metal-organic frameworks it is known that magnetic exchange interactions can be mediated by the organic ligands through a superexchange mechanism [253]. In these systems both ferromagnetic and antiferromagnetic exchange interactions can be observed [253]. The superexchange mechanism is based on the spin polarization of the frontier orbitals, in general π-orbitals, and follows qualitatively a simple alternation rule [309]. Hence, an odd number of linker atoms in the pathway leads to ferromagnetic exchange coupling and an even number yields an antiferromagnetic coupling. Of course all possible pathways have to be considered. Figure 4.25 depicts the case of the Fe-T4PT network. Here the blue and red color correspond to the two different spin-polarizations, respectively. Applying the alternation rule results in ferromagnetic coupling between the neighboring Fe sites based on the alternating spin-polarization of first layer T4PT molecules. The second layer T4PT molecules can not cause the exchange coupling, since they do not link neighboring Fe centers. The ferromagnetic superexchange is consistent with the ferromagnetic Heisenberg-type interaction J_i derived from the simulations of the experimental magnetization curves.

4.4.4   Conclusions

In conclusion, we observed the formation of ordered Fe-T4PT islands mediated by metal-ligand bonds between the Fe atoms and the pyridine end groups of the T4PT molecules. An additional T4PT molecule is centered on top of each Fe site. Thus, the Fe-T4PT network exhibits a bilayer structure,
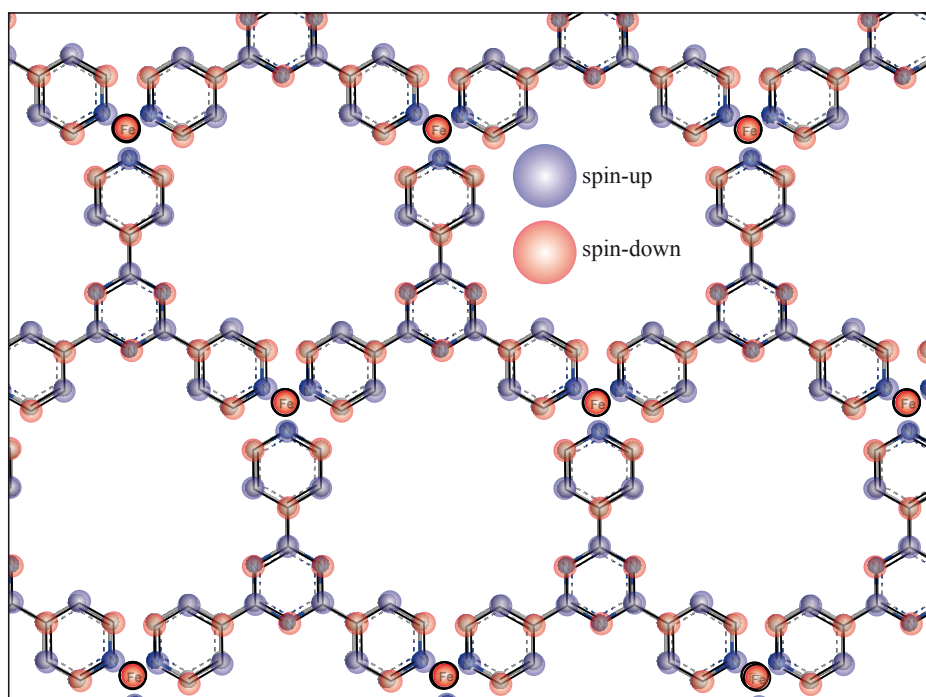
Figure 4.25:   Schematic representation of the alternating spin-polarization along the organic backbone of the first layer T4PT molecules within the Fe-T4PT network.

even in the submonolayer regime. The presence of this double-layer indicates a strong interaction between the Fe site and central ring of the second layer T4PT molecule. The Fe sites are thus encaged in three-dimensional coordination cavities, which can help to prevent a strong hybridization with the underlying Au(111) surface. This can essentially be useful to preserve the magnetic properties of the magnetic metal atoms.

Further XAS measurements combined with multiplet calculations reveal that the coordinated Fe sites exhibit a +2 oxidation state and spin state $S = 2$. Furthermore, the magnetic moments of the Fe sites reveal a strong magnetic anisotropy with an easy-axis out-of-plane direction caused by the ligand-field formed by the surrounding ligands. A large magnetic anisotropy is an essential requirement to stabilize a correlated magnetic state in such a low-dimensional system.

Additional field dependent XMCD measurements reveal that the magnetic moments of the Fe sites are ferromagnetically coupled. The Fe-T4PT is therefore the first metal-organic network on surface exhibiting a ferromagnetic ground state. The underlying coupling mechanism is presumably a superexchange mechanism mediated by the organic T4PT linkers. We estimated a ferromagnetic exchange coupling in the case of a dominating nearest neighbor interaction of the order of $J = 80 \ \mu$eV.

In view of potential applications an increase of the magnetic stability would be desirable. This can be achieved by increasing the magnetic anisotropy or the magnetic coupling strengths of the magnetic moments, for example by using smaller molecules with stronger functional end groups that would give rise to a stronger ligand field.

An intriguing question that arises is how we can control the bilayer and single-layer formation. This will be the topic of the next section, where we analyze the role of different end groups of the organic

linkers.

4.5 Triggering the Formation of a Single or Bilayer Metal-Organic Network

The bilayer formation in the case of the Fe-T4PT network is an interesting new approach to introduce a magnetic anisotropy through the ligand crystal field and also to decouple the metal atom from the surface. As shown in the previous chapter it also allows to mediate a magnetic exchange coupling. The resulting network architecture is the result of a multitude of interactions between the molecular functional end groups, the metal species and the underlying surface. In particular, the formation of the bilayer relies on strong interaction of the pyridine end groups and the central ring with the metal center. Additional interactions, like hydrogen-bonds, between the second layer and first layer molecules may further stabilize the bilayer formation. A rising question is, if we can control the bilayer formation, for example, by changing the functional end groups or the central part of the molecule. In the case of T4PT the central part of the molecule is a triazine ring, with three nitrogen atoms. A possible scenario is, that those three nitrogen atoms form bonds to the metal atom. On the other hand, also an interaction between the transition metal cation and the π-system of the aromatic moiety can provoke the bilayer formation. These non-covalent bonding forces originate from the quadrupole moment of the aromatic system [281–284]. A simple experiment would be to replace the triazine with a benzene ring to verify this assumption. The exchange of the functional end groups may also prevent the double-layer formation.

We start with the metal-organic network consisting of Co atoms and 1, 3, 5-Tri(pyridin-4-yl)benzene (T4PB) molecules. T4PB is a triangular molecule and its molecular structure is shown in Fig. 4.26. The second discussed network is composed of Co atoms and 2, 4, 6-Tris(4-benzonitrile)-1, 3, 5-triazine (T4CPT) molecules.

4.5.1 Structural Properties of the Co-T4PB Network

Deposition of T4PB molecules on the Au(111) metal surface at room temperature leads to the formation of extended ordered molecular islands as those shown in Fig. 4.27(a). Closer inspection of the T4PB molecular lattice reveals a rhombic unit cell with the lattice parameters $a = 1.1 \pm 0.1$ *nm*, $b = 1.1 \pm 0.1$ *nm*, enclosed by an angle of $\alpha = 60° \pm 1°$. The molecules lie flat on the surface, which is common for two-dimensional organic molecules on metal surfaces [219] (see Fig. 4.27(b)). An analysis of the adsorption configuration reveals that all terminal nitrogen atoms of the pyridine
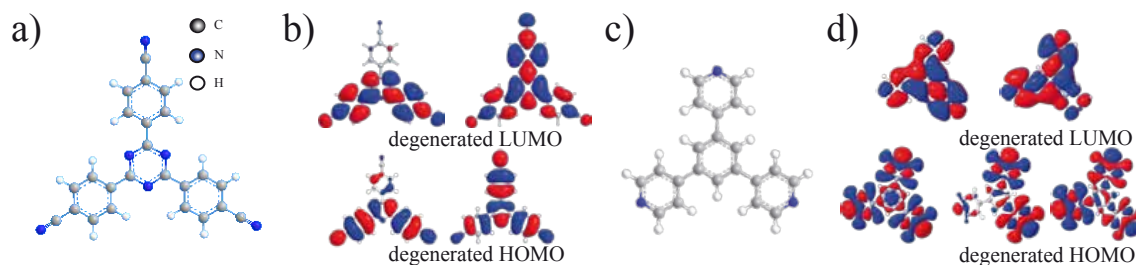

Figure 4.26: Molecular structure of T4CPT (a) and T4PB (c). DFT simulation of the degenerated LUMO and HOMO of the T4CPT (b) and the T4PB (d) molecule using the RB3LYP functional and the 3-21G basis set. The isocontour was set to 0.005.
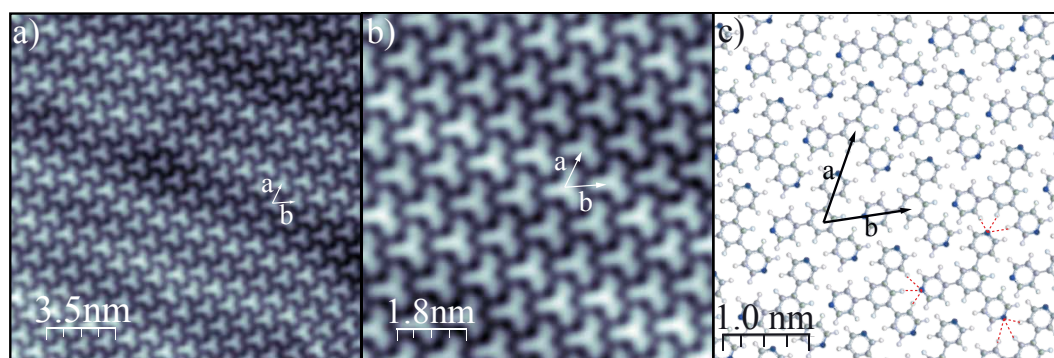
Figure 4.27:   (a) STM topography image of a large ordered T4PB island (scanning parameters: $V_S = 0.38$ V, $I_T = 0.28$ nA). (b) Zoom-in of the ordered T4PB island (scanning parameters: $V_S = 0.38$ V, $I_T = 0.28$ nA). (c) Structural model of the self-assembled T4PB layer.

end groups of T4PB point to hydrogen atoms of neighboring T4PB molecules as indicated by the red dashed lines in Fig. 4.27(c). The average distance between the electronegative N atoms and the H atoms amounts to ≈ 2 Å, typical for electrostatic intermolecular bonding patterns. The observation of the soliton lines of the Au(111) herringbone reconstruction below the T4PB island (Fig. 4.27(a)) indicates that the molecular only weakly interacts with the underlying surface [41].

Subsequent deposition of Co atoms triggers the formation of Co-T4PB islands. Fig. 4.28(a) and (b) show two enlarged STM topographic images of a Co-T4PB island taken at different sample bias voltages. Fig. 4.28(a) shows a honey comb structure with a three-fold bonding motif. The structure is similar to the case of the previously discussed Fe-T4PT network (cf section 4.4). The T4PB molecules presents a triangular shape associated with the three T4PB pyridine groups. Changing the sample bias voltage above 1.0 V leads to a change of the appearance of the coordinated Co-T4PB island (Fig. 4.28(b)). The T4PB molecules appear now as three bright protrusions also associated with the three pyridine groups of the T4PB molecules. Thus, the structural properties and also the bias dependence of the Co-T4PB islands is very similar to the Fe-T4PT system. Also domain boundaries can be observed as indicated by the black dashed line in Fig. 4.28(b). Above the boundary the triangular shaped features are orientated upwards, and below they are pointing downwards (indicated by the red circles in Fig. 4.28(b)). These findings lead to the same conclusion like in the case of the Fe-T4PT system: the Co-T4PB system exhibits a bilayer structure.

Fig. 4.28(c) and (d) show the proposed structure model of the three-dimensional Co-T4PB layer of the first (c) and second layer (d), respectively. In the first Co-T4PB layer every Co atom is surrounded by three pyridine end groups of three T4PB molecules forming three-fold bonding node. The distance between neighboring Co sites is about $r_{Co} = 1.3 \pm 0.1$ nm. The Co-N distance can be estimated to ≈ 2 Å, which is consistent with bond lengths of active nitrogen sites and transition metal atoms shown in previous experiments and DFT studies [18, 267].

The second layer consists of T4PB molecules which are adsorbed with their benzene ring (cf Fig. 4.28(c)) on top of the Co sites. The second layer molecules are slightly tilted about 29° with respect to the first layer molecules (see Fig. 4.28(c)). The interaction of the second layer T4PB molecules with the Co sites is presumably based on interactions between the π-system of the T4PB molecules and Co metal cations [310, 311]. The bonding configuration can be further stabilized by
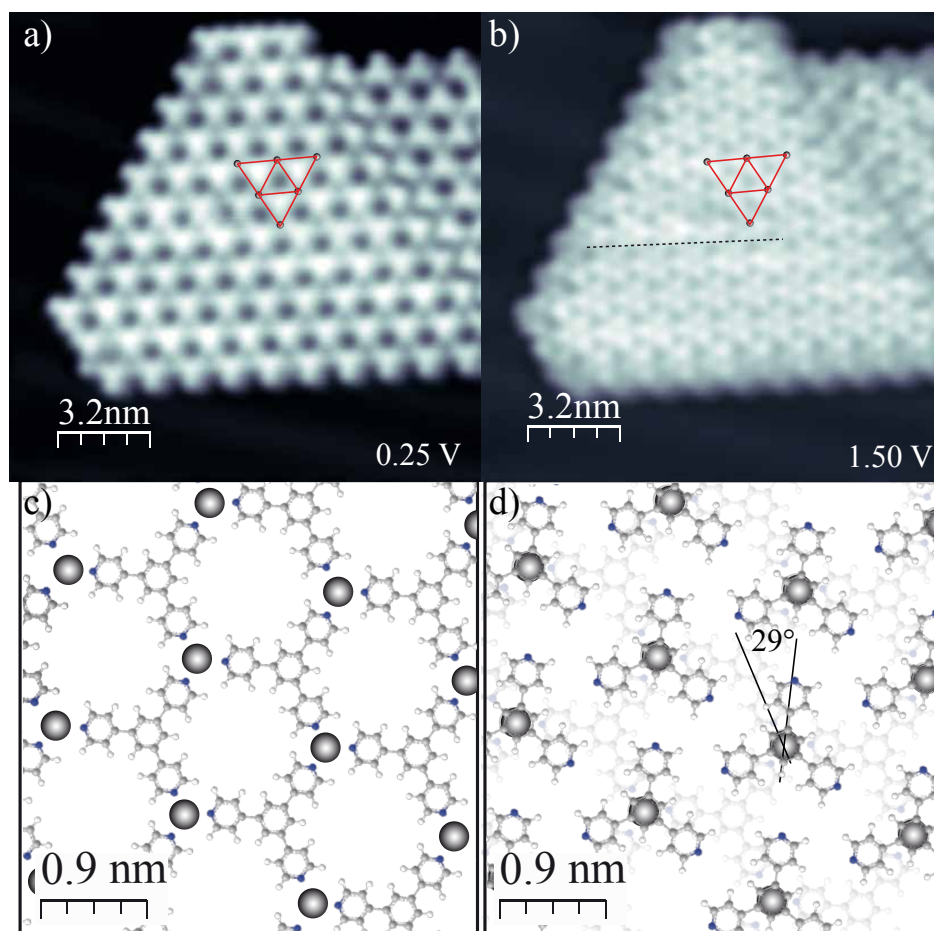
Figure 4.28: (a) and (b) show STM topography images at different sample bias voltages (I_T = 0.33 nA, V_S = 0.25 V (b) and V_S = 1.5 V (c)) of the Co-T4PB island. The red triangles indicate the orientation of the T4PB molecules. The black dashed line represents a domain boundary, cf text. (c) and (d) show the proposed structure of the first and second layer of Co-T4PB network, respectively. Co atoms are three-fold coordinated by three T4PB molecules. The second layer T4PB molecules are centered at the Co sites and are tilted about $29°$.

additional π-π or H-π interactions of the second layer pyridine end groups with the underlying T4PB molecules [285, 286]. The structural properties of the Co-T4PB and the Fe-T4PT are very similar and indicate that also in the case of the Fe-T4PT system the bonding of the topmost molecules and the Fe atoms is based on the interaction of the π-system with the metal cation [281–284]. Theory calculations reveal that such non-covalent metal cation-π-interaction can be of the order of several eV [310–312] and are therefore comparable to bond energies of metal-ligand interactions [15, 267].

4.5.2   Inelastic Features of the Co-T4PB Network

In order to investigate the electronic structure of the Co-T4PB network we performed dI/dV spectra taken in a small energy window at the Co (A), T4PB pyridine (B) and T4PB center (C) (see of Fig. 4.29(a)). The spectra reveal the presence of symmetric step-like features localized around the
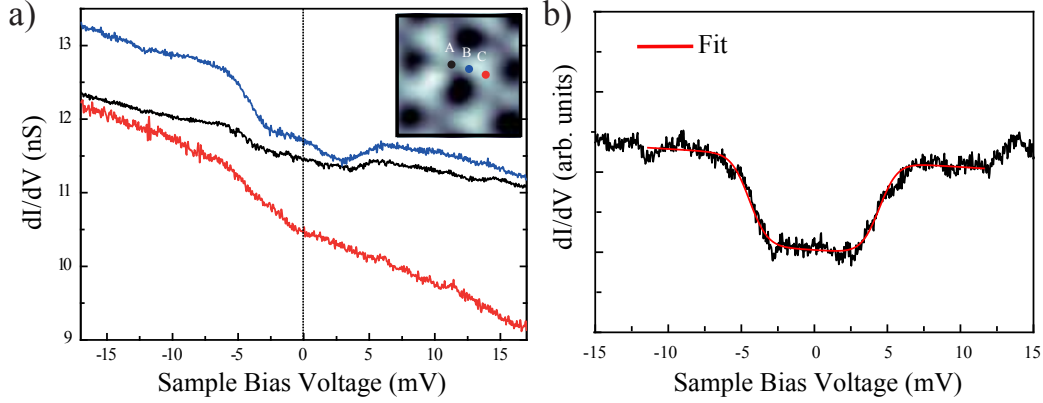
Figure 4.29: (a) High resolution dI/dV spectra around E_F on different positions of the Co-T4PB network as indicate in the inset: Co (A), T4PB (B), and hollow (C) site. (V_T = 18 mV, I_T = 0.3 nA, V_{ac} =1 mV rms at 877 Hz). The spectrum at position (B) shows a step-like feature. The spectra are shifted vertically for clarity. (b) Fit of blue dI/dV spectrum in (a) using equation 4.21 (red solid line). The best fit parameters are Δ_{vib} = 4.5 $\pm$ 0.1 meV and T_{eff} = 5.5$\pm$ 0.2 K. The experimental settings were T_{exp} = 4.8 K, V_{rms} = 1 mV. A linear background was subtracted from the spectrum.

Fermi energy E_F. In general step-like features in STS can be attributed to inelastic tunneling processes, i.e. either spin-flips [79] or vibrational excitations [77].

To extract the energetic positions of the inelastic features we used the following expression to fit the steps in the IETS spectrum [68, 313]:

$$\frac{dI}{dV} = A + B \cdot (\Omega(\frac{eV + \Delta_{In}}{k_B T_{eff}}) + \Omega(-\frac{eV - \Delta_{In}}{k_B T_{eff}})) \qquad (4.21)$$

$$\Omega(x) = \frac{1 + (x-1)e^x}{(e^x - 1)^2} \qquad (4.22)$$

A and *B* are the elastic and inelastic contribution to the conductance, respectively. The inelastic steps are centered at energies $\pm\Delta_{In}$. Furthermore the expression accounts for a thermal broadening of 5.4 $k_B T_{eff}$ [68, 313]. T_{eff} is an effective temperature. The best fit of spectrum (B) in Fig. 4.29(a) is shown as a red solid line in Fig. 4.29(b). Fitting the inelastic feature of about 9 different dI/dV spectra yields an average value for the position of the inelastic feature of Δ_{vib} = 4.7 $\pm$ 0.4 meV. The normalized change of conductance $\Delta G/G$ (%) in the dI/dV spectrum at position (B) in Fig. 4.29 is about $\approx$ 6%, which is in line with the typical values for vibrational features [78, 80] (cf section 2.3.5). This finding tentatively lead us to the conclusion that the inelastic feature originates from a vibrational excitation.

DFT simulation of the free gas-phase T4PB molecule reveal several very low lying (below 10 meV) molecular vibrations (cf appendix A.3). The lowest vibrational mode exhibits an energy close to 5 meV (cf appendix A.3). Those low lying vibrational modes correspond to rotations of the pyridine end groups as indicated in Fig. 4.30(d) and involve almost no deformation of the central benzene ring. Furthermore these vibrations are asymmetric, that means that the displacement of the three pyridine end groups is different.

The above discussed inelastic feature exhibits a spatial dependence as it can already be noticed in the
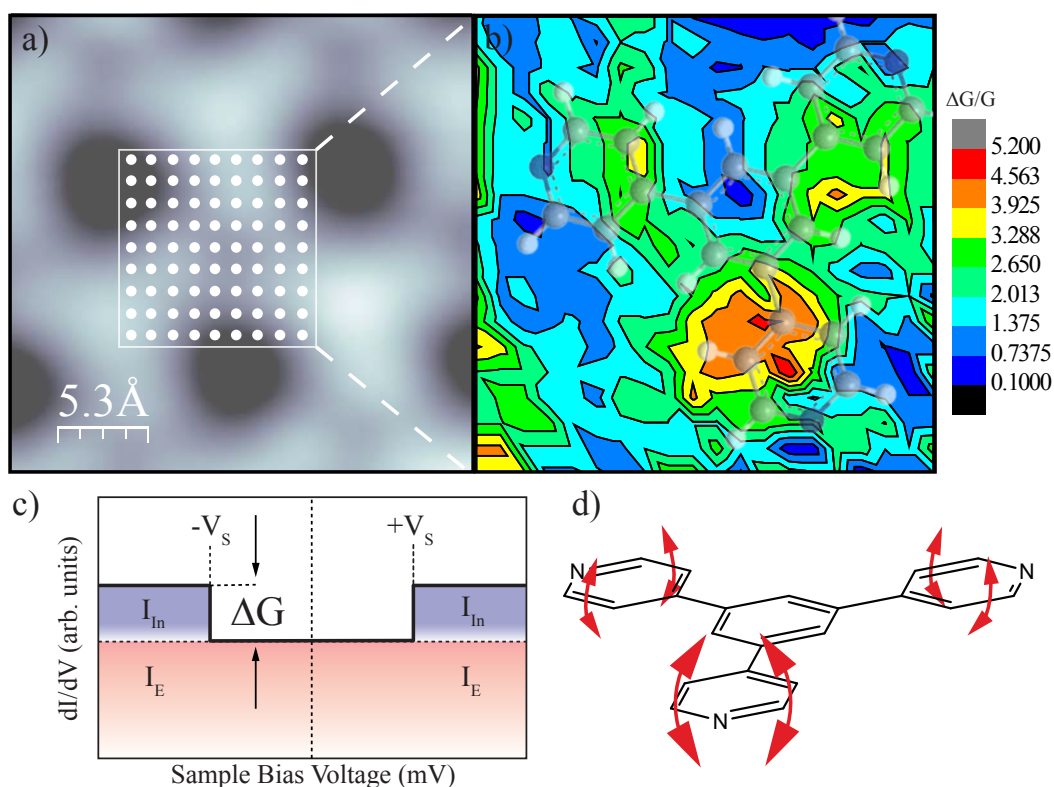
Figure 4.30: (a) STM topography image of the Co-T4PB metal-organic network (V_T = 550 mV, I_T = 0.26 nA). The white square indicates the measurement dI/dV grid. At each position of the grid a high resolution dI/dV spectrum was recorded. (b) Spatially resolved presentation of the normalized change of conductance $\Delta G/G(\%)$. A model of a second layer T4PB molecule is superimposed to the grid. The orientation of the second layer T4PB is determined by imaging the island at different sample bias voltage and recording differential conductance dI/dV maps. (c) Schematic conductance spectrum showing the individual contributions of the tunneling paths. The inelastic and elastic tunneling contributions are labeled with I_{In} and I_E, respectively. (d) Vibrational excitation of the T4PB molecule with an energy of ν_{vib} = 5.21 meV. The vibrational mode refers to rotational vibrations of the pyridine end groups.

dI/dV spectra shown in Fig. 4.29(a). To investigate its spatial distribution we recorded a dI/dV grid. Figure 4.30(a) illustrates the method. The STM tip is moved along the intersections of a lateral grid above the Co-T4PB network as indicated by the white square in Figure 4.30(a). At each point (white circles) of the dI/dV grid a dI/dV spectrum in a small energy range is taken and the normalized change of conductance $\Delta G/G$ (%) is then extracted from each spectrum. The definition of ΔG is explained in Fig. 4.30(c). In the case of a vibrational feature the normalized change of conductance $\Delta G/G$ is proportional to the excitation probability of the related vibrational mode [6]. Thus, the spatial mapping of the normalized change of conductance $\Delta G/G$ (%) allows to resolve spatial variations of the vibrational mode and to map its symmetry. The two-dimensional map of the signal $\Delta G/G$ clearly shows a maximum signal at the three pyridine end groups of the topmost second layer T4PB molecule. However, the $\Delta G/G$ is not evenly distributed over the three pyridine end groups. The spatial distribution of $\Delta G/G$ is in line with the asymmetric vibrational modes found by the DFT simulations. These finding suggests the identification of the inelastic feature as a vibrational excitation of the topmost T4PB molecule.

Since Co atoms are present in the Co-T4PB network, the inelastic feature could also originate from a spin-flip excitation of the Co magnetic moment. Even so the magnetic Co atom is encaged in a three-dimensional coordination cavity tunneling electrons could still excite spin-flip processes either mediated by the π-system of the organic ligand [279] or directly by the tunneling electrons in the case that the topmost T4PB is transparent for tunneling electrons in the low sample bias regime. Further XMCD measurements have to be carried out to investigate the spin state and the magnetic anisotropy of the Co atoms within the network to elucidate a possible magnetic origin of the inelastic feature. However, at first sight, the spatial distribution and the low change of conductance of the inelastic excitations favors the explanation of vibrational modes.

4.5.3   Structural Properties of the Co-T4CPT Network

Let us now change the molecular linker from T4PB to T4CPT to investigate the effect of different functional end groups of the organic linker on the network architecture. The molecular structure of T4CPT is depicted in Fig. 4.26(a). T4CPT exhibits a central triazine ring and three benzonitrile end groups, which are also known to form strong coordination bonds to transition metal atoms [28, 267, 315]. First we discuss the structural and electronic properties of T4CPT molecules on Au(111). Fig. 4.31(a) shows a typical self-assembled ordered T4CPT islands. The T4CPT molecules present a triangular shape associated with the three benzonitrile end groups. The T4CPT molecular lattice exhibits a rhombic unit cell with lattice parameters $a = 2.6 \pm 0.1$ nm, $b = 1.3 \pm 0.1$ nm, enclosed by an angle of $\alpha = 60° \pm 1.0°$. The molecules are adsorbed flat on the surface indicated by their triangular shape. The structural model in Fig. 4.31 reveals that the T4CPT island is stabilized by hydrogen bonds between the nitrogen atoms of the benzonitrile end groups of T4CPT and hydrogen atoms of neighboring T4CPT molecules as indicated by the red dashed lines in Fig. 4.31(b). The average distance between the electronegative N atoms and the H atoms amounts to ≈ 2 Å, comparable to the case of T4PB. The observation of the soliton lines of the Au(111) herringbone reconstruction below the T4CPT island (Fig. 4.31(a)) evidences that the molecular only weakly interacts with the underlying surface [41] as it happened also in the case of T4PB.

---

[6]The normalized change of conductance $\Delta G/G$ does not depend on the STS set point (I, V) and enables a better comparison between different dI/dV spectra. $\Delta G/G$ presents a lower limit of the inelastic fraction of the inelastic channel [314].
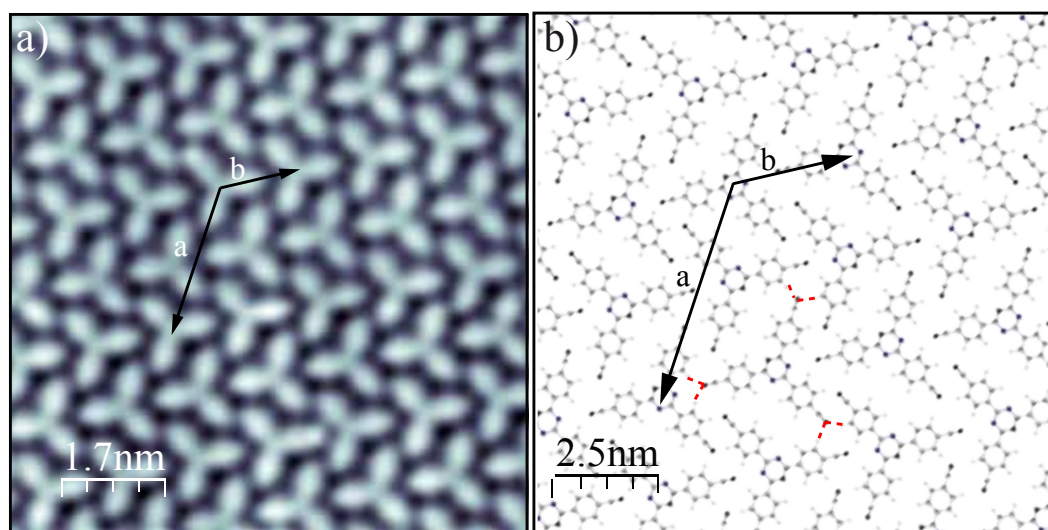
Figure 4.31:   (a) STM topography image of a large ordered T4CPT island (scanning parameters: $V_S = 0.5$V, $I_T = 0.15$ nA). (b) Structural model of the self-assembled T4CPT layer. The red dashed lines indicate hydrogen bond between benzonitrile end groups and hydrogen atoms of neighboring T4CPT molecules.

Fig. 4.32(a) shows a topographic image after subsequent deposition of Co atoms and T4CPT molecules on a clean Au(111) surface. The STM contrast is completely different to the one in Fig. 4.31(a) of the pristine T4CPT molecules on Au(111). Again the T4CPT molecules appear with a triangular shape and the bonding pattern has a three-fold symmetry. Thus Fig. 4.32(b) depicts an coordinated Co-T4CPT island with a similar appearance like in the case of the Co-T4PB and the Fe-T4PT networks.

In order to check for the existence of second layer molecules, we imaged the Co-T4CPT layer at different sample bias voltages. All STM topography images in the bias window from 0.2 V to 2.0 V reveal a three-fold bonding motif. At higher bias voltages the T4CPT molecules appear as disc-like features in the STM topography. No change of the three-fold symmetry or orientation like for the Co-T4PB or Fe-T4PT coordination network can be observed (cf Figure 4.32(c)). Also at negative sample bias voltages the network shows a three-fold bonding node. These findings indicate the absence of an additional second layer in the system. One possible explanation is that the benzonitrile end groups of T4CPT molecule form stronger metal-ligand bonds compared to the Co-pyridine bonds of the Co-T4PB network, which prevents the second layer formation. The absence of a second layer in the Co-T4CPT system implies a lower number of ligands, which can result in a smaller Co-surface distance. This can have an impact on the magnetic properties of the Co atoms within the Co-T4CPT network.

In order to check the electronic properties of the layer we take dI/dV spectra shown in Figure 4.33(a). It depicts several dI/dV spectra at the Co site, triazine ring and at the bare Au(111) metal surface. Only at the Co site a broad resonance with a maximum centered at -190 mV below E_F is visible that overlaps with the Fermi energy E_F. Both the spectra on the bare Au(111) metal surface and at the triazine ring of the T4CPT molecule do not show this feature (cf Fig. 4.33(a)). Its spatial localization is revealed by a constant current dI/dV map taken at an energy of -180 mV shown in Fig. 4.33(b) on the middle. The red triangle indicates the position of a T4CPT molecule as can be determined from
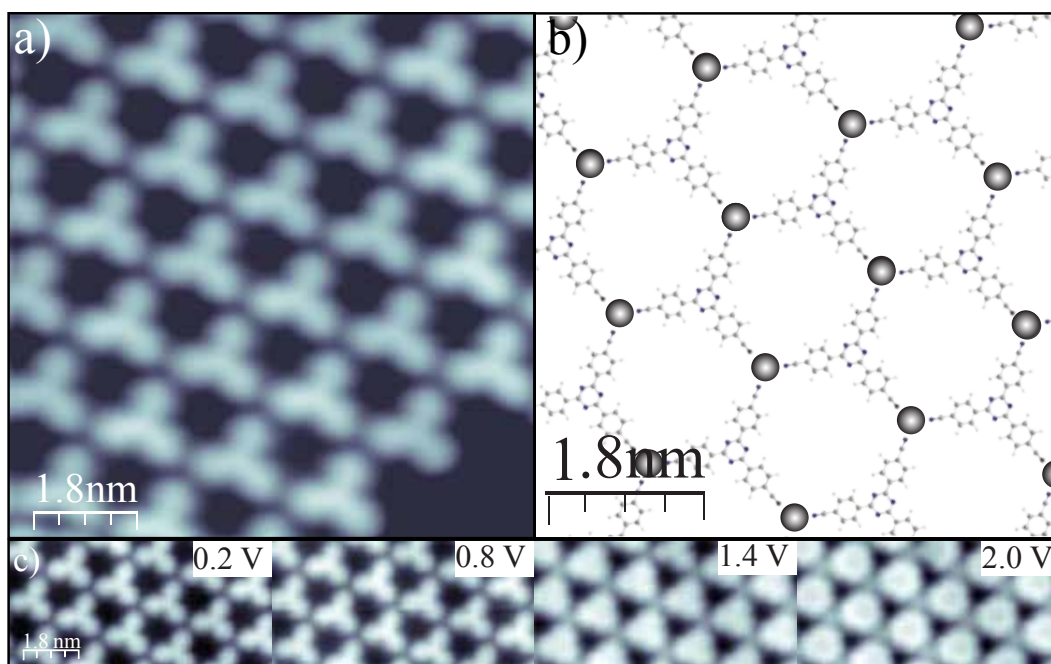
Figure 4.32:   (a) Large scale STM topography image of the coordinated Co-T4CPT islands on the Au(111) surface (I_T = 0.5 nA, V_S = 0.51 V). (b) Enlarged STM topography images of the Co-T4CPT coordinated island (I_T = 0.3 pA, V_S = 0.01 V). (c) Bias dependence of the Co-T4CPT network (I_T = 0.5 nA).

the corresponding simultaneously recorded STM topography image on the left side of Fig. 4.33(b). The feature at -190 mV is located around the Co sites and exhibits a triangular shape. A dI/dV map taken at an energy of +40 mV does not show these features but represents the topography (cf 4.33). This indicates that an electronic state, tentatively associated with the Co atoms within the Co-T4CPT network, is localized close to the Fermi energy E_F. The single-layer structure of the Co-T4CPT layer implies a reduced number of ligands for the Co atoms. This can lead to a stronger hybridization with the underlying surface. In the case of single Co atoms on Au(111) a Kondo resonance can be detected [164, 168] caused by the interaction of the spin 1/2 degenerated ground state of the Co atoms and the conduction electrons. So let us now check for magnetic fingerprints of the Co-T4CPT network.

4.5.4   Magnetism of the Co-T4CPT Network

We use dI/dV spectroscopy close to the Fermi energy E_F to investigate possible magnetic signatures of the Co-T4CPT network. Figure 4.34(a) shows several differential conductance dI/dV spectra at different positions of the Co-T4CPT network as indicated in the small inset in Fig. 4.34(a). At the Co site the presence of a narrow dip-like feature at E_F is revealed with a FWHM of 7.7± 0.5 mV, whereas the spectrum recorded at the center of the T4CPT triazine ring is essentially flat and do not show the dip-like feature.

The line shape and the energetic position close to E_F suggest that the narrow dip-like feature observed at the Co sites within the Co-T4CPT network can be associated with a Kondo resonance. Fig-
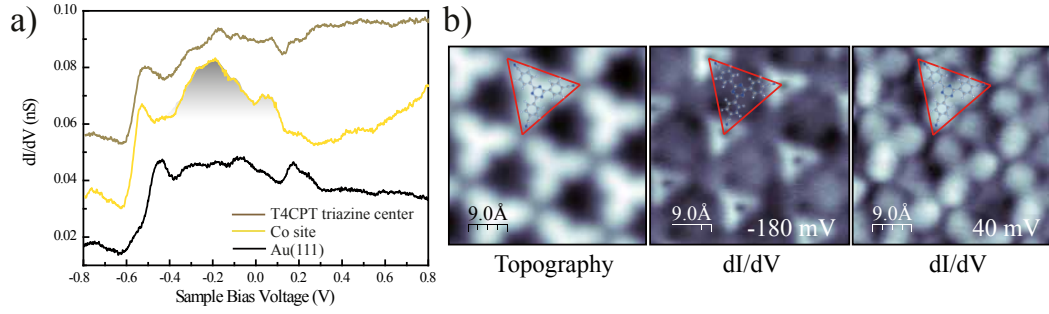
Figure 4.33: (a) dI/dV spectra at a Co site, T4CPT triazine center, and at the bare Au(111) metal surface ($I_T = 0.59$ nA, $V_T = 850$ mV, $V_{ac} = 7$ mV rms at 897 Hz). (b) STM topography image (left) and two constant current dI/dV map of the Co-T4PT network at a sample bias voltage of $V_T = -180$ mV (middle) and $V_T = +40$ mV (right) ($I_T = 0.49$ nA, $V_{ac} = 10$ mV rms at 897 Hz).
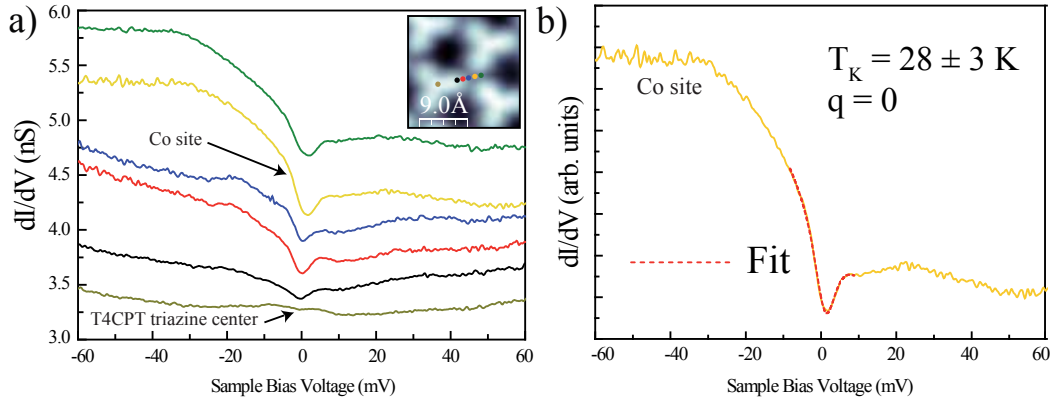
Figure 4.34: Differential conductance dI/dV spectra at several different positions of a Co-T4CPT island ($I_T = 2.5$ nA, $V_T = 67$ mV, $V_{ac} = 500$ μV rms at 897 Hz). The positions of the differential conductance dI/dV spectra are indicated in the small inset. (b) Differential conductance dI/dV spectrum at the Co site with a Fano fit. The best fit parameters are $q = 0$ and $T_K = 28 \pm 3$ K. The experimental settings were $T = 4.8$ K and $V_{rms} = 500$ μV rms.

ure 4.34(b) shows a Fano fit of this feature reproducing the experimental line shape. The fit includes a linear background. The best fit parameters are $q = 0$ and $T_K = 28 \pm 3$ K.

An important requirement for the Kondo effect to occur is, that there is spin $m_S = 1/2$ degenerated ground state, which interacts via spin-scattering processes with the conduction electrons of the surface (see section 3.3). Thus, the Co atoms in the Co-T4CPT network exhibit either a $S = 1/2$ or a $S = 3/2$ spin state with a easy-plane magnetic anisotropy [7]. However, further XMCD and XAS measurements have to be performed to clarify the spin state of the Co atoms within the Co-T4CPT islands and also for possible magnetic exchange coupling.

---

[7]Only then the $m_S = 1/2$ is the spin ground state (see section 4.2.2).

4.5.5   Conclusions

In conclusion, we demonstrated the effect of different functional end groups on the symmetry of metal-organic architectures. Co atoms and T4PB molecules with pyridine end groups form a bilayer Co-T4PB network, similar to the case of Fe-T4PT. Every Co atom is coordinated to three pyridine groups of three different T4PB molecules forming a three-fold bonding node. An additional T4PB molecule is located on top of each Co site. This finding indicates that the triazine ring of the topmost T4PB molecule is bonding by its π-system to the Co metal center. Additional STS measurements reveal the presence of inelastic tunneling feature at an energy of $\Delta = 4.7 \pm 0.4$ meV. The spatial distribution of this feature resembles the position and orientation of the topmost T4PB molecule. Combined with DFT simulations we tentatively identified this inelastic feature as a vibrational excitation of the topmost T4PB molecule of the Co-T4PB network.

The Co-T4CPT network also shows a three-fold coordination motif. Three cyano end groups of three different T4CPT molecules are linked by a central Co atom. In contrast to the Co-T4PB and Fe-T4PT network, the Co-T4CPT metal-organic network consists of a monolayer as revealed by its bias dependence. Apparently, the formation of the bilayer system is not favored. The single-layer formation suggests a strong metal-ligand recognition of the Co atoms and the T4CPT cyano termination groups. The absence of a second layer implies a lower number of ligands, which can lead to a smaller Co-surface distance. Thus, the hybridization with the underlying surface can become important. STS of the Co-T4CPT network reveals the presence of Fano-like feature close to the Fermi energy E_F at the Co sites, which can be identified as a Kondo resonance. Therefore, the Co magnetic moment is screened by the conduction electrons of the Au(111) metal surface.

The two discussed examples illustrate how the change of the molecular functional groups affects the resulting network architecture. In this regard, it would be interesting to study the impact of the different network architectures on the magnetic properties of the Co sites and also the magnetic exchange coupling, since we have clear indications that in the case of the Co-T4CPT system the Co-surface hybridization leads to a screening of the Co magnetic moment.

In the present thesis different classes of sub-monolayer supramolecular assemblies on metal surfaces were investigated by low-temperature STM, XAS, XMCD and DFT. The first part of the thesis focused on the charge distribution, charge transfer and the interactions with the underlying metal surface of adsorbed layers with components of organic and alkali materials having strong acceptor or donor character. The second part dealt with metal-organic networks with transition metals and investigated their structural, electronic, and magnetic properties.

As a first step we resolved the charge distribution in a monolayer formed by Na atoms and the organic acceptor TCNQ on a Au(111) metal surface by a combined approach of STM and DFT. Interestingly, the interaction of TCNQ molecules and Na atoms is sufficient to dissolve NaCl islands indicating a very strong donor-acceptor recognition. One electron is transferred from the Na atom to the TCNQ acceptor. STS reveals the spatial localization of a Kondo resonance, stemming from an unpaired electron, on top of the Na sites. Additional DFT calculations show that the Na $3s$ electron is transferred to the organic acceptor species TCNQ. Apparently, these two results contradict each other. Experimental and theoretical LDOS maps reveal that the TCNQ SOMO extends over the Na site, thus cloaking the positively charged Na atom. The spatial extension of the SOMO gives rise to the atypical spatial distribution of the Kondo resonance. In this respect, one important finding is that we have shown, how a molecular orbital deforms in the presence of a strong local charge. Another finding is that the Kondo effect survives, even though the corresponding molecular orbital is mainly localized above the cationic Na atoms. In this prospect, it would be interesting to exploit the influence of a localized charge on the Kondo effect to steer its local distribution and maybe to tune some of its unpaired spin properties like, for instance, the Kondo temperature T_K of the system.

The influence of the underlying surface on the electronic properties was negligible in the case of the Na-TCNQ system, but this is not the case for the two other compounds explored: Na-TNAP and TTF-TNAP. In the case of Na-TNAP two different TNAP species within the Na-TNAP layer are revealed. Only TNAP molecules adsorbed close to the soliton lines of the Au(111) herringbone reconstruction show a Kondo resonance implying a single unpaired electron in the TNAP SOMO. Since the bonding motif is the same throughout the Na-TNAP layer and a charge transfer with the underlying Au(111) surface can be excluded by the fact that the herringbone reconstruction is intact, all TNAP molecules are presumably charged with one electron. Hence, the absence of the Kondo effect for TNAP molecules at the fcc/hcp sites of the Au(111) surface is related to a different molecule-surface

interaction. Within the molecules, which show the Kondo resonance, its intensity is strongest at the Na site, similar to the case of Na-TCNQ and its line shape changes drastically along the TNAP backbone. This is explained within the Fano quantum interference picture. The Kondo line shape is the result of different competing tunneling paths, whose strength is changing gradually by moving from the Na sites to the TNAP center. This indicates that the three-dimensional extension of the SOMO orbital leads to different weights of the tunneling paths.

Adding TTF to a precovered TNAP/Au(111) sample triggers the self-assembling of ordered structures of alternating TNAP and TTF rows. The TTF-TNAP layer exhibits a strong interaction with the underlying surface indicated by the disappearance of the herringbone reconstruction of the Au(111) underneath the molecular layer. In this case, the lowest unoccupied molecular orbital (LUMO) of the free TNAP molecule shifts well below the Fermi level of the Au(111) metal substrate. The TNAP is thus charged with more than one electron. The enhanced charge transfer is attributed to a sizable interaction of the molecular layer with the Au(111) surface and the presence of the metal surface, which can not only act as an additional charge reservoir, but also can help to stabilize a high charge state by screening effects.

Another approach used in this thesis to grow ordered self-assembled nanostructures is based on the formation of metal-ligand bonds between transition metal atoms and functionalized molecules. Transition metal atoms allow to design networks with intriguing magnetic properties. Changing one of its components, either the organic linker or the metal atom, leads not only to new network architectures, but also changes electronic or magnetic properties of the system. We investigated four different networks consisting of different molecules and metal atoms: Cu-T4PT (1), Fe-T4PT (2), Co-T4PB (3), and Co-T4CPT (4). All molecules exhibit a triangular shape and differ in the type of functional end groups (T4PT: pyridine, T4PB: pyridine, T4CPT: benzonitrile) and the central ring (T4PT: triazine, T4PB: benzene, T4CPT: triazine)

An interesting aspect of such metal-organic networks is their adaptivity and robustness on different surfaces. We studied the metal-organic network of Cu atoms and the organic linker T4PT on a Cu(111) surface and Ag(111) surface, respectively. The structural and electronic properties of the thus formed Cu-T4PT networks are identical indicating the minor role of the underlying surface. The network architecture is mainly ruled by the metal-ligand bond. On both surfaces a hexagonal metal-organic network is formed, where two T4PT molecules are linked by a central Cu atom. The formation of the metal-ligand bond involves also a very small charge transfer of 0.03 e^- from Cu atom to the pyridine end groups of the T4PT molecule as revealed by DFT calculations. Further XAS and XMCD experiments reveal that the Cu atoms are in a d^{10} state and therefore have no magnetic moment.

The change of the $3d$ transition metal atom from Cu to Fe not only triggers a change of the network architecture, but also of its magnetic properties. The Fe-T4PT network shows a very intriguing double-layer structure even in the sub-monolayer regime. The first layer exhibits a three-fold bonding motif formed by three pyridine end groups of three T4PT molecules linked by a central Fe atom. An additional T4PT molecule is centered on top of the central Fe atom. This finding indicates a strong interaction of the central part of the top T4PT molecules with the Fe centers. The formation of a double-layer network structure is one important result of the present thesis and represents a promising route to reduce the interaction of metal atoms with the underlying substrate and at the same time to introduce a ligand field leading to magnetic anisotropy. Further XMCD measurements reveal that the Fe

atoms have a high-spin state $S = 2$ and an easy-axis magnetic anisotropy. Hence the Fe-T4PT network presents an ordered array of high spin metal atoms. Field-dependent magnetization curves reveal a ferromagnetic coupling between the Fe centers of the Fe-T4PT network with a Curie-temperature of $T_C = 1.9$ K. The ferromagnetic coupling is presumably mediated by the T4PT molecules by a superexchange interaction. Hence, the Fe-T4PT network demonstrates the unique occurrence of a magnetic coupling in a metal-organic network on a surface. This can be the starting point for the design of new magnetic materials for potential applications. In this prospect it is important to further increase the stability of a magnetic ground state of the network against thermal fluctuations. This can be done by designing new ligands which would lead to an increased magnetic anisotropy and coupling strength. Furthermore the present results also arise different questions for future investigations, for example to add new functionalities to the molecules, like switching components, to switch the magnetic coupling by an external stimulus "on" and "off".

By changing the functional end groups of the molecular linker we are able to trigger the formation of single or bilayer networks. Similar to the Fe-T4PT network also the Co-T4PB network exhibits a double-layer structure. STS measurements reveal the presence of a vibrational feature in the Co-T4PB network. Its spatial distribution coincides with localization of the pyridine end groups of the topmost T4PB molecule (second layer). The double-layer formation in the cases of Fe-T4PT and Co-T4PB evidences that the interaction of the topmost molecules with the metal sites is based on π-interactions rather than the formation of single metal-ligand bonds, since T4PB consists of a central benzene ring, in contrast, T4PT exhibits a triazine ring with nitrogen species.

The Co-T4CPT network shows only a single layer structure with a threefold bonding motif. While T4PB has pyridine end groups with N terminations, T4CPT exhibits benzonitrile end groups with cyano terminations. The absence of second-layer molecules is attributed to the stronger metal-ligand interaction between the cyano end groups of the T4CPT molecules and the Co atoms. The missing of an additional ligand on top of the Co sites provokes a larger interaction with the underlying metal surface. This manifests in a Kondo resonance at the Co sites of the Co-T4CPT network. In conclusion, the functionality of organic linkers has a significant impact on the resulting network architecture and implies also different interactions of the central metal atom with the underlying metal surface. These findings call for further investigations of the magnetic properties to study the influence of the different ligands and network architectures on properties like the magnetic anisotropy, coupling strength, etc..

The presented results on the structural, electronic and magnetic properties of molecule-based nanostructures on metal surfaces address several fundamental aspects regarding the functionalization of surfaces. From a technological viewpoint the charge distribution and charge transfer at the interface is of great importance, since these two effects determine other properties like the conductance, magnetism or catalytic reactivity. The findings also show that the combination of organic molecules and metal atoms is a promising pathway to grow ensembles of nanostructures with a high degree of order and intriguing magnetic properties. This is an important step towards the realization of molecular magnetic devices.

APPENDIX

A.1   Molecular Dynamics Calculations

Molecular dynamics (MD) simulations using the *Tinker* code [220] were employed to find the energetically most stable adsorption configurations of the organic molecules on the Au(111) metal surface investigated in the present thesis. The force field parameter set *MM*3 as implemented in the tinker code was used to described conjugated hydrocarbons [221]. The molecular dynamics simulations are based on the numerical solution of the Newton's equations of motion of each atom of the molecular system. Hence, every atom is described as a single particle. The potential energy of the total system is then calculated in terms of the force fields. The force fields or interatomic interactions are described by simple force constants (spring constants). MD simulations allow the adequate description of interatomic forces and distances of hydrocarbons.

The starting configuration consisted of three slabs of Au atoms with the dimension 65 x 65 x 10 Å^3 with the *Miller* indexes 111 and 15 TNAP molecules placed flat within a square lattice on the outermost Au(111) slab. The minimization protocol to find the energetically most stable adsorption configuration was as follows: an annealing algorithm cools the molecule/surface system exponentially from the starting temperature of 600 K to 0 K in 100000 steps in 1.0 fs. The annealing algorithm is followed by a subsequent minimization using the *newton* procedure and a target *RMS* gradient of 10^{-6}. This above described procedure is performed 10 times to ensure to find a energetic minimum. The most common adsorption configuration of the molecular ensemble was then used for a structural model with respect to the experimentally obtained adsorption configuration. The such obtained ground state configuration was again subject to further annealing algorithm from 80 K to 0 K in 100000 steps in 1.0 fs.

A.2   Computational Details of the Simulations of X-Ray Absorption Spectra

The structural optimization of the free T4PT molecule and the T4PT-$(CuH)_3$ cluster was done using the DZVP basis sets. In the calculation of the XA signals of the free T4PT molecule and the T4PT-

(CuH)$_3$ cluster, corresponding to core excitations of the carbon and the nitrogen species, the *IGLO −III type* ([$7s6p2d$]) basis sets [316] was applied for the core excited carbon or nitrogen centers. This allows the adequate description of the inner shell relaxation effects. The rest of the nitrogen and carbon centers are included as an effective core potentials (ECPs) for the 1s shell and [$3s3p1d$] valence basis sets. This prevents the mixing of the 1s core orbitals [317, 318] and also Ref. [319].

In the evaluation of the theoretical N 1s x-ray absorption spectra of the free T4PT molecule and the T4PT-(CuH)$_3$ cluster dipole transition from cores to unoccupied orbitals are considered [85]. The polarization-resolved spectral intensities $I(E, \vec{e})$ are obtained from the corresponding dipole transition matrix elements $\vec{m} = (m_x, m_y, m_z)$ and the angle-dependent factors of the incoming x-ray beam, which is described by the polarization vector $\vec{e} = (e_x, e_y, e_z)$. Hence, the polarization-resolved spectral intensities $I(E, \vec{e})$ reads as follows:

$$I(E, \vec{e}) = \kappa \cdot E \cdot (\vec{m} \cdot \vec{e})^2, \ m = \langle \phi_f | q \cdot r | \phi_{core} \rangle. \tag{A.1}$$

Where κ corresponds to a scaling factor, the parameter E describes the transition energy, and the transition dipole vectors m imply the initial core orbital ϕ_{core} and final excited state orbitals ϕ_f.

Free gas phase T4PT molecules are randomly orientated in space, hence, the calculated spectral intensities $I(E, \vec{e})$ of (A.1) have to be averaged over all polarization directions $\vec{e}$ for comparison with the experimental data. The polarization-averaged intensities $I(E)$ reads:

$$I(E) = \int \int I(E, \vec{e}) d\Omega = \frac{2\pi}{3} \cdot \kappa \cdot E \cdot (m_x^2 + m_y^2 + m_z^2). \tag{A.2}$$

However, in the present case, the T4PT molecules are adsorbed on a metal surface forming self-assembled planar networks. On both the Ag(111) and Cu(111) surfaces the spectral intensities $I(E, \vec{e})$ have to be averaged over all azimuthal polarization (or x-ray beam) directions $\vec{e}$ with respect to the surface normal for comparing the theoretical and experimental spectra. The intensity $I(E, \Theta)$ as function of the polar angle Θ of the polarization vector $\vec{e}$ reads:

$$I(E, \Theta) = \int I(E, \Theta) d\phi. \tag{A.3}$$

Comparing the two above described intensities $I(E, \Theta)$ and $I(E)$ for the magic angle Θ_{magic} = 54.7° yields:

$$I(E, \Theta_{magic}) = \pi \cdot \kappa \cdot E \cdot (m_x^2 + m_y^2 + m_z^2) cos^2(\Theta_{magic}) = \frac{1}{2} I(E). \tag{A.4}$$

A transition potential approach [320] in combination with a double basis set technique [321] is used to calculate the core excited final states and the corresponding transition energies E and dipole matrix elements m. The approach relies on the application of a half occupied 1s core orbital at the excitation centers in the T4PT molecule and the T4PT-(CuH)$_3$ cluster including the partial electronic relaxation due to the presence of the excited electron. The above described approach accounts for final state relaxation effects up to second order in the energy. Hence, a balance between the two relaxation mechanisms (core and valence type) is achieved [322]. In order to simulate the instrumental, vibrational, and life-time broadening the transition energies E and corresponding dipole transition matrix elements m are convoluted with Gaussian function with a full width at half maximum (FWHM) value of 0.7 eV below the ionization threshold. The broadening is linearly increased to 4 eV up to 10 eV above threshold.

Vibrational Modes		
Mode	Energy (meV)	
	6-31G	6-311G
1	5.21	5.51
2	5.57	5.80
3	5.74	5.82
4	5.95	6.08
5	7.17	7.21
6	7.43	7.49
7	14.47	14.50

Table A.1:   The vibrational modes of the T4PT molecule using the B3PYL (B3PW91) functional with the 6-311G (6-31G) basis set.

The above discussed potential approach does not fully account for the electronic core hole relaxation of the excited final state. This effect can be corrected by shifting all excitation energies by the difference of the ionization potential computed with the transition potential method and the corresponding value from Δ Kohn-Sham (ΔSCF) calculations. Hence, the excitation energies of nitrogen are shifted about 1.5 to 1.8 eV and the ones of the carbon about 1.3 to 1.7 eV. In order to account for relativistic effects a further upward shift of the computed spectra by 0.18 eV for nitrogen and 0.08 eV for carbon is applied [323]. A detailed description of the presented method is given in the References [320, 321, 324–326]. Many examples proof the validity of the here described method [325–335].

A.3   Molecular Vibrations of T4PB

We calculated the vibrational modes of the free T4PB molecule using DFT based approach. For the calculation of the vibrational excitation spectrum the molecular structure of the T4PB molecule was first optimized. The results using the B3PYL (B3PW91) functional and the 6-31G (6-311G) basis set is summarized in Table A.1(Table A.1). In total 111 different vibrational modes can be identified.

CFS- Crystal Field Splitting
DFT- Density Functional Theory
DOS- Density of States
ECP- Effective Core Potentials
FWHM- Full Width Half Maximum
HOMO- Highest Occupied Molecular Orbital
LDOS- Local Density of States
LUMO- Lowest Unoccupied Molecular Orbital
MOT- molecular orbital theory
PDOS- Projected Density of States
T4PB- 1,3,5-Tri(pyridin-4-yl)benzene
T4PT- 2,4,6-tris(4-pyridyl)-1,3,5-triazine
T4CPT- 2,4,6-Tris(4-benzonitrile)-1,3,5-triazine
TCNQ- 7,7,8,8-tetracyanoquinodimethane
TNAP- 11,11,12,12-tetracyanonaptho-2,6-quinodimethane
TTF- Tetrathiafulvalene
SOMO- Singly Occupied Molecular Orbital
STM- Scanning Tunneling Microscopy
STS- Scanning Tunneling Spectroscopy
SUMO- Singly Unoccupied Molecular Orbital
XA- X-ray Absorption
XAS- X-ray Absorption Spectroscopy
XMCD- X-ray Magnetic Circular Dichroism
ZBR- Zero Bias Resonance
ZFS- Zero Field Splitting

C

PUBLICATIONS AND PRESENTATIONS

Publications

- *Enhanced Charge Transfer in a Monolayer of the Organic Charge Transfer Complex TTF-TNAP on Au(111)* by T. R. Umbach, I. Fernández-Torrente, J. Ladenthin, J. I. Pascual, K. J. Franke *J. Phys. Condens. Matter* **2012**, 5, 354003

- *Ferromagnetic Coupling of Mononuclear Fe Centers in a Self-Assembled Metal-Organic Network on Au(111)* by T. R. Umbach, M. Bernien, C. F. Hermanns, A. Krüger, V. Sessi, I. Fernández-Torrente, P. Stoll, J. I. Pascual, K. J. Franke, W. Kuch *Phys. Rev. Lett.*, **2012**, 109, 267207.

- *Atypical Charge Redistribution over a Charge-Transfer Monolayer on a Metal Surface* by T. R. Umbach, I. Fernńdez-Torrente, M. Ruby, F. Schulz, C. Lotze, R. Rurali, M. Persson, J. I. Pascual, K. J. Franke *New Journal of Physics* **2013**, accepted

- *Combined STM and XAS Study of a Metal-Organic Network* by T. R. Umbach, M. Bernien, C. F. Hermanns, K. Hermann, L. Sun, H. Mohrmann, A. Krüger, N. Krane , Z. Yang, K. J. Franke, J. I. Pascual, W. Kuch in preparation

Talks and Poster

- 2010 March T. R. Umbach, R. Drost, I. Fernández-Torrente, J. I. Pascual, K.J. Franke "Doped charge transfer salts" (Talk) DPG Spring Meeting of the Condensed Matter Section, Dresden

- 2011 March T. R. Umbach, I. Fernández-Torrente, J. Ladenthin, M. Kleinert, R. Drost, Ri. Rurali, J. I. Pascual, and K. J. Franke "Interplay of acceptor and donor species in charge-transfer complexes" (Talk) DPG Spring Meeting of the Condensed Matter Section, Regensburg

  T. R. Umbach, C. F. Hermanns, A. Krüger, Z. Yang, I. Fernández-Torrente, N. Krane, M. Bernien, C. Czekelius, K. J. Franke, J. I. Pascual and W. Kuch "Structure and magnetism of Mn-tetrapyridyl porphyrin molecules on Ag(111)"(Poster) DPG Spring Meeting of the Condensed Matter Section, Regensburg

- 2011 August T. R. Umbach, I. Fernández-Torrente, M. Kleinert, R. Drost, J. I. Pascual, and K. J. Franke "Local charge distribution in self-assembled donor-acceptor complexes on Au(111)" (Talk) ECOSS, Breslau

- 2012 March T. R. Umbach, I. Fernández-Torrente, J. I. Pascual, and K. J. Franke "Local charge distribution in self-assembled donor-acceptor complexes on Au(111)" (Poster) DPG Spring Meeting of the Condensed Matter Section, Berlin

  T. R. Umbach, C. F. Hermanns, M. Bernien, A. Krüger, I. Fernández-Torrente, P. Stoll, K. J. Franke , J. I. Pascual, and W. Kuch "Magnetic coupling in metal organic networks on surfaces" (Talk) DPG Spring Meeting of the Condensed Matter Section, Berlin

- 2012 July T. R. Umbach, I. Fernández-Torrente, M. Kleinert, M. Persson, R. Rurali, J. I. Pascual, and K. J. Franke "Intramolecular charge distribution in a doped organic electron acceptor: Na-TCNQ on Au(111)" (Talk) ICN+T 2012, Paris

- 2012 September T. R. Umbach, I. Fernńdez-Torrente, J. Ladenthin, M. Kleinert, R. Drost, R. Rurali, J. I. Pascual, and K. J. Franke "Charge transfer process inside self-assembled Na-TCNQ complex on Au(111)" (Talk) SOS12 and SPSTM 4 2012, Timmendorfer Strand

- 2013 March T. R. Umbach, M. Bernien, C. Hartmann, A. Krüger, J. N. Ladenthin, C. Czekelius, K. J. Franke, J. I. Pascual, and W. Kuch "Structural and magnetic properties of pyridyl and benzonitrile-based metal-organic networks" (Talk) DPG Spring Meeting of the Condensed Matter Section 2013, Regensburg

Invited Talks

- 2012 June T. R. Umbach "Charge transfer complexes on metal surfaces" (invited Talk) AG Sokolowski, department of theoretical and physical chemistry, Bonn

- 2013 February T. R. Umbach " Magnetism of metal-organic networks on metal surfaces" "Charge transfer process inside self-assembled Na-TCNQ complex on Au(111)" (invited Talk) IBM, Zürich

Bibliography

[1] Ferain, I., Colinge, C. A., and Colinge, J.-P. *Nature* **479**(7373), 310–316 (2011).

[2] UMC bekennt sich zur 20-Nanometer-Fertigungstechnik (web site article). July (2012). visted July 20th 2013, http://www.heise.de/ct/meldung/UMC-bekennt-sich-zur-20-Nanometer-Fertigungstechnik-1630001.html.

[3] Wettrennen um 14-Nanometer-Technik (web site article). December (2012). visted July 20th 2013, http://www.heise.de/ct/meldung/Wettrennen-um-14-Nanometer-Technik-1774147.html.

[4] Ito, T. and Okazaki, S. *Nature* **406**(6799), 1027–1031 (2000).

[5] Zhirnov, V., Cavin, R., Hutchby, J., and Bourianoff, G. *Proc. IEEE* **91**(11), 1934–1939 (2003).

[6] Feynman, R. P. *Eng. Sci.* **23**, 2236 (1960).

[7] Fuechsle, M., Miwa, J. A., Mahapatra, S., Ryu, H., Lee, S., Warschkow, O., Hollenberg, L. C. L., Klimeck, G., and Simmons, M. Y. *Nat. Nano.* **7**(4), 242–246 (2012).

[8] Song, H., Kim, Y., Jang, Y. H., Jeong, H., Reed, M. A., and Lee, T. *Nature* **462**(7276), 1039–1043 (2009).

[9] Binnig, G., Rohrer, H., Gerber, C., and Weibel, E. *Phys. Rev. Lett.* **49**, 57–61 (1982).

[10] Binnig, G., Quate, C. F., and Gerber, C. *Phys. Rev. Lett.* **56**, 930–933 (1986).

[11] Loth, S., Baumann, S., Lutz, C. P., Eigler, D. M., and Heinrich, A. J. *Science* **335**(6065), 196–199 (2012).

[12] Crommie, M. F., Lutz, C. P., and Eigler, D. M. *Science* **262**(5131), 218–220 (1993).

[13] Khajetoorians, A. A., Wiebe, J., Chilian, B., Lounis, S., Blügel, S., and Wiesendanger, R. *Nat. Phys.* **8**(6), 497–503 (2012).

[14] Gomes, K. K., Mar, W., Ko, W., Guinea, F., and Manoharan, H. C. *Nature* **483**(7389), 306–310 (2012).

[15] Barth, J. V. *Ann. Rev. Phys. Chem* **58**, 375–407 (2007).

[16] Li, Y., Xiao, J., Shubina, T. E., Chen, M., Shi, Z., Schmid, M., Steinrck, H.-P., Gottfried, J. M., and Lin, N. *J. Am. Chem. Soc.* **134**(14), 6401–6408 (2012).

[17] Gambardella, P., Stepanow, S., Dmitriev, A., Honolka, J., de Groot, F. M. F., Lingenfelder, M., Gupta, S. S., Sarma, D. D., Bencok, P., Stanescu, S., Clair, S., Pons, S., Lin, N., Seitsonen, A. P., Brune, H., Barth, J. V., and Kern, K. *Nat. Mat.* **8**(3), 189–193 (2009).

[18] Stepanow, S., Lin, N., Payer, D., Schlickum, U., Klappenberger, F., Zoppellaro, G., Ruben, M., Brune, H., Barth, J. V., and Kern, K. *Angew. Chem., Int. Ed.* **46**(5), 710–713 (2007).

[19] Shi, Z., Liu, J., Lin, T., Xia, F., Liu, P. N., and Lin, N. *J. Am. Chem. Soc.* **133**(16), 6150–6153 (2011).

[20] Stepanow, S., Lin, N., and Barth, J. V. *J. Phys.: Condens. Matter* **20**(18), 184002 (2008).

[21] Stepanow, S., Lingenfelder, M., Dmitriev, A., Spillmann, H., Delvigne, E., Lin, N., Deng, X., Cai, C., Barth, J. V., and Kern, K. *Nat. Mater.* **3**(4), 229–233 (2004).

[22] Tait, S. L., Langner, A., Lin, N., Stepanow, S., Rajadurai, C., Ruben, M., and Kern, K. *J. Phys. Chem. C* **111**(29), 10982–10987 (2007).

[23] Barth, J. V., Weckesser, J., Cai, C., Gänter, P., Bärgi, L., Jeandupeux, O., and Kern, K. *Angew. Chem., Int. Ed.* **39**(7), 1230–1234 (2000).

[24] Fernández-Torrente, I., Monturet, S., Franke, K. J., Fraxedas, J., Lorente, N., and Pascual, J. I. *Phys. Rev. Lett.* **99**(17), 176103 (2007).

[25] Fernández-Torrente, I., Kreikemeyer-Lorenzo, D., Strzecka, A., Franke, K. J., and Pascual, J. I. *Phys. Rev. Lett.* **108**, 036801 (2012).

[26] Pawin, G., Wong, K. L., Kwon, K.-Y., and Bartels, L. *Science* **313**(5789), 961–962 (2006).

[27] Otero, R., Lukas, M., Kelly, R. E. A., Xu, W., Lgsgaard, E., Stensgaard, I., Kantorovich, L. N., and Besenbacher, F. *Science* **319**(5861), 312–315 (2008).

[28] Schlickum, U., Decker, R., Klappenberger, F., Zoppellaro, G., Klyatskaya, S., Ruben, M., Silanes, I., Arnau, A., Kern, K., Brune, H., and Barth, J. V. *Nano Lett.* **7**(12), 3813–3817 (2007).

[29] Fernández-Torrente, I., Franke, K. J., and Pascual, J. I. *Phys. Rev. Lett.* **101**(21), 217203 (2008).

[30] Theobald, J. A., Oxtoby, N. S., Phillips, M. A., Champness, N. R., and Beton, P. H. *Nature* **424**(6952), 1029–1031 (2003).

[31] Altman, E. I. and Colton, R. J. *Phys. Rev. B* **48**, 18244–18249 (1993).

[32] Rogero, C., Pascual, J. I., Gomez-Herrero, J., and M. Baro, A. *J. Chem. Phys.* **116**, 832 (2002).

[33] Wäckerlin, C., Iacovita, C., Chylarecka, D., Fesser, P., Jung, T. A., and Ballav, N. *Chem. Commun.* **47**, 9146–9148 (2011).

[34] Clark, C., Hassanien, A., Khan, S., Braun, K.-F., Tanaka, H., and Hla, S.-W. *Nat. Nano.* **5**(4), 261–265 (2010).

[35] Abdurakhmanova, N., Floris, A., Tseng, T.-C., Comisso, A., Stepanow, S., deVita, A., and Kern, K. *Nat. Commun.* **3**, 940 (2012).

[36] Gambardella, P., Rusponi, S., Veronese, M., Dhesi, S. S., Grazioli, C., Dallmeyer, A., Cabria, I., Zeller, R., Dederichs, P. H., Kern, K., Carbone, C., and Brune, H. *Science* **300**(5622), 1130–1133 (2003).

[37] Grill, L., Dyer, M., Lafferentz, L., Persson, M., Peters, M. V., and Hecht, S. *Nat. Nano.* **2**(11), 687–691 (2007).

[38] Lafferentz, L., Eberhardt, V., Dri, C., Africh, C., Comelli, G., Esch, F., Hecht, S., and Grill, L. *Nat. Chem.* **4**(3), 215–220 (2012).

[39] Hanke, F. and Björk, J. *Phys. Rev. B* **87**, 235422 (2013).

[40] Mugarza, A., Lorente, N., Ordejón, P., Krull, C., Stepanow, S., Bocquet, M.-L., Fraxedas, J., Ceballos, G., and Gambardella, P. *Phys. Rev. Lett.* **105**, 115702 (2010).

[41] Sun, J. T., Gao, L., He, X. B., Cheng, Z. H., Deng, Z. T., Lin, X., Hu, H., Du, S. X., Liu, F., and Gao, H.-J. *Phys. Rev. B* **83**, 115419 (2011).

[42] Ishii, H., Sugiyama, K., Ito, E., and Seki, K. *Adv. Mater.* **11**(8), 605–625 (1999).

[43] Braun, S., Salaneck, W. R., and Fahlman, M. *AdV. Mater.* **21**(14-15), 1450–1472 (2009).

[44] Torrente, I. F., Franke, K. J., and Pascual, J. I. *J. Phys.: Condens. Matter* **20**(18), 184001 (2008).

[45] Bode, M. *Rep. Prog. Phys.* **66**(4), 523 (2003).

[46] Zhang, R., Zhang, Y., Dong, Z. C., Jiang, S., Zhang, C., Chen, L. G., Zhang, L., Liao, Y., Aizpurua, J., Luo, Y., Yang, J. L., and Hou, J. G. *Nature* **498**(7452), 82–86 (2013).

[47] Wu, S. W., Nazin, G. V., and Ho, W. *Phys. Rev. B* **77**, 205430 (2008).

[48] Chen, C., Bobisch, C. A., and Ho, W. *Science* **325**(5943), 981–985 (2009).

[49] Schneider, N. L., Lü, J. T., Brandbyge, M., and Berndt, R. *Phys. Rev. Lett.* **109**, 186601 (2012).

[50] Schneider, N. L. and Berndt, R. *Phys. Rev. B* **86**, 035445 (2012).

[51] Berndt, R., Gaisch, R., Gimzewski, J. K., Reihl, B., Schlittler, R. R., Schneider, W. D., and Tschudy, M. *Science* **262**(5138), 1425–1427 (1993).

[52] Tersoff, J. and Hamann, D. R. *Phys. Rev. B* **31**(2), 805–813 (1985).

[53] Chen, W., Madhavan, V., Jamneala, T., and Crommie, M. F. *Phys. Rev. Lett.* **80**(7), 1469–1472 (1998).

[54] Bardeen, J. *Phys. Rev. Lett.* **6**, 57–59 (1961).

[55] Lang, N. D. *Phys. Rev. B* **34**, 5947–5950 (1986).

[56] Selloni, A., Carnevali, P., Tosatti, E., and Chen, C. D. *Phys. Rev. B* **31**, 2602–2605 (1985).

[57] Gross, L., Moll, N., Mohn, F., Curioni, A., Meyer, G., Hanke, F., and Persson, M. *Phys. Rev. Lett.* **107**, 086101 (2011).

[58] Gonzalez-Lakunza, N., Fernández-Torrente, I., Franke, K. J., Lorente, N., Arnau, A., and Pascual, J. I. *Phys. Rev. Lett.* **100**(15), 156805 (2008).

[59] Bjork, J., Matena, M., Dyer, M. S., Enache, M., Lobo-Checa, J., Gade, L. H., Jung, T. A., Stohr, M., and Persson, M. *Phys. Chem. Chem. Phys.* **12**, 8815–8821 (2010).

[60] Seitsonen, A. P., Lingenfelder, M., Spillmann, H., Dmitriev, A., Stepanow, S., Lin, N., Kern, K., and Barth, J. V. *J. Am. Chem. Soc.* **128**(17), 5634–5635 (2006).

[61] Franke, K. J., Schulze, G., Henningsen, N., Fernández-Torrente, I., Pascual, J. I., Zarwell, S., Rück-Braun, K., Cobian, M., and Lorente, N. *Phys. Rev. Lett.* **100**, 036807 (2008).

[62] Zandvliet, H. J. and van Houselt, A. *Annu. Rev. Anal. Chem.* **2**, 37–55 (2009).

[63] Wiesendanger, R. *Scanning Probe Microscopy and Spectroscopy*. Cambrdige University Press, (1994).

[64] Feenstra, R. M. *Phys. Rev. B* **50**, 4561–4570 (1994).

[65] Feenstra, R., Stroscio, J. A., and Fein, A. *Surface Science* **181**(12), 295 – 306 (1987).

[66] Klein, J., Léger, A., Belin, M., Défourneau, D., and Sangster, M. J. L. *Phys. Rev. B* **7**, 2336–2348 (1973).

[67] Singh, U. R., Enayat, M., White, S. C., and Wahl, P. *Rev. Sci. Instrum.* **84**(1), 013708 (2013).

[68] Lambe, J. and Jaklevic, R. C. *Phys. Rev.* **165**, 821–832 (1968).

[69] Kröger, J., Limot, L., Jensen, H., Berndt, R., Crampin, S., and Pehlke, E. *Prog. Surf. Sci.* **80**(1-2), 26 – 48 (2005).

[70] Binnig, G., Frank, K. H., Fuchs, H., Garcia, N., Reihl, B., Rohrer, H., Salvan, F., and Williams, A. R. *Phys. Rev. Lett.* **55**, 991–994 (1985).

[71] Becker, R. S., Golovchenko, J. A., and Swartzentruber, B. S. *Phys. Rev. Lett.* **55**, 987–990 (1985).

[72] Wahl, P. *Local Spectroscopy of Correlated Electron Systems at Metal Surfaces*. PhD thesis, University of Konstanz, (2005).

[73] Hörmandinger, G. *Phys. Rev. B* **49**, 13897–13905 (1994).

[74] Wagner, C., Franke, R., and Fritz, T. *Phys. Rev. B* **75**, 235432 (2007).

[75] Ziegler, M., Néel, N., Sperl, A., Kröger, J., and Berndt, R. *Phys. Rev. B* **80**, 125402 (2009).

[76] Krenner, W., Kühne, D., Klappenberger, F., and Barth, J. V. *Sci. Rep.* **3**, 1–7 (2013).

[77] Ho, W. *J. Chem. Phys* **117**, 11033 (2002).

[78] Pascual, J. I. *Eur. Phys. J. D* **35**, 327–340 (2005).

[79] Heinrich, A. J., Gupta, J. A., Lutz, C. P., and Eigler, D. M. *Science* **306**, 5695 (2006).

[80] Franke, K. J. and Pascual, J. I. *Journal of Physics: Condensed Matter* **24**(39), 394002 (2012).

[81] Gauyacq, J.-P., Lorente, N., and Novaes, F. D. *Prog. Surf. Sci.* **87**(5-8), 63 – 107 (2012).

[82] Pavliček, N., Swart, I., Niedenführ, J., Meyer, G., and Repp, J. *Phys. Rev. Lett.* **110**, 136101 (2013).

[83] Loth, S., Lutz, C. P., and Heinrich, A. J. *New J. Phys.* **12**(12), 125021 (2010).

[84] Stöhr, J. *J. Electr. Spectr. Rel. Phen.* **75**(0), 253 – 272 (1995).

[85] Stöhr, J. *NEXAFS spectroscopy.* Springer, Berlin, New York,, (1992).

[86] Hubbell, J. H., Gimm, H. A., and Overbo, I. *Journal of Physical and Chemical Reference Data* **9**(4), 1023–1148 (1980).

[87] Stöhr, J. and Siegmann, H. *Magnetism.* Springer, (2006).

[88] Stöhr, J. *J. Magn. Magn. Mater* **200**(1-3), 470 – 497 (1999).

[89] Kapusta, C., Fischer, P., and Schütz, G. *J. All. Comp.* **286**(1-2), 37 – 46 (1999).

[90] Kuch, W. *Abbildende magnetische Mikrospektroskopie*. (2002).

[91] Carra, P., Thole, B. T., Altarelli, M., and Wang, X. *Phys. Rev. Lett.* **70**, 694–697 (1993).

[92] Thole, B. T., Carra, P., Sette, F., and van der Laan, G. *Phys. Rev. Lett.* **68**, 1943–1946 (1992).

[93] Stöhr, J. and König, H. *Phys. Rev. Lett.* **75**, 3748–3751 (1995).

[94] Stöhr, J. *J. Electr. Spectr. Rel. Phen.* **75**(0), 253 – 272 (1995).

[95] Šipr, O., Minŕ, J., and Ebert, H. *EPL (Europhysics Letters)* **87**(6), 67007 (2009).

[96] Kuch, W., Gao, X., and Kirschner, J. *Phys. Rev. B* **65**, 064406 (2002).

[97] Bruno, P. *Phys. Rev. B* **39**, 865–868 (1989).

[98] Weller, D., Stöhr, J., Nakajima, R., Carl, A., Samant, M. G., Chappert, C., Mégy, R., Beauvillain, P., Veillet, P., and Held, G. A. *Phys. Rev. Lett.* **75**, 3752–3755 (1995).

[99] Li, J., Schneider, W.-D., Berndt, R., Bryant, O. R., and Crampin, S. *Phys. Rev. Lett.* **81**(20), 4464–4467 (1998).

[100] Barth, J. V., Brune, H., Ertl, G., and Behm, R. J. *Phys. Rev. B* **42**, 9307–9318 (1990).

[101] Wang, Y., Hush, N. S., and Reimers, J. R. *Phys. Rev. B* **75**, 233416 (2007).

[102] Komeda, T., Isshiki, H., and Liu, J. *Sci. Technol. Adv. Mater* **11**(5), 054602 (2010).

[103] Cheng, Z. H., Gao, L., Deng, Z. T., Liu, Q., Jiang, N., Lin, X., He, X. B., Du, S. X., and Gao, H.-J. *J. Phys. Chem. C* **111**(6), 2656–2660 (2007).

[104] Cheng, Z. H., Gao, L., Deng, Z. T., Jiang, N., Liu, Q., Shi, D. X., Du, S. X., Guo, H. M., and Gao, H.-J. *J. Phys. Chem. C* **111**(26), 9240–9244 (2007).

[105] Min, B., Alemozafar, A., Biener, M., Biener, J., and Friend, C. *Topics in Catalysis* **36**(1-4), 77–90 (2005).

[106] Soe, W.-H., Manzano, C., De Sarkar, A., Chandrasekhar, N., and Joachim, C. *Phys. Rev. Lett.* **102**, 176102 (2009).

[107] Comstock, M. J., Cho, J., Kirakosian, A., and Crommie, M. F. *Phys. Rev. B* **72**, 153414 (2005).

[108] Böhringer, M., Morgenstern, K., Schneider, W.-D., Berndt, R., Mauri, F., De Vita, A., and Car, R. *Phys. Rev. Lett.* **83**, 324–327 (1999).

[109] Chambliss, D. D., Wilson, R. J., and Chiang, S. *Phys. Rev. Lett.* **66**(13), 1721–1724 (1991).

[110] Zöphel, S. *Der Aufbau eines Tieftemperatur-Rastertunnelmikroskops und Strukturunter-suchungen auf vicinalen Kupferoberflche.* PhD thesis, Fu Berin, (2000).

[111] Horcas, I., Fernndez, R., Gomez-Rodrguez, J. M., Colchero, J., Gomez-Herrero, J., and Baro, A. M. *Rev. Sci. Instrum.* **78**(1), 013705 (2007).

[112] Bernien, M. *X-Ray Absorption Spectroscopy of Fe Complexes on Surfaces: Electronic Inter-actions and Tailoring of the Magnetic Coupling.* PhD thesis, FU Berlin, (2009).

[113] Li, G., Shrotriya, V., Huang, J., Yao, Y., Moriarty, T., Emery, K., and Yang, Y. *Nat. Mater.* **4**(11), 864–868 (2005).

[114] Gänes, S., Neugebauer, H., and Sariciftci, N. S. *Chem. Rev.* **107**(4), 1324–1338 (2007).

[115] Samuel, I. D. W. and Turnbull, G. A. *Chem. Rev.* **107**(4), 1272–1295 (2007).

[116] Dimitrakopoulos, C. and Malenfant, P. *AdV. Mater.* **14**(2), 99–117 (2002).

[117] Braga, D. and Horowitz, G. *AdV. Mater.* **21**(14-15), 1473–1486 (2009).

[118] Baldo, M. A., O'Brien, D. F., You, Y., Shoustikov, A., Sibley, S., Thompson, M. E., and Forrest, S. R. *Nature* **395**(6698), 151–154 (1998).

[119] Grimsdale, A. C., Leok Chan, K., Martin, R. E., Jokisz, P. G., and Holmes, A. B. *Chem. Rev.* **109**(3), 897–1091 (2009).

[120] Xiao, L., Chen, Z., Qu, B., Luo, J., Kong, S., Gong, Q., and Kido, J. *AdV. Mater.* **23**(8), 926–952 (2011).

[121] Kahn, A., Koch, N., and Gao, W. *J. Polym. Sci.: Part B: Polym. Phys.* **41**(21), 2529–2548 (2003).

[122] Pennec, Y., Auwarter, W., Schiffrin, A., Weber-Bargioni, A., Riemann, A., and Barth, J. V. *Nat. Nano.* **2**(2), 99–103 (2007).

[123] Klappenberger, F., Kühne, D., Krenner, W., Silanes, I., Arnau, A., Garciá de Abajo, F. J., Klyatskaya, S., Ruben, M., and Barth, J. V. *Phys. Rev. Lett.* **106**, 026802 (2011).

[124] Lobo-Checa, J., Matena, M., Mller, K., Dil, J. H., Meier, F., Gade, L. H., Jung, T. A., and Sthr, M. *Science* **325**(5938), 300–303 (2009).

[125] Allemand, P.-M., Khemani, K. C., Koch, A., Wudl, F., Holcer, K., Donovan, S., Grner, G., and Thompson, J. D. *Science* **253**(5017), 301–302 (1991).

[126] Narymbetov, B., Omerzu, A., Kabanov, V. V., Tokumoto, M., Kobayashi, H., and Mihailovic, D. *Nature* **407**(6806), 883–885 (2000).

[127] Blundell, S. J. and Pratt, F. L. *J. Phys.: Condens. Matter* **16**(24), R771 (2004).

[128] Ferlay, S., Mallah, T., Ouahes, R., Veillet, P., and Verdaguer, M. *Nature* **378**, 701–703 (1995).

[129] Nalwa, H. S. *AdV. Mater.* **5**(5), 341–358 (1993).

[130] Krishnan, A., Pal, S., Nandakumar, P., Samuelson, A., and Das, P. *Chem. Phys.* **265**(3), 313 – 322 (2001).

[131] Matsuzaki, H., Fujita, W., Awaga, K., and Okamoto, H. *Phys. Rev. Lett.* **91**(1), 017403 (2003).

[132] Okamoto, H., Ikegami, K., Wakabayashi, T., Ishige, Y., Togo, J., Kishida, H., and Matsuzaki, H. *Phys. Rev. Lett.* **96**(3), 037405 (2006).

[133] Uji, S., Shinagawa, H., Terashima, T., Yakabe, T., Terai, Y., Tokumoto, M., Kobayashi, A., Tanaka, H., and Kobayashi, H. *Nature* **410**, 908–91 (2001).

[134] Kushch, N. D., Dyachenko, O. A., Lyubovskii, R. B., Pesotskii, S. I., Kartsovnik, M. V., Kovalev, A. E., Cassoux, P., and Kobayashi, H. *Adv. Mater. Opt. Electron.* **7**(2), 57–60 (1997).

[135] Kobayashi, A., Udagawa, T., Tomita, H., Naito, T., and Kobayashi, H. *Chem. Lett.* **22**(12), 2179–2182 (1993).

[136] Nam, M.-S., Ardavan, A., Blundell, S. J., and Schlueter, J. A. *Nature* **449**, 584–587 (2007).

[137] Jäckel, F., Watson, M. D., Müllen, K., and Rabe, J. P. *Phys. Rev. Lett.* **92**, 188303 (2004).

[138] Koch, N., Duhm, S., Rabe, J. P., Vollmer, A., and Johnson, R. L. *Phys. Rev. Lett.* **95**, 237601 (2005).

[139] Samorí, P., Severin, N., Simpson, C. D., Müllen, K., and Rabe, J. P. *J. Am. Chem. Soc.* **124**(32), 9454–9457 (2002).

[140] Gong, J.-R., Wan, L.-J., Lei, S.-B., Bai, C.-L., Zhang, X.-H., and Lee, S.-T. *J. Phys. Chem. B* **109**(5), 1675–1682 (2005).

[141] Keil, M., Samori, P., dos Santos, D. A., Birgerson, J., Friedlein, R., Dkhissi, A., Watson, M., Mullen, K., Bredas, J. L., Rabe, J. P., and Salaneck, W. R. *J. Chem. Phys* **116**(24), 10854–10860 (2002).

[142] Gao, W. and Kahn, A. *Appl. Phys. Lett.* **79**(24), 4040–4042 (2001).

[143] Xue, J. and Forrest, S. R. *Phys. Rev. B* **69**, 245322 (2004).

[144] Blochwitz, J., Pfeiffer, M., Fritz, T., and Leo, K. *Appl. Phys. Lett.* **73**(6), 729–731 (1998).

[145] Toyota, N., Lang, M., and Müller, J. *Low-Dimensional Molecular Metals*. Springer, (2007).

[146] Mulliken, R. S. *J. Am. Chem. Soc.* **74**(3), 811–824 (1952).

[147] Metzger, R. M. *J. Chem. Phys* **57**(5), 2218–2219 (1972).

[148] Metzger, R. M. *J. Am. Chem. Soc.* **66**(6), 2525–2533 (1977).

[149] Harutyunyan, H., Callsen, M., Allmers, T., Caciuc, V., Blügel, S., Atodiresei, N., and Wegner, D. *Chem. Commun.* **49**, 5993–5995 (2013).

[150] Brede, J., Atodiresei, N., Kuck, S., Lazić, P., Caciuc, V., Morikawa, Y., Hoffmann, G., Blügel, S., and Wiesendanger, R. *Phys. Rev. Lett.* **105**, 047204 (2010).

[151] Jrome, D. *Chem. Rev.* **104**(11), 5565–5592 (2004).

[152] Khanna, S. K., Pouget, J. P., Comes, R., Garito, A. F., and Heeger, A. J. *Phys. Rev. B* **16**(4), 1468–1479 (1977).

[153] Haas, W. D. and Berg, G. V. D. *Physica* **3**(6), 440 – 449 (1936).

[154] Sarachik, M. P., Corenzwit, E., and Longinotti, L. D. *Phys. Rev.* **135**, A1041–A1045 (1964).

[155] Kondo, J. *Phys. Rev.* **169**, 437–440 May (1968).

[156] Hewson, A. C. *The Kondo Problem to Heavy Fermions*. Cambridge University Press, (1997).

[157] Kouwenhoven, L. and Glazman, L. *Physics World* **33** (2001).

[158] Ternes, M., Heinrich, A. J., and Schneider, W.-D. *J. Phys.: Condens. Matter* **21**(5), 053001 (19pp) (2009).

[159] Goldhaber-Gordon, D., Göres, J., Kastner, M. A., Shtrikman, H., Mahalu, D., and Meirav, U. *Phys. Rev. Lett.* **81**(23), 5225–5228 (1998).

[160] Schrieffer, J. R. and Wolff, P. A. *Phys. Rev.* **149**(2), 491–492 (1966).

[161] Haldane, F. D. M. *Phys. Rev. Lett.* **40**, 416–419 (1978).

[162] Choi, T., Bedwani, S., Rochefort, A., Chen, C.-Y., Epstein, A. J., and Gupta, J. A. *Nano Lett.* **10**(10), 4175–4180 (2010).

[163] Otte, A. F., Terne, s. M., von Bergmann, K., Loth, S., Brune, H., Lutz, C. P., Hirjibehedin, C. F., and Heinrich, A. J. *Nat. Phys.* **4**, 847 (2008).

[164] Madhavan, V., Chen, W., Jamneala, T., Crommie, M. F., and Wingreen, N. S. *Phys. Rev. B* **64**(16), 165412 (2001).

[165] Zhao, A., Li, Q., Chen, L., Xiang, H., Wang, W., Pan, S., Wang, B., Xiao, X., Yang, J., Hou, J. G., and Zhu, Q. *Science* **309**(5740), 1542–1544 (2005).

[166] Gao, L., Ji, W., Hu, Y. B., Cheng, Z. H., Deng, Z. T., Liu, Q., Jiang, N., Lin, X., Guo, W., Du, S. X., Hofer, W. A., Xie, X. C., and Gao, H.-J. *Phys. Rev. Lett.* **99**(10), 106402 (2007).

[167] Goldhaber-Gordon, D., Shtrikman, H., Mahalu, D., Abusch-Magder, D., Meirav, U., and Kastner, M. A. *Nature* **391**(6663), 156–159 (1998).

[168] Madhavan, V., Chen, W., Jamneala, T., Crommie, M. F., and Wingreen, N. S. *Science* **280**(5363), 567–569 (1998).

[169] Li, J., Schneider, W.-D., Berndt, R., and Delley, B. *Phys. Rev. Lett.* **80**, 2893–2896 (1998).

[170] Plihal, M. and Gadzuk, J. W. *Phys. Rev. B* **63**, 085404 (2001).

[171] Abrikosov, A. *Physics* **2**, 5–20 (1965).

[172] Suhl, H. *Phys. Rev.* **138**, A515–A523 (1965).

[173] Fano, U. *Phys. Rev.* **124**(6), 1866–1878 (1961).

[174] Cornaglia, P. S. and Balseiro, C. A. *Phys. Rev. B* **67**, 205420 (2003).

[175] Nagaoka, K., Jamneala, T., Grobis, M., and Crommie, M. F. *Phys. Rev. Lett.* **88**(7), 077205 (2002).

[176] Acker, D. S. and Hertler, W. R. *J. Am. Chem. Soc.* **84**(17), 3370–3374 (1962).

[177] Acker, D. S., Harder, R. J., Hertler, W. R., Mahler, W., Melby, L. R., Benson, R. E., and Mochel, W. E. *J. Am. Chem. Soc.* **82**(24), 6408–6409 (1960).

[178] Milin, B., Pou-Amrigo, R., Viruela, R., and Ort, E. *J. Molec. Struct. (Theochem)* **709**(1-3), 97 – 102 (2004).

[179] Faulques, E., Leblanc, A., Molini, P., Decoster, M., Conana, F. Guerchais, J., and Sala-Pala., J. *Spectrochimica Acta* **51**, 805–819 (1995).

[180] Milin, B., Pou-Amrigo, R., Viruela, R., and acute accent], E. O. *Chem. Phys. Lett.* **391**(1-3), 148 – 151 (2004).

[181] Murgich, J. *J. Chem. Phys* **68**(2), 611–615 (1978).

[182] Murgich, J. *J. Chem. Phys* **68**(2), 611–615 (1978).

[183] Melby, L. R., Harder, R. J., Hertler, W. R., Mahler, W., Benson, R. E., and Mochel, W. E. *J. Am. Chem. Soc.* **84**(17), 3374–3387 (1962).

[184] Umland, T. C., Allie, S., Kuhlmann, T., and Coppens, P. *J. Phys. Chem.* **92**(22), 6456–6460 (1988).

[185] Murgich, J. and Pissanetzky, S. *Chem. Phys. Lett.* **18**(3), 420 – 422 (1973).

[186] Jonkman, H. T., van der Velde, G. A., and Nieuwpoort, W. C. *Chem. Phys. Lett.* **25**(1), 62 – 65 (1974).

[187] Khanna, S. K., Bright, A. A., Garito, A. F., and Heeger, A. J. *Phys. Rev. B* **10**(6), 2139–2143 (1974).

[188] Torrance, J. B. *Acc. Chem. Res.* **12**(3), 79–86 (1979).

[189] Roder, H., Hahn, E., Brune, H., Bucher, J.-P., and Kern, K. *Nature* **366**, 141–143 (1993).

[190] Lukas, S., Witte, G., and Wöll, C. *Phys. Rev. Lett.* **88**, 028301 (2001).

[191] Gambardella, P., Blanc, M., Brune, H., Kuhnke, K., and Kern, K. *Phys. Rev. B* **61**, 2254–2262 (2000).

[192] Murray, P. W., Brookes, I. M., Haycock, S. A., and Thornton, G. *Phys. Rev. Lett.* **80**, 988–990 (1998).

[193] Cai, J., Ruffieux, P., Jaafar, R. ., Bieri, M., Braun, T., Blankenburg, S., Muoth, M., Seitsonen, A. P., Saleh, M., Feng, X., Mullen, K., and Fasel, R. *Nature* **466**, 470–473 (2010).

[194] Torrance, J. B. and Silverman, B. D. *Phys. Rev. B* **15**(2), 788–801 (1977).

[195] Metzger, R. M. and Bloch, A. N. *J. Chem. Phys* **63**(12), 5098–5107 (1975).

[196] Palermo, V., Palma, M., and Samor, P. *AdV. Mater.* **18**(2), 145–164 (2006).

[197] Mohn, F., Gross, L., Moll, N., and Meyer, G. *Nat. Nano.* **7**(4), 227–231 (2012).

[198] Bennewitz, R., Barwich, V., Bammerlin, M., Loppacher, C., Guggisberg, M., Baratoff, A., Meyer, E., and Güntherodt, H.-J. *Surf. Sci.* **438**(1-3), 289 – 296 (1999).

[199] Repp, J., Meyer, G., and Rieder, K.-H. *Phys. Rev. Lett.* **92**, 036803 (2004).

[200] Torrente, I. F., Franke, K. J., and Pascual, J. I. *Int. J. Mass Spectrom.* **277**(1-3), 269 – 273 (2008).

[201] Konno, M. and Saito, Y. *Acta Crystallogr. Sect. B* **30**(5), 1294–1299 (1974).

[202] Konno, M. and Saito, Y. *Acta Crystallogr. Sect. B* **31**(8), 2007–2012 (1975).

[203] Mo, X.-L., Chen, G.-R., Cai, Q.-J., Fan, Z.-Y., Xu, H.-H., Yao, Y., Yang, J., Gu, H.-H., and Hua, Z.-Y. *Thin Solid Films* **436**(2), 259 – 263 (2003).

[204] Farges, J., Brau, A., and Dupuis, P. *Sol. Stat. Comm.* **54**(6), 531 – 535 (1985).

[205] Mass Jr., E. T. *Mater. Res. Bull.* **9**(6), 815 – 826 (1974).

[206] Berzinsh, U., Gustafsson, M., Hanstorp, D., Klinkmüller, A., Ljungblad, U., and Mårtensson-Pendrill, A.-M. *Phys. Rev. A* **51**, 231–238 (1995).

[207] Sansonetti, J., Martin, W., and Young, S. *Handbook of Basic Atomic Spectroscopic Data.* National Institute of Standards and Technology, (2005).

[208] Ashcroft, N. W. and Mermin, N. D. *Festkörperphysik.* Oldenbourg, (2005).

[209] Metzger, R. M., Arafat, E. S., and Kuoff, C. S. *J. Chem. Phys* **78**(5), 2706–2709 (1983).

[210] Kresse, G. and Furthmüller, J. *Phys. Rev. B* **54**, 11169–11186 (1996).

[211] Kresse, G. and Joubert, D. *Phys. Rev. B* **59**, 1758–1775 (1999).

[212] Klimeš, J., Bowler, D. R., and Michaelides, A. *Phys. Rev. B* **83**, 195131 (2011).

[213] Faraggi, M. N., Jiang, N., Gonzalez-Lakunza, N., Langner, A., Stepanow, S., Kern, K., and Arnau, A. *J. Phys. Chem. C* **116**(46), 24558–24565 (2012).

[214] Jono, R., Fujisawa, J.-i., Segawa, H., and Yamashita, K. *J. Phys. Chem. Lett.* **2**(10), 1167–1170 (2011).

[215] Ujsaghy, O., Kroha, J., Szunyogh, L., and Zawadowski, A. *Phys. Rev. Lett.* **85**(12), 2557–2560 (2000).

[216] Romero, M. and Aligia, A. A. *Phys. Rev. B* **83**, 155423 (2011).

[217] Zhao, A., Hu, Z., Wang, B., Xiao, X., Yang, J., and Hou, J. G. *J. Chem. Phys* **128**(23), 234705 (2008).

[218] Kanai, K., Akaike, K., Koyasu, K., Sakai, K., Nishi, T., Kamizuru, Y., Nishi, T., Ouchi, Y., and Seki, K. *Appl. Phys. A Mater. Sci. Process* **95**, 309–313 (2009).

[219] Sohnchen, S., Lukas, S., and Witte, G. *J. Chem. Phys* **121**(1), 525–534 (2004).

[220] Ponder, J. W. and Richards, F. M. *J. Comp. Chem.* **8**(7), 1016–1024 (1987).

[221] Allinger, N. L., Li, F., Yan, L., and Tai, J. C. *J. Comp. Chem.* **11**(7), 868–895 (1990).

[222] Braun, S. and Salaneck, W. R. *Chem. Phys. Lett.* **438**(4-6), 259 – 262 (2007).

[223] Rangger, G. M., Hofmann, O. T., Romaner, L., Heimel, G., Bröker, B., Blum, R.-P., Johnson, R. L., Koch, N., and Zojer, E. *Phys. Rev. B* **79**(16), 165306 (2009).

[224] Wu, S. W., Ogawa, N., and Ho, W. *Science* **312**(5778), 1362–1365 (2006).

[225] Knorr, N., Schneider, M. A., Diekhöner, L., Wahl, P., and Kern, K. *Phys. Rev. Lett.* **88**(9), 096804 Feb (2002).

[226] Huang, P. and Carter, E. A. *Nano Lett.* **8**(4), 1265–1269 (2008).

[227] Mugarza, A., Krull, C., Robles, R., Stepanow, S., Ceballos, G., and Gambardella, P. *Nat. Commun.* **2**, 490– (2011).

[228] Perera, U. G. E., Kulik, H. J., Iancu, V., Dias da Silva, L. G. G. V., Ulloa, S. E., Marzari, N., and Hla, S.-W. *Phys. Rev. Lett.* **105**, 106601 (2010).

[229] Iancu, V., Deshpande, A., and Hla, S.-W. *Nano Lett.* **6**(4), 820–823 (2006).

[230] Iancu, V., Deshpande, A., and Hla, S.-W. *Phys. Rev. Lett.* **97**(26), 266603 (2006).

[231] Leoni, T., Guillermet, O., Walch, H., Langlais, V., Scheuermann, A., Bonvoisin, J., and Gauthier, S. *Phys. Rev. Lett.* **106**, 216103 (2011).

[232] Park, H., Park, J., Lim, A. K. L., Anderson, E. H., Alivisatos, A. P., and McEuen, P. L. *Nature* **407**(6800), 57–60 (2000).

[233] Park, J., Pasupathy, A. N., Goldsmith, J. I., Chang, C., Yaish, Y., Petta, J. R., Rinkoski, M., Sethna, J. P., Abruna, H. D., McEuen, P. L., and Ralph, D. C. *Nature* **417**(6890), 722–725 (2002).

[234] Tao, N. J. *Nat. Nano.* **1**(3), 173–181 (2006).

[235] Haddon, R. C., Hebard, A. F., Rosseinsky, M. J., Murphy, D. W., Duclos, S. J., Lyons, K. B., Miller, B., Rosamilia, J. M., Fleming, R. M., Kortan, A. R., Glarum, S. H., Makhija, A. V., Muller, A. J., Eick, R. H., Zahurak, S. M., Tycko, R., Dabbagh, G., and Thiel, F. A. *Nature* **350**(6316), 320–322 (1991).

[236] Pfeiffer, M., Leo, K., Zhou, X., Huang, J., Hofmann, M., Werner, A., and Blochwitz-Nimoth, J. *Organ. Electron.* **4**(2-3), 89 – 103 (2003).

[237] Yamachika, R., Grobis, M., Wachowiak, A., and Crommie, M. F. *Science* **304**(5668), 281–284 (2004).

[238] Epstein, A. J., Lipari, N. O., Sandman, D. J., and Nielsen, P. *Phys. Rev. B* **13**(4), 1569–1579 (1976).

[239] Hubbard, J. *Phys. Rev. B* **17**(2), 494–505 (1978).

[240] Berger, P. A., Dahm, D. J., Johnson, G. R., Miles, M. G., and Wilson, J. D. *Phys. Rev. B* **12**(10), 4085–4089 (1975).

[241] Pouget, J., Khanna, S., Denoyer, F., Comés, R., Garito, A., and Heeger, A. *Phys. Rev. Lett.* **37**, 437 (1976).

[242] Berlinsky A. J., C. J. F. and Larry, W. *Candian Journal of Chemistry* **52**, 3373–3377 (1974).

[243] Engler, E. M., Kaufman, F. B., Green, D. C., Klots, C. E., and Compton, R. N. *J. Am. Chem. Soc.* **97**(10), 2921–2922 (1975).

[244] Hesper, R., Tjeng, L. H., and Sawatzky, G. A. *Europhys. Lett.* **40**(2), 177–182 (1997).

[245] Carbone, C., Gardonio, S., Moras, P., Lounis, S., Heide, M., Bihlmayer, G., Atodiresei, N., Dederichs, P. H., Bgel, S., Vlaic, S., Lehnert, A., Ouazi, S., Rusponi, S., Brune, H., Honolka, J., Enders, A., Kern, K., Stepanow, S., Krull, C., Balashov, T., Mugarza, A., and Gambardella, P. *Adv. Funct. Mater.* **21**(7), 1212–1228 (2011).

[246] Bader, S. D. *Rev. Mod. Phys.* **78**, 1–15 (2006).

[247] Khajetoorians, A. A., Wiebe, J., Chilian, B., and Wiesendanger, R. *Science* **332**(6033), 1062–1064 (2011).

[248] Tsukahara, N., Shiraki, S., Itou, S., Ohta, N., Takagi, N., and Kawai, M. *Phys. Rev. Lett.* **106**(18), 187201 (2011).

[249] Franke, K. J., Schulze, G., and Pascual, J. I. *Science* **332**(6032), 940–944 (2011).

[250] Wende, H., Bernien, M., Luo, J., Sorg, C., Ponpandian, N., Kurde, J., Miguel, J., Piantek, M., Xu, X., Eckhold, P., Kuch, W., Baberschke, K., Panchmatia, P. M., Sanyal, B., Oppeneer, P. M., and Eriksson, O. *Nat. Mater.* **6**(7), 516–520 (2007).

[251] Hermanns, C. F., Tarafder, K., Bernien, M., Krüger, A., Chang, Y.-M., Oppeneer, P. M., and Kuch, W. *AdV. Mater.* **25**(25), 3473–3477 (2013).

[252] Fabris, S., Stepanow, S., Lin, N., Gambardella, P., Dmitriev, A., Honolka, J., Baroni, S., and Kern, K. *Nano Lett.* **11**(12), 5414–5420 (2011).

[253] McCleverty, J. A. and Ward, M. D. *Acc. Chem. Res.* **31**(12), 842–851 (1998).

[254] Repp, J., Meyer, G., Rieder, K.-H., and Hyldgaard, P. *Phys. Rev. Lett.* **91**, 206102 (2003).

[255] Morrish, A. H. *The Physical Principles of Magnetism*. John Wiley & Sons Ltd., (1966).

[256] White, R. M. *Quantum Theory of Magnetism*. Springer-Verlag Berlin Heidelberg, (2006).

[257] Hirjibehedin, C. F., Lutz., C. P., and Heinrich, A. *Science* **312**, 5776 (2006).

[258] Hirjibehedin, C. F., Lin, C.-Y., Otte, A. F., Ternes, M., Lutz, C. P. Jones, B. A., and Heinrich, A. J. *Science* **317**, 5842 (2007).

[259] Otte, A. F., Ternes, M., Loth, S., Lutz, C. P., Hirjibehedin, C. F., and Heinrich, A. J. *Phys. Rev. Lett.* **103**(10), 107203 (2009).

[260] Tsukahara, N., Noto, K., Ohara, M.and Shiraki, S., Takagi, N., Takata, Y., Miyawaki, J., Taguchi, M., Chainani, A., Shin, S., and Kawai, M. *Phys. Rev. Lett.* **102**, 167203 (2009).

[261] Dai, D., Xiang, H., and Whangbo, M.-H. *J. Comp. Chem.* **29**(13), 2187–2209 (2008).

[262] Pryce, M. H. L. *Proc. Phys. Soc.* **25**, 63 (1950).

[263] Li, M.-X., Miao, Z.-X., Shao, M., Liang, S.-W., and Zhu, S.-R. *Inorg. Chem.* **47**(11), 4481–4489 (2008).

[264] Marschall, M., Reichert, J., Weber-Bargioni, A., Seufert, K., Auwärter, W., Klyatskaya, S., Zoppellaro, G., Ruben, M., and Barth, J. V. *Nat. Chem.* **2**(2), 131–137 (2010).

[265] Wang, W., Shi, X., Wang, S., Liu, J., Van Hove, M. A., Liu, P. N., Zhang, R.-Q., and Lin, N. *Phys. Rev. Lett.* **110**, 046802 (2013).

[266] Liu, J., Lin, T., Shi, Z., Xia, F., Dong, L., Liu, P. N., and Lin, N. *J. Am. Chem. Soc.* **133**(46), 18760–18766 (2011).

[267] Henningsen, N., Rurali, R., Limbach, C. Drost, R., Pascual, J., and Franke, K. J. *J. Phys. Chem. Lett.* **2**, 55–61 (2011).

[268] Pivetta, M., Pacchioni, G. E., Schlickum, U., Barth, J. V., and Brune, H. *Phys. Rev. Lett.* **110**, 086102 (2013).

[269] Martnez-Galera, A. J., de la Torre, B., Ugeda, M. M., and Gomez-Rodriguez, J. M. *J. Phys. Chem. C* **116**(17), 9568–9574 (2012).

[270] Hermann, K. and Pettersson, L. G. M. (2011).

[271] Hammer, B., Hansen, L. B., and Nôrskov, J. K. *Phys. Rev. B* **59**, 7413–7421 (1999).

[272] Perdew, J. P., Burke, K., and Ernzerhof, M. *Phys. Rev. Lett.* **77**, 3865–3868 (1996).

[273] Frenking, G. and Fröhlich, N. *Chemical Reviews* **100**(2), 717–774 (2000).

[274] Bagus, P. S., Hermann, K., and Charles W. Bauschlicher, J. *The Journal of Chemical Physics* **81**(4), 1966–1974 (1984).

[275] Kortright, J. B., Lincoln, D. M., Edelstein, R. S., and Epstein, A. J. *Phys. Rev. Lett.* **100**(25), 257204 (2008).

[276] Kuch, W., Salvietti, M., Gao, X., Lin, M.-T., Klaua, M., Barthel, J., Mohan, C. V., and Kirschner, J. *Phys. Rev. B* **58**, 8556–8565 (1998).

[277] Ebert, H., Stöhr, J., Parkin, S. S. P., Samant, M., and Nilsson, A. *Phys. Rev. B* **53**, 16067–16073 (1996).

[278] Meier, F., Zhou, L., Wiebe, J., and Wiesendanger, R. *Science* **320**(5872), 82–86 (2008).

[279] Chen, X., Fu, Y.-S., Ji, S.-H., Zhang, T., Cheng, P., Ma, X.-C., Zou, X.-L., Duan, W.-H., Jia, J.-F., and Xue, Q.-K. *Phys. Rev. Lett.* **101**(19), 197208 (2008).

[280] Wahl, P., Simon, P., Diekhoner, L., Stepanyuk, V. S., Bruno, P., Schneider, M. A., and Kern, K. *Phys. Rev. Lett.* **98**(5), 056601 (2007).

[281] Ma, J. C. and Dougherty, D. A. *Chem. Rev.* **97**(5), 1303–1324 (1997).

[282] Dougherty, D. A. *Acc. Chem. Res.* **46**(4), 885–893 (2013).

[283] Mahadevi, A. S. and Sastry, G. N. *Chem. Rev.* **113**(3), 2100–2138 (2013).

[284] Kumpf, R. and Dougherty, D. *Science* **261**(5129), 1708–1710 (1993).

[285] Burley, S. and Petsko, G. *Science* **229**(4708), 23–28 (1985).

[286] Hunter, C. A., Lawson, K. R., Perkins, J., and Urch, C. J. *J. Chem. Soc., Perkin Trans. 2* , 651–669 (2001).

[287] Flechtner, K., Kretschmann, A., Steinrck, H.-P., and Gottfried, J. M. *J. Am. Chem. Soc.* **129**(40), 12110–12111 (2007).

[288] Isvoranu, C., Knudsen, J., Ataman, E., Schulte, K., Wang, B., Bocquet, M.-L., Andersen, J. N., and Schnadt, J. *J. Chem. Phys* **134**(11), 114711 (2011).

[289] Repp, J., Meyer, G., Stojković, S. M., Gourdon, A., and Joachim, C. *Phys. Rev. Lett.* **94**(2), 026803 (2005).

[290] Takada, M. and Tada, H. *Chem. Phys. Lett.* **392**(1-3), 265 – 269 (2004).

[291] Mikaelian, G., Ogawa, N., Tu, X. W., and Ho, W. *J. Chem. Phys* **124**(13), 131101 (2006).

[292] Nazin, G. V., Qiu, X. H., and Ho, W. *Phys. Rev. Lett.* **95**(16), 166103 (2005).

[293] van der Laan, G. and Kirkman, I. W. *J. Phys.: Condens. Matter* **4**(16), 4189 (1992).

[294] Zheng, F., Parez-Dieste, V., McChesney, J., Luk, Y.-Y., Abbott, N. L., and Himpsel, F. *Surf. Sci.* **587**(3), L191 – L196 (2005).

[295] Regan, T. J., Ohldag, H., Stamm, C., Nolting, F., Lüning, J., Stöhr, J., and White, R. L. *Phys. Rev. B* **64**, 214422 (2001).

[296] Halcrow, M. A. *Polyhedron* **26**(14), 3523 – 3576 (2007).

[297] Cowan, R. D. *The Theory of Atomic Structure and Spectra*. Univ. California Press, Berkeley, (1981).

[298] Stavitski, E. and de Groot, F. M. *Micron* **41**(7), 687 – 694 (2010).

[299] Mermin, N. D. and Wagner, H. *Phys. Rev. Lett.* **17**, 1133–1136 (1966).

[300] Bruno, P. *MRS Proceedings* **231** (1991).

[301] Fischer, B. and Klein, M. W. *Phys. Rev. B* **11**(5), 2025–2029 (1975).

[302] Bal-Monod, M. T. *Phys. Rev. B* **36**, 8835–8836 (1987).

[303] Hyldgaard, P. and Persson, M. *J. Phys.: Condens. Matter* **12**(1), L13 (2000).

[304] Patrone, P. N. and Einstein, T. L. *Phys. Rev. B* **85**, 045429 (2012).

[305] Zhou, L., Wiebe, J., Lounis, S., Vedmedenko, E., Meier, F., Blügel, S., Dederichs, P. H., and Wiesendanger, R. *Nat. Phys.* **6**(3), 187–191 (2010).

[306] Stepanyuk, V. S., Baranov, A. N., Tsivlin, D. V., Hergert, W., Bruno, P., Knorr, N., Schneider, M. A., and Kern, K. *Phys. Rev. B* **68**, 205410 (2003).

[307] Simon, E., Újfalussy, B., Lazarovits, B., Szilva, A., Szunyogh, L., and Stocks, G. M. *Phys. Rev. B* **83**, 224416 (2011).

[308] Reinert, F., Nicolay, G., Schmidt, S., Ehm, D., and Hüfner, S. *Phys. Rev. B* **63**(11), 115415 (2001).

[309] Bellini, V., Lorusso, G., Candini, A., Wernsdorfer, W., Faust, T. B., Timco, G. A., Winpenny, R. E. P., and Affronte, M. *Phys. Rev. Lett.* **106**, 227205 (2011).

[310] Zhang, X. and Wang, J. *The Journal of Physical Chemistry A* **112**(2), 296–304 (2008). PMID: 18085759.

[311] Pandey, R., Rao, B. K., Jena, P., and Blanco, M. A. *Journal of the American Chemical Society* **123**(16), 3799–3808 (2001).

[312] Diefenbach, M. and Trage, C. S. H. *Helv. Chem. Acta* **86**, 1008 (2003).

[313] Kogan, A., Amasha, S., Goldhaber-Gordon, D., Granger, G., Kastner, M. A., and Shtrikman, H. *Phys. Rev. Lett.* **93**, 166602 (2004).

[314] Pascual, J. and Lorente, N. *Single-molecule Vibrational Spectroscopy and Chemistry*. World Scientific, (2006).

[315] Shi, X. Q., Lin, C., Minot, C., Tseng, T.-C., Tait, S. L., Lin, N., Zhang, R. Q., Kern, K., Cerda, J. I., and Van Hove, M. A. *J. Phys. Chem. C* **114**(40), 17197–17204 (2010).

[316] Kutzelnigg, W., Fleischer, U., and Schindler, M. *NMR Basic Principles and Progress*. Springer, Berlin, New York, (1990).

[317] Nyberg, M. PhD thesis, Stockholm University, (2000).

[318] Pettersson, L. G. M., Wahlgren, U., and Gropen, O. *J. Chem. Phys.* **86**, 2176–2184 (1987).

[319] Cavalleri, M., Hermann, K., Knop-Gericke, A., Hvecker, M., Herbert, R., Hess, C., Oestereich, A., Dbler, J., and Schlgl, R. *J. Catal.* **262**, 215–223 (2009).

[320] Triguero, L., Pettersson, L. G. M., and gren, H. *Phys. Rev. B* **58**, 8097–8110 (1998).

[321] Ågren, H., Carravetta, V., Vahtras, O., and Pettersson, L. G. M. *Chem. Phys. Lett.* **222**, 75–81 (1994).

[322] Slater, J. C. and Johnson, K. H. *Phys. Rev. B* **5**, 844–853 (1972).

[323] Takahashi, O. and Pettersson, L. G. M. *J. Chem. Phys.* **121**, 10339–10345 (2004).

[324] Leetmaa, M., Ljungberg, M. P., Lyubartsev, A., Nilsson, A., and Pettersson, L. G. M. *J. Electr. Spectr. Rel. Phen.* **177**, 135–157 (2010).

[325] Kolczewski, C., Puttner, R., Plashkevych, O., Agren, H., Staemmler, V., Martins, M., Snell, G., Schlachter, A. S., Sant'Anna, M., Kaindl, G., and Pettersson, L. G. M. *J. Chem. Phys* **115**(14), 6426–6437 (2001).

[326] Kolczewski, C. and Hermann, K. *J. Chem. Phys* **118**(16), 7599–7609 (2003).

[327] Kolczewski, C., Puttner, R., Martins, M., Schlachter, A. S., Snell, G., Sant'Anna, M. M., Hermann, K., and Kaindl, G. *J. Chem. Phys* **124**(3), 034302 (2006).

[328] Cavalleri, M., Naslund, L.-A., Edwards, D. C., Wernet, P., Ogasawara, H., Myneni, S., Ojamae, L., Odelius, M., Nilsson, A., and Pettersson, L. G. M. *J. Chem. Phys* **124**(19), 194508 (2006).

[329] Wernet, P., Nordlund, D., Bergmann, U., Cavalleri, M., Odelius, M., Ogasawara, H., Näslund, L. A., Hirsch, T. K., Ojamäe, L., Glatzel, P., Pettersson, L. G. M., and Nilsson, A. *Science* **304**(5673), 995–999 (2004).

[330] Öström, H., Ogasawara, H., Näslund, L.-A., Pettersson, L. G. M., and Nilsson, A. *Phys. Rev. Lett.* **96**, 146104 (2006).

[331] Schiros, T., Haq, S., Ogasawara, H., Takahashi, O., Öström, H., Andersson, K., Pettersson, L., Hodgson, A., and Nilsson, A. *Chem. Phys. Lett.* **429**(4-6), 415 – 419 (2006).

[332] Cavalleri, M., Hermann, K., Guimond, S., Romanyshyn, Y., Kuhlenbeck, H., and Freund, H.-J. *Catalysis Today* **124**(1-2), 21 – 27 (2007).

[333] Guo, C. S., Hermann, K., Hävecker, M., Thielemann, J. P., Kube, P., Gregoriades, L. J., Trunschke, A., Sauer, J., and Schlögl, R. *J. Phys. Chem. C* **115**(31), 15449–15458 (2011).

[334] Piantek, M., Miguel, J., Krüger, A., Navío, C., Bernien, M., Ball, D. K., Hermann, K., and Kuch, W. *J. Phys. Chem. C* **113**(47), 20307–20315 (2009).

[335] Guo, C. S., Sun, L., Hermann, K., Hermanns, C. F., Bernien, M., and Kuch, W. *J. Chem. Phys* **137**(19), 194703 (2012).

Acknowledgments

Firstly, I want to thank Prof. Katharina Franke for giving me the opportunity of working in her group and for the support and motivation during the last years. I deeply thank her for her scientific advice and her open ear for any kind of problem.

I also want to express my special thanks to Prof. Wolfgang Kuch, who always was a great help in any respect and for reading my thesis.

I would also like to thank Prof. Nacho Pascual for his help and teaching me some of his huge knowledge on physics. I furthermore want to thank all the members of the AG Franke, AG Pascual and AG Kuch for the positive social environment: Isabel Fernández-Torrente, Paul Stoll, Zechao Yang, Gelavizh Ahmadi, Bo Chen, Xianwen Chen, Martina Corso, Robert Drost, Nino Hatter, Benjamin Heinrich, Michael Kleinert, Janina Ladenthin, Anna Strozecka, Christian Lotze, Fabian Schulz, and Gunnar Schulze. Special thanks go to Isa for teaching me how to use a STM and for proof-reading of the present thesis.

I owe a lot to Felix Hermanns, Alex Krüger and Matthias Bernien with whom I had the pleasure to spend weeks at BESSY and the ESRF. I enjoy remembering the great cafeteria with its great food at the ESRF. In this respect I also want to thank the technical staff of the two synchrotons: Violetta Sessi, Kurt Kummer, Nick Brookes, and Eugen Weschke

My gratitude goes also to Birgit Darbisch, always helping with the bureaucracy, and to Christian Roth, who was a great help regarding all technical questions about STM.

I also have to mention the fruitful collaboration with the theory groups of Prof. M. Persson, Dr. R. Rurali, Dr L. Sun, and Prof. K. Hermann supporting us with theoretical simulations helping us to interpret our observations and results.

Last but not least, I want to express all my gratitude to my family, friends and specially to Alena. They always remembered me also to enjoy live. The most important thing.

It is gratefully acknowledged the financial support from the Sfb 658.